Nanomechanical
Quantum Systems

Sample: IndCoupV7_C5   Operator: Philip E. Schmidt   Time span: 2015-2019

Der Anfang ist nicht das reine Nichts, sondern ein Nichts, von dem etwas ausgehen soll; es ist zugleich das Seyn schon enthalten. Der Anfang enhält also beydes, Seyn und Nichts; ist die Einheit von Seyn und Nichts; - oder ist Nichtseyn, das zugleich Seyn und Seyn, das zugleich Nichtseyn ist.

Georg W. F. Hegel, *Wissenschaft der Logik*, Band **1**, Nürnberg 1812

TECHNISCHE UNIVERSITÄT MÜNCHEN

Lehrstuhl E23 für Technische Physik

Walther-Meißner-Institut für Tieftemperaturforschung
der Bayerischen Akademie der Wissenschaften

Nanomechanical Quantum Systems

Philip Ernst Schmidt

Vollständiger Abdruck der von der Fakultät für Physik der Technischen
Universität München zur Erlangung des akademischen Grades eines

Doktors der Naturwissenschaften

genehmigten Dissertation.

Vorsitzender: Prof. Dr. Michael Knap

Prüfer der Dissertation: 1. Prof. Dr. Rudolf Gross

2. Prof. Dr. Menno Poot

Abstract

The decay of quantum mechanical states with high masses remains experimentally not tested even after 120 years of quantum mechanics. This arises from the difficulty of the generation of massive quantum objects. Cavity optomechanics is a promising approach to address this fundamental question. In this thesis we investigate doubly-clamped nanomechanical aluminum string oscillators coupled to quantum electrodynamical circuits, based on superconducting microwave resonators containing Josephson junctions which act as lossless nonlinear inductors. The Josephson junctions are either integrated into the resonator or part of a quantum bit element coupled to an electromechanical resonator. With our coupling scheme, we realize for the first time an inductive coupling between a nanomechanical and an electronic resonator with a coupling strength exceeding previously reported values. We theoretically study the physics of the coupled electromechanical system, discuss the basics of electromechanics and address the key features of quantum electrodynamical circuits including the imposed limitations in the photon number by the Josephson junctions. We also derive the noise contributions and assess them in the context of low photon numbers. We also acquaint the experimental setups and present a cryogenic interferometer that allows to measure mechanical motion with microwaves for low radiation pressures. Moreover we set up an experiment for the investigation of quantum bits in the time domain.

The first nanomechanical system studied consists of a transmon qubit and a nanomechanical string oscillator that are capacitively coupled to a microwave resonator. This configuration allows for an individual control of both elements and thus a read-out of the microwave resonator's photon occupation spanning over a range of nine orders of magnitude from lowest to highest detected excitation. In addition, we resolve the decoherence of the quantum bit coupled to the electromechanical resonator, which is limited by the dephasing of the qubit state.

We further derive an expression for the strength of the inductive coupling presented in the second sample. We show that theoretically the coupling strength can be tuned either by the applied magnetic field, or by varying the resonance frequency of the microwave resonator. Both tuning possibilities are then confirmed experimentally and the total coupling strength of $1.6\,\mathrm{kHz}$ is determined by microwave spectroscopy of the mechanically induced sidebands for the string being in thermal equilibrium. This allows to gain insight into the noise contributions. The noise analysis shows that a sub-attonewton force precision is achievable in the low photon number regime. Moreover, the nanostring is externally driven, which leads to mechanical sidebands of the microwave resonance frequency. By this we can measure phonon numbers of the order of several billions. We conclude by

discussing possible future research lines.

The results presented in this work are an important step towards the investigation of macroscopic quantum states, allow for new sensing applications and the storage of quantum information in mechanical states.

Zusammenfassung

Der Zerfall quantenmechanischer Zuständen mit hohen Massen ist auch nach 120 Jahren seit Entdeckung der Quantenmechanik experimentell nicht überprüft. Dies beruht auf der schwierigen Erzeugung von massiven Quantenobjekten. Hohlraum-Optomechanik is ein vielversprechender Ansatz um diese fundamentale Frage zu beantworten. In dieser Arbeit untersuchen wir doppelt eingespannte nanomechanische Saitenoszillatoren aus Aluminium die an quantenelektrodynamische Schaltkreise gekoppelt sind, welche aus supraleitenden Mikrowellenresonatoren mit Josephson Kontakten bestehen, die wiederum als verlustfreie nichtlineare Induktivitäten dienen. Die Josephson Kontakte sind entweder im Resonator integriert oder als Teil eines Quantenbits an einen elektromechanischen Resonator gekoppelt. Mit unserem Kopplungsschema realisieren wir erstmalig eine induktive Kopplung zwischen nanomechanischen und elektrischem Resonator mit einer Kopplungstärke größer als bisher berichtet.

Wir untersuchen die Theory des gekoppelten elektromechanischen Systems, diskutieren die Grundlagen der Elektromechanik und besprechen grundlegende Eigenschaften von quantenelektrodynamischen Schaltkreisen inklusive der Limitierungen in der Photonenzahl durch die Josephson Kontakte. Außerdem untersuchen wir die Rauschanteile und bewerten diese im Zusammenhang mit geringen Photonenzahlen.

Wir erläutern auch die experimentellen Aufbauten und stellen ein kryogenes Interferometer vor, dass die Untersuchung mechanischer Auslenkungen bei niedrigem Strahlendruck erlaubt. Zusätzlich installieren wir ein Experiment zur Untersuchung von zeitlichen Abläufen bei Quantenbits.

Das erste untersuchte nanomechanische System besteht aus einem Transmon-Quantenbit und einer nanomechanischen Saite die jeweils beide kapazitiv an einen Mikrowellenresonator gekoppelt sind. Diese Konfiguration erlaubt die individuelle Kontrolle beider Elemente und dadurch eine Auslese der Photonenzahl des Mikrowellenresonators über neun Größenordnungen zwischen niedrigster und höchster Besetzung. Zusätzlich bestimmen wir die Kohärenz des Quantenbits, das an den Resonator gekoppelt ist, welche durch die Dephasierung des Quantenbit-Zustandes limitiert ist.

Ferner berechnen wir eine Gleichung für die Stärke induktiven Kopplung bei der zweiten Probe. Wir zeigen, dass die theoretische Kopplung entweder durch das angelegte magnetische Feld oder durch Variation der Resonanzfrequenz des Mikrowellenresonators eingestellt werden kann. Beide Einstellmöglichkeiten werden dann experimentell bestätigt und eine maximale Stärke von 1.62 kHz bestimmt, unter Zuhilfenahme von Mikrowellenspektroskopie der mechanisch induzierten Seitenbänder der Saite im thermischen Gleichgewicht.

Dies erlaubt uns auch Einblick in die Rauschanteile. Diese Rauschanalyse zeigt, dass eine Kraftsauflösung unterhalb von atto-Newton mit niedrigen Photonenzahlen erreicht wird. Zudem wird die Nanosaite auch extern angeregt, was zu mechanischen Seitenbändern des Mikrowellenresonators führt. Dadurch können Phononenzahlen im Bereich mehrerer Milliarden gemessen werden. Wir beenden die Untersuchungen mit einem Ausblick auf weitere mögliche Studien.

Die Ergebnisse in dieser Arbeit stellen einen wichtigen Schritt zur Untersuchung von makroskopischen Quantenzuständen dar, sie zeigen neue Anwendungen in der Sensorik, sowie die Speicherung von Quanteninformation in mechanischen Zuständen.

Contents

Chapter 1

Introduction

The worthwhile problems are the ones you can really solve or help solve, the ones you can really contribute something to. [...] No problem is too small or too trivial if we can really do something about it.

Richard Feynman, [1], 1966

Among all physical foundations, quantum physics might have changed the view on the world the most. This is due to its predictions, like superposition [2], entanglement [3, 4], tunneling [5], being counter-intuitive to our classical world. Of course, even today our everyday life is influenced by quantum physics allowing for the realization of lasers [6] or more recent quantum computers [7], to mention just two examples. However, we do not directly experience quantum physics in our life which is taking place on macroscopic scales where quantum phenomena are not observable. This is referred to as the quantum measurement problem [8], where the question arises, why and how the quantum superposition decays with the particle mass, preventing such observations. Similar, and connected to this issue of massive quantum objects, the question emerges how quantum mechanics relates to gravity.

Since cavity optomechanics can be implemented with systems having masses over 20 orders of magnitude, it seems the ideal candidate to address these challenges [9]. There, the light field of an optical cavity is influenced by a mechanical oscillator, e.g. by mounting one mirror plate on a suspended element. The combination of massive test objects with optical quantum states allows to investigate nature on the Planck-scale [10]. Using optomechanics, recently gravitational waves have been detected for the first time [11]. However, the light-matter interaction is based on the radiation pressure [12], which is a rather low force on the single-photon single-phonon scale. Switching from optical cavities to superconducting microwave resonators, which have a high quality and small mode volume gave rise to the area of (resonator) electromechanics [13]. Using a photon number enhanced radiation pressure (or an effective coupling) the strong coupling regime between microwave resonator and nanomechanical oscillator was entered [14], ground state cooling of the mechanical motion was demonstrated [15] and squeezed states were realized which allow for an enhanced measurement precision [16–18]. Yet, the underlying states of these experiments were all Gaussian (coherent states of harmonic oscillators), as the intrinsic coupling was not sufficient to generate non-gaussian ones, such as Fock states. So nonlinear elements are

required for the generation of arbitrary quantum states. In superconducting circuits, this can be realized by combining linear microwave resonators and Josephson junction based quantum bits, leading to the prospering field of circuit quantum electrodynamics (c-QED) [19, 20]. First experiments on such hybrid systems including superconducting quantum bits and nanomechanical oscillators proved the generation of quantum mechanical states on the picogram scale [21–27].

Recently the study of levitated superconducting micro spheres was proposed [28]. The study of such objects on the ng-scale allows to falsify some common theories on the collapse model [29]. In these experiments dc-SQUIDs are required to detect the motion of the levitating sphere in a magnetic field. So far however, mechanical motion has only been read-out in a direct current configuration [30–33], not via a microwave resonator and so without the capability for sideband cooling of the mechanical motion. Therefor, the detection of the motion via a SQUID integrated in a microwave resonator is desired to study ground state cooled mechanical quantum motion.

Within this thesis we study two hybrid systems based on circuit QED integrating a doubly clamped nanomechanical string resonator. One consists of a transmon qubit and a nanostring capacitively coupled to one and the same microwave resonator. Using both systems we can calibrate the photon numbers in the resonator ranging 9 orders of magnitude from the lowest to highest detected occupation [34]. The second system realizes for the first time a microwave read-out of a mechanical motion via a dc-SQUID, as required for the detection of the levitating quantum spheres. We achieve this by integrating a nanostring in the loop of a dc-SQUID that shunts a microwave resonator as proposed by Ref. [35–38]. By this inductive coupling scheme we find a single photon-phonon coupling of $1.62 \pm 0.12\,\text{kHz}$, which exceeds current realizations in electromechanical resonators, where previously $280\,\text{Hz}$ were found [24]. The remaining thesis is structured as follows:

The key theoretical concepts to provide a general understanding on the electromechanical systems are explained in chapters 2-4. Chapter 2 gives an overview of resonance effects and discusses a classical, driven harmonic oscillator in time and frequency domain. We then derive the results for a quantum mechanical treatment and compare them to the classical result, to summarize the requirements for the observation of nonclassical states. We give a brief overview on the effects of Duffing nonlinearities at the end.

The next chapter 3 introduces the field of superconducting circuits including Josephson junctions as nonlinear elements, which we require for the detection of the string's motion. At first, the single Josephson junction is discussed in detail, followed by the combination of two junctions in a superconducting loop, the so-called dc-SQUID configuration. In addition, we derive potential limitations imposed by the integration of the SQUID. A description of flux tuneable resonators follows. These resonators consist of a microwave coplanar waveguide resonator shunted to ground by a dc-SQUID. Finally, we explore the principles of a transmon qubit. Such c-QED elements will provide the quantum part of this thesis.

Chapter 4 reviews opto- and electromechanical interactions. At first, general optomechanical interactions are discussed, and realizations in nano-electromechanics are introduced. Then, we exploit the mechanical displacement spectra. Also we have a look at the dependence of the electromechanical noise contributions, in particular depending on the photon numbers in the microwave resonator. By the use of nonlinear Josephson elements, some limitations on reachable photon numbers are imposed, so these consideration are of special

interest. Further, we discuss sideband cooling of the mechanical element and the behavior of the microwave resonator when the strings are externally driven.

The experimental, cryogenic environment is introduced in chapter 5. Here, we introduce a cryogenic microwave interferometer for the detection of nonlinear electromechanical circuits. This interferometer allows the detection of mechanical signals with a reduced photon number present in the system. This is of particular interest for nonlinear electromechanical resonators, e.g. when Josephson elements are present. We give a short example based on an electromechanical resonator coupled to a transmon qubit. Afterwards, we introduce a measurement setup for time domain measurements on qubits, and explain the measurement principle, as well as the data acquisition. The chapter concludes with a brief overview of the applied pulse sequences.

A nanomechanical hybrid c-QED device is analyzed in chapter 6. It consists of a microwave resonator that is capacitively coupled to a nanostring oscillator and a transmon qubit. We show the fabrication process, as well as the individual control of the elements, which allow for an ultra-wide range photon number calibration, spanning over nine orders of magnitude. Further, the transmon qubit is investigated in the time domain. We use this study to characterize its decoherence channels. We summarize the time domain results and deduct potential improvements for future sample generations.

Chapter 7 then focuses on inductively coupled nano-electromechanics, that is, a mechanical compliant string oscillator coupled inductively to the Josephson inductance of a flux tunable microwave resonator. The coupling mechanism is based on a mechanical modulation of the SQUID loop. The area change modulates the magnetic flux threading the SQUID loop when a magnetic field is applied. This in turn modulates the SQUID inductance and thereby the eigenfrequency of the microwave resonator. Due to the nonlinearity of the Josephson inductance the single photon-phonon coupling is increased, which is of special interest for the study of quantum mechanical states and realizes a microwave read-out of mechanical motion via SQUID.

Finally in chapter 8 we summarize the results within this thesis and give an outlook on possible future research directions on nanomechanical quantum systems at the Walther-Meißner-Institut.

Chapter 2

The harmonic oscillator

It's always fun to learn something new about quantum mechanics.

Benjamin Schumacher

In this chapter, we give a detailed overview on classical, harmonic oscillators. We describe its excitation in time and frequency domain and analyze the respective decay rates. Further, we discuss the mechanical susceptibility describing the sting's response to an external drive. As the doubly clamped nanostring oscillator is a three dimensional object, we will discuss how the mechanical system and a superconducting microwave resonator can be described as harmonic oscillators. After discussing the classic harmonic oscillator, we will turn to the quantum mechanical harmonic oscillator. We highlight the differences between a classical and quantum mechanical oscillator. By this we find requirements for the observation of quantum mechanical states in the literal sense. We conclude with a brief summary on quantum mechanical Duffing oscillators.

2.1 The classical harmonic oscillator

We start the treatment with the general equation of motion for a damped, harmonic oscillator with driven external force [39]. We will solve the equation in the complex space for a complex coordinate $X(t)$. The physical displacement $x(t)$ of the oscillator is simply described by the real part of the complex coordinate:

$$\partial_t^2 X + \frac{2}{T_{\text{cor}}} \partial_t X + \Omega_0^2 X = F e^{i\Omega t} \tag{2.1}$$

where we have introduced the general displacement X, the relaxation time T_{cor}, the angular eigenfrequency of the oscillator Ω_0, and an external driving force of amplitude F and frequency Ω. Within this thesis we will consider only so-called high quality oscillators with decay rates $T_{\text{cor}}^{-1} \ll \Omega_0^1$.
We solve the equation of motion using the concept of a homogenous and a particular solution.

2.1.1 Undriven harmonic oscillator

The homogenous solution is given by

$$X_{\text{hom}}(t) = C_1 e^{-\frac{t}{T_{\text{cor}}} - i\tilde{\Omega}_0 t} + C_2 e^{-\frac{t}{T_{\text{cor}}} + i\tilde{\Omega}_0 t}, \tag{2.2}$$

where we introduced the damped eigenfrequency $\tilde{\Omega}_0 = \sqrt{\Omega_0^2 - T_{\text{cor}}^{-2}}$, which we will approximate via the undamped eigenfrequency Ω_0, due to the low damping of the investigated oscillators. We then can describe the displacement of the oscillator $x(t) = \text{Re}[X(t)]$ and identify the integration constants C_1, C_2 with an oscillation amplitude A and phase δ

$$x_{\text{hom}}(t) = A e^{-\frac{t}{T_{\text{cor}}}} \cos\left(\Omega_0 t + \delta\right). \tag{2.3}$$

The motion consists of an exponentially damped amplitude and a periodic oscillation with frequency Ω_0. The two independent integration constants A and δ have to be chosen to fulfill the boundary conditions [39]. We calculate the time derivative of the displacement, corresponding to its velocity and hence the momentum of the oscillator by:

$$v_{\text{hom}}(t) = \partial_t x_{\text{hom}}(t) \approx A \Omega_0 e^{-\frac{t}{T_{\text{cor}}}} \sin\left(\Omega_0 t + \delta\right). \tag{2.4}$$

The approximation is set to make clear that we investigate only highly coherent systems $(T_{\text{cor}} \ll \Omega_0)$. We find that the velocity becomes rescaled with Ω_0 and phase shifted by $\pi/2$. For simplicity, we introduce the rescaled momentum $p^\star = v_{\text{hom}}/\Omega_0$, such that the rescaled momentum is proportional to the momentum $p = m v_{\text{hom}}$, including the total mass m of the oscillator object. The benefit of the rescaled momentum is, that its amplitude has the same dimension as the displacement. We plot the time trace of both x_{hom} (blue) and $p^\star$ (red) in Fig. 2.1a), for an example parameter set of

$$\frac{\Omega_0}{2\pi} = 1\,\text{Hz} \quad A = 1 \quad T_{\text{cor}} = 10\,\text{s}. \tag{2.5}$$

In agreement with the Eqs. (2.3-2.4) they obey an exponential decay by t/T_{cor} (black dotted line) and phase difference of $\pi/2$.

Next, we display the time evolution in the phase space, that is a parametrization of the coordinates x_{hom} and v_{hom}. Any point $[x_{\text{hom}}(t_1), v_{\text{hom}}(t_1)]$ in the phase space represents the *state* of the system at the point's corresponding time (t_1). Hence, the trajectory displays the time evolution of the oscillator's state. The phase space for the analyzed oscillator is found in Fig. 2.1b). As we plot via the normalized momentum, we find a spiral (in general elliptically) decaying towards the center of the phase space, corresponding to zero energy. The direction of the trajectory indicates the time direction. In addition to the example parameters of Eq. 2.5, we also plot a high coherent case with $T_{\text{cor}}' = 1000\,\text{s}$ (grey). Here, the plotted timescale is much lower than the decoherence time and so the total energy remains identical. In the phase space this corresponds to the observed circle of constant radius.

In Eq. (2.1) we have introduced the equation of motion with a decay time T_{cor} of the amplitude of motion $X(t)$. However, in experiments we will employ a continous-wave setup, that is a constant measurement tone and investigate the spectral components of it. For this, we are now going to briefly discuss the motional amplitude in frequency space [c.f. Eq. (2.3)]. So, we perform a Fourier transformation on the example dataset and plot the transmission amplitude over angular frequency in panel c) in analogy to Ref. [39]. The amplitude is normalized, as its precise value depends on the definition of the Fourier transformation and its prefactors.

We find a Lorentzian lineshape with slight asymmetry for the weak damped (blue) and
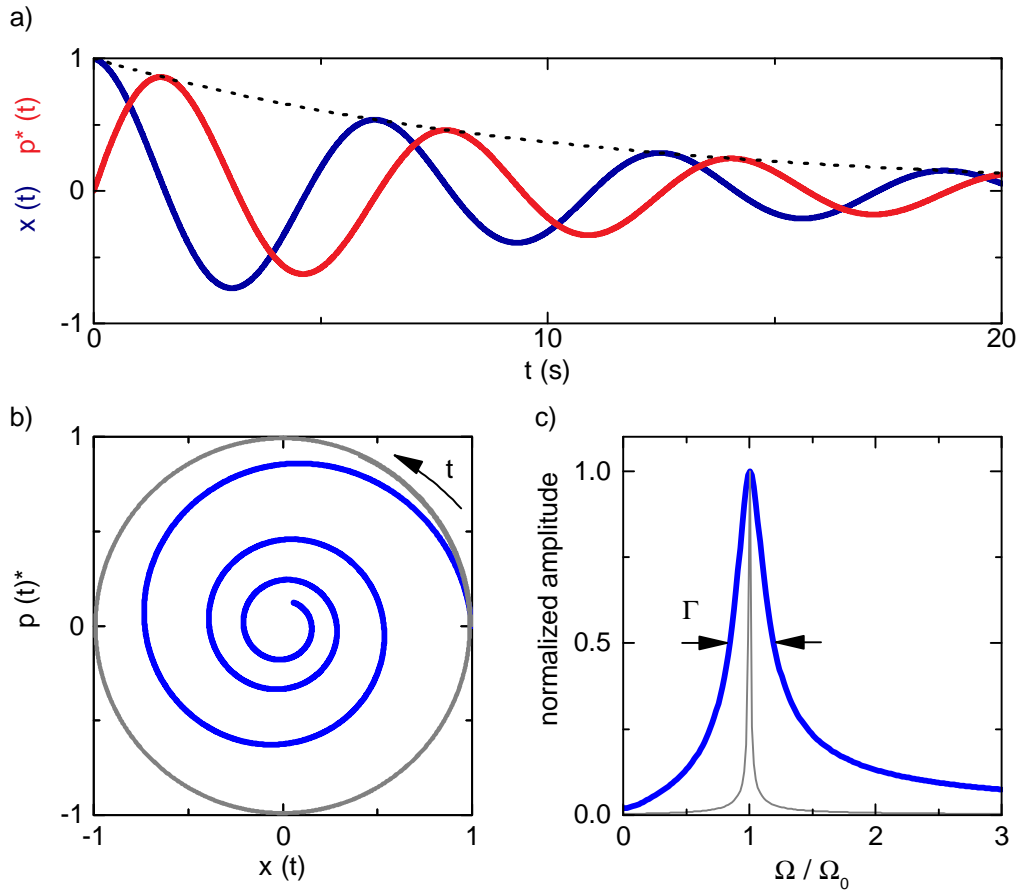
Figure 2.1: *Solutions of an undriven, damped harmonic oscillator* Panel a) shows the time trace for the position (blue) and momentum (red). A phase offset of $\pi/2$ is observed in agreement with Eqs. (2.3 - 2.4). The amplitudes decay exponentially with t/T_{cor} (black dotted line). In panel b) the time trace in phase space is shown for the parameters of panel a) (blue) and a higher coherent scenario (grey). We find decaying spirals, having a counter-clockwise rotations indicate the time direction. For the high coherent oscillator almost no decay is observed. The normalized Fourier amplitude of the displacement is displayed panel c). A Lorentzian lineshape of decay rate Γ is found. The slight asymmetry arises from the relative high damping (blue) in contrast to the high quality scenario (grey).

negligible asymmetry for the high coherent case (grey), which is closer to the experimental data explored later. We will refer to the *full with at half maximum* (FWHM) in frequency space and the linewidth $\Gamma = 2\pi \cdot \mathrm{FWHM}$ corresponding to the FWHM in angular frequencies. Between the decay time of the motion amplitude and the Fourier linewidth we find the correlation [40]

$$\frac{\Gamma}{2\pi} = \frac{2}{T_{\mathrm{cor}}}, \tag{2.6}$$

and so we can attribute Γ to the energy decay of the system. This becomes clear, when looking at the motion amplitude decay ($\propto t/T_{\mathrm{cor}}$) and so for the energy decay we find $\propto x^2(t) \propto 2t/(T_{\mathrm{cor}})$. By this association we can express the quality of the system as the ratio of stored energy to the dissipated energy [40]:

$$Q = \frac{\Omega_0}{\Gamma}, \tag{2.7}$$

and the introduced high coherent systems within this thesis have $Q > 10^3$.

2.1.2   Driven harmonic oscillator with damping

In the previous section we have discussed the equation of motion for an harmonic oscillator in the absence of an external driving force, related to the homogenous solution of Eq. (2.1). Next, we solve the particular solution X_{part} by introducing the susceptibility χ:

$$X_{\text{part}}(t) = \chi(\Omega)F e^{i\Omega t}, \tag{2.8}$$

relating the displacement to a general force. We note, that the principle of a susceptibility derived here is found in many area of physics, e.g. describing the response of a material in an electric or magnetic field. We calculate the susceptibility by solving Eq. (2.1) with the ansatz for the particular solution of Eq. (2.8) to [39]:

$$\chi(\Omega) = \left[\Omega_0^2 - \Omega^2 + i\Gamma\Omega\right]^{-1}. \tag{2.9}$$

The susceptibility is derived in the frequency domain and so, to determine the time trace of the full solution, we Fourier transform (FT) it to obtain spatial information. Further, by the linearity of the equation of motion the full solution of the displacement can be derived from the real part of the complex solution. In summary we find [39]

$$x(t) = \text{Re}\left\{X_{\text{hom}} + FT\left[\chi(\Omega)F e^{i\Omega t}\right]\right\}, \tag{2.10}$$

which describes the general time evolution of the mechanical displacement. The start parameters and boundary conditions determine the precise trajectory. The corresponding momentum is derived similar to the homogenous solution via $p = m\partial_t x(t)$.

2.2   Classical mechanical oscillators and electrical resonators

The results given in the previous section were derived for the general case of a damped, driven, and harmonic oscillator. Now, we will discuss how we can use these results to describe the two systems studied in this thesis: i) nanomechanical, doubly clamped string **oscillators** and ii) superconducting, coplanar waveguide microwave **resonators**. A brief overview is given in Table 2.1, a detailed discussion found in Ref. [41]. We like to note, that the correspondences given here is done for the classical oscillator. However, a quantum mechanical treatment reveals identical correspondences.

We like to highlight an important aspect here, that is the effective mechanical mass m_{eff} we have introduced. It arises from the reduction of the three dimensional motion of a doubly clamped nanostring to a one dimensional oscillator. We can identify an effective mass by comparing the stored energy in the nanostring with length l, width w, thickness t and material density ρ, considering only displacements $u(x)$ (no bending) [42]

$$E_{\text{string}} = \frac{1}{2}\rho w t \Omega^2 \int\limits_{-l/2}^{l/2} u(x)^2 \cdot dx, \tag{2.11}$$

with the energy stored in a harmonic one dimensional oscillator with effective mass and maximum displacement x_{m}

$$E_{\text{oscillator}} = \frac{1}{2}m_{\text{eff}}\Omega^2 x_{\text{m}}. \tag{2.12}$$

Harmonic oscillator	Nanostring oscillators	Electric resonators
Force	Actuation F	Voltage U
Velocity	Momentum $\partial_t x$	Current I
Amplitude	Displacement x	Charge Q
Mass	Effective Mass m_{eff}	Inductance L
Compliance	Pre-stress σ	Charge C^{-1}
Linewidth	Damping Γ_{m}	Resistance / Impedance R
Resonance frequency	$\Omega_{\text{m}} = \sqrt{\sigma/\rho}(2l)^{-1}$	$\omega_{\text{c}} = \sqrt{1/LC}$

Table 2.1: *From harmonic oscillators to nanostring oscillators and superconducting microwave resonators.*

Hereby, we define the effective mass as

$$m_{\text{eff}} = \frac{\rho w t}{x_{\text{m}}^2} \int\limits_{-l/2}^{l/2} u(y)^2 \cdot dy. \tag{2.13}$$

We find, that the effective mass depends on the square of the displacement profile as mode shape of the nanomechanical string. In highly stressed doubly clamped nanostrings the displacement follows $u \propto \cos(\pi y/l)$ for the fundamental mode [43]. Then, the effective mass is given by $m_{\text{eff}} = m/2$. For unstressed strings a ratio of $m_{\text{eff}} = 0.4m$ is found due to the difference of the mode shape [43]. The devices discussed in this thesis operate in the high tensile stress limit.

2.3 Quantum mechanical treatment of an harmonic oscillator

In the following section we will discuss the quantum mechanical treatment of an one dimensional harmonic oscillator in the absence of an external drive. This allows to compare between quantum mechanical and classical mechanical solutions.

2.3.1 The quantum mechanical harmonic oscillator

We start the discussion by introducing the position operator $\hat{x}$ and momentum operator $\hat{p} = i\hbar\partial_x$. The corresponding Schrödinger equation of the harmonic oscillator then reads:

$$\left[-\frac{\hbar^2}{2m}\partial_x^2 + \frac{m\Omega^2}{2}x^2 \right] \Psi(x) = E\Psi(x). \tag{2.14}$$

We further introduce the characteristic length,

$$x_{\text{o}} = \sqrt{\frac{\hbar}{\Omega m}}, \tag{2.15}$$

which is connected to the zero-point motion via $x_{\mathrm{zpm}} = x_{\mathrm{o}}/\sqrt{2}$. In addition, we introduce the creation[†] and annihilation operator

$$
\begin{aligned}
a_{\mathrm{o}}^{\dagger} &= \frac{\Omega m x - i\hbar\partial_x}{\sqrt{2\Omega m\hbar}} = \frac{1}{\sqrt{2}}\left(\frac{x}{x_{\mathrm{o}}} - x_{\mathrm{o}}\partial_x\right) \\
a_{\mathrm{o}} &= \frac{\Omega m x + i\hbar\partial_x}{\sqrt{2\Omega m\hbar}} = \frac{1}{\sqrt{2}}\left(\frac{x}{x_{\mathrm{o}}} + x_{\mathrm{o}}\partial_x\right),
\end{aligned}
\tag{2.16}
$$

which follows the commutation relation $[a_{\mathrm{o}}, a_{\mathrm{o}}^{\dagger}] = 1$. By this we can rewrite Eq. (2.14) in the form

$$
\hbar\Omega\left(a_{\mathrm{o}}^{\dagger}a_{\mathrm{o}} + \frac{1}{2}\right)\Psi(x) = E\Psi(x),
\tag{2.17}
$$

and so the remaining task is to find the eigenvalues $\hbar\Omega(a_{\mathrm{o}}^{\dagger}a_{\mathrm{o}}+1/2)$ for the number operator $n = a_{\mathrm{o}}^{\dagger}a_{\mathrm{o}}$ in the form $n\psi_{\nu} = \nu\psi_{\nu}$.

The lowest possible eigenvalue is $\nu = 0$, for which $a_{\mathrm{o}}\psi_0 = 0$ [44]. Then, the corresponding differential equation for the ground state is

$$
\left(\frac{x}{x_{\mathrm{o}}^2} + \partial_x\right)\psi_0 = 0,
\tag{2.18}
$$

which is solved by

$$
\psi_0 = C_{\mathrm{q}} \cdot \exp\left[-\frac{1}{2}\left(\frac{x}{x_{\mathrm{o}}}\right)^2\right].
\tag{2.19}
$$

The integration constant is obtained from the normalization of $\langle\psi|\psi\rangle \equiv 1$ to a value of $C = (\sqrt{\pi}x_{\mathrm{o}})^{-1/2}$. However this only solves $n = 0$, but all higher orders can be reduced using the attributes of the creation and annihilation operators to the ground state via [44]

$$
\psi_n = \frac{1}{\sqrt{n}}a_{\mathrm{o}}^{\dagger}\psi_{n-1} = \frac{1}{\sqrt{n!}}\left(a_{\mathrm{o}}^{\dagger}\right)^n\psi_0.
\tag{2.20}
$$

By this we find the full solution of the differential equation, and so also of Eq. (2.17) [44]. By the use of Hermite polynomials [45]

$$
H_n(x) = (-1)^n e^{x^2}\partial_x^n e^{-x^2},
\tag{2.21}
$$

we can express the wave function in the common way of [44]:

$$
\Psi_n = \frac{1}{\sqrt{2^n n!\sqrt{\pi}x_{\mathrm{o}}}}\exp\left[-\frac{1}{2}\left(\frac{x}{x_{\mathrm{o}}}\right)^2\right]H_n\left(\frac{x}{x_{\mathrm{o}}}\right).
\tag{2.22}
$$

The corresponding expectation value of the eigenenergy is quantized and of the shape

$$
E_n^{\mathrm{qm}} = \hbar\Omega\left(n + \frac{1}{2}\right).
\tag{2.23}
$$

The oscillation amplitude is described as wave, so its location density $\rho_{\mathrm{x}}^{\mathrm{qm}}$ is found by

$$
\rho_{\mathrm{x}}^{\mathrm{qm}} = \Psi_n\Psi_n^{\star}.
\tag{2.24}
$$

The wavefunctions given by Eq. (2.22) are displayed in Fig. 2.2a). For the ground state we find a Gaussian distribution centered at the origin. By increasing the occupation the wave function spreads out in space. We find a point (axis) symmetry for odd (even) occupations. The wavefunctions are offset by the expectation value of the eigenenergy. As the wavefunction decay over length, the energy value is found at the edges of the plot. The ground state energy is given by $E_0 = \hbar\Omega/2$.
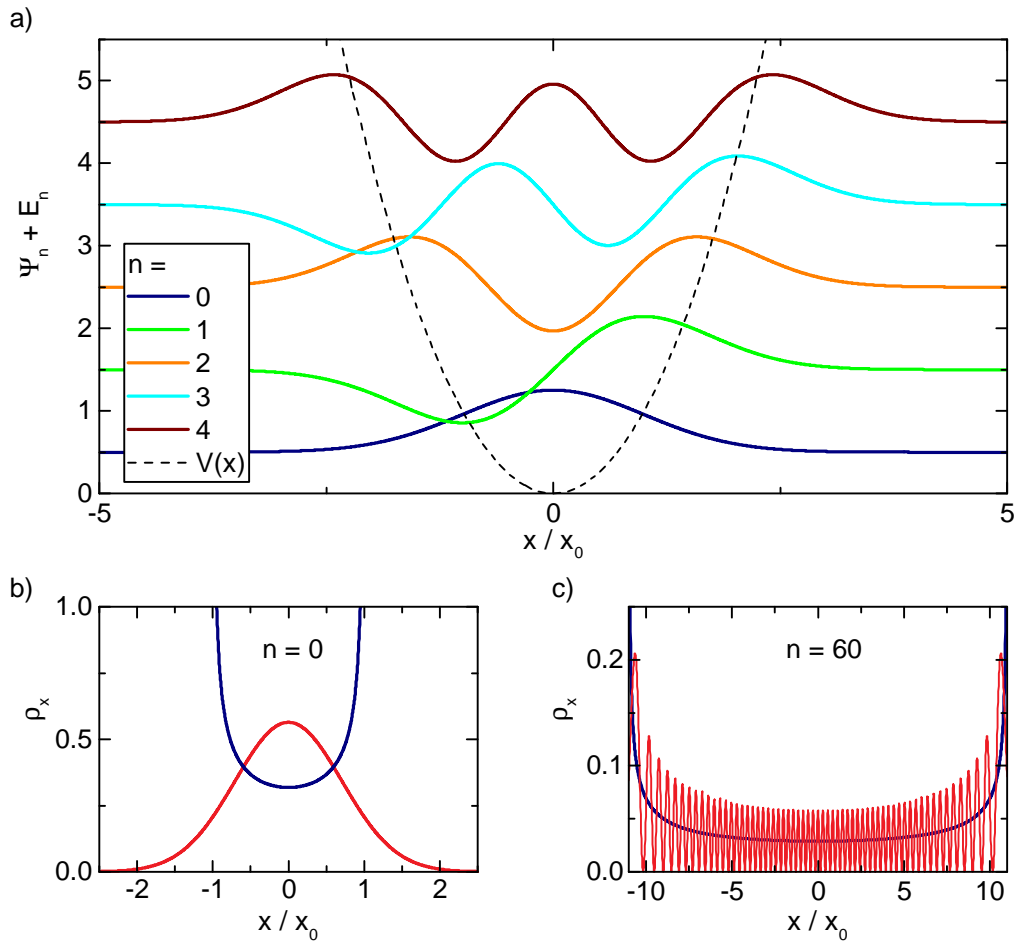
Figure 2.2: *The harmonic quantum mechanical oscillator.* In panel a) the wavefunctions Ψ_n are plotted for the lowest five states. The higher the excitation value, the further the wavefunction reaches into space. Additionally, the wavefunctions are offset by the expectation value of the corresponding eigenenergy for clarity. The harmonic potential is indicated by a black dotted line. Panel b) displays the probability density for a classical harmonic oscillator (blue) and quantum mechanical oscillator (red) for an occupation of $n = 0$. The most likely position of the quantum state is at the center, while in the classical case its at the edge of the oscillation (here at $x = 1$). This changes at higher occupations as found in panel c) for $n = 60$. Here, the probability density of the quantum mechanical state oscillates around the classical value and so the classical treatment is a good approximation. We like to note, that the comparison of the quantum and classical ground state shown here is only an illustration for the understanding between classical and quantum physics.

2.3.2 Comparison to classical oscillators

With the results obtained above we can now discuss the differences between the quantum and classical harmonic oscillator. For a comparison, we define a classical probability density in analogy to the quantum probability density [cf. Eq. (2.25)] [44]

$$\rho_{\mathrm{x}}^{\mathrm{cl}} = \frac{1}{\pi x_{\mathrm{o}}^n \sqrt{1 - (x/x_{\mathrm{o}}^n)^2}}, \tag{2.25}$$
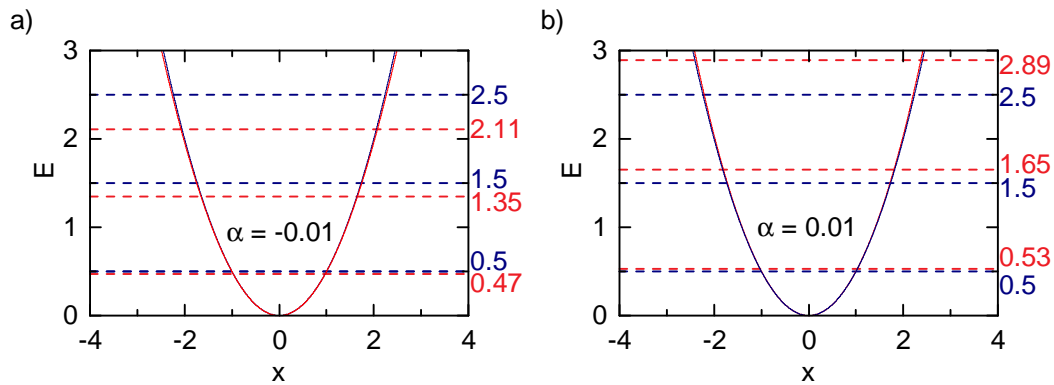
Figure 2.3: *Harmonic and Duffing potential.* The potential of an harmonic (blue) and Duffing oscillator (red) are plotted for a nonlinearity of $\alpha = -0.01$ in panel a) and $\alpha = +0.01$ in panel b) is shown as straight lines. Due to the weak nonlinearity almost no difference in the potential is found. Additionally the corresponding energy states are calculated. They differ significantly besides the weak anharmonicity.

assuming a classical, undamped oscillation of $x^{\mathrm{cl}} = x_{\mathrm{o}}^n \sin(\Omega t)$ [cf. Eq. (2.3)] and a potential energy of $E^{\mathrm{cl}} = m\Omega^2 (x/x_{\mathrm{o}}^n)^2/2$. We link the classical displacement to the characteristic quantum length via

$$x_{\mathrm{o}}^n = x_{\mathrm{o}}\sqrt{2n+1}, \tag{2.26}$$

in dependence of the occupation value n. With the derived equations we compare the classical $\rho_{\mathrm{x}}^{\mathrm{cl}}$ and quantum mechanical probability density $\rho_{\mathrm{x}}^{\mathrm{qm}}$ in Fig. 2.2 for the ground state in panel b) and an occupation of $n = 60$ in panel c).

For the ground state we find the quantum mechanical probability, similar to the wavefunction, centered around the origin. This is in contrast to the classical expectation, where the highest probability is found at $x/x_{\mathrm{o}} = x_{\mathrm{o}}^n = \pm 1$ for the vacuum state. However, at higher occupations the quantum probability starts to oscillate and the expectation position is shifted towards the edges. We show this by plotting both densities for an excitation value of 60 in Fig. 2.2c). Here, the quantum mechanical density fluctuates, but the classical treatment follows the center of the quantum mechanical oscillation amplitude very well.

We conclude, that for an observation of nanomechanical quantum or non-classical states occupation values close to the ground state are required, as otherwise deviations from the classical state become smaller and smaller with increasing occupation.

Within this thesis the lowest occupation we find in our mechanical oscillators is $n_{\mathrm{m,xx}} \approx 140$, and so a classical mechanical treatment seems sufficient.

2.4   Nonlinear effects in resonant systems

We will conclude the discussion of resonant systems by having a look at deviations from the harmonic model. Here, we want to indicate the relation of the nonlinear terms with respect to the physics of Josephson junctions and highly driven mechanical strings. The physics of nonlinear responses and oscillations is very rich and intensively discussed (cf. Ref. [46]). Typically, for the treatment of nonlinear oscillations an additional term is added

to the Hamiltonian of an harmonic oscillator [cf. Eq. (2.17)] , in particular a quartic term as [47]

$$H = \hbar\Omega \left(a_{\mathrm{o}}^{\dagger} a_{\mathrm{o}} + \frac{1}{2} \right) + \alpha \left(a_{\mathrm{o}} + a_{\mathrm{o}}^{\dagger} \right)^4 . \tag{2.27}$$

The potential shape is often discussed in the context of classical Duffing oscillators [48]. The corresponding energy expectation values are found by [47]

$$E_n = \hbar\Omega \left(n + 1/2 \right) - \alpha \left(6n^2 + 6n + 3 \right) . \tag{2.28}$$

This will be of special interest in the next sections, as we use Josephson nonlinear elements for our quantum circuits, that we can describe via [45]

$$\cos(\varphi) = 1 - \varphi^2 + \varphi^4 + \mathcal{O}(\varphi^6), \tag{2.29}$$

and therefore resemble the shape of a harmonic oscillator with a quartic perturbation term.

Chapter 3

Circuit quantum electrodynamics

Das hier ist ein völlig anderes Biest, gemacht für das Multiversum.

Hartmut Neven, about quantum computers in [7], 2019

In this chapter, we introduce superconductivity as a macroscopic wave phenomena describing the superconducting state. This wavefunction allows for a transmission through a tunneling barrier, the Josephson junction. Adding two of those in a superconducting loop comprises a dc-SQUID, which is one of the building blocks of our devices. Further, we discuss another building block, namely microwave resonators. Then a SQUID is integrated in such a microwave resonator. This allows the resonator to be tuned in frequency, and also adds a nonlinearity to the system. We further discuss what happens when the nonlinearity is enhanced by design, leading to transmon qubits. This type of qubit is then discussed in detail, especially in terms of a strong interaction with a microwave light field and the resulting effects, like the ac-Stark shift.

3.1 From the macroscopic wavefunction to Josephson physics

Superconductivity can be understood by the concept of a macroscopic wavefunction. That is a condensation of bosonic cooper pairs obeying one and the same wavefunction derived from the Schrödinger equation of a single particle in the presence of a vector A and scalar Φ potential

$$\left[\frac{1}{2m} \left(\frac{\hbar}{i} \nabla - qA \right)^2 + q\Phi \right] \Psi = i\hbar \partial_t \Psi, \tag{3.1}$$

with the mass of the condensed cooper pairs m, which is twice the mass of an electron ($m = 2m_\mathrm{e}$). Same applies for the charge of the considered particle ($q = -2e$). We then interpret the complex wavefunction consisting of an amplitude, linked to the cooper pair density $\langle \Psi | \Psi^\star \rangle = \rho_\mathrm{c}$, and a phase of the collective state φ_c [49]

$$\Psi = \sqrt{\rho_\mathrm{c}} e^{i\varphi_\mathrm{c}}. \tag{3.2}$$

The conclusions how to describe superconductivity by this approach are discussed in Ref. [50]. We will now consider two superconducting areas separated by a non-conductive

intersection. In contrast to a classical scenario, the quantum mechanical wavefunction can reach into the adjacent area for small potentials. So, the quantum mechanical transmission differs from the classical derivation [51]. Such intersections are named Josephson junctions. The superconductive current across the junction, $I = q/m\mathrm{Re}[\Psi(-i\hbar)\Psi]$, is found to be [52]

$$I = I_\mathrm{c}\sin\theta, \tag{3.3}$$

which is know as first Josephson equation. Here, we have introduced the gauge invariant phase difference between the two areas of [52]

$$\theta = \varphi_\mathrm{c}^2 - \varphi_\mathrm{c}^1 - \frac{2\pi}{\Phi_0}\int\limits_1^2 Adl, \tag{3.4}$$

where $\Phi_0 = h/2e$ is the flux quantum [53, 54], and the numerical indices 1 or 2 refer to the area of the intersection. The time derivative of the phase difference is known as second Josephson equation

$$\partial_t\theta = \frac{2\pi}{\Phi_0}V. \tag{3.5}$$

The Josephson equations state, that up to a critical value I_c, a superconducting current is send across the junction and if a voltage V is applied across it, an oscillating current appears. Taking Eqs. (3.3) and (3.5) to determine the energy stored in the system we quantify the Josephson energy, similar to a potential energy

$$E_\mathrm{J} = \int\limits_0^t IVdt = E_\mathrm{J}^0\left(1 - \cos(\theta)\right), \tag{3.6}$$

with $E_\mathrm{J}^0 = \Phi_0 I_\mathrm{c}/(2\pi)$. We see, that we can identify the phase difference θ as a position, or angle in a mechanical analogue [52]. The time derivative of the phase change is attributed to a kinetic energy or momentum. This can be derived by considering the two superconducting interfaces as a capacitor with capacitance C_J. The stored energy in this capacitor is

$$E = \frac{1}{2}C_\mathrm{J}V^2 = \frac{1}{2}C_\mathrm{J}\left(\frac{\Phi_0}{2\pi}\right)^2(\partial_t\theta)^2, \tag{3.7}$$

which is typically compared to the charging energy across the junction $E_\mathrm{C} = e^2/(2C_\mathrm{J})$, which describes the energy required to charge the capacitance with an elementary charge [52].

If we consider a small change of the phase $\delta\theta$ at a given, arbitrary phase θ_0 we find a change in current $\delta I = I_\mathrm{c}\cos\delta\theta$, as well as a change in Josephson energy

$$\delta E_\mathrm{J} = \frac{E_\mathrm{J}^0\sin(\theta_0)}{I_\mathrm{c}\cos(\theta_0)}\delta I \;\rightarrow L_\mathrm{J} = \frac{\Phi_0}{2\pi I_\mathrm{c}\cos(\theta)}, \tag{3.8}$$

we can associate this change with the Josephson induction as $\delta E_\mathrm{J} = LI\delta I$. As this result is obtained from the change of the charge carriers δI (cf. Tab. 2.1) it becomes clear, that the Josephson inductance behaves as a kinetic inductance [55].

3.2 Superconducting quantum interference devices

Next we connect two Josephson junctions in a superconducting loop, having a critical current of $I_{c,i}$ and phase difference θ_i. This configuration is called direct current superconducting quantum interference device (dc-SQUID). As the superconducting loop obeys flux quantization the global phase difference between the single junctions becomes [56]

$$\theta_2 - \theta_1 = \frac{2\pi\Phi_{\text{ext}}}{\Phi_0}, \tag{3.9}$$

derived from Eq. (3.4). Here we introduce the external flux $\Phi_{\text{ext}} = B_{\text{ext}}A_{\text{loop}}$ determined by the applied external field B_{ext} through the SQUID loop A_{loop}. Via Kirchhoffs law, we find the maximal critical current in a dc-SQUID to be in general [57]

$$I_\Sigma^{\text{m}} = I_\Sigma \left| \cos\left(\pi\frac{\Phi_{\text{ext}}}{\Phi_0}\right) \right| \sqrt{1 + d^2\tan^2\left(\pi\frac{\Phi_{\text{ext}}}{\Phi_0}\right)} = 2I_{\text{c}} \left| \cos\left(\pi\frac{\Phi_{\text{ext}}}{\Phi_0}\right) \right|. \tag{3.10}$$

Here, we describe the sum of the current through both junctions $I_\Sigma = I_{c1} + I_{c2}$ and account for an asymmetry between the two junctions with $d = (I_{c1} - I_{c2})/I_\Sigma$. Within this thesis we only consider $d = 0$ corresponding to the right hand side of the equation.

The total current is derived as in classical parallel circuits by adding the single branches ($I_\Sigma = I_{c1} + I_{c2}$). By these considerations we find the Josephson energy of the SQUID to be [56]

$$E_{\text{J}}^{\text{squid}} = \frac{\Phi_0 I_\Sigma}{2\pi} \left[1 - \cos\left(\frac{\pi\Phi_{\text{ext}}}{\Phi_0}\right) \right]. \tag{3.11}$$

As the inductors in a parallel circuit add reciprocally, the Josephson inductance of a dc-SQUID with two identical junctions is half of the single junction value

$$L_{\text{J}}^{\text{squid}} = \frac{\Phi_0}{2\pi I_\Sigma \left| \cos(\pi\Phi_{\text{ext}}/\Phi) \right|}. \tag{3.12}$$

These equations can be derived similar to Eqs. (3.6) and (3.8) in Sec. 3.1.

An important aspect when designing such SQUIDs is the fact, that the considerations above only hold for a low self inductance of the SQUID loop ring ($L_{\text{Loop}} = L_{\text{kin}} + L_{\text{geo}}$), which is obtained by the kinetic L_{kin} and the geometric L_{geo} contribution. The ratio of the loop inductance to Josephson inductance is described by the screening parameter β_{L} [56]

$$\beta_{\text{L}} \equiv \frac{2L_{\text{Loop}}I_{\text{c}}}{\Phi_0}. \tag{3.13}$$

An important design aspect for devices is the fact that for high values of β_{L} the tuning range of the critical current is reduced [56], e.g. for a screening parameter of $\beta_{\text{L}} = 1$ the maximum critical current tunes from $2I_{\text{c}}$ to $1I_{\text{c}}$, and therefor no longer reaches the minimum of 0. Further, at high β_{L} values, the critical current to flux curve becomes hysteretic. When the SQUID is inserted into a microwave resonator this can happen for values even below $\beta_{\text{L}} = 1$ [58], so we aim for a design value of $\beta_{\text{L}} < 0.1$. In the following, we will give a brief discussion on a potential sample design.

First, the kinetic inductance of the SQUID is in our device design dominated by the thin

and long mechanical string oscillators. Previous studies on devices from our lab showed that the kinetic inductance is best expressed by the 'dirty limit' with [59–61]:

$$L_{\text{kin}} = \frac{\hbar \rho_{\text{n}} l}{\pi \Delta_0 wt} = 45 \, \text{fH} \mu\text{m} \cdot \frac{l}{wt} [\mu\text{m}]. \tag{3.14}$$

Here, we introduced the normal resistivity of the superconductor ρ_{n}, the energy gap of aluminum at zero temperature Δ_0, and the string design (l, w, t) as discussed in Sec. 2.2. So an estimation for a typical string having a cross-section of $wt = 0.1 \times 0.1 \, \mu\text{m}^2$ and length of $l = 20 \, \mu$ results in a kinetic inductance of $90 \, \text{pH}$ of the SQUID.

Second, the geometric inductance is derived by the geometry of the conductor loop modeled as classical rf-circuit [61–63]

$$L_{\text{geo}}/0.4 \, [\mu\text{H}] = 2d - 2(l_{\text{Loop}} + b) + s - l_{\text{Loop}} \ln(d + l_{\text{Loop}}) - b \ln(d + b) + (l + b) \ln\left(\frac{4l_{\text{Loop}} b}{S}\right), \tag{3.15}$$

with the SQUID loop diagonal d, consisting of the SQUID loop width b and the SQUID loop length l_{Loop} as well as the wire diameter $S = 2(t^2 + w^2)^{1/2}$. In total, we find a geometric inductance of $22 \, \text{pH}$ for a SQUID loop length which is dominated by the string's length $l_{\text{Loop}} \approx l$, a SQUID width of $2 \, \mu\text{m}$ and the string parameters given above. This shows that the dominant part of the loop inductance stems from the kinetic inductance, which is given by the thin, long strings realizing the mechanical element.

We can now estimate the achievable critical current for such mechanical SQUIDs assuming a target screening parameter of $\beta_{\text{L}} = 0.1$ to

$$I_{\text{c}}^{\text{design}} = \frac{\beta_{\text{L}} \Phi_0}{2L_{\text{Loop}}} = 0.9 \, \mu\text{A}. \tag{3.16}$$

This value is from a fabricational point of view no issue to design [64, 65]. However as we will see later, this corresponds to a photon number on the order of $n_{\text{crit}} \approx 10$ photons, which makes the detection of an electromechanical signal challenging.

3.3   Flux tunable microwave resonators

Next we are going to discuss the ground mode of a flux tunable resonator, in particular, a superconducting coplanar waveguide (CPW) resonator in $\lambda/4$ configuration with a dc-SQUID at the current anti-node. By the tunable inductance of the dc-SQUID, the joined system can be treated as a distributed-element resonator with a lumped element tunable inductance [58], see Fig. 3.1a). As the dc-SQUID was already introduced, we will now discuss the bare microwave resonator and later combine both systems.

We model the coplanar waveguide with a inductance and capacitance per unit length [66, 67]

$$L_{\text{l}} = \frac{\mu_0}{4} \frac{K(k_0')}{K(k_0)} \quad C_{\text{l}} = \frac{4\epsilon_0 \epsilon_{\text{eff}}}{4} \frac{K(k_0)}{K(k_0')}. \tag{3.17}$$

Here K describe the complete elliptic integral of the first kind. Further, the parameters $k_0 = w_{\text{c}}/(w_{\text{c}} + 2s_{\text{c}})$ and $k_0' = \sqrt{1 - k_0^2}$ are defined by the waveguides center conductor width w_{c} and the gap between it and the ground plane s_{c}. The phase velocity of the microwave $v_{\text{phase}} = 1/\sqrt{L_{\text{l}} C_{\text{l}}} = c/\sqrt{\epsilon_{\text{eff}}}$ is defined by the speed of light in vacuum c and the effective dielectric constant ϵ_{eff}. Additionally, the resonator impedance $Z = \sqrt{L_{\text{l}}/C_{\text{l}}}$
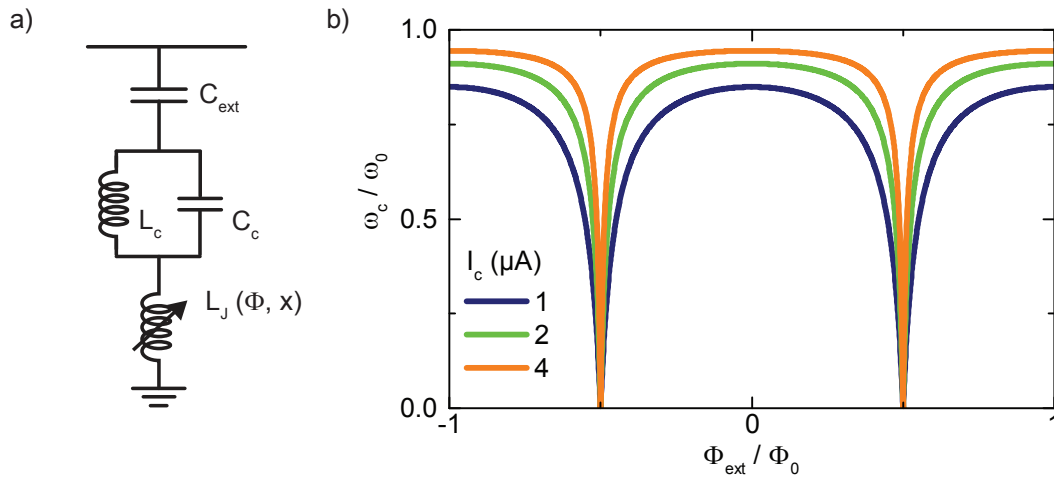
Figure 3.1: *Flux tunable resonators in a nutshell.* The modeled circuit is sketched in panel a) consisting of a distributed element coplanar waveguide resonator in $\lambda/4$ configuration, shorted to ground by a dc-SQUID. Panel b) shows the flux tuning of the resonance frequency in accordance to Eq. (3.22) for different critical currents at the Josephson junctions. We find a periodic behavior, tuning down to zero frequency. The maximum frequency and the slope of the tuning is influenced by the critical current.

is typically designed such, that it matches the $50\,\Omega$ environment of the electric setup. For the discussed case of a shorted $\lambda/4$ resonator, the wavelength corresponds to $l_c = \lambda/4$ on resonance to the electric circuit, defined by the inductance and capacitance of an equivalent lumped circuit L_c, C_c such that [68, 69]

$$\omega_0 = \frac{1}{\sqrt{L_c C_c}} = \frac{\pi}{2l_c\sqrt{L_l C_l}}, \tag{3.18}$$

with the equivalent total inductance $L_c = 8L_l l_c/\pi^2$ and capacitance $C_c = C_l l_c/2$. For a typical resonator of $\omega_c/2\pi = 7.5\,\text{GHz}$ matched to $50\,\Omega$ this corresponds to values of $L_c = 1.1\,\text{nH}$ and $C_c = 440\,\text{fF}$. By examining these parameters it becomes clear, why we focus only on the capacitance of the CPW within this work, as the coupling capacitance is typically smaller than $10\,\text{fF}$ [70] and the Josephson capacitance on a similar scale around $15\,\text{fF}$ [71] and therefor do not influence the resonance frequency significantly.

To determine the flux tunable resonator's eigenfrequency ω_c following the approach mentioned above [cf. Fig. 3.1a)], a transcendental equation has to be solved [58, 72, 73]

$$\frac{\pi\omega_c}{2\omega_0}\tan\left(\frac{\pi\omega_c}{2\omega_0}\right) = \frac{2\pi^2}{\Phi_0^2}L_c E_s(\Phi_{\text{ext}}). \tag{3.19}$$

Here, we have introduced the flux energy of the dc-SQUID as [58]

$$E_s(\Phi_{\text{ext}}) = \frac{\Phi_0^2}{(2\pi)^2}\frac{1}{L_J(\Phi_{\text{ext}}) + L_{\text{Loop}}/4}, \tag{3.20}$$

consisting of contributions from the Josephson junctions and the geometric loop inductance, for details on the determination of the SQUID inductance refer to Ref. [74]. To explicitly determine the resonator frequency tuning, we expand the left hand side of Eq. (3.19) around the sweet spot, where $\omega_c/\omega_0 \approx 1$

$$\frac{\pi\omega_c}{2\omega_0}\tan\left(\frac{\pi\omega_c}{2\omega_0}\right) \approx -\frac{1}{\omega_c/\omega_0 - 1} - 1 + \mathcal{O}(\frac{\omega_c}{\omega_0} - 1). \tag{3.21}$$

The deviations between l.h.s. and r.h.s. are less than 0.5% for the experiments in this work. Combining the approximation with the left hand side of Eq. (3.19) we find the microwave resonator frequency tuning with the applied external flux [58]

$$\omega_{\mathrm{c}}(\Phi_{\mathrm{ext}}) = \omega_0 \left(1 + \frac{L_{\mathrm{J}}(\Phi_{\mathrm{ext}}) + L_{\mathrm{Loop}}/4}{L_{\mathrm{c}}}\right)^{-1}, \tag{3.22}$$

for moderate flux bias around $\Phi_{\mathrm{ext}}/\Phi_0 \approx n \in \mathbb{Z}$. As the dc-SQUID can act as nonlinear element, we briefly estimate the effect of the nonlinearity. The energy spacing between two adjacent levels is derived to be [72]

$$\delta E_n = -\frac{6n^2 + 6n + 3}{4}B_\omega E_{\mathrm{c}} \quad \text{with} \quad B_\omega = \frac{\frac{1}{4}\cos^2\left(\frac{\pi\omega_{\mathrm{c}}}{2\omega_0}\right)}{1 + 2\frac{\pi\omega_{\mathrm{c}}}{2\omega_0}/\sin\left(\frac{\pi\omega_{\mathrm{c}}}{2\omega_0}\right)}, \tag{3.23}$$

with the charging energy of the microwave resonator $E_{\mathrm{c}} = (2e^2)/(2C_{\mathrm{c}})$. The similarity to Eq. (2.29) is not a coincidence as both results relate to a Duffing potential. Therefore, we can directly associate the nonlinearity of the FTR to $\alpha = B_\omega E_{\mathrm{c}}/4$, which scales with $(E_{\mathrm{c}}(1/48 - (L_{\mathrm{c}}\alpha' I_{\mathrm{c}})^2)$. This nonlinearity is dominated by the charging energy, but diluted by a term influenced by the critical current, the total conductor inductance and the corresponding prefactors α'. This is similar but in contrast to highly nonlinear systems, e.g. transmon qubits, where the nonlinearity depends only on the charging energy ($\alpha = -E_{\mathrm{c}}$), see Sec. 3.4.2.

In Fig. 3.1b) we plot the resonance frequency of Eq. (3.22) for a CPW resonator as function of the flux through the SQUID loop for various critical currents ranging from $I_{\mathrm{c}} = 1$ to $4\,\mu\mathrm{A}$. We find a periodic behavior in Φ_0. Starting from a maximum transition frequency, that shifts with the critical current, the frequency tunes to zero, with a slope depending on the critical current. The quantitative dependence of the critical current to those two parameters can be derived from Eq. (3.22).

For now, we like to conclude on the results of flux tunable resonator, briefly discuss desired design parameters, and the limits imposed by the other components in inductively coupled electromechanical systems.

As we will see, the electromechanical single photon-phonon coupling strength scales with the slope of the frequency tuning, cf. Sec. 7.1. Additionally, the effective coupling can be enhanced in electromechanics by increasing the photon number in the microwave resonator. Both aspects demand to design the critical current as high as possible, as both increase the slope [cf. Fig. 3.1b)], and reduces the nonlinearity of the SQUID [Eq. (3.23)]. However, this is in contrast to the aspect of flux hysteresis [cf. Eq. (3.16)], which will lead to undesired jumps for a flux bias point, and also reduces the available tuning range respectively the accessible slope. For this we keep the critical current within the calculated limit of Eq. (3.16), resulting in a system which is more stable to operate. To compensate the tuning range, we design the microwave resonator at a bare resonator frequency around $7.5\,\mathrm{GHz}$, close to the limit of the cryogenic amplifiers ($8\,\mathrm{GHz}$), so that a larger tuning range becomes accessible (down to $4\,\mathrm{GHz}$) and the restrictions of the slope are overcome. The limitations on the low photon numbers in the nonlinear microwave resonator, imposed by the SQUID, are bypassed by enhancing the phonon number resulting in a higher electromechanical signal, as discussed in Sec. 5.2.
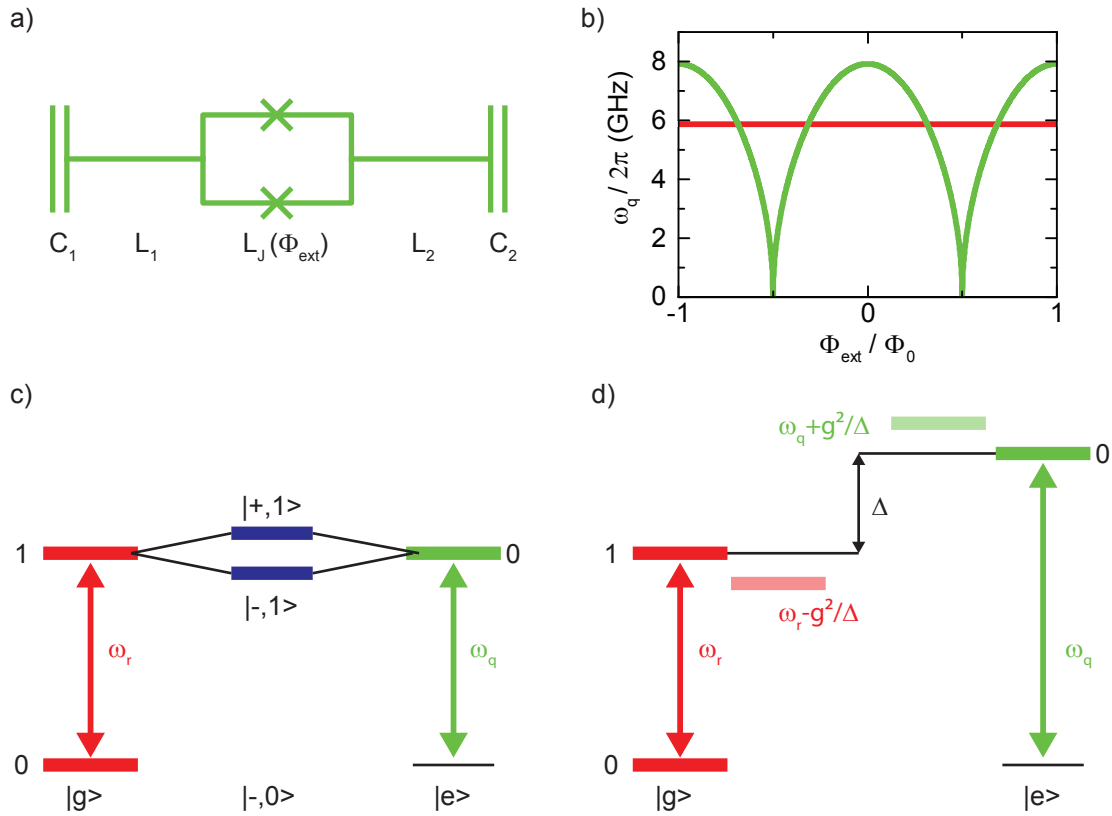
Figure 3.2: *Transmon parameters derived from a shorted transmission line.* Panel a) displays the model of a dc-SQUID in a transmission line ($\lambda/2$-configuration). For a transmon qubit the CPW length is shortened so that L_c is reduced. The size of the capacitors define the nonlinear regime E_J/E_C. Panel b) shows the frequency tuning of the transmon qubit explored in Sec. 6 (green). From a maximum transition frequency with vanishing tuning slope the frequency tunes periodically in Φ_0. Further the fixed frequency CPW read-out resonator is indicated (red). Panel c) and d) sketch a tuneable two-level system strongly coupled to a fixed frequency resonator. In panel c) when they are on resonance with each other. The strong coupling results in an avoided crossing with a frequency separation of twice the coupling strength. Panel d) displays the off-resonant scenario: the TLS and resonator are tuned by a dispersive shift. In the case of a transmon qubit as quasi TLS, its nonlinearity has to be taken into account for the determination of the dispersive shift (not shown).

3.4   Transmon qubits

3.4.1   From nonlinear transmission lines to quantum bits

In the following we switch from a $\lambda/4$ CPW-resonator shunted to ground by a dc-SQUID to a $\lambda/2$ resonator. Nevertheless the dc-SQUID remains at the current anti-node. By this we can consider the system as a dc-SQUID with two LC elements, see Fig. 3.2a). So far, we have found a finite nonlinearity of such systems, describing the energy spacing between two adjacent levels. When the nonlinearity is sufficiently large that the spacing in energy δE_n overcomes the decay rate of the resonator κ, the levels can be independently adressed and the system acts as a (quasi-) two level system (TLS).

As the nonlinearity of such systems can be defined by the charging energy of the system $E_C = 2e/C_\Sigma$ diluted by the inductance of the LC elements (see Sec. 3.3 and Ref. [57]), reducing the length of the LC elements increases the nonlinearity. We can relate the

Josephson (potential) energy to the charging (kinetic) energy E_J/E_C, which then does relate the nonlinearity in terms of the dominating Josephson energy. When the nonlinearity is increased sufficiently such that the system can be treated as a quasi two-level system, we reach the so-called **trans**mission line shunted plas**mon** oscillation (transmon) qubit regime $(50 < E_J/E_C)$ [75], or the charge qubit / cooper pair box regime $E_J/E_C \approx 1$ [19]. This regime can be realized by an appropriate design of the charging capacitance. The capacitor plates can also be used to address the qubit, which lead to the development of the so-called x- or g-mon qubits [76, 77].

We note, that Ref. [57] derived the generation of squeezed states in FTRs and showed that by the increased nonlinearity of transmon qubits the generation of cat states becomes feasible.

3.4.2 Details on transmon qubits

Combining the energy contributions as introduced in Eqs. (3.7) and (3.11) applied to the transmon circuit, cf. Fig. 3.2a), we obtain the transmon Hamiltonian [75]

$$H_T = \frac{1}{2}C_\Sigma \left(\frac{\Phi_0}{2\pi}\right)^2 (\partial_t \theta)^2 + E_J^{\text{squid}} \left[1 - \cos(\theta)\right]. \tag{3.24}$$

Here, the capacitance of the shunt and the Josephson junction is described by C_Σ. As the phase difference θ can associated to a position (cf. Sec. 3.1), one can identify the above equation as a particle in a cos-potential, like a rotor of angle θ in a gravitational field of effective mass and charge in a homogenous magnetic field set by Φ_{ext} [75]. The effective mass of it is described by $C_\Sigma[\Phi_0/(2\pi)]^2$. In the transmon regime, as $E_C \ll E_J$, the particle is well trapped within one period of the potential, corresponding to a large effective mass. So this mechanical analog must not be confused with the RCSJ-model typically used to describe the dynamics of a single Josephson junction in a tilted washboard potential [52]. We note, that the Josephson energy is described by $E_J = 2E_J^0|\cos(\pi\Phi_{\text{ext}}/\Phi_0)|$, with E_J^0 the Josephson energy of a single junction with critical current I_c [75].

Developing the above equation for the cosine leads to a splitting of the eigenenergies in a Duffing manner [75]

$$E_n = -E_J + \sqrt{8E_J E_C}\left(n + \frac{1}{2}\right) - \frac{E_C}{12}\left(6n^2 + 6n + 3\right), \tag{3.25}$$

where in the transmon literature the nonlinearity is defined as $\alpha = -E_C/\hbar$ [75]. This corresponds to the nonlinearity of Sec. 3.4.1 in the limit $L_c \to 0$ of a short transmission line. The ground state is found around the plasmon frequency of the SQUID $\hbar\omega_q = \sqrt{8E_J E_C}$. We display the frequency tuning of the transmon qubit in Fig. 3.2b) (green), for a system similar to the one analyzed in Sec. 6.

We find periodic behavior in Φ_{ext}/Φ_0, with the maximum transition frequency located at integer ratios and at a frequency of about $8\,\text{GHz}$. This spot is referred to as sweet spot, since the tuning slope $\partial_\Phi \omega_q = 0$. So flux noise is efficiently avoided and the quality the highest. From the sweet spot the qubit tunes down to zero. In the figure we have further indicated the position of the fixed frequency read-out resonator (red), but without a coupling present between the two systems, the influence of such a coupling is discussed next.

3.4.3 Qubit interaction with light

In a first iteration we can assume the transmon qubit as an effective two-level system if the anharmonicity is sufficiently larger than the qubit linewidth κ_{q}. The investigated system in Sec. 3.2 indeed obeys $\alpha/2\pi = 188\,\mathrm{MHz} \gg \kappa_{\mathrm{q}}/2\pi = 7\,\mathrm{MHz}$. Approximating the transmon as TLS one can write the Hamiltonian using Pauli-Matrix σ_{z} as [78]

$$H_{\mathrm{T}} = \frac{1}{2}\hbar\omega_{\mathrm{q}}\sigma_{\mathrm{z}}, \tag{3.26}$$

identical to an isolated spin in a magnetic field, or an artificial atom. The qubit state can hence be intuitively described as a vector in a Bloch sphere. However, the reduction to a two-level system is insufficient for a transmon qubit, due to its relatively low anharmonicity in comparison to a pure two-level system, realized by e.g. a charge qubit. In the following we will discuss the light-matter interaction of a two-level system in general and then take the finite transmon anharmonicity into account.

If the systems are coupled strongly the interaction of a light source with a two-level system is described via the quantum Rabi model, derived for cQED systems in Ref. [79]. Strong coupling means that the coupling strength g_{q} is larger than the loss rates of the subsystems κ, κ_{q}. If the coupling is well below the system energies it is sufficient to apply the Jaynes-Cummings model [80, 81]

$$H_{\mathrm{T}} = \frac{\hbar\omega_{\mathrm{q}}}{2}\sigma_{\mathrm{z}} + \hbar\omega_{\mathrm{c}}\left(a^{\dagger}a + \frac{1}{2}\right) + \hbar g_{\mathrm{q}}\left(\sigma_{+}a + \sigma_{-}a^{\dagger}\right), \tag{3.27}$$

which consists of the qubit term, the microwave read-out resonator with (fixed) eigenfrequency ω_{c}, and an interaction term, where an excitation in the qubit can be created by absorption of a photon ($\sigma_{+}a$), or the qubit excitation can create a photon in the microwave resonator $\sigma_{-}a^{\dagger}$. Analyzing the interaction, one finds that it is depending on the detuning between qubit and resonator $\Delta_{\mathrm{qc}} = \omega_{\mathrm{q}} - \omega_{\mathrm{c}}$, so we discuss two scenarios:

Resonant interaction   In the resonant regime $\Delta_{\mathrm{qc}} \approx 0$ and due to the strong coupling a dressed state between resonator and qubit is observed, having an avoided crossing of $2g_{\mathrm{q}}$. This is schematically depict in Fig. 3.2c). It can be shown [82], that the states are transferred with the so-called Rabi frequency $\Omega_{\mathrm{Rabi}} = \sqrt{\Delta_{\mathrm{qc}}^2 + \Omega_{\mathrm{q}}^2}$, where Ω_{q} describes the driving strength of the qubit.

Dispersive interaction   In the dispersive regime ($\Delta_{\mathrm{qc}} \gg g_{\mathrm{q}}$), the Jaynes-Cummings Hamiltonian can be expressed as [81]

$$H_{\mathrm{T}}^{\mathrm{disp}} = \frac{1}{2}\omega_{\mathrm{c}}\sigma_{\mathrm{z}} + (\omega_{\mathrm{c}} + \chi\sigma_{\mathrm{z}})\left(a^{\dagger}a + \frac{1}{2}\right). \tag{3.28}$$

Here, we have introduced the dispersive coupling strength or shift χ. Equation (3.28) states that the microwave resonator frequency becomes an effective one, depending on the qubit state and the dispersive shift χ, as indicated in Fig. 3.2d). This allows to determine the qubit state via the resonator, as explained in Sec. 5.3.1 in detail.

Importantly, the dispersive shift for a transmon qubit is expressed by [75]

$$\chi = \frac{g_{\mathrm{q}}^2}{\Delta_{\mathrm{qc}}}\frac{\alpha}{\hbar\Delta_{\mathrm{qc}} + \alpha}. \tag{3.29}$$

We see, that for a perfect two-level system, where $\alpha \to \infty$, the second term cancels. Then the dispersive shift is sufficiently described by g_q^2/Δ_{qc}. For the transmon qubit however this leads to a reduced shift in opposite direction, as $\alpha/\hbar < 0 < \Delta_{qc}$. We note, that the anharmonicity also allows for an enhanced, positive dispersive shift in the so-called straddling regime, for $0 < \Delta_{qc} < |\alpha/\hbar|$ [75].

But the dispersive shift not only influences the microwave resonator, it also acts on the qubit state, as discussed next, and indicated in Fig. 3.2d) for an ideal two-level system.

3.4.4 Ac-Stark shift of a transmon qubit

Rearranging Eq. (3.28) in terms of σ_z we find

$$H_T^{disp} = \left(\frac{1}{2}\omega_c + \chi a^\dagger a + \frac{1}{2}\chi\right)\sigma_z + \omega_c a^\dagger a + \frac{\omega_c}{2}. \tag{3.30}$$

Here we see, that the dispersive shift also acts on the qubit, and interpreting $a^\dagger a \equiv \bar{n}_c$, the average photon number in the microwave resonator, we can observe a photon dependent shift of the qubit, the ac-Stark shift $\propto \chi\bar{n}_c$, as well as a photon number independent one, the Lamb shift $\chi/2$. When the resonator-qubit system is well characterized, this allows for a precise determination of the photon numbers in the microwave resonator, as shown in Sec. 6.5.

From this the main benefit of transmon qubits become clear: their relative long coherence times. Flux noise is sufficiently screened by tuning the transmon on the sweet spot. Then a dominant loss mechanism remaining is charge noise, thermal random excitations on the microwave resonator ($\langle n_{phot}\rangle$) causing the qubit frequency to change due to the ac-Stark shift. This leads to a dephasing of the qubit state. Via the large capacitances of the transmon, the anharmonicity is reduced, and so the dispersive shift takes the form of Eq. (3.29). Designing the sweet spot above the straddeling regime, the transmon qubit coherence benefits from the reduced ac-Stark shift. However, as the shift is reduced, so is the read-out sensibility. Yet, the frequency tuneability of the transmon qubit allows to set it either in the straddeling regime for read-out or to the sweet spot for storage. By this one benefits in both ways from the anharmonicity, making transmon qubits nowadays the working horses of cQED.

We like to note, that Eqs. (3.28) and (3.30) respectively, are linearized. So for higher photon numbers a correctional term $\propto \bar{n}_c^2$, the so-called cross-Kerr has to be taken into account [83].

3.4.5 Limitation in photon numbers induced by the Josephson nonlinearity

We have seen, that the nonlinearity is typically enhanced when reducing the critical current, cf. Sec. 3.2. So the nonlinear systems can reach a critical photon number, when the oscillating current exceeds the critical current of the Josephson junctions and the dc-SQUID switches into the voltage state. The critical number is reached for [57]

$$n_c^{squid} = \frac{E_J}{\hbar\omega_c(n)}. \tag{3.31}$$

We like to note, that the calculations above are performed for the current/excitation in the dc-SQUID, which is in contrast to the critical photon number in the (fixed-frequency)

microwave resonator when reading out a transmon qubit via the dispersive shift. Here, the effective coupling has to remain within the detuning Δ_{qc} [84]:

$$n_{\mathrm{crit}}^{\mathrm{disp}} = \frac{\Delta_{\mathrm{qc}}^2}{4g_{\mathrm{q}}^2}.$$

(3.32)

Chapter 4

Electromechanical interactions

In the upcoming chapter we will frame the context of nano-electromechanical coupled systems. We start by a brief summary of cavity optomechanics and move forwards how to realize such by using superconducting microwave resonators as optical cavities coupled to nanomechanical string oscillators. Further, we will introduce the mechanical displacement spectra and the imposed noise contributions via electromechanical detection. We discuss a realistic measurement setup and the imposed limitations when using nonlinear Josephson quantum circuits as electric resonators. In addition, we discuss sideband cooling realized by the high frequency resonators. At the end, we consider the scenario of externally driven strings, and how we can boost the effective frequency shifts exceeding the resonator decay rate that we will later determine experimentally.

4.1 From cavity optomechanics to quantum nano-electromechanics

4.1.1 Optomechanics in a nutshell

We start by considering an optical resonator, consisting of two mirrors separated by a length l_c. The ground mode of the resonator then is determined by $\omega_c/2\pi = v_{\text{phase}}/2l_c$. The optical case typically holds $v_{\text{phase}} = c$. By connecting one mirror plate to a mechanical oscillator, the length of the resonator becomes dependent on the mechanical position and so also the resonator's eigenfrequency. We show this in Fig. 4.1a) schematically.

We see a Fabry-Perot interferometer of two mirrors (blue) coupled to the environment with a rate κ_{ext} and internal losses κ_{int}. The suspended mirror couples to a mechanical oscillator (brown) of displacement $x(t)$ and a damping rate Γ_m with a single photon-phonon rate of g_{m0} (red). When we describe the position $x = x_{t0}(t = 0) + x(t)$ by a rest position set to $_{t0} = 0$, and a time depending shift of the oscillator. The linearized optomechanical frequency is then found by:

$$\omega_c(x) = \omega_c(x_0) + (\partial_x \omega_c)x(t). \tag{4.1}$$
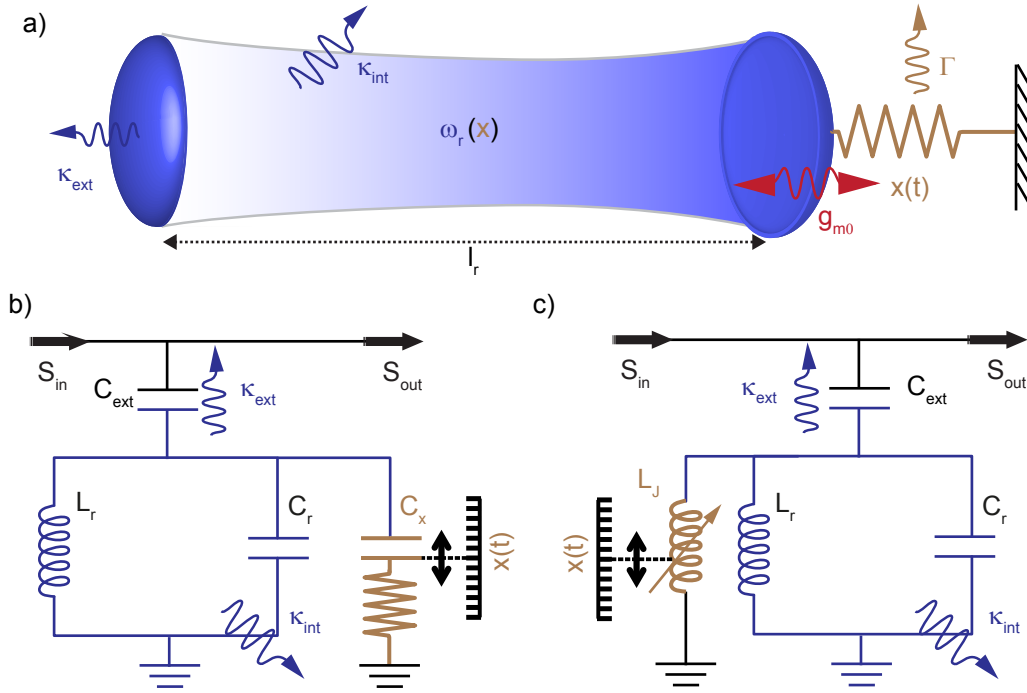
Figure 4.1: *From opto- to electromechanics.* Panel a) shows an optomechanical resonator consisting of two mirror plates of separation length l_c setting the eigenfrequency of the resonator ω_c. One mirror is connected to a mechanical spring. A position change in the mechanical element alters the length of the resonator and hereby the resonator's eigenfrequency depends on the state of the displacement of the mechanical oscillator [$\omega_c(x)$]. The translation of the mechanical motion to a frequency change is described by the single photon-phonon coupling strength g_{m0}. Further, the system's damping constants are indicated: κ_{int}, κ_{ext} for the internal and external losses of the optical resonator, as well as Γ_m for the mechanical oscillator. Switching from optical to electrical resonators their eigenfrequency is determined by the inductance and capacitive of the circuit. Panel b) and c) indicate the working principle of such electromechanical hybrid systems for a capacitively (b) and inductively (c) coupled realization. In either case an additional capacitance or inductance that depends on the state of the mechanical oscillator is inserted to the LC-resonator.

Here, we associate the microwave resonator's frequency with ω_c when the mechanical oscillator has a displacement of $x = 0$. In addition, the coupling is associated by $\partial_x\omega_c = G$. So far, we have treated the system classically, however a quantum mechanical description is desired for the investigation of non-classical states. A review on the topic is found in [86]. We focus on a short summary, starting by the Hamiltonian of the system [9]:

$$\hat{H} = \hbar\omega_c(x)\left(\hat{a}^\dagger\hat{a} + \frac{1}{2}\right) + \hbar\Omega_m\left(\hat{b}^\dagger\hat{b} + \frac{1}{2}\right), \tag{4.2}$$

where we describe the system by two harmonic oscillators: the mechanical one with eigenfrequency Ω_m and the optical resonator having a mechanical displacement sensitivity $\omega_c(x)$. The corresponding ladder operators are $\hat{a}$ ($\hat{b}$) for the optical (mechanical) oscillators. We determine the excitation numbers by the operation $\hat{a}^\dagger\hat{a} = \bar{n}_c$ for the photons and $\hat{b}^\dagger\hat{b} = n_m$

for the phonons. We describe the displacement $\hat{x}$ in agreement with the already introduced Eqs. (2.15) and (2.26).

$$\hat{x} = x_{\text{zpm}} \left(\hat{b}^\dagger + \hat{b} \right), \quad \text{with } x_{\text{zpm}} = \sqrt{\frac{\hbar}{2m_{\text{eff}} \Omega_{\text{m}}}}. \tag{4.3}$$

Here, we have used the zero-point motion of the mechanical element $x_{\text{zpm}}^2 = \langle 0 | \hat{x}^2 | 0 \rangle$ [9], with the mechanical vacuum state $|0\rangle$. By this we find the total displacement $\hat{x} = x_{\text{zpm}} \sqrt{2 n_{\text{m}}}$, which can separately be derived from the thermal occupation [87, 88]

In the quantum mechanical treatment, we describe the resonance frequency of the microwave resonator for small displacements with $\hbar \omega_{\text{c}}(x)(\hat{a}^\dagger \hat{a}) \approx \hbar(\omega_0 - G\hat{x})(\hat{a}^\dagger \hat{a})$ by using Eq. (4.1) and assuming small displacements [9][1]. From this we derive the electromechanical interaction term to

$$\hat{H}_{\text{int}} = -\hbar G \hat{x} \hat{a}^\dagger \hat{a} = -\hbar g_{\text{m0}} \hat{a}^\dagger \hat{a} \left(\hat{b}^\dagger + \hat{b} \right), \tag{4.4}$$

introducing the single-photon-phonon coupling strength $g_{\text{m0}} = G x_{\text{zpm}}$. Note that this interaction strength determines the time required for a photon to be converted into a phonon and vice versa. The radiation pressure in such an opto- or electromechanical system is given by [9]

$$\hat{F}_{\text{ba}} = -\frac{d\hat{H}_{\text{int}}}{d\hat{x}} = \hbar \frac{g_{\text{m0}}}{x_{\text{zpm}}} \hat{a}^\dagger \hat{a}, \tag{4.5}$$

which results in an important aspects of optomechanics: the radiation pressure is rather weak. Even for a relatively high coupling strength of $g_{\text{m0}}/2\pi = 500\,\text{Hz}$ and a corresponding zero-point motion of $x_{\text{zpm}} = 50\,\text{fm}$, it is about $7\,\text{aN}$ per photon. However, the additive per photon shows one of the benefits of optomechanics: when populating the optical resonator by $1.5 \cdot 10^8$ [34], the total backaction force is boosted to about $1\,\text{nN}$, which is measurable with commercial available micro balances [89]. We see, that the weak radiation pressure can be compensated by populating the microwave resonator. We will discuss details of the backaction force when we consider the noise contribution of electromechanical systems in Sec. 4.2. For now we want to transition from an optical resonator to the field of nano-electromechanics.

4.1.2 Nano-electromechanical realizations

To realize a nano-electromechanical device, we replace the optical resonator by an electric LC resonant circuit which is typically operated in the microwave regime. The microwave resonator frequency then is determined by the (total) contributions of inductance and capacitance $\omega = \sqrt{1/L_{\text{c}} C_{\text{c}}}$, c.f. Sec. 3.3. As in the optical scenario [c.f. Fig. 4.1a)], we can attribute a length to the microwave resonator $\omega = v_{\text{phase}}/\lambda$ with a phase velocity v_{phase} and the wavelength λ. For the phase velocity we have to consider an effective dielectric constant $\epsilon_{\text{eff}} = 6.4$ [64], as we use silicon based microchips with superconducting aluminum for our microwave resonators. So, the microwave resonator lengths are on the order of some mm for $\lambda/4$ resonators and frequencies in the low GHz regime. When operating these chips in a cryogenic environment of $100\,\text{mK}$ we find the resonator to be naturally in the ground state, as $\bar{n}_{\text{c}}^{\text{th}} = k_{\text{B}} T_{\text{cryo}}/(\hbar \omega) = 0.3$ for a frequency of $\omega_{\text{c}}/2\pi = 7\,\text{GHz}$. As the eigenfrequency of

---

[1]the minus sign takes care that a positive displacement results in a reduced resonator frequency, for $G > 0$

the electric resonator is determined by the combination of capacitance and inductance, we can identify possible implementation categories for the electromechanical interaction:

Capacitively coupled electromechanics Here, an additional capacitance with a mechanically compliant capacitance is integrated in the circuit, see Fig. 4.1b). This was first introduced in the form of a doubly clamped nanomechanical string oscillator [13], acting as an additional capacitance in the circuit. Further Ref. [90] addressed the capacitive coupling by changing the dielectric within the capacitor plates using a non-metalized, ultra high-Q dielectric string resonator. The weak coupling strength of the nanostrings was soon overcome by changing from a string to a drum oscillator, that allowed the observation of strong coupling [14] and ground state cooling of the mechanical element [15], which was later also achieved in optical phononic [91] and electronic phononic crystals [92], as well as for a membrane in a 3D microwave cavity [93]. The drum oscillators in superconducting resonators later were squeezed below the standard quantum limit [16, 94], as well as coherent state transfer between the microwave and mechanical systems [95].
The capacitive coupling can also act on nonlinear circuits like Josephson based quantum bits. A state transfer between such a circuit and a piezoelectric resonator was demonstrated in [96], however the high mechanical decoherence limited the mechanical storage time. In addition, electromechanical Rabi oscillations were found when integrating a nanostring in a transmon circuit [97]. Thermal states where transferred between a electromechanical drum resonator and a phase qubit in Ref. [22]. The observation of a mechanical superposition state was found by using a qubit as non-classical state source on a separate microchip coupled to an electromechanical resonator [24].
Here, however, we will integrate a transmon qubit capacitively coupled to an electromechanical circuit consisting of a microwave resonator and a doubly-clamped nanomechanical string oscillator. We will show the individual control of qubit, microwave resonator, and mechanical oscillator. The combination of those systems allows for an ultra-wide range photon number calibration, with photon numbers deviating by nine orders of magnitude, see Sec. 6.

Inductively coupled electromechanics Similar to the capacitive coupling an inductive coupling can be realized with a mechanical dependent inductance added to the circuit, as sketched in Fig. 4.1c). The approach of integrating a nanomechanical dc-SQUID, that is a dc-SQUID with a released nanostring, into a superconducting resonator was first proposed by [35], however coupling strength and radiation pressure where kept on a moderate level. In a follow up paper, the authors showed, that the nonlinearity of the dc-SQUID in the microwave resonators induces a nonlinearity, leading to a Duffing spring-softening of the resonator. The authors claim that by this nonlinearity a closer cooling to the ground state, as well as position detection closer to the standard quantum limit becomes possible [36]. Later it was shown that the vacuum coupling strength can theoretically exceed the damping of the microwave resonator, entering the single photon-phonon ultrastrong coupling regime. By this a mechanical induced dynamical Casimir effect can be observed [37]. Further Ref. [38] showed that the integration of dc-SQUID with asymmetric junctions allows to determine higher order couplings at the degenerate point of $\Phi_{\text{ext}} = \Phi/2$.
These proposals built up on initial work by van der Zant *et al.* [30], which read-out the motion of a nanomechanical dc-SQUID via a direct current [31–33].

We will show first experimental data on such a system by integrating a mechanical dc-SQUID including a $20\,\mu$m long nanostring at the current anti-node of a quarter-wavelength coplanar waveguide resonator, see Sec. 7.

4.2   Noise considerations

In the following section we introduce the mechanical displacement spectrum and discuss its contributions for measurements in thermal equilibrium to the environment. We will additionally have a look at the measurement induced noise spectra, such as imprecision and back-action induced uncertainties. We conclude by calculating a realistic scenario and highlight the imposed limits due to nonlinear effects in the electric circuits. We discuss the obtained findings in terms of improvements for the measurement setup.

4.2.1   Thermal motion of a nanostring

Next we will discuss an electromechanical displacement spectrum and its components. For this, we first focus on the mechanical displacement spectra of the nanostring, which we assume to be in thermal equilibrium with the environment at a temperature of 125 mK. As the string's eigenfrequency is at the low single-digit MHz-regime, it is thermally excited and a classical treatment is sufficient, a quantum mechanical treatment of the following calculation is found in [98]. The string's (double sided) noise power spectral density is defined as [9]

$$S_{\mathrm{xx}}(\Omega) \equiv \int\limits_{-\infty}^{\infty} \langle x(t)x(0) \rangle e^{i\Omega t} \cdot dt. \tag{4.6}$$

We like to note, that here we used the angular frequency $(\Omega/2\pi = f)$ spectrum $S_{\mathrm{xx}}(\Omega)$, which can be transferred to the direct frequency spectrum $S_{\mathrm{xx}}(f) = S_{\mathrm{xx}}(\Omega)/2\pi$ [2][43]. For a physical interpretation we link this to the spectral density $\langle |\tilde{x}(\Omega)|^2 \rangle$, where $\tilde{x}(\Omega)$ describes the Fourier transform of the time trajectory of the mechanical displacement for a specific measurement time τ, c.f. Sec. 2.1. The link is realized via the Wiener-Khinchin theorem which results in the spectral density approaching S_{xx} for $\tau \to \infty$ [9], and we relate the area of the measured power spectral density to match the variance of the mechanical displacement [9]:

$$\int\limits_{-\infty}^{\infty} S_{\mathrm{xx}}(\Omega) \frac{d\Omega}{2\pi} = \langle x^2 \rangle. \tag{4.7}$$

By the equipartition theorem it is stated, that the system's energy is distributed with $1/2k_{\mathrm{B}}T$ per degree of freedom [99]. Therefor, in thermal equilibrium, the energy is distributed by

$$\frac{1}{2}k_{\mathrm{B}}T = \frac{1}{2}m_{\mathrm{eff}}\Omega^2 \langle x^2 \rangle \to \langle x^2 \rangle = \frac{k_{\mathrm{B}}T}{m_{\mathrm{eff}}\Omega^2}. \tag{4.8}$$

In combination with Eq. (4.7) we see, that when the environmental temperature is reduced, the signal area is also shrinking. This requires a detection efficiency close to the quantum limit the closer the quantum regime is approached.

Next we introduce the mechanical susceptibility relating the string's motion coordinate

---

[2]an additional factor of 2 can arise from single or double sided detection

to an external force $x(\Omega) = \chi_{\mathrm{m}}(\Omega) F_{\mathrm{ex}}(\Omega)$, again defined in the angular frequency space, see also Eq. (2.9). It can be derived by solving the equation of motion of an individual[3] nanostring in (angular) frequency space to

$$\chi_{\mathrm{m}}(\Omega) = \left[m_{\mathrm{eff}} \left(\Omega_{\mathrm{m}}^2 - \Omega^2 \right) - i \cdot m_{\mathrm{eff}} \Gamma_{\mathrm{m}} \Omega \right]^{-1}. \tag{4.9}$$

Then, assuming thermal equilibrium, the fluctuation dissipation theorem allows to express the thermal noise power spectral density to [9]

$$S_{\mathrm{xx}}^{\mathrm{th}}(\Omega) = 2 \frac{k_{\mathrm{B}} T}{\Omega} \mathrm{Im}(\chi_{\mathrm{m}}), \tag{4.10}$$

corresponding to Lorentzian features at the frequencies $\pm \Omega_{\mathrm{m}}$ (double sided) having a linewidth Γ_{m}. Now we quantified the spectral density of the nanostring. We see, that it linearly depends on the string's temperature. Later, we will make use of this relation to determine the vacuum coupling strength of the electromechanical system. Now two questions arise from this derivation: first, this calculation was done neglecting any noise contributions. How is the electromechanical and technical noise influencing the spectra? And second: When discussing nanomechanical quantum systems, why is the semi-classical treatment valid in this scenario?

Regarding the second part this treatment is justified, as the environmental temperature at $125\,\mathrm{mK}$ is still much higher than the quantum mechanical ground state ($0.4\,\mathrm{mK}$ for a resonance frequency of $\Omega_{\mathrm{m}}/2\pi = 6.343\,\mathrm{MHz}$). In a quantum mechanical treatment the displacement density is found to be [98]

$$S_{\mathrm{xx}}^{\mathrm{th}}(\Omega) = 2 \frac{\hbar}{1 - e^{\hbar\Omega/(k_{\mathrm{B}}T)}} \mathrm{Im}(\chi_{\mathrm{m}}). \tag{4.11}$$

This expression approaches (4.10) for $\hbar\Omega \ll k_{\mathrm{B}}$. So when investigating the classical thermal noise power spectral density of a temperature of $125\,\mathrm{mK}$ and a mechanical frequency of $\Omega_{\mathrm{m}}/2\pi = 6.343\,\mathrm{MHz}$ the deviations between the quantum [Eq. (4.11)] and the classical description [Eq. (4.10)] are negligible.

4.2.2   Frequency noise contribution

So far, we have analyzed the mechanical displacement density of a nanostring. When such a string is coupled to an opto- or electronic resonator the string's displacement modulates the resonator frequency as discussed in Sec. 4.1.1. When the microwave resonator is investigated by a spectroscopy tone, the mechanical motion adds sidebands as a phase modulation onto the tone.

In the following we will discuss the noise contributions from the phase imprecision and the back-action onto the electromechanical system in such a realization. We do this for a probe tone on resonance to the electric resonator ($\Delta_{\mathrm{p}} = \omega_{\mathrm{p}} - \omega_{\mathrm{c}} = 0$). By this the mechanical motion modulates the phase response of the probe tone. A direct and important conclusion from this is that the probe tone's phase fluctuations determine the noise level of the measurement [17]. This noise floor can be reduced by increasing the drive power, as the

---

[3]assuming no back-action to the resonator

statistical phase imprecision readout scales $\propto \sqrt{\bar{n}_c}$. The quantum limited (no additional noise phonons $n_{\mathrm{add}} = 0$) imprecision spectrum reads [9]

$$S_{\mathrm{xx}}^{\mathrm{imp}}(\Omega) = \frac{\kappa x_{\mathrm{zpm}}^2}{16\bar{n}_c g_{\mathrm{m0}}^2}\left(1 + 4\frac{\Omega^2}{\kappa^2}\right). \tag{4.12}$$

We find the imprecision noise floor to reduce when using high quality resonators (κ small). This increases the transduction from mechanical motion to the cavity. Additionally, high electromechanical couplings increase this translation, here the noise floor is decreased quadratically. When reaching the standard quantum limit, the use of squeezed light enables the reduction of the phase noise and herby improves the imprecision noise [17]. Besides that, it seems obvious to simply increase the amount of photons. However, this increases the back-action force, see Eq. (4.5). The back-action force noise is described by [9]:

$$S_{\mathrm{FF}}^{\mathrm{ba}}(\Omega) = \bar{n}_c \frac{4\hbar^2 g_{\mathrm{m0}}^2}{\kappa x_{\mathrm{zpm}}^2}\left(1 + 4\frac{\Omega^2}{\kappa^2}\right)^{-1}, \tag{4.13}$$

for which we find a linear increase in the photon number. Under the assumption of optimal detection we now have found the universal result $S_{\mathrm{xx}}^{\mathrm{imp}}(\Omega)S_{\mathrm{FF}}^{\mathrm{ba}}(\Omega) = \hbar^2/4$, which reflects the Heisenberg uncertainty principle: increasing the amount of photons reduces the phase noise, but at the same time increases the amplitude fluctuations, leading to an increased back-action force. We find the photon numbers for the optimum total displacement noise floor Min $\left[S_{\mathrm{xx}}^{\mathrm{imp}} + S_{\mathrm{xx}}^{\mathrm{ba}}\right]$, where we have translated the back-action force spectral density into a displacement density via $S_{\mathrm{xx}}^{\mathrm{ba}} = S_{\mathrm{FF}}^{\mathrm{ba}}(\Omega)|\chi_{\mathrm{m}}(\Omega)|^2$ to

$$\bar{n}_c^{\mathrm{opt}}(\Omega) = \frac{x_{\mathrm{zpm}}^2}{8g_{\mathrm{m0}}^2}\frac{\kappa^2 + 4\Omega^2}{\hbar\kappa}|\chi_{\mathrm{m}}(\Omega)|. \tag{4.14}$$

We see, that we can push the optimal photon number towards small numbers by increasing the electromechanical coupling strength g_{m0}. The corresponding spectral density of the optimal photon number can be associated to the nanostring's zero-point motion as the standard quantum limited displacement density

$$S_{\mathrm{xx}}^{\mathrm{sql}}(\Omega) = \hbar|\mathrm{Im}(\chi_{\mathrm{m}}(\Omega))|. \tag{4.15}$$

For a nanostring as introduced in Sec. 7.2 this corresponds to a value of $S_{\mathrm{xx}}^{\mathrm{sql}}(\Omega_{\mathrm{m}}) = \hbar/(m_{\mathrm{eff}}\Gamma_{\mathrm{m}}\Omega_{\mathrm{m}}) = 2.8 \cdot 10^{-29}\,\mathrm{m^2 s}$ on resonance to the mechanical element. We reach this low value by the use of thin, annealed aluminum nanostrings.

Taken the obtained findings together we quantify the total measured spectrum for the case of quantum limited detection described by the individual terms introduced before as

$$S_{\mathrm{xx}}^{\mathrm{total}} = S_{\mathrm{xx}}^{\mathrm{th}}(\Omega) + S_{\mathrm{xx}}^{\mathrm{imp}}(\Omega) + S_{\mathrm{FF}}^{\mathrm{ba}}(\Omega)|\chi_{\mathrm{m}}(\Omega)|^2. \tag{4.16}$$

We can express this in terms of the standard quantum limit (which was defined by the minimum of the last two terms). So the relation to the thermal spectrum remains, which is simply

$$S_{\mathrm{xx}}^{\mathrm{th}}(\Omega)/S_{\mathrm{xx}}^{\mathrm{sql}}(\Omega) = 2\frac{k_{\mathrm{B}}T}{\hbar\Omega} = 2n_{\mathrm{m}}^{\mathrm{th}}, \tag{4.17}$$

calculated by Eq. (4.10) and (4.15). It is remarkably, that this result is independent of the mechanical frequency.
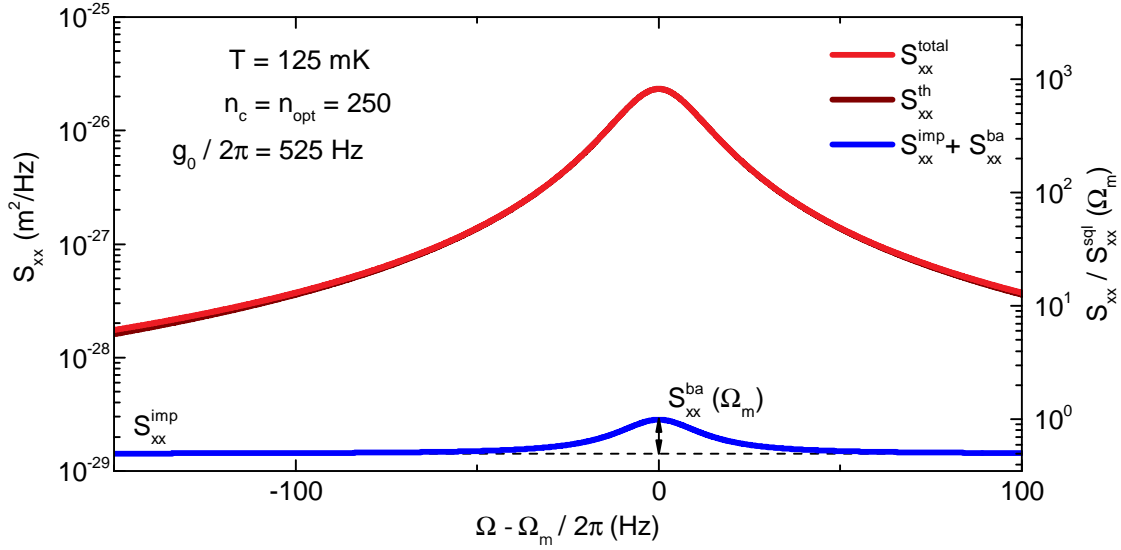
Figure 4.2: *Frequency noise contributions at optimal drive power.* We derive the ideal total signal
(red), the thermal motion spectra of the nanostring (brown), as well as electromechanical noise
contributions at an optimal drive power (blue) consisting of the back-action and impression
noise (black dotted line). We note, that on mechanical resonance both noise contributions
are equal at the optimal driving point. The right axis was calibrated in units of the standard
quantum limit of the string.

4.2.3   Thermal displacement spectras

Now we have derived all electromechanical noise sources contributing to the displacement
spectra. In Fig. 4.2 we plot the expected spectrum and contributions for an optimal
photon number $\bar{n}_{\mathrm{c}}^{\mathrm{opt}}(\Omega_{\mathrm{m}})$, at a temperature of $125\,\mathrm{mK}$, and for a mechanical element as
later discussed (for parameters see Sec. 7.2). We do this using Eqs. (4.9)-(4.16).

As the string is thermally populated ($n_{\mathrm{m}} = 410$) and the electromechanical noise
reduced by assuming an ideal detection and optimal driving, we find the measured
total spectrum (red) only slightly above the thermal spectra of the nanostring (brown).
This is expected as for the given parameters on resonance ($\Omega = \Omega_{\mathrm{m}}$) Eq. (4.10) states
$S_{\mathrm{xx}}^{\mathrm{th}} = 2.3 \cdot 10^{-26}\mathrm{m}^2/\mathrm{Hz}$ and Eqs. (4.12), (4.13) predict $S_{\mathrm{xx}}^{\mathrm{imp}} + S_{\mathrm{xx}}^{\mathrm{ba}} = 2.8 \cdot 10^{-29}\mathrm{m}^2/\mathrm{Hz}$.
Further for the ratio between the electromechanical noise terms ($S_{\mathrm{xx}}^{\mathrm{imp}} + S_{\mathrm{xx}}^{\mathrm{ba}}$) is found to be
$2n_{\mathrm{m}} = 820$, in agreement to Eq. (4.17). Also note, that at the resonance point $S_{\mathrm{xx}}^{\mathrm{imp}} = S_{\mathrm{xx}}^{\mathrm{ba}}$,
which is hidden in the logarithmic scale of the figure. When the thermal occupation
of the nanostring is reduced to reach quantum mechanical states (c.f. Sec. 2.3.2), the
high ratio between $S_{\mathrm{xx}}^{\mathrm{th}}$ and $S_{\mathrm{xx}}^{\mathrm{imp}} + S_{\mathrm{xx}}^{\mathrm{ba}}$ is shrinking [see Eq. (4.17)]. Especially when
considering imperfect detection (e.g. $S_{\mathrm{xx}}^{\mathrm{imp}} \to S_{\mathrm{xx}}^{\mathrm{imp}} + S_{\mathrm{xx}}^{\mathrm{tech}}$ [17]). Therefor the experimental
investigation of nonclassical states benefits greatly by the installation of quantum limited
amplifiers, in particular Josephson Parametric Amplifiers (JPAs) reducing the amplifier
noise considerably. We like to note, that for a full quantum mechanical description the
classical displacement spectrum has to be replaced by the quantum distribution (Eq. 4.11),
which was not done here due to the high thermal excitation.
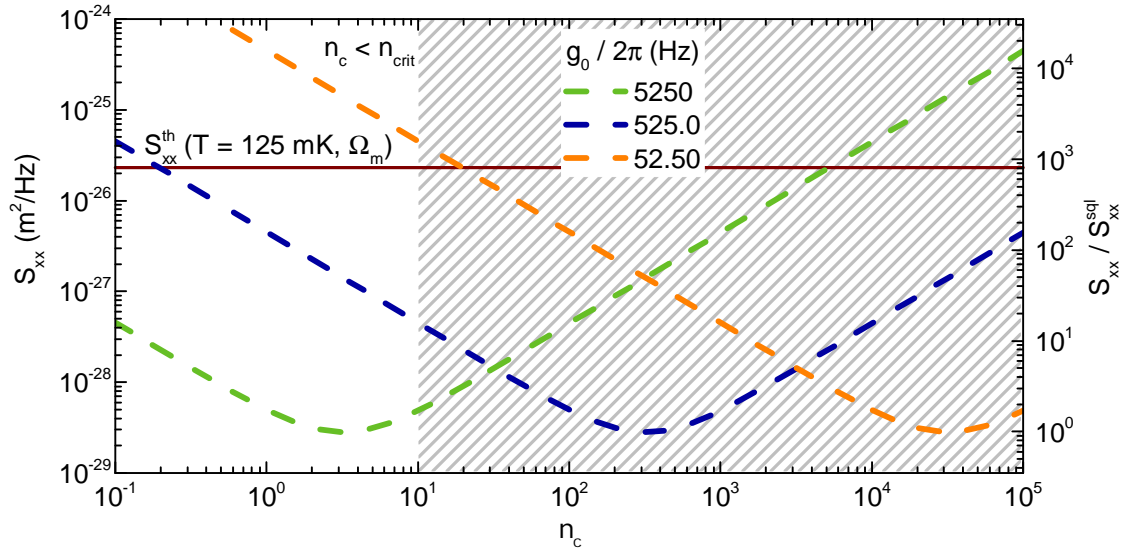
Figure 4.3: *Electromechanical noise versus photon numbers.* The graph shows the total ideal electromechanical noise for three different coupling strengths. The experimental scenario of about 500 Hz coupling is shown in blue, a weaker one in orange and a stronger coupled scenario in green. As the nonlinearity of the electric resonator limits us to photon numbers of the order of 10 (area above in grey), the detected signal height becomes drastically reduced. Only for the stronger coupling scenario the optimal drive power can be reached.

Although, the optimal photon number cannot always be reached. One potential scenario in which this limitation can occur is when the electromechanical interaction is so weak, that the required photons for the optimal photon number are high enough that the resonator becomes unstable, or the experiment gets heated up by the probe tone power. Another scenario arises within this thesis, as we use nonlinear elements, in particular Josephson junctions. Their intrinsic nonlinearity limits the amount of photons we can apply to the circuit (c.f. Sec. 3.4.5), before the electric resonator stops acting harmonic. We discuss such photon number limitations quantitatively in Fig. 4.3, using similar parameters as in Fig. 4.2, that is: zero detuning $\omega_\mathrm{p} = \omega_\mathrm{c}$, on resonance to the mechanical string $\Omega = \Omega_\mathrm{m}$, optimal detection $S_\mathrm{xx}^\mathrm{tech} = 0$, an environmental temperature of 125 mK and the string's parameter as introduced in Sec. 7.2. We plot the electromechanical noise contributions in blue for a coupling of $g_\mathrm{m0}/2\pi = 525\,\mathrm{Hz}$, equivalent to Fig. 4.2, as well as a weaker (orange) and stronger (green) coupling. In both figures 4.2 and 4.3 the blue line indicates the electromechanical noise contribution to the displacement spectrum. In Fig. 4.2 this is shown for an optimal photon number over the angular frequency Ω, while in Fig. 4.3 this is plotted on resonance to the mechanical string ($\Omega = \Omega_\mathrm{m}$) as a function of the inserted photons. So, while in the first figure imprecision and back-action noise contributed equally, we now find the imprecision noise dominating below $\bar{n}_\mathrm{c}^\mathrm{opt}$ in $\propto 1/\bar{n}_\mathrm{c}$, while after the optimal photon number, the back-action noise becomes dominant ($\propto \bar{n}_\mathrm{c}$). As we will later show in Sec. 7.4.3 for the working spot we analyze, the photon number is limited to about $\bar{n}_\mathrm{c} = 10$ by the microwave resonator including the SQUID (grey area). Furthermore the developed measurement schemes will be performed around $\bar{n}_\mathrm{c} \approx 1\,\mathrm{photon}$. Independent of the photon number, the thermal displacement is always found at $S_\mathrm{xx}^\mathrm{th} = 2.3 \cdot 10^{-26}\,\mathrm{m^2/Hz}$ (brown solid line). So when we reduce the photon num-

bers from the optimal point of 318 to 10 or 1, the background is increasing (following the blue dashed line), which reduces the signal to noise ratio. We find ratios of 820, 51, and 4 for photon numbers of $\bar{n}_c = 318, 10, 1$. By this the electronic setup has to be well optimized, so that the observation of the nanostring remains feasible.

We find the noise contributions shifting quadratically in the photon numbers when changing the electromechanical vacuum strength in accordance to Eq. (4.14). For weaker coupling (orange) an observation of the mechanical motion is not possible given the limitations imposed by the nonlinear Josephson elements. Higher coupling (green) allows to shift the optimal photon number within the reach of the electric resonator. For the realization of inductive coupling (c.f. Sec. 7) this can be achieved by higher magnetic fields. However in our experiments, the currents inducing the external field via an external coil already started heating the sample and so, the moderate coupled scenario (blue) had to be examined.

We discuss contributions by the measurement detection (S_{xx}^{tech}) in Sec. 7.6.5, on the basis of our experimental data.

4.3   Electromechanical sideband cooling

To investigate the radiation pressure induced dynamical back-action effects, we employ the input-output formalism, in a semi-classical limit, valid if photon and phonon numbers are sufficiently large, such that we can describe the resonator field amplitude via $a(t) = \langle \hat{a}(t) \rangle$ and the nanostring's position by $x(t) = \langle \hat{x}(t) \rangle$. We find two coupled differential equation [9]:

$$\partial_t a(t) = -\frac{\kappa}{2} a(t) - i(\omega_c - G x(t)) a(t) + \sqrt{\frac{\kappa_{ext}}{2}} s_{in}(t), \qquad (4.18)$$

$$m_{eff} \partial_t^2 x(t) = -m_{eff} \Omega^2 x(t) - m_{eff} \Gamma_m \partial_t x(t) + \hbar G |a(t)|^2. \qquad (4.19)$$

When solving these equations for a weak test force, the calculated response is equivalent to the modified mechanical susceptibility, for which one finds [9]

$$\chi_{m,eff} = \left\{ m_{eff} \left[\Omega_m^2 - \Omega^2 + 2\Omega \delta\Omega_m(\Omega) - i\Omega\Gamma_m - i\Omega\Gamma_{opt}(\Omega) \right] \right\}^{-1}. \qquad (4.20)$$

Where we introduced modifications in comparison to Eq. (2.9) by the electromechanical interaction for the mechanical spring constant leading to a shift $\delta\Omega_m$, and to an additional damping rate Γ_{opt}. For the electromechanical changes now follows [9]

$$\delta\Omega_m(\Omega) = \bar{n}_c g_{m0}^2 \frac{\Omega_m}{\Omega} \left[\frac{\Delta_{mc} + \Omega}{(\Delta_{mc} + \Omega)^2 + (\kappa/2)^2} + \frac{\Delta_{mc} - \Omega}{(\Delta_{mc} - \Omega)^2 + (\kappa/2)^2} \right], \qquad (4.21)$$

$$\Gamma_{opt}(\Omega) = \bar{n}_c g_{m0}^2 \frac{\Omega_m}{\Omega} \left[\frac{\kappa}{(\Delta_{mc} + \Omega)^2 + (\kappa/2)^2} - \frac{\kappa}{(\Delta_{mc} - \Omega)^2 + (\kappa/2)^2} \right]. \qquad (4.22)$$

We note, that a quantum mechanical treatment of the interaction Hamiltonian lead to similar equations in the quantum regime, as derived in [43, 100], which differ from this semiclassical calculations only for phonon numbers in the single digit regime [101].

The total damping on resonance to the mechanical oscillator becomes an effective linewidth

$$\Gamma_{eff} = \Gamma_m + \Gamma_{opt}(\Omega_m), \qquad (4.23)$$
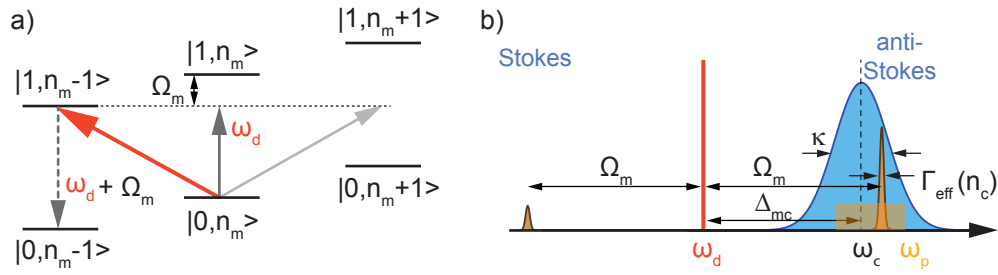
Figure 4.4: *Schematical depiction of sideband cooling in electromechanics.* Panel a) Raman transition diagram. The mechanical element has an eigenfrequency in the low megahertz regime. The electromechanical photon-phonon interaction causes Stokes and anti-Stokes sidebands on the drive tone ω_d. In general three processes on those sidebands can be found: the indicated red transition removing a phonon from the mechanical oscillator. Second the photon can be absorbed by the electric resonator (grey) and third a phonon in the mechanical element can be created (light grey). By setting the drive tone detuning, these processes can be selectively switched on and off. For a detuning of $-\Omega_m$, the phonon annihilation is the dominant scattering process, where the inserted drive tone photon and a removed phonon scatter into the electric resonator, effectively cooling the mechanical mode. Panel b) displays the EMIA configuration, with the mechanical sidebands shown in brown, a red detuned drive tone, setting the photon numbers in the microwave resonator (blue). An additional weak probe tone around the resonator frequency (orange) interferes with the scattered photons, leading to the electromechanically induced absorption

with the electromechanical contribution from Eq. (4.22). We see, that depending on the drive tone frequency detuning $\Delta_{mc} = \omega_d - \omega_c$, we can increase or decrease the effective linewidth. The decrease can even lead to a self-oscillation regime [102, 103].

We will now interpret this result physically, with focusing on a scenario when the drive tone is red detuned ($\Delta_{mc} = -\Omega_m$), corresponding to an effective cooling of the mechanical mode. For this we start by having a look of this scenario in the transition diagram found in Fig. 4.4a).
The sidebands generated by the mechanical element on the microwave resonator allow for two further scattering processes besides an absorption of the drive photon by the resonator (grey): i) via a Stokes process (light grey), the inserted photon creates a phonon in the mechanical oscillator. The required energy is taken from the photon and it remains with $\Delta_{mc} = \omega_d - \omega_c = +\Omega_m$. ii) the anti-Stokes process (red), when a phonon is removed from the oscillator to scatter with the probe photon into the resonator. We can associate these scatterings with a rate A^- (anti-Stokes) and A^+ (Stokes), and so we can describe the electromechanical damping with [9]:

$$\Gamma_{opt}(\Omega_m) = A^- - A^+. \tag{4.24}$$

In comparison with Eq. (4.22) we directly find the corresponding rates. In a quantum mechanical treatment, they can be derived from Fermi's golden rule [98]. In a continous wave experiment, we can measure the steady-state solution of the phonon population by comparing the linewidth change via [9]:

$$n_m^{cooled} = \frac{A^+ + n_m^{th}\Gamma_m}{\Gamma_{opt} + \Gamma_m} = \frac{n_m^{th}\Gamma_m}{\Gamma_{eff}}, \tag{4.25}$$

where the right equivalent is only valid for the case of an optimal red-sideband drive ($\Delta_{\mathrm{mc}} = +\Omega_{\mathrm{m}}$). Equivalently we can determine the final mode temperature when switching from particle to a temperature picture $T_{\mathrm{final}} = T_{\mathrm{init}}\Gamma_{\mathrm{m}}/\Gamma_{\mathrm{eff}}$ [9]. A detailed derivation on the final occupation up to second order can be found in [15, 104].

We briefly like to discuss the fundamental limit of sideband cooling, which is in the resolved sideband regime ($\kappa \ll \Omega_{\mathrm{m}}$) given by [9]:

$$n_{\mathrm{m}}^{\min} = \left(\frac{\kappa}{4\Omega_{\mathrm{m}}} \right)^2 < 1. \tag{4.26}$$

This demonstrates the importance of designing the electromechanical samples in the resolved sideband regime. If the devices are not in this regime, the result of Eq. (4.26) is larger 1, preventing ground state cooling.

We briefly want to discuss what happens when a second weak probe tone is switched on, scanning along the scattered anti-Stokes photons around the microwave resonator frequency. The experimental scheme is depicted in Fig. 4.4b). When we consider the microwave resonator to be of a $\lambda/2$ one, measured in transmission (experimental situation in Sec. 6), the microwave probe tone is only detected on resonance to the electric resonator, as otherwise the signals are blocked by it. Under the influence of a strong drive tone (red) applied to the electromechanical resonator in the red-sideband configuration, anti-Stokes photons are generated at $\omega_{\mathrm{d}}+\Omega_{\mathrm{m}} \approx \omega_{\mathrm{c}}$ in a Lorentzian lineshape with the effective mechanical damping rate Γ_{eff} (brown). As these upconverted photons now destructively interfere with the probe tone (orange), we find an electromechanically induced absorption (EMIA) or transparency (EMIT) depending on the microwave transmission. The EMIA/EMIT feature is a Lorentzian peak with linewidth Γ_{eff}. When sweeping the drive tone power, the amount of resonator photons is changed. Plotting the effective linewidth over drive power, we can calibrate the photon numbers, as it remains the only free fit parameter, if the electromechanical resonator was precharacterized before properly.

4.4 Coherent mechanical excitations in electromechanical systems

In the following we consider an externally driven mechanical motion of a nanostring. As we will consider coherent motion of the nanostring, a classical treatment is sufficient. We will focus on the results of the calculations and refer for details of the calculation to App. G. One possible realization for such a scenario can be a piezo actuator shaking the electromechanical system [90], alternatively the coherent motion can also be excited by a blue sideband drive [105]. By a proper choice of the probe tone and the intrinsic low radiation pressure force [cf. Eq. (4.5)], the electromechanical backaction becomes negligible. This decouples the electromechanical differential equations and we solve for the string's motion [cf. Eq. (4.19)]:

$$x(t) = x_0 \sin(\Omega_{\mathrm{m}} t). \tag{4.27}$$

Here the motion amplitude x_0 is the maximum displacement which is a consequence of the external driving force. By this only Eq. (4.18) has to be solved for an applied input field of $s_{\mathrm{in}}(t)$:

$$\partial_t a(t) + \left[\frac{\kappa}{2} - i\left(\omega_{\mathrm{c}} - Gx(t)\right) \right] a(t) = \sqrt{\kappa_{\mathrm{ext}}} s_{\mathrm{in}}(t). \tag{4.28}$$

The solution of this inhomogeneous differential equation is constructed from the homogenous solution $a_h(t)$ for $s_{in}(t) = 0$ and a partial solution $a_p(t)$. The full solution is given by their sum. For the homogenous solution we find

$$a_h(t) = \exp\left[\left(-\frac{\kappa}{2} + i\omega_c\right)t + i\beta\cos\left(\Omega_m t\right)\right], \tag{4.29}$$

where we have introduced the dimensionless parameter [105]

$$\beta = \frac{Gx_0}{\Omega_m}. \tag{4.30}$$

This parameter relates the maximum frequency shift of the microwave rsonator Gx to the energy scale of the mechanical element. The numerator resembles the shape of a driven coupling as $Gx_0 = g_{m0}\sqrt{2n_m}$, similar to the effective (undriven) coupling $g = g_{m0}\sqrt{\bar{n}_c}$ typically used in electromechanical systems [9, 14].

In the following, we use Bessel-functions of first kind and n-th order $J_n(\beta)$ to describe the oscillations on exponential functions. This concept has been used successfully to calculate the response of Josephson junctions to ac-driven voltages [45, 52, 105]

$$\exp\left[-i\beta\cos(\Omega_m t)\right] = \sum_{n=-\infty}^{\infty} (-i)^n J_n(\beta)\exp(in\Omega_m t). \tag{4.31}$$

Then the particular solution is given by

$$a_p = \sqrt{\kappa_{ext}}s_{in} \sum_{n,m=-\infty}^{\infty} \frac{(i)^{m-n}J_n(\beta)J_m(\beta)\exp\left\{i[\omega + (n-m)\Omega_m]t\right\}}{\frac{\kappa}{2} + i(\Delta_p + n\Omega_m)}. \tag{4.32}$$

The solution to the differential equation (4.28) is given by $a_h(t) + a_p(t)$. However, the exponential decay of $a_h(t)$ with $\kappa/2$ [cf. Eq. q. (4.29)] in combination with typical measurement bandwidths of $1\,\text{kHz}$ allows to neglect $a_h(t)$. Thus, the steady state solution of the resonator field is described by $a_p(t)$.

So the detected output field transmitted through the mechanically driven sample becomes $s_{out} = s_{in}\exp(i\omega t) - \sqrt{\kappa_{ext}}a_p(t)$. Then the complex transmission parameter is found to be

$$S_{21} = \frac{s_{out}}{s_{in}} = 1 - \sqrt{\kappa_{ext}}\,a_p(t)/s_{in}\exp(-i\omega t)$$

$$= 1 - \kappa_{ext} \sum_{n,m=-\infty}^{\infty} \frac{(i)^{m-n}J_n(\beta)J_m(\beta)\exp\left[i(n-m)\Omega_m t\right]}{\frac{\kappa}{2} + i(\Delta_p + n\Omega_m)} \tag{4.33}$$

Another important fact is that we perform the experiment using a network analyzer. Thus the device only records signals on resonance with the probe. Thus we have to consider only vanishing rotations of the signal [set by $\exp(i(n-m)\Omega_m t)$] when $m = n$. We use this simplification when we later compare the absolute transmission of the signal to the data [105]

$$|S_{21}|^2 = 1 - \kappa_{ext}\left(\kappa - \kappa_{ext}\right) \sum_{n=-\infty}^{\infty} \frac{[J_n(\beta)]^2}{(\kappa/2)^2 + (\Delta_p + n\Omega_m)}, \tag{4.34}$$

in agreement with Ref. [100] for capacitively coupled electromechanics.

Intermediately driven strings   In the following we will discuss the solution of Eq. (4.28) in the sense $\beta \ll 1$, for which we will linearize in β. We do this to interpret the result physically.

The homogenous solution remains fast decaying and so is not of further interest. The linearized particular solution reads:

$$a_{\text{p,w}} = \sqrt{\kappa_{\text{ext}}} \frac{s_{\text{in}}(t)}{\frac{\kappa}{2} + i\Delta_{\text{p}}}$$

$$\left\{ 1 + 2\beta\Omega_{\text{m}} \frac{-2\Omega_{\text{m}}\cos(\Omega_{\text{m}}t) + (\kappa + 2i\Delta_{\text{p}})\sin(\Omega_{\text{m}}t)}{(\kappa + 2i\Delta_{\text{p}})\left[\kappa + 2i(\Delta_{\text{p}} + \Omega_{\text{m}})\right](i\kappa + 2(-\Delta_{\text{p}} + \Omega_{\text{m}}))} \right\}. \tag{4.35}$$

Again, the output field is quantified by $s_{\text{out,w}} = -\sqrt{\kappa_{\text{ext}}}a_{\text{p,w}}$, which allows to similarly calculate the scattering parameter $S_{21,\text{w}}$, which is for an on-resonance microwave drive ($\Delta_{\text{p}} \to 0$) given by

$$S_{21,\text{w}} = 1 - \frac{\kappa_{\text{ext}}}{\kappa} + i2\frac{\kappa_{\text{ext}}}{\kappa}\beta\Omega_{\text{m}}\frac{2\Omega_{\text{m}}\cos(\Omega_{\text{m}}t) - \kappa\sin(\Omega_{\text{m}}t)}{\kappa^3 + 4\kappa\Omega_{\text{m}}^2}. \tag{4.36}$$

In this notation we can directly determine the real and imaginary part of the scattering parameter and transform them for a physical interpretation of the results in transmission $|S_{21,\text{w}}|^2$ and phase ϕ. Starting with the transmission, we find

$$|S_{21,\text{w}}|^2 = S_{21,\text{w}}\bar{S}_{21,\text{w}} = 1 - 2\frac{\kappa_{\text{ext}}}{\kappa} + 2\left(\frac{\kappa_{\text{ext}}}{\kappa}\right)^2 + 4\left(\frac{\kappa_{\text{ext}}^2}{\kappa^2}\beta^2\Omega^2(\ldots)^2\right) \approx \left(1 - \frac{\kappa_{\text{ext}}}{\kappa}\right)^2. \tag{4.37}$$

Here, we abbreviated the fraction of Eq. (4.36) to $(\ldots)$, as it is of no further interested for this estimation. We see no effect of the nanostring on the transmission signal for weak mechanical excitations. However, having a look at the phase, we find:

$$\varphi = \arctan\left[\frac{\text{Im}\left(S_{21,\text{w}}\right)}{\text{Re}\left(S_{21,\text{w}}\right)}\right] = \arctan\left[\frac{2\frac{\kappa_{\text{ext}}}{\kappa}\beta\Omega_{\text{m}}(\cdots)}{1 - \frac{\kappa_{\text{ext}}}{\kappa}}\right] \propto \Omega_{\text{m}}\beta = Gx_0. \tag{4.38}$$

The proportionality is introduced as we assume small displacements, leading to the small angle in the argument of the arc tangent. This results in a modulation of the microwave resonator's phase. In other words, the mechanical mode is transformed linearly into a phase change of the resonator, while the transmission remains unchanged. Only for higher displacements or coupling strengths the absolute value of the transmission begins to be influenced by the string, showing sidebands with a splitting of the mechanical frequency, see Eq. (4.34). When the induced modulation becomes comparable to the frequency of the string, mechanical sidebands occur in the transmission, as discussed above.

Alternatively to the introduced approach, one can reduce the results from the strongly driven calculations by only taking $n = \{0, \pm 1\}$ into account for the Bessel functions of first kind, e.g. derived in [106], leading to similar results.

How such modulations are detected in experiments is detailed in Sec. 5.2.

5

Low noise detection

The remaining problem is just one of implementation.

Frank Deppe, during Qubit-Group meeting, 04.06.2019

In this section we like to give a short overview on the experimental environment and the techniques required to measure mechanical motion, as well as quantum mechanical states on the low photon level.

For this we introduce the cryostat with a brief discussion of the microwave setup. Then we discuss the implementation of a microwave interferometer at cryogenic temperatures to study electromechanical circuits limited by the available radiation pressure due to nonlinear Josephson elements. We will describe the working principle and show the functionality on an exemplary dataset.

Another aspect is the implementation of a time-domain spectroscopy that allows to study the qubit, and (hopefully) in future studies the mechanical decoherence directly. We derive the dispersive shift of the transmon qubit on the microwave resonator, that allows us to determine the qubit state. Further, we introduce the specific setup we utilized within this thesis. Also aspects of the data acquisition are presented. We conclude by discussing the pulse schemes employed here.

5.1 Low temperature environments

To operate our microwave circuits on the single quantum level, we operate the device at a temperature in the millikelvin regime. For this we use a commercial dry dilution fridge, a *Triton 400* from *Oxford Instruments* [107]. The working principle of such dry fridges, as discussed in detail in Ref. [108], allows for a large sample environment, and requires no filling with liquified helium. In Fig. 5.1 a) a photo of this cryostat is shown. The base temperature of about $50\,\mathrm{mK}$ ensures that microwave circuit elements are indeed in their thermal ground state. Further, radiation is screened by a variety of thermal shields. However, special care has to be taken on the microwave setup, since it has to be prevented that room temperature radiation reaches the sample, as sketched in Fig. 5.1b) for an exemplary configuration: The input lines are heavily attenuated using so-called microwave attenuators, which are thermally coupled to the corresponding temperature stage. Their
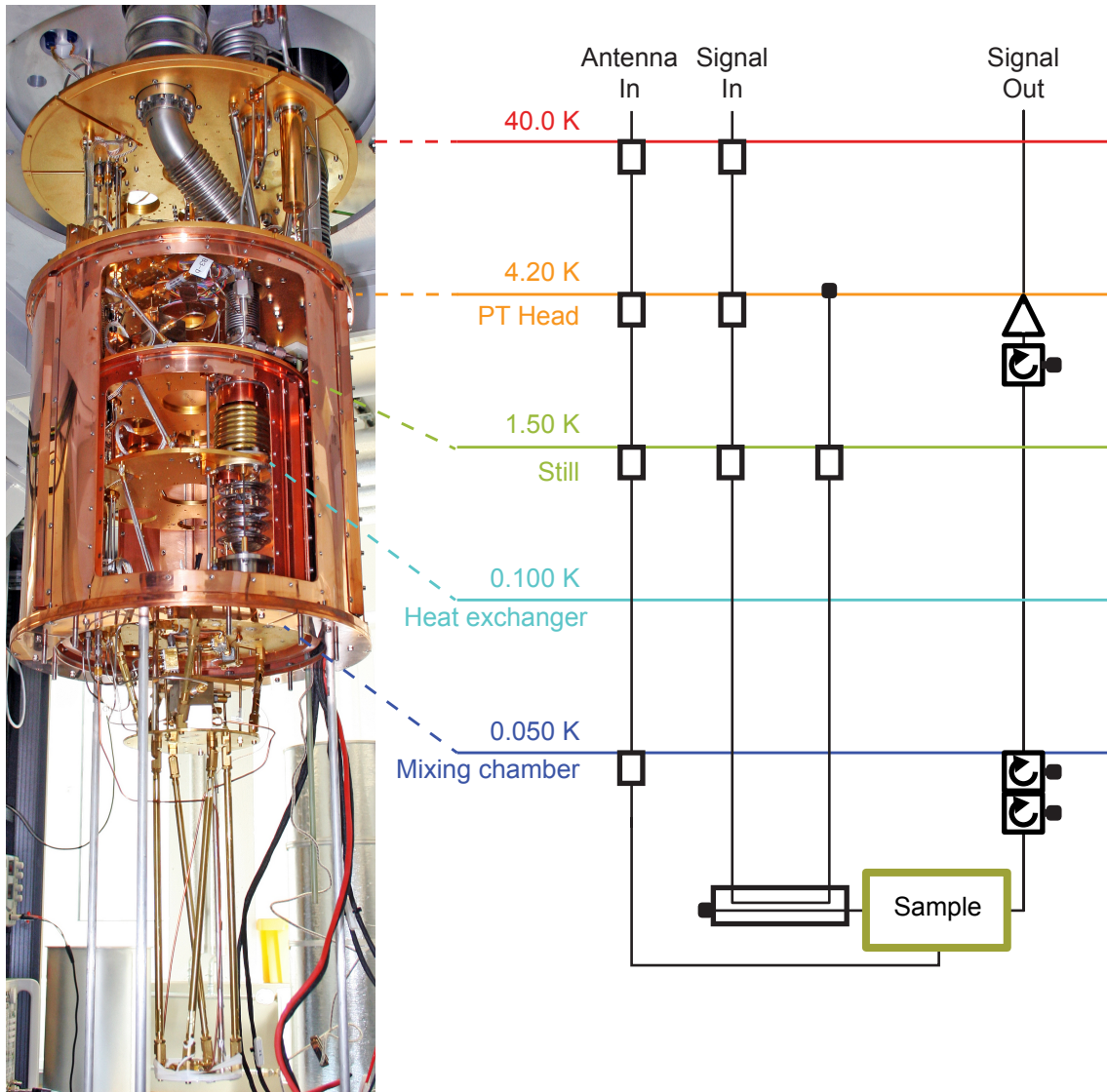
Figure 5.1: *Triton cryostat.* An image of the open Triton fridge is shown in panel a), where the individual temperature stages can be found. In addition, a sketch of an exemplary microwave wiring through the stages is depicted in panel b). We use attenuators or couplers on the input lines, as well as circulators and a HEMT amplifier for the outgoing signals, to overcome thermal noise.

dissipated power heats the respective temperature stage and therefor the power dissipation has to be considered when planning the microwave circuit. One option to circumvent power dissipation on the mixing chamber plate is to use microwave couplers. They consist of two microwave lines capacitively coupled to each other. By this only a fraction of the signal enters the sample stage. This acts effectively as an attenuation between the lines, but without power dissipation at the mixing chamber stage. Most of the signal passes the mixing chamber and is shunted to a $50\,\Omega$ resistor at the PT-head stage. At this stage the cryostat's cooling power is much higher than on the mixing chamber. A downside of such couplers is the need for an additional microwave line as well as the device dimensions.
When passing through the sample the signal enters the output line that consists of circulators preventing the noise to enter. The circulator has three ports, in which the incoming

signal is directed to the next port, effectively rotating the signal between the ports, as indicated by its name. So, incoming noise from room temperature is dissipated at a $50\,\Omega$ resistor, while the sample signal is passing the circulators with negligible loss.

As the signals stemming from the investigated device are typically rather weak they have to be amplified before being send to the room temperature detection setup. Within our experiments we use dc-SQUIDs as circuit elements, which allow to investigate magnetic fields with high resolution. On the other side this high sensitivity requires a screening of background fields, like the earth magnetic field. Superconducting materials are good candidates to screen magnetic fields, due to their perfect diamagnetism. We make use of this principle when screening our samples from magnetic fields by aluminum boxes, as shown in App. C. We detail the setups used for the experiments in App. A.
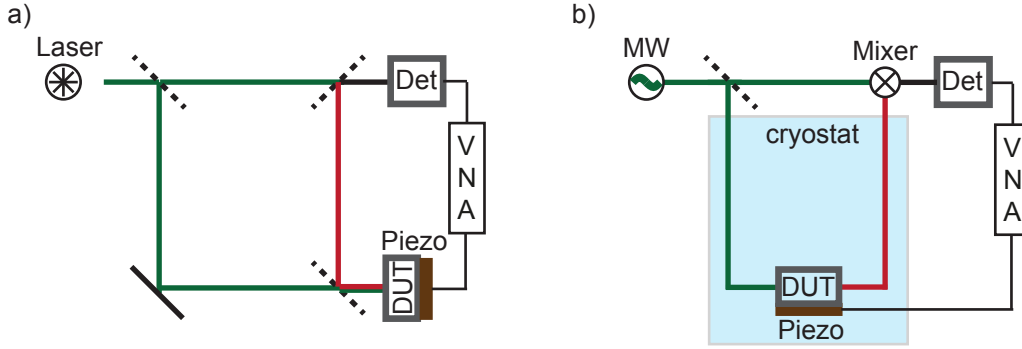
5.2 Cryogenic microwave interferometer

In this thesis we study circuit QED systems coupled to mechanical motion of nanostrings, similar to electromechanics with superconducting resonators [13]. Yet in our systems the critical current of the Josephson junctions limit the amount of photons $\bar{n}_\mathrm{c}$ that typically are used to boost the effective coupling $g = \sqrt{\bar{n}_\mathrm{c}}\,g_\mathrm{m0}$. A compensation of this by a Junction array which allows for higher currents however reduces the vacuum coupling strength. So we designed a single loop SQUID and overcome this restriction using a different approach, that also shortens the required measurement times: we have developed a microwave interferometer working at millikelvin temperatures. In our interferometer the electromechanical signal, to be precise the frequency fluctuations $\delta\omega_\mathrm{d}$, are enhanced by exciting the mechanical motion via a piezo actuator. In the following we discuss such an interferometer in detail.

5.2.1 Setup / Working principle

For an insight in the working principle of the cryogenic interferometer we have a brief look at a room temperature optical interferometer, as developed in [64], shown in Fig. 5.2a):

A laser beam is split up in two arms, where one is reflected by the sample, mounted on a piezo actuator. The reflected beam is send back to interfere with the first, unperturbed one and these interferences are detected using a photo diode. The inteference of the two beams results in a light intensity modulated at the detector diode. Hereby displacements can be measured. We create a coherent string motion by an external mechanical drive using a vector network analyzer. It compares the drive signal send to the piezo with the incoming voltage of the detector at the drive frequency Ω. When the mechanical frequency Ω_m matches Ω the string is excited effectively, resulting in a large displacement amplitude. By that, the displacement is measured and the string's eigenfrequency Ω_m identified.

In the cryogenic interferometer, in contrast, a microwave source instead of a laser beam is used. The signal tone ω_p is send to the sample that is placed in a cryostat and contains an electromechanical device. Similar to the room temperature interferometer, the sample is actuated by a piezo crystal of frequency Ω. On resonance ($\Omega = \Omega_\mathrm{m}$) the nanostring is excited and so displaced, which leads to a change in the complex transmission of the microwave resonator. Hereby, the mechanical motion is modulation on the incident microwave probe tone as mechanical sidebands at $\omega_\mathrm{p} \pm \Omega_\mathrm{m}$. At room temperature the probe

Figure 5.2: *Cryogenic microwave interferometer.* Panel a) displays an optical interferometer at room temperature, as introduced by [64]. An incoming laser beam is guided to the sample, that is excited by a frequency Ω using a vector network analyzer. The reflected light interacts with the nanostring, interferes with itself, and so the mechanical motion is obtained. The interferometric signal is collected by a photon detector, which is connected to the VNA. By this we measure the string's motion sensitively. Panel b) sketches a cryogenic electromechanical interferometer. Here a microwave tone probes an electromechanical resonator on its eigenfrequency. Again, the sample including the resonator, is actuated by a piezo crystal, sweeping the excitation frequency Ω. When excitation and string frequency are matched, the mode frequency is excited inducing an elongation $\bar{x}$. Since the electromechanical frequency depends on the mechanical state [cf. Eq. (4.1)], a transmission change of the homodyne down converted probe tone is detected.

signal is interfered with a second tone of identical frequency using an I-Q mixer and directly detected by a vector network analyzer. The analyzer records the power modulation as [90]

$$P_{\text{hom}}(\Omega) \propto \frac{K(\Omega)}{\Omega^2}\delta\omega_{\text{d}}^2 = \frac{K(\Omega)G^2}{\Omega^2}x_0^2, \tag{5.1}$$

with the driven frequency shift amplitude $\delta\omega_{\text{d}} = Gx_0$ using $G = g_{\text{m0}}/x_{\text{zpm}}$ and $x_0 = x_{\text{zpm}}\sqrt{2n_{\text{m}}}$ for a further analysis. Here we have placed a proportionality since the exact solution depends on the detection of the microwave signal as single or doubled sided spectrum [43]. In addition, the transfer function on resonance to the microwave resonator has to be quantified [106]:

$$K(\Omega) = \frac{16\kappa_{\text{ext}}^2\Omega^2}{\kappa^2(\Omega^2 + \kappa^2/4)}, \tag{5.2}$$

for which we determine the resonator decay rates in-situ by microwave spectroscopy. Next, by plotting the mechanical resonance frequency fluctuations via

$$\delta\omega_{\text{d}}(\Omega_{\text{m}}) = \sqrt{\frac{P_{\text{hom}}(\Omega_{\text{m}})\Omega^2}{K(\Omega)}} = \sqrt{n_{\text{m}}}g_{\text{m0}}, \tag{5.3}$$

we get a signal response directly proportional to the vacuum coupling strength. The benefit of this method is that the frequency shift of the electromechanical resonator is significantly enhanced (n_{m} up to 10^9) in comparison to regular thermal motion measurements, where n_{m} is $\approx 10^3$, and hence the amount of photons in the microwave resonator can be reduced. In the following, we will give a short example of such measurements on a transmon qubit coupled to an electromechanical resonator. We will focus only on results related to the cryogenic interferometer, further details on this sample are discussed in Sec. 6.

We start by sweeping the flux bias of the transmon qubit via an external superconducting
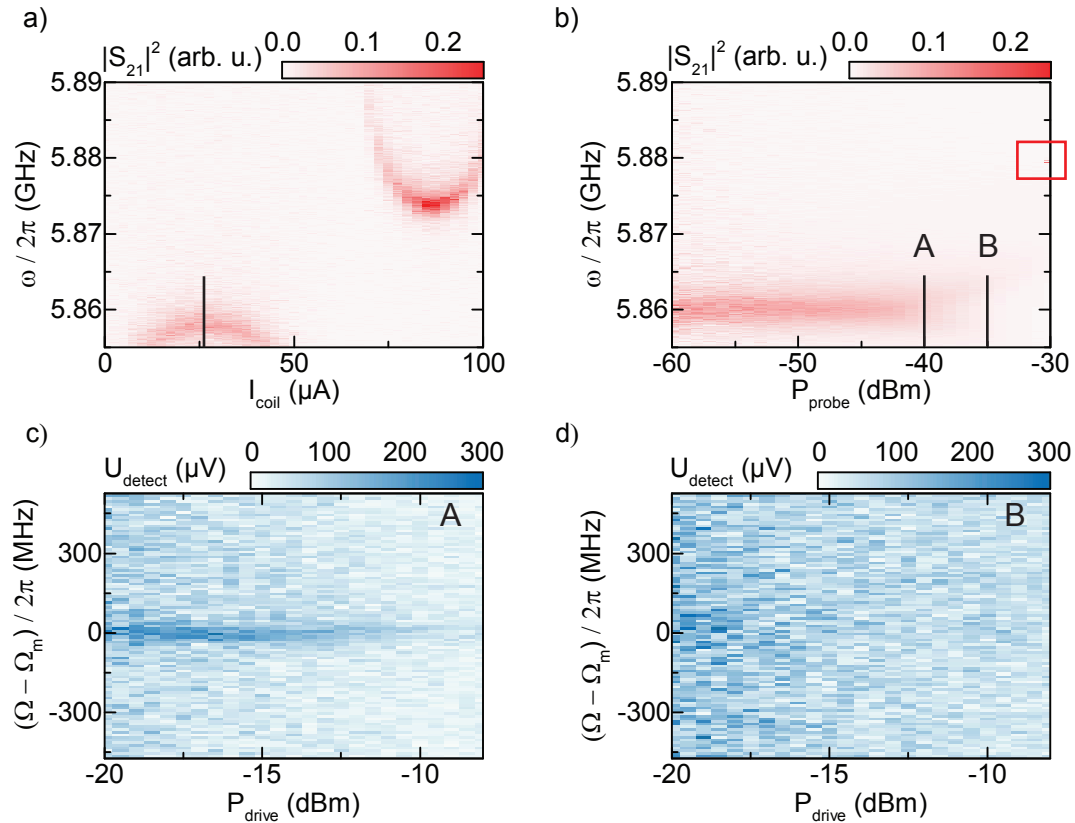
Figure 5.3: *Low photon read-out of an electromechanical QED system.* Panel a) shows the transmon-resonator transmission over applied field. We find the qubit positioned at the sweet spot at a coil current of $27\,\mu$A, and a resonator frequency of about $5.86\,$GHz. The undisturbed resonator frequency is found at $5.875\,$GHz. We fix I_{coil} to the maximum transition frequency of the transmon qubit and sweep the probe tone power, as shown in panel b). At about $-45\,$dBm probe power the transmon-resonator system becomes unstable with reduced transmission and it vanishes completely after reaching the critical photon number of $\bar{n}_{\text{c}} \approx 120$ at about $-40\,$dBm. For high powers the bare mw-resonator frequency becomes visible (red square). The photon numbers scale linear to the probe tone power and range in this figure from 1.2 to 1200. Panel c) displays the recorded detector voltage of the driven nanostring for a probe tone power of 60 photons, indicated by A in b). The string is clearly visible until about $-15\,$dBm piezo drive power, from where on it vanishes. We speculate, that the drive tone induces dissipation and thus heating. With the temperature changing, the magnetic field bias is influenced, e.g. by paramagnetic effects. This changes the effective B-field bias and so shifts the microwave resonator. In panel d) we repeat the previous measurement, yet with a higher probe power close to the critical photon number. No string signature is found.

coil, while recording the microwave transmission through the device. Results are shown in Fig. 5.3a). We find an avoided crossing between transmon qubit and microwave resonator, attributed to the strong coupling between them. For $I_{\text{coil}} = 27\,\mu$A we find the resonator transmission to reach a maximum, which indicates that the qubit is positioned at its maximum transition frequency, the so-called sweet spot. Here, the point of best transmission through the sample has a local maximum at $5.860\,$GHz. We fix the coil current to the mentioned value and sweep the probe tone power and frequency through the sample. The microwave transmission is found in Fig. 5.3b). At weak probe powers a lorentzian transmission peak is found at the resonator's eigenfrequency. When the probe tone is further increased (at about $-45\,$dBm or 60 photons) the transmission reduces more and more. At

high powers spikes in the transmission become observable (red square) at the resonators undisturbed frequency of about 5.875 GHz (see digital version for clarity).

Next we will compare the nanostring's motion measured via the cryogenic interferometer configuration for two different photon numbers, indicated by A and B in Fig. 5.3b), which correspond to 30 or 120 photons, respectively. The probe tone frequency was set to 5.860 GHz.

In both cases we sweep the drive power send to the piezo and record the transmission change in P_{hom} around the mechanical resonance. Results are shown in Fig. 5.3c) and d). In the case of 30 photons a clear indication of the string is found, having an eigenfrequency of $\Omega_m/2\pi = 3.0530$ MHz. For very high drive powers the signal starts to disappear. We speculate that this comes from heating effects. The high drive power is dissipated on the sample, so that the environment heats up. Paramagnetic materials then change the effective B-field bias of the transmon qubit, which shifts the microwave transmission out of resonance. Similar effects have been observed in Ref. [64]

For higher photon numbers, one would expect the electromechanical interaction to be increased by a factor of 2 due to the higher radiation pressure. Yet, we observe no feature that we can attribute to the nanostring. This can be explained when looking at the resonator transmission in Fig. 5.3b). Due to the nonlinear interaction causing a bifurcation, the transmission is broadened. By this, the transfer function is changed, such that the motion of the string is insufficient to overcome the background noise floor.

So we can conclude that the introduced cryogenic interferometer allows to operate the electromechanical hybrid systems at low photon numbers, sufficiently low to operate highly nonlinear elements, as we have shown exemplary in Fig. 5.3.

5.2.2 Phase-independent homodyne conversion

By coupling our mechanical element to circuits with Josephson junctions acting as nonlinear inductance, the frequency of the electric resonator becomes flux tunable. This requires a detection principle that is frequency independent. For this we have developed a technique based on the commonly used homodyne detection, as follows:

We start by recording the microwave transmission of an electromechanicals system via a homodyne down-conversion, similar to the previous introduced cryogenic interferometer [cf. Fig. 5.2b)]. In such a scenario a microwave oscillation of the upper path acts as local oscillator, while the second path through the sample carries the mechanical oscillations. We can describe the general microwave signals via:

$$
\begin{aligned}
\text{MW1} &= A_1 \exp\left[i\omega_1 t + \phi_1\right] \\
\text{MW2} &= A_2 \exp\left[i\omega_2 t + \phi_2\right].
\end{aligned}
\tag{5.4}
$$

Here A_i and ω_i refer to the complex transmission amplitude and frequency of path 1 or 2 respectively, while the phase ϕ_1 corresponds to the phase delay of the signal due to the length of the upper path, and ϕ_2 carries the delay of the microwave circuit. Using an I-Q-mixer both signals are multiplied:

$$
\text{MW1} \cdot \text{MW2} = (X + iY)\exp\left(i(\omega_1 + \omega_2)t + \Delta\phi\right),
\tag{5.5}
$$

where we introduced the complex amplitude $X + iY = A_1 A_2/2$ depending on the microwave transmission through the interferometer, and the phase difference $\Delta\phi = \phi_1 - \phi_2$.

In homodyne detection configuration, that is $\omega_1 = -\omega_2$, the oscillations of the carrier frequency are reduced to 0. We can then associate real and imaginary part with the I (in-phase) and Q (out-of-phase) output of the IQ-mixer as (w.l.o.g.)

$$I = X\cos(\Delta\phi) - Y\sin(\Delta\phi),$$
$$Q = Y\cos(\Delta\phi) + X\sin(\Delta\phi). \tag{5.6}$$

The information of the mechanical string is modulated on the microwave transmission only on the imaginary part for the typical weakly driven strings, cf. Sec. 4.4, and takes the shape of $Y = Y_0 + \kappa_{\mathrm{ext}}/2Gx\cos(\Omega_{\mathrm{m}}t)$ [100].

By this we find the probe tone modulation of the string rotated between I and Q in dependence of the phase difference, which acts as rotation angle. For a fixed frequency resonator, a phase shifter allows to set the phase shift such, that the interaction is displayed in only one quadrature, that is later detected via a spectral analyzer. This however is only applicable for fixed frequencies. For a tuneable resonator, we add the two quadratures phase shifted by $\pi/2$ on all time dependent signals. This leads to

$$I(t) + Q^{\pi/2}(t) = -\frac{\kappa_{\mathrm{ext}}}{2}Gx\left(\sin(\Delta\phi)\cos(\Omega_{\mathrm{m}}t) - \cos(\Delta\phi)\sin(\Omega_{\mathrm{m}}t)\right) =$$
$$I(t) + Q^{\pi/2}(t) = -\frac{\kappa_{\mathrm{ext}}}{2}Gx\sin\left(\Delta\phi - \Omega_{\mathrm{m}}t\right), \tag{5.7}$$

which corresponds to oscillations at Ω_{m} proportional to Gx, independent of the phase (as the recorded bandwidth is much lower than Ω_{m}), and so also for any microwave resonator frequency.

5.3 Time domain measurements

Before we introduce the time domain setup, we will give a short overview on the dispersive read-out of a transmon qubit, which is the basic experimental technique for insights in the transmon characteristic for both continuous wave, as well as time domain measurements. Then we will discuss the setup configuration in detail and some technical aspects on the noise screening. We will conclude by an overview of common pulse sequences one can employ to measure the qubit decoherence.

5.3.1 Dispersive read-out

We start by looking at the phase transmission of the microwave resonator and the transmon qubit being positioned at its maximum transition frequency. For parameters based on Ref. [34] this corresponds to $\omega_{\mathrm{c}}/2\pi = 5.860\,\mathrm{GHz}$ and $\Delta_{\mathrm{qc}}/2\pi = (\omega_{\mathrm{q}} - \omega_{\mathrm{c}})/2\pi = 2.056\,\mathrm{GHz}$. Including the linewidth of the resonator of $\kappa/2\pi = 2.0\,\mathrm{MHz}$ and $\kappa_{\mathrm{ext}}/2\pi = 1.0\,\mathrm{MHz}$, we can plot the phase transmission of the scattering parameter [109], as we show in red in Fig. 5.4.

We find the phase changing by π with highest change on resonance (max. $\partial_\omega\phi$). This transition is valid for an unexcited qubit ($|g\rangle$), as the resonators eigenfrequency appears according to the qubit state shifted by $\sigma_{\mathrm{z}}\chi$, cf. Eq. (3.28), where σ_{z} describes the projection of the qubit state on the z-axis, while χ denotes the dispersive shift of the transmon qubit, cf. Eq. (3.29). We plot the shifted phase transmission for a fully excited transmon ($|e\rangle$) in Fig. 5.4 (green). In that case the resonator is shifted by 2χ, as indicated by the
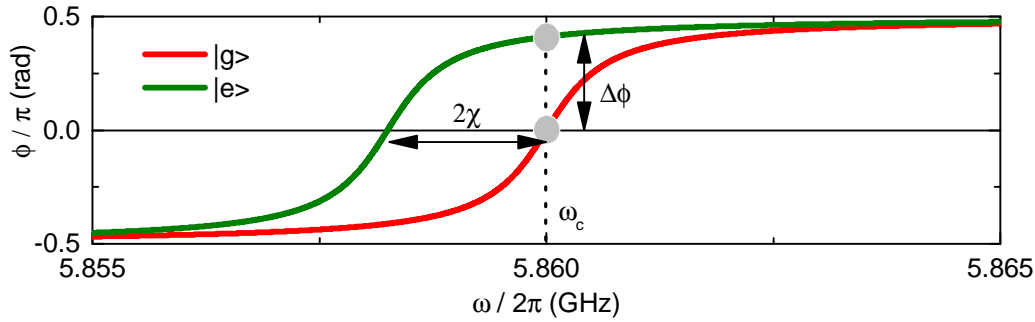
Figure 5.4: *Dispersive read-out of a transmon qubit.* We plot the phase transmission of a microwave resonator coupled to a transmon qubit as a function of the probe frequency. When the transmon is not externally excited (red), a phase shift of π is observed. When exciting the transmon (green) the resonance frequency is shifted and a finite phase shift $\Delta\phi$ can be observed, as indicated by the black arrow.

black arrows. χ was determined by a coupling strength of $g_{\mathrm{q}}/2\pi = 134\,\mathrm{MHz}$, and an anharmonicity of $\alpha/h = -188\,\mathrm{MHz}$.

We can now make use of this shift to read-out the qubit state by applying a constant probe tone on resonance to the unexcited qubit, as indicated by a grey dot in Fig. 5.4. On excitation the resonator's phase is shifted (second grey dot) determining the phase shift ($\Delta\phi$ on the y-axis in Fig. 5.4).

We like to note, that this setup is somehow similar to an electromechanical read-out introduced before (cf. Sec. 5.2), where the phase transmission is analogue to the transfer function K, and the dispersive shift corresponds to the induced frequency fluctuations. In other words the electric resonator is the investigated system, while the transmon parameters determine how much the resonator is influenced by an external spectroscopy drive.

5.3.2   Devices

An illustration of the time domain setup is found in Fig. 5.5. We control the pulse shapes by a *Keysight 81160A* pulse function arbitrary noise generator as an arbitrary waveform generator (AWG). In general this allows us to design an arbitrary waveform, even up to optimal control pulses, yet in our case we used rectangular pulse shapes for simplicity. It turned out to excite the qubit sufficiently.

These pulses are then send to the I-input of a *Rhode&Schwarz SGS 100A* vector signal generator, while the Q input is shunted by $50\,\Omega$. The output of the SGS source excites the qubit via an external antenna on the chip.

The second pulse channel is used for the read-out, controlling a *Rhode&Schwarz SMF 100A* microwave generator. By this we apply a probe tone in dispersive read-out configuration as described in Sec. 5.3.1. After the cryogenic part the signal is filtered by a *MiniCircuits VBFZ-5500-S+* bandpass and amplified by a *Agile MwT AMT-A0033.* Then it enters a *Marki IQ 0307 LXP* IQ-mixer. Here, the signal is homodyne downconverted by a local oscillator tone from an *Agilent/Keysight E8257D* signal generator.

The I and Q quadrature paths are identically build up consisting of coaxial cables (black) or, as we found it is a critical part of the noise screening, *true blue* microwave wires (blue).
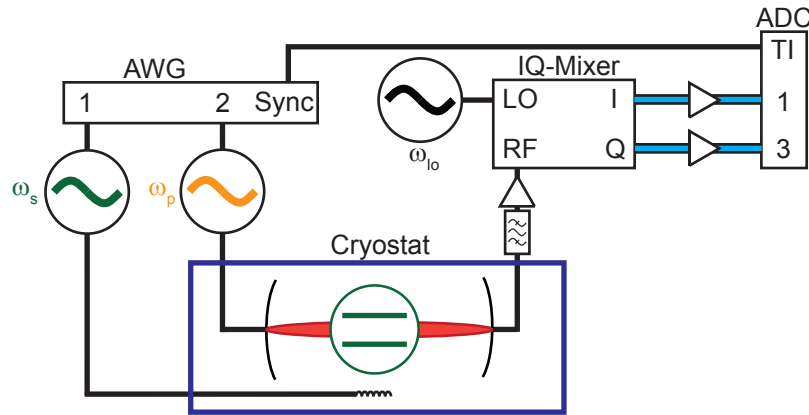
Figure 5.5: *Electric configuration for time resolved qubit spectroscopy.* We use an arbitrary
waveform generator (AWG) to control the spectroscopic drive (s) and probe tone (p) source.
Via an antenna the spectroscopic drive sends pulses of defined length to the transmon qubit.
The probe tone is measuring the microwave resonator transmission, which depends on the
qubit state. So a read-out of the transmon qubit is achieved. The signal is sent out of the
cryostat, filtered by a bandpass and amplified via a room temperature amplifier. Afterwards, it
is homodyne downconverted in an IQ-mixer, using a third microwave source (LO). Then I and
Q quadrature are amplified with identical amplifiers and sent to an analog-digital converter
(ADC) which we use as a detector. The ADC is synchronized to the AWG. During the
measurements we found out, that the connecting wires between IQ-mixer and ADC are prone
to pick up noise, as further explained in the text.

The signal is further amplified by a *Femto DHPVA-200* amplifier and then detected by
a *GaGe Razor CSE1642* analogue-digital converter (ADC), that is synchronized to the
AWG. The hardware was controlled using the WMI measurement tool *DollRotate* for
which individual VIs were written by H. Huebl and S. Weichselbaumer.
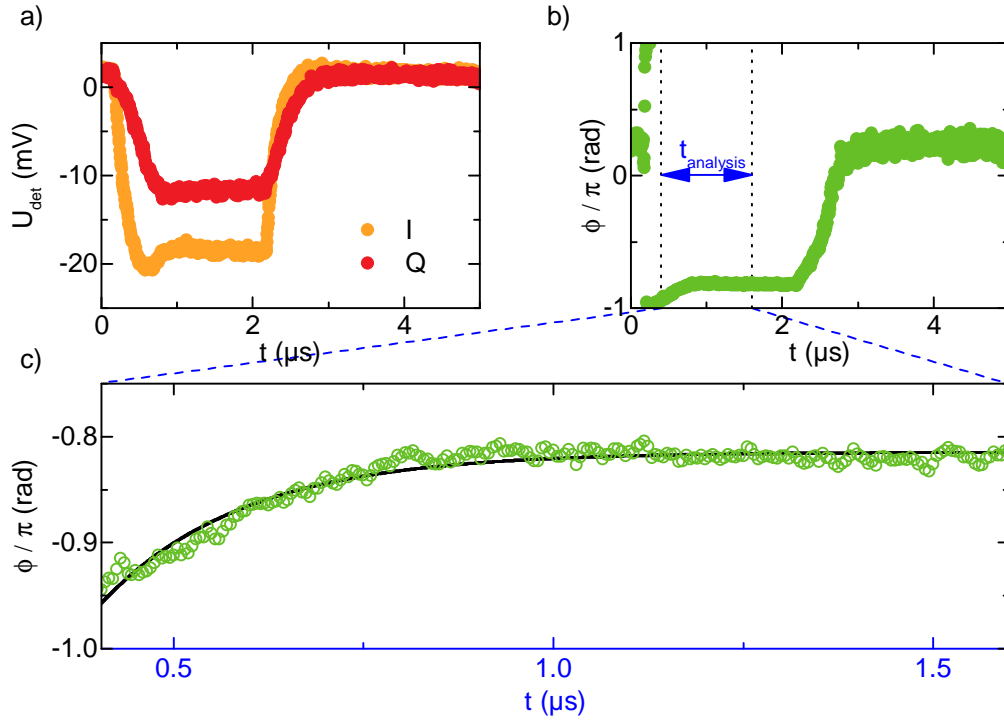
5.3.3 Data acquisition

Now we will discuss the measurement principle by an example on driven Rabi-oscillations,
as shown in Fig. 5.6. For the example case we employ a $\tau_{\mathrm{dR}} = 5\,\mathrm{ns}$ long spectroscopy tone
on resonance to the qubit via its antenna, as well as a $2\,\mu\mathrm{s}$ long read-out pulse, directly send
after the excitation pulse (at $t = 5\,\mathrm{ns}$) via the transmission line. We start the measurement
at $t = 0$ and record both voltages at the I and Q input, see Fig. 5.6a). The measurements
are repeated by the averaging factor with the recorded voltages averaged for each time
point. Results are shown in Fig. 5.6a) for I (orange) and Q (red).
At first the voltages fluctuate around $2\,\mathrm{mV}$ before they go to $-18\,\mathrm{mV}$ and $-12\,\mathrm{mV}$ during
the read-out pulse. This confirms that the read-out tone is activated. When it is turned
off again, the voltage drops back to the initial value of $2\,\mathrm{mV}$. In addition, we find a certain
delay time between the start of the measurements and the recording of about $0.25\,\mu\mathrm{s}$ when
looking at the end of the read-out pulse.
As the I and Q quadrature are orthogonal, we can derive the complex transmission by
w.l.o.g. $S = I + iQ$ and determine the transmission amplitude $|U_{\mathrm{det}}| = |S|$ and phase
$\phi = \mathrm{Arg}[S]$.
The extracted phase is shown in Fig. 5.6b). Here we find a phase of $\pi/4$ when the read-out
tone is off. For an active read-out, the phase changes by π. Due to the periodicity of the

Figure 5.6: *Details on the data acquisition.* In panel a) the recorded voltages at the ADC are displayed for I (orange) and Q (red) traces starting with fluctuations around 2 mV, before the read-out pulse is detected. This manifests by a drift, saturating after about 1 μs. When the read-out pulse is turned off after 2 μs the voltage drops back to the initial background value. We can calculate the probe tone transmission amplitude and phase from the both quadratures and plot the phase shift in panel b). We find the background fluctuations before and after the read-out pulse at about 0.25π. Due to the probe tone the phase shifts above π and therefore reappears at −π. When the pulse arrives at the detector, an exponential increase in the phase is observed, saturating at approx. −0.8π. After the read-out pulse the data drifts back to the initial background value. We show an analysis of this trace in panel c) for the analysis time (indicated in blue). The exponential decay is well described by a model from which we can extract the phase shift Δφ (black solid line).

Arg-function its flipped by 2π and keeps increasing up to −0.8π where it saturates during the read-out pulse. Afterwards its dropping back to the initial value.

For an analysis of the transmon qubit's projection along the z-axis due to the excitation pulse, we focus on a specific time frame $t_{analysis}$ as indicated by the blue arrow in Fig. 5.6b). The starting time at $t_{analysis}$ is defined by the pulse length (5 ns) and a delay time of 400 ns making sure the read-out pulse has reached the detector. A length of $t_{analysis} = 1.2$ μs is sufficient to stay within the read-out pulse for the longest excitation pulses (not shown in this example). To sum up, we analyze the phase change from $t = [405 - 1605]$ ns as shown in Fig. 5.6c).

An exponential increase from 0.95 to 0.8π is found, which comes from a shifted transmon frequency by the probe tone due to the ac-Stark shift. We model this phase shift by

$$\phi = A_0 \exp\left(\frac{-t}{\tau}\right) + \phi_0. \tag{5.8}$$

By this we determine a decay amplitude of $-3.88(-1.24\pi)$ rad, a phase offset of $-2.56(0.81\pi)$ rad, and a decay rate of 187 ns, which leads to a phase value of $\phi(t_{analysis} =$
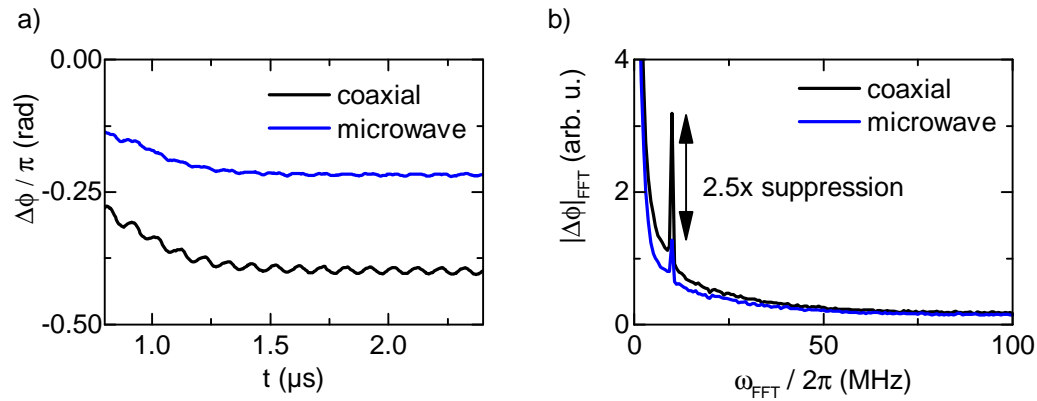
Figure 5.7: *Time resolved measurement noise.* In panel a) averaged time traces of the read-out pulse for wiring configuration 1 (black) and 2 (blue) are shown. In both cases periodic fluctuations are found, in configuration 2 the total amount of signal is reduced but also the elongation of the fluctuations. Panel b) displays the amplitude of a discrete Fourier-analysis on the recorded time traces. In both wiring configurations a dominant peak is found at 10 MHz for both configuration. In the second wiring this peak is reduced but an additional peak at 20 MHz is arising. Nevertheless on average the frequency distribution is reduced in comparison to the first wiring.

$0) = 3.01 (0.96\pi)$. We conclude our analysis by subtracting this from the phase offset leading to the induced phase shift

$$\Delta\phi = \phi(t_{\text{analysis}} = 0) - \phi_0 = 0.448 \, (0.143\pi) \, \text{rad}. \tag{5.9}$$

Finally we have extracted the first data point of Fig. 6.12. As it will become clear at a later stage this phase shift corresponds to an excitation probability slightly below 0.5 (right axis), which is close to the equatorial plane of the Bloch sphere. The other datapoints of this figure are achieved by a systematic sweep of the pulse length τ_{dR}.

5.3.4 Technical noise screening

For long averages we become sensitive to noise sources from the outside world, as we are going to explain in the following. For this, we repeat a measurement, one time with regular BNC cables (black in Fig. 5.5) and with *True Blue* microwave wires (blue in Fig. 5.5). The measurement consists of a single read-out pulse, $\bar{n}_c \approx 10$, averaged 150,000 times. We calculate the transmission magnitude, as introduced before, and plot the results in Fig. 5.7a).

Similar to Fig. 5.6c) we find an exponential increase, roughly from -0.28π saturating at -0.40π so a phase shift of $\Delta\phi_{\text{BNC}} = -0.12\pi$. In an analogue way we find $\Delta\phi_{\text{TB}} = -0.08\pi$. Beside this, an additional feature stands out after such a long averaging: finite oscillations on the signal with a distinct frequency, which seem to be reduced by the higher screening of the *True Blue* wires. For a detailed analysis we perform a Fourier analysis on the time trace as shown in Fig.5.7b). It reveals a distinct peak for both cases arising at exactly 10 MHz. This frequency contribution can be linked to the microwave sources being synchronized among each other on 10 MHz. For the *True Blue* wires we find a reduction of these contributions by 2.5. Including the reduced phase shift by the lower transmission of the wires, we end up by an improvement on the signal to noise ratio of 1.7, and so we kept

Figure 5.8: *Applied qubit pulse schemes.* Within this thesis four different pulse schemes were applied to a transmon qubit to investigate its decoherence.

the microwave wire configuration for all other time domain measurements shown in this thesis.

We note, that such noise contribution have been observed before and advanced shielding techniques for this were engineered and discussed in detail, cf. Ref. [110].

5.3.5 Pulse schemes

In the following, we will discuss the pulse schemes we apply to the investigated transmon qubit within this thesis. As these techniques have been well established, we focus on a short summary and introduce our notation. More details on such schemes are reviewed in Ref. [111].

We give an overview of the applied pulse schemes in Fig. 5.8. We used rectangular pulse shapes with a rise time of 1 ns. AWG channel 1 controlled the spectroscopy tone (green) sent to the qubit antenna, while channel 2 regulated the read-out pulse through the microwave resonator (orange).

In the **driven Rabi** configuration a drive pulse with frequency ω_s, a specific driving strength, and duration τ_{dR} is send to the qubit. The spin vector along the Bloch sphere now starts to rotate induced by this drive in dependence of the drive tone detuning $\omega_s - \omega_q$ and the drive strength. By applying a probe tone directly after τ_{dR} we measure the qubit state along the z-direction on the Bloch sphere. When this projection is plotted over τ_{dR} for zero detuning one finds the so called Rabi-oscillations having a Rabi frequency ω_{Rabi} which allows to determine the length of $\pi/2$ and π pulses. In reality, these oscillations decay exponentially with τ_{Rabi} corresponding to the energy decay time T_1, before it reaches a steady state solution on the equatorial plane. Another potential decay in this pulse sequence can occur when noisy tones are applied. Since in this sequence the drive pulse is constantly on, the qubit is sensitive to such effects. When driving the qubit out of resonance the spin vector no longer rotates along the z-direction which leads to an higher frequency ω_{Rabi} and the decay becomes influenced by dephasing processes $\tau_{Rabi} \neq T_1$.

For the **Rabi decay** we send a π pulse on resonance to the transmon qubit, shifting it to a full excitation. Next it decays, in contrast to the driven Rabi sequence unperturbed by any drive, before its projection along the z-Axis is read-out again. We found $\tau_{decay} \approx \tau_{Rabi}$,

indicating low induced noise of our microwave pulses.

Both Rabi sequences focus on the energy decay of the qubit. Yet the spin vector has a phase component, which dephases if the transmon qubit's energy is fluctuating, for example by photon fluctuations on the microwave resonator [112].

To investigate such dephasing processes a **Ramsey** sequence can be applied. It consists of a $\pi/2$ pulse, that shifts the qubit state along the equatorial plane. Here, the spin vector is sensitive to dephasing processes, that it undergoes within a waiting time τ_{Ramsey}. Then it is shifted on the z-axis by a second $\pi/2$ pulse, and its projection again read-out directly. On resonance to the transmon qubit the bare dephasing is observed equivalent to T_2, while off-resonant the qubit contains energy components and therefore T_2^* is found by the exponential decay rate T_{Ramsey} extracted from the Ramsey oscillations.

Another method to determine the dephasing is the **Spin Echo** or Hahn sequence. Its similar to the Ramsey sequence, besides a π pulse send in between the $\pi/2$ pulses, with an identical waiting time τ_{SE} in between the pulses. This π pulse rotates the vector so that the dephasing is refocused. This introduced time reversal allows then to screen $1/f$ noise and field asymmetries [110], and hence their influence can be determined by comparing the Spin Echo dephasing with the Ramsey dephasing.

We experimentally employ these pulse schemes to analyze a transmon qubit coupled to an electromechanical resonator in Sec. 6.6.

6

Ultra-wide range photon number calibration

What we'd like to do is put these vibrations of the [mechanical element] in a quantum state, so it's in two places at once: it's vibrating up and, at the same time, it's vibrating down.

John D. Teufel, [113], 2017

In the following we study a hybrid microchip consisting of a transmon qubit coupled to an electromechanical microwave resonator. As such systems, based on superconducting circuits, are prime candidates for investigating quantum properties of mechanical motion [16, 22, 94, 114–119].

In particular, we will show the photon number calibration via both the qubit and the nanostring for an occupation between nine orders of magnitude, based on Ref. [34]. To this end we start by theoretically introducing the applied methods, detail the fabrication process and the utilized setup. Afterwards, the elements of the microchip are characterized individually to determine the photon numbers in the following. Further, the transmon qubit coherence is characterized in detail, using time domain measurements.
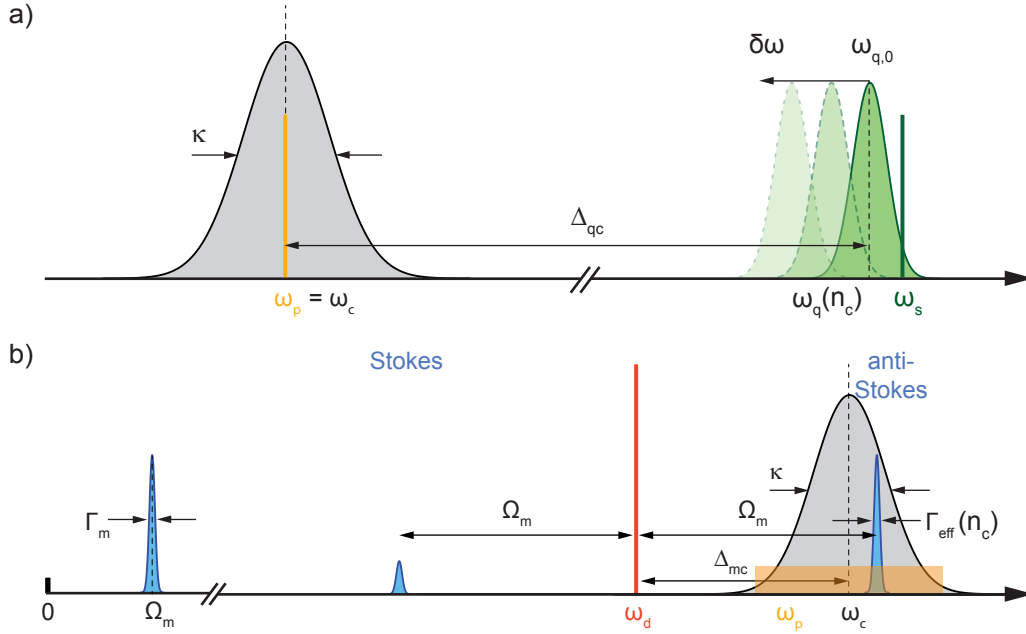
6.1   Methods for photon number calibration

We will start the introduction of the investigated system by giving a short theoretical overview, beginning with the description of the average photon number in the microwave resonator. Our device then offers two complementary approaches to calibrate this photon number, namely the ac-Stark effect [78, 120–122] of the transmon qubit, as well as electromechanically induced absorption [15, 103, 123, 124] of the aluminum nano-string which will be discussed.

We describe the average photon number of a double sided microwave resonator ($\lambda/2$) with symmetric input and output coupling rates κ_{ext} by [9, 98]

$$\bar{n}_{\mathrm{c}} = \frac{P_{\mathrm{p}}}{\hbar\omega_{\mathrm{p}}} \frac{\kappa_{\mathrm{ext}}/2}{(\kappa/2)^2 + \Delta_{\mathrm{p}}^2}. \tag{6.1}$$

Here, $\Delta_{\mathrm{p}} = \omega_{\mathrm{p}} - \omega_{\mathrm{c}}$ is the detuning between the resonance frequency ω_{c} and the incident microwave probe tone ω_{p}. In experiment, it is typically difficult to determine the input

Figure 6.1: *Methods for an ultra-wide range photon number calibration.* Panel a) the average photon number $\bar{n}_c$ can be calibrated via the transmon qubit as its bare transition frequency $\omega_{q,0}$ is influenced by the average photon number leading to the so-called ac-Stark shift $\delta\omega(\bar{n}_c)$ (light green). To determine this shift we use a spectroscopy tone ω_s (dark green). Panel b) displays the photon number calibration via the electromechanical interaction. The mechanical element (blue) has an eigenfrequency Ω_m in the low megahertz regime. The electromechanical photon-phonon interaction causes Stokes and anti-Stokes sidebands on the drive tone ω_d (red). Choosing this drive frequency such that the anti-Stokes sideband is in close proximity to the mw resonator ω_c scattering processes removing phonons from the string become active. In combination with the drive photons these phonons can interfere with weak probe photons around the mw frequency (orange) leading to electromechanically induced absorption.

power P_p incident to the input port of the microwave resonator. Therefore, calibration experiments are employed and the discrepancy between the applied power sent to the experiment P_{appl} and P_p is parametrized as an effective loss parameter $\mathcal{L} = P_p/P_{appl}$. The discrepancies between the applied P_{appl} and setted power on the measurement instruments P_{set} will be discussed in the measurements section 6.3. Hence, Eq. (6.1) becomes

$$\bar{n}_c = \frac{2P_{appl}}{\hbar\omega_p\left(\kappa^2 + 4\Delta_p^2\right)} \underbrace{\mathcal{L}\kappa_{ext}}_{x}, \tag{6.2}$$

where we further combined the effective loss parameter $\mathcal{L}$ and the external coupling rate of the microwave resonator κ_{ext} to a total loss coefficient x[1]. Next we discuss how we can corroborate this calibration factor for low powers via the transmon qubit, x_{qb}, and for high drive powers using the string oscillator, x_{EMIA}.

6.1.1 Photon number calibration via the ac-Stark shift

For a determination of the microwave photon number we set the transmon qubit in the dispersive regime, that is a sufficient detuning between it and the microwave resonator.

---

[1]within this chapter we refer to x as photon calibration factor, not a displacement as elsewhere in the thesis

The system is then described by the Hamiltonian quantified in Eq. (3.30). The dispersive shift of the transmon qubit obeys Eq. (3.29).

In case the anharmonicity α is small compared to the detuning of transmon to resonator $\Delta_{qc} = \omega_q - \omega_c$ and if the detuning Δ_{qc} is large compared to the transmon-microwave resonator coupling g_q, the transition frequency of the qubit ω_q shifts as a function of $\bar{n}_c$ by [75]:

$$\delta\omega = 2\frac{g_q^2}{\Delta_{qc}}\frac{\alpha}{\alpha + \hbar\Delta_{qc}}\bar{n}_c(\kappa). \tag{6.3}$$

With a proper sample characterization we determine the parameters necessary to calculate the ac-Stark shift per photon, quantifying the parameters of the right hand side of the equation.

For the experimental investiagation of $\delta\omega(\bar{n}_c)$ we have summarized the experimental configuration and show all relevant frequencies in Fig. 6.1a)

We start by measuring the ac-Stark shift via a probe tone through the mw resonators ω_p on resonance to it (orange), while sweeping a second tone ω_s to perform spectroscopy of the qubit (green) which enables the determination of the qubit frequency ω_q. Systematically sweeping the probe tone power we find $\delta\omega(P_{appl})$. By this we can then directly obtain the microwave resonator photon number. For a comparison with the electromechanical system we then derive the corresponding calibration factor x_{qb} via Eq. (6.2).

Note, that this calibration scheme is limited to low photon numbers due to the multi-level nature of the transmon qubit and the conditions imposed by the dispersive limit of about 10^2 [84].

### 6.1.2 Photon number calibration via the electromechanical interaction

At higher photon numbers we employ the electromechanical induced absorption of the microwave drives. This is realized by driving one mechanical eigenfrequency below the microwave resonator $\omega_d \approx \omega_c - \Omega_m$. This creates an anti-Stokes field inside the resonator at $\omega_d + \Omega_m$, as indicated in Fig. 6.1b). A second (weak) tone probes this anti-Stokes field as both fields interfere with each other. This results in a transparency, absorption or reflection signature of the complex transmission of the probe tone. The details of the signature depend on the specific setup of the measurement configuration [9, 103, 123, 125, 126]. In any case this drive tone effectively cools the eigenmode of the mechanical oscillator (see section 4.3) as it is highly thermally excited (for typical values $n_m = k_B T_{cryo}/(\hbar\Omega_m) \approx 10^3$). Then the effectively cooled mode has an increased linewidth described by [123, 125, 126]

$$\Gamma_{eff} = \Gamma_m \left(1 + \frac{4g_{m0}^2}{\kappa\Gamma_m}\frac{2P_{appl}x_{EMIA}}{\hbar\omega_d\left(\kappa^2 + 4\Delta_{mc}^2\right)}\right). \tag{6.4}$$

Since the parameters of Eq. (6.4) can be characterized we can calibrate x_{EMIA} by determine this linewidth. This only works if the effective broadening is sufficiently large in comparison to the bare mechanical oscillator linewidth, hence for high photon numbers in contrast to the calibration mechanism of the qubit.

6.2 Fabrication of a nanomechanical c-QED device

For a quantitative comparison of x_{qb} and x_{EMIA} we designed a hybrid device consisting of a superconducting mw resonator, a transmon qubit, and a doubly clamped nanostring
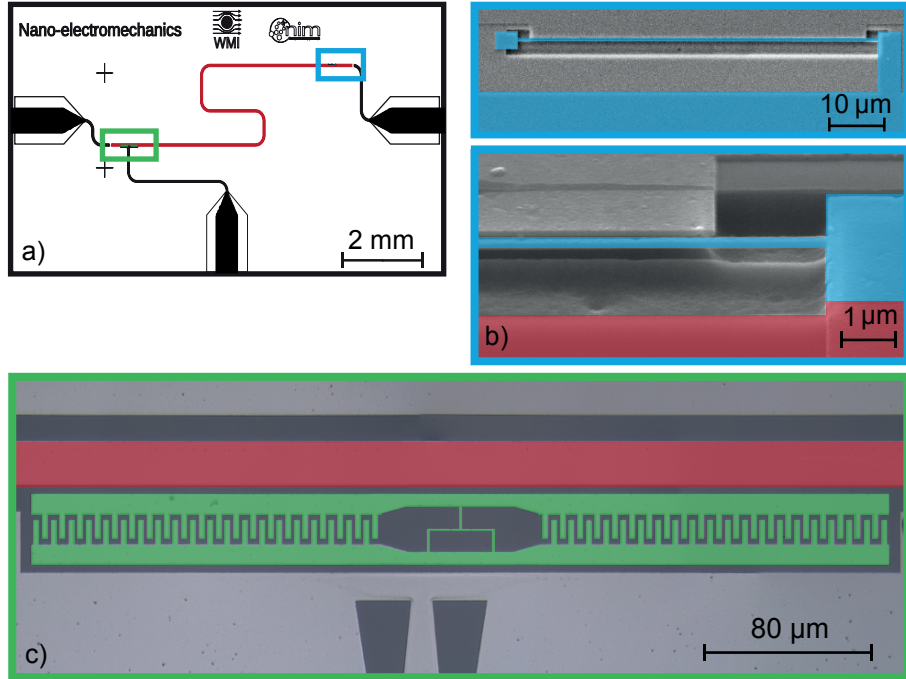
Figure 6.2: *Sample layout and microscopic images.* Panel a) displays the chip layout including the $\lambda/2$ coplanar waveguide microwave resonator (red), the transmon qubit (green box), and the aluminum nanostring oscillator (blue box). In panel b) a scanning electron micrograph of the $60\,\mu$m long nanostring is shown, including a a zoom to the right clamp. We tilded the zoomed image to make the successful release visible. The transmon qubit antenna is depicted at the bottom of the panel c).

oscillator. An overview of this layout as well as microscope images are found in Fig. 6.2. We will describe an overview of the fabrication steps, details are found in Ref. [127]. Afterwards we will briefly summarize the sample parameters.

Fabrication starts with a $6\times 10\,\text{mm}^2$ highly resistive ($> 10\text{k}\Omega\text{cm}$) single crystalline silicon substrate. Using negative resist, electron-beam (e-beam) lithography and a lift-off process, a $100\,\text{nm}$ thick aluminum coplanar waveguide (CPW) resonator, capacitively coupled to an input and output line, is patterned on the chip. This step already includes the definition of the nanomechanical string oscillator with a length of $60\,\mu$m and a string-ground plane separation of $120\,\text{nm}$. Additionally, we also leave a pocket in the ground plane of the microwave resonator for the later placement of the transmon qubit. After Al evaporation and lift-off, the sample is annealed at $300\,^\circ\text{C}$ for 30 minutes to generate a tensile stress in the aluminum thin film. In a next step, the tuneable transmon qubit is fabricated on the chip using e-beam lithography, aluminum shadow evaporation and lift-off techniques [128, 129]. In addition to the microwave input and output ports of the resonator, we use a broadband antenna next to the transmon to apply ω_s. To release the nano-string oscillator, we define an etching window using e-beam lithography with positive resist. We then use two reactive ion etching steps to release the string: (i) We start with an anisotropic RIE process, (ii) followed by an isotropic process to under-etch the nano-string. Finally, the remaining resist is removed by solvent followed by critical point drying.

An analysis of the final sample parameters using electron microscopy confirmed an aluminum thickness of $120\,\text{nm}$ for the electro- and mechanical resonator, as well as a string

width of 230 nm. Hence the mechanical resonator has a total mass of $m = V_{\text{beam}}\rho_{\text{Al}} = 1.66\,\mu\text{m}^3 \cdot 2.70\,\text{g/m}^3 = 4.5\,\text{pg}$. For doubly clamped nanomechanical oscillators the effective mass in good approximation is given by $m_{\text{eff}} = 1/2m$, cf. Sec. 2.2. The string is separated 160 nm from the ground plane, leading to a coupling of $g_{\text{m0}}/2\pi = 0.31\,\text{Hz}$. At a fridge temperature of $T_{\text{cryo}} \approx 50\,\text{mK}$ we found a string eigenfrequency of $\Omega_{\text{m}}/2\pi = 3.15018\,\text{MHz}$, from which we determine a zero point motion $x_{\text{zpm}} = \sqrt{\hbar/(2m_{\text{eff}}\Omega_{\text{m}})}$ of 35 fm, cf. Eq. (4.3). The intrinsic damping rate of the mechanical oscillator is found to be $\Gamma_{\text{m}}/2\pi = 12.4\,\text{Hz}$, leading to a ultra-high quality factor of $Q_{\text{m}} \approx 2.5 \cdot 10^5$. This is of particular interest as the thermal coherence then corresponds to $\tau_{\text{thermal}} = \hbar Q_{\text{m}}/(k_B T_{\text{cryo}}) = 38\,\mu\text{s}$.

When the transmon qubit is tuned down to its minimum frequency, far away from the resonator frequency, the bare microwave resonator frequency $\omega_{\text{c}}/2\pi = 5.875\,\text{GHz}$ is observed. Its linewidth depends on both, the working point of the transmon qubit, as well as the photon number. Therefor the mw resonator linewidth is discussed in a seperate section 6.4.3.

The maximum of the excited qubit mode, found at the sweet spot, is determined by $\omega_{\text{q}}/2\pi = 7.916\,\text{GHz}$, leading to a detuning of $\Delta_{\text{qc}}/2\pi = 2.056\,\text{GHz}$. In addition, we find a transmon nonlinearity of $\alpha/h = -188\,\text{MHz}$, and a transmon-resonator coupling of $g_{\text{q}}/2\pi = 134\,\text{MHz}$. The decoherence of the transmon qubit is discussed in detail in Sec. 6.6.5 and Sec. 6.6.

6.3 Spectroscopic configuration for an ultra-wide range photon number calibration

The microwave setup, sketched in Fig. 6.3, consists of several microwave sources to excite the qubit (ω_{s}, green) via an antenna, a drive (ω_{d}, red) and probe tone (ω_{p}, orange) joined at a power combiner, as well as a local oscillator (ω_{lo}, black). The signal inputs are heavily attenuated before they enter the sample and its antenna. Afterward, circulators guide the signal to a bandpass and a cryogenic HEMT, before it enters room temperature again. There, the signal is further amplified (not shown) and divided in two arms using a beam splitter. One percent is sent to a vector network analyzer (VNA) to determine the complex scattering parameter S_{21}. The rest is homodyne downconverted via a mixer to analyze its spectral densities using a spectral analyzer (SA). Further details on the employed devices are specified in Sec. A.1.
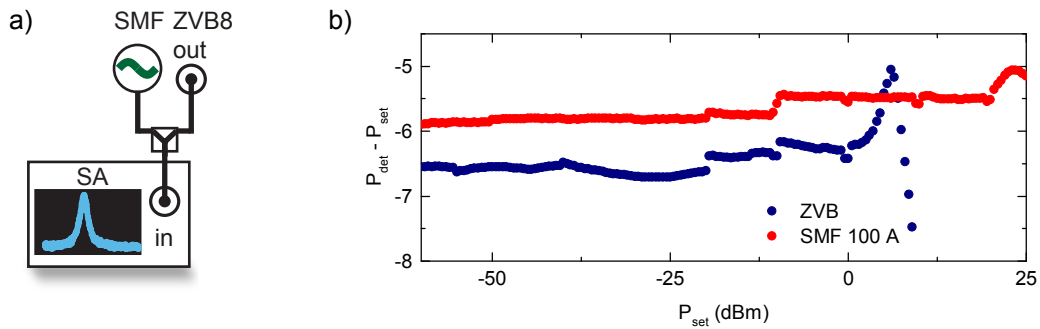
As in this configuration the photon numbers can be set by the drive or probe tone, a power calibration of the set power on the device P_{set} becomes necessary. For this we we record the transmitted power after the power combiner for each mw source individually, as depicted in Fig. 6.4a).

That allows us to determine a damping factor $K_{\text{i}}(\omega, P)$ as

$$P_{\text{appl}} = K_{\text{i}}(\omega, P)P_{\text{set}}. \tag{6.5}$$

Here, the index i indicates the individual device ($i \in \{\text{d}, \text{p}\}$). As pointed out, this power calibration is required for each drive frequency and power. Figure 6.4b) shows such a calibration measurement over eight orders of magnitude in power. On average we find a derivation of about 1 dBm. We can then use the calibrated power P_{appl} for a comparison of the determined photon numbers.

Figure 6.3: *Spectroscopy framework.* Three microwave sources carry the red-sideband drive tone ω_d, qubit spectroscopy tone ω_s, and local oscillator ω_{lo}. The vector network analyzer (VNA) probes and analyzes the microwave resonator transmission. Furthermore, a spectrum analyzer records the sideband fluctuations of the mechanical oscillator. The output signal of the microwave resonator is preamplified with a cryogenic HEMT amplifier at 4 K, followed by post-amplification at room temperature (not shown).

6.4 Continuous wave spectroscopy on the hybrid system

In the following section we present our results of a transmon qubit coupled to an electromechanical microwave resonator in continuous wave (cw) spectroscopy. For the calibration of the resonator's photon number we start by characterizing the individual interactions between transmon and nanostring to it. Then we discuss the resonator linewidth as it directly influences the photon number. We conclude by analyzing the transmon decoherence so we can compare the cw results with the pulsed measurements showed in the next section.

6.4.1 Transmon-resonator interaction

Now we focus on interactions between the microwave resonator and the transmon qubit. The $\lambda/2$ microwave coplanar waveguide resonator has a fixed frequency defined by its geometry, as introduced in Sec. 3.3. The transmon qubit, on the contrary, is a highly nonlinear oscillator based on a capacitively shunted dc-SQUID loop [75]. Furthermore, its flux dependent Josephson-energy $E_J(\Phi)$ [cf. Eq. (3.6)] allows to tune the qubit frequency

Figure 6.4: *Calibration of the microwave sources.* Panel a) shows the experimental setup. The output of a microwave source (SMF) and the vector network analyzer (VNA) are joined via a power combiner. The emitted power is determined via spectral analyzer. Panel b) displays the power calibration K over P_{set} for the microwave source SMF (SMF, red) and VNA (ZVB, blue).

via an externally applied magnetic flux. We located the transmon at the electric field anti-node of the coplanar waveguide resonator mediating a capacitive coupling between the two circuit elements.

In Fig. 6.5 a) we display the absolute scattering parameter $|S_{21}|^2$ of a low probe tone, coming from the VNA, through the microwave resonator with an equivalent average resonator photon number $\bar{n}_c = 1.7$ as function of the applied dc bias flux. This dataset shows the characteristic fingerprint of strong coupling between transmon qubit and resonator, i.e. an avoided crossing around $\Phi/\Phi_0 = 0.28$ with an higher (ω_+) and lower (ω_-) frequency branch. Additionally, we confirm the expected periodic behavior of the frequency evolution of the coupled system stemming from the flux quantization in the SQUID loop. When the transmon qubit is tuned to its minimum frequency (e.g. at $\Phi/\Phi_0 = 0.5$) the pure resonator transmission frequency is observed at $\omega_c/2\pi = 5.875$ GHz with a linewidth of $\kappa/2\pi = (1.468 \pm 0.022)$ MHz.

In panel b) of figure 6.5 we plot the peak separation $\omega_+ - \omega_-$ around the anti-crossing for $\bar{n}_c < 1$. From the minimal splitting we can extract the transmon-resonator coupling as $\mathrm{Min}[\omega_+ - \omega_-] = 2g_q$. By this we determine a coupling strength of $g_q/2\pi = (134.1 \pm 2.3)$ MHz.

Tuning the transmon qubit away from the resonator, in the dispersive regime, the probed resonance frequency of the microwave resonator is depending on the qubit state via Eq. (3.28). Hence, when driving the qubit selectively with ω_s while probing the resonator's transmission, two-tone spectroscopy of the qubit state is performed, see Sec. 5.3.1. We show such spectroscopy on the transmon qubit in Fig. 6.6. From panel a) we determine a qubit frequency ($|g\rangle \leftrightarrow |e\rangle$ transition) of $\omega_q/2\pi = (7.916 \pm 0.001)$ GHz at the sweet spot of $\Phi = 0$.

As the transmon qubit is not an ideal two-level system, its anharmonicity α is reducing the ac-Stark shift, making the transmon less sensitive to shot noise of the microwave resonator [75]. To determine its anharmonicity we increase the spectroscopy amplitude at $\Phi/\Phi_0 = 0$. Then multi-photon processes become observable [130, 131]. We find the two-photon transition $|g\rangle - |f\rangle$ at $\omega_{gf}/4\pi = (7.822 \pm 0.001)$ GHz determining a transmon anharmonicity

a)
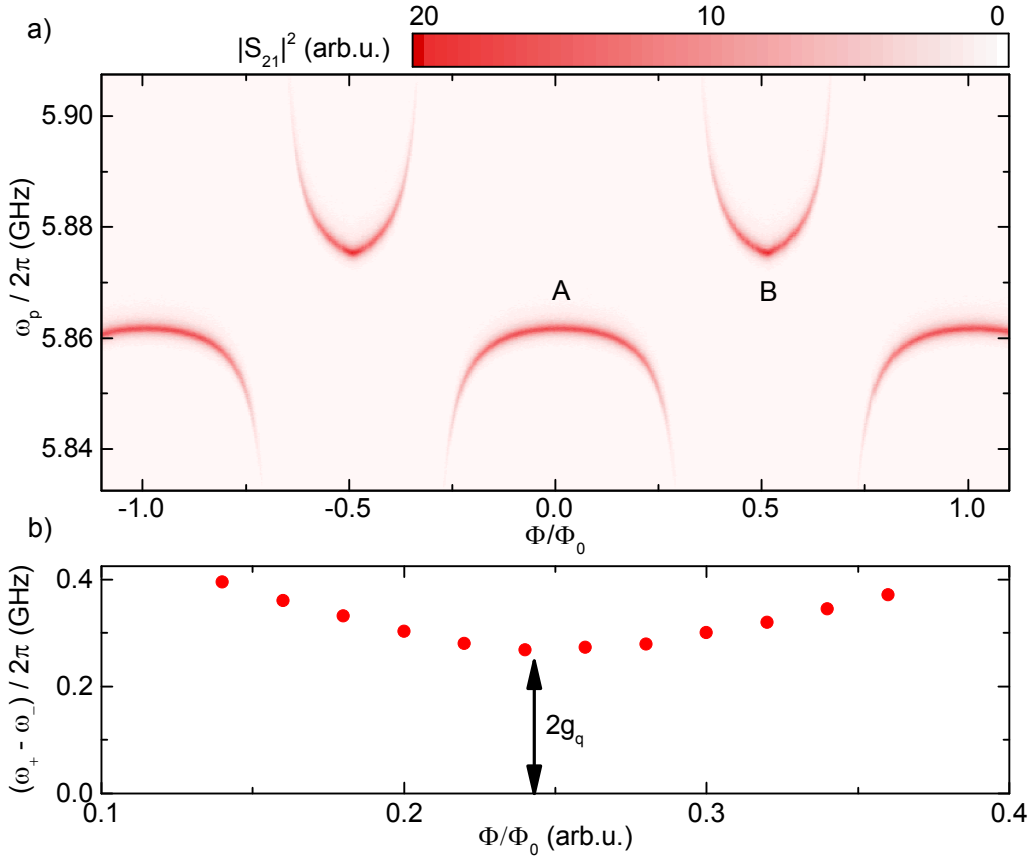
Figure 6.5: *Resonant transmon qubit and microwave resonator interaction.* Panel a) Microwave transmission $|S_{21}|^2$ of the sample versus applied magnetic flux Φ. We observe a periodic tuning with integer flux ratio. Tuning the transmon on resonance with the microwave resonator a splitting is observed. Panel b) displays the extracted splitting around an anti-crossing, from which the transmon-resonator coupling is determined.

$\alpha/h = -(188 \pm 1)\,\text{MHz}$, as $\alpha/\hbar = 2\omega_q - \omega_{gf}$. For transmon qubits this is equivalent to the negative charging energy, cf. Sec. 3.4.2.

The ratio between Josephson and charging energy is an important transmon characterization parameter. As we can express the transmon frequency via $\omega_q = \sqrt{8E_J E_C}/\hbar$ [75], we get a ratio of $E_J/E_C = 222$, far away from the charge qubit regime [75].

6.4.2 Electromechanical interactions

Now, we aim to characterize the nanostring and the respective electromechanical coupling strength. For this we study symmetric sideband spectroscopy of the nanostring's thermal motion as used in Refs. [103, 106, 123, 132] and reveal a photon-phonon coupling strength of $g_{m0}/2\pi = 0.308\,\text{Hz}$.

At large, we probe the microwave resonator on resonance ($\omega_p = \omega_c$) including a defined frequency modulation and record the homodyne downconverted frequency fluctuations induced by the nanostring. Figure 6.7a) displays the measured power spectral density detected by a spectral analyzer. The thermal motion at $365\,\text{mK}$ of the nanostring is shown in the middle of the graph with a mechanical eigenfrequency of $\Omega_m/2\pi = 3.15018\,\text{MHz}$ and
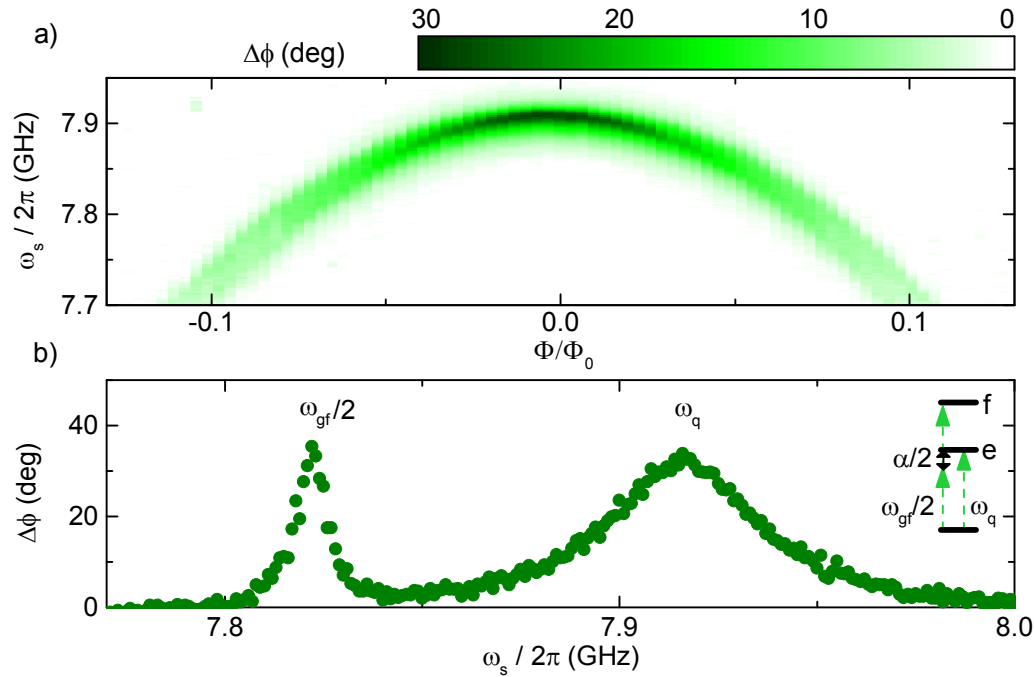
Figure 6.6: *Dispersive transmon qubit read-out.* Panel a) two-tone spectroscopy on the transmon qubit revealing its transition frequency ω_q as a function of the applied flux. The maximum frequency is observed at zero flux. Displayed is the phase change of the probe signal through the microwave resonator. Panel b) Strong driving the transmon qubit at the sweet spot $\Phi_{ext}/\Phi_0 = 0$ (green dots) reveals the single photon $|g\rangle \leftrightarrow |e\rangle$ transition at ω_q as well as the two photon $|g\rangle \leftrightarrow |f\rangle$ transition at ω_{gf} as schematically depicted on the right.

a linewidth of $(33.5 \pm 0.1)\,\text{Hz}$ indicating an ultra-high Q-factor of about 10^5. Further we find a power spectral densitiy of $S_{PP}(\Omega_m) = 4.8\,\text{pW/Hz}$. The frequency modulation of the probe tone (having $\Omega_{mod}/2\pi = 3.1498\,\text{MHz}$ and $\Omega_\phi/2\pi = 80\,\text{Hz}$) results in a sharp peak found on the left, from which we determine $S_{PP}(\Omega_{mod}) = 2.85\,\text{nW/Hz}$. By comparing the thermal motion amplitude with the calibration amplitude we are able to determine the integrated displacement noise $\langle\delta\omega^2\rangle$ (for details see [103, 106, 123]):

$$\langle\delta\omega^2\rangle = \int_{-\infty}^{\infty} S_{\omega\omega}(\omega)\frac{d\omega}{2\pi} = \frac{\phi_0^2 \Omega_m^2 \Gamma_m}{4\text{ENBW}} \cdot \frac{S_{PP}(\Omega_m)}{S_{PP}(\Omega_{mod})} = 2g_{m0}^2 n_m. \tag{6.6}$$

In our experiment we were applying a phase modulation of $\phi_0 = \Omega_\phi/\Omega_{mod} \approx 2.5 \cdot 10^{-5}$, and a measurement bandwidth ENBW of $1\,\text{Hz}$.

We want to note, that the electromechanical interaction can cause a back-action on the nanostring by the drive tone, resulting in a finite back-action temperature [$n_m \rightarrow k_B(T_{ba} + T_{sample})/\hbar\Omega_m$]. To take this possibility into account, we next record the frequency fluctuations while cooling the cryostat. The integrated displacement noise of this experiment is found in Fig. 6.7b). We resolve the expected linear behavior rising with $s/(2\pi)^2 = (1.253 \pm 0.035)\,\text{kHz}^2/\text{K}$, resulting in single photon-phonon coupling rate of:

$$g_{m0} = \sqrt{\frac{s\hbar\Omega_m}{k_B}} = 2\pi \cdot (0.308 \pm 0.004)\,\text{Hz}, \tag{6.7}$$

The determined vacuum coupling strength is lower but close to the previously determined ones achieved with pure aluminum coupled electromechanical resonators ($g_{m0}/2\pi =$
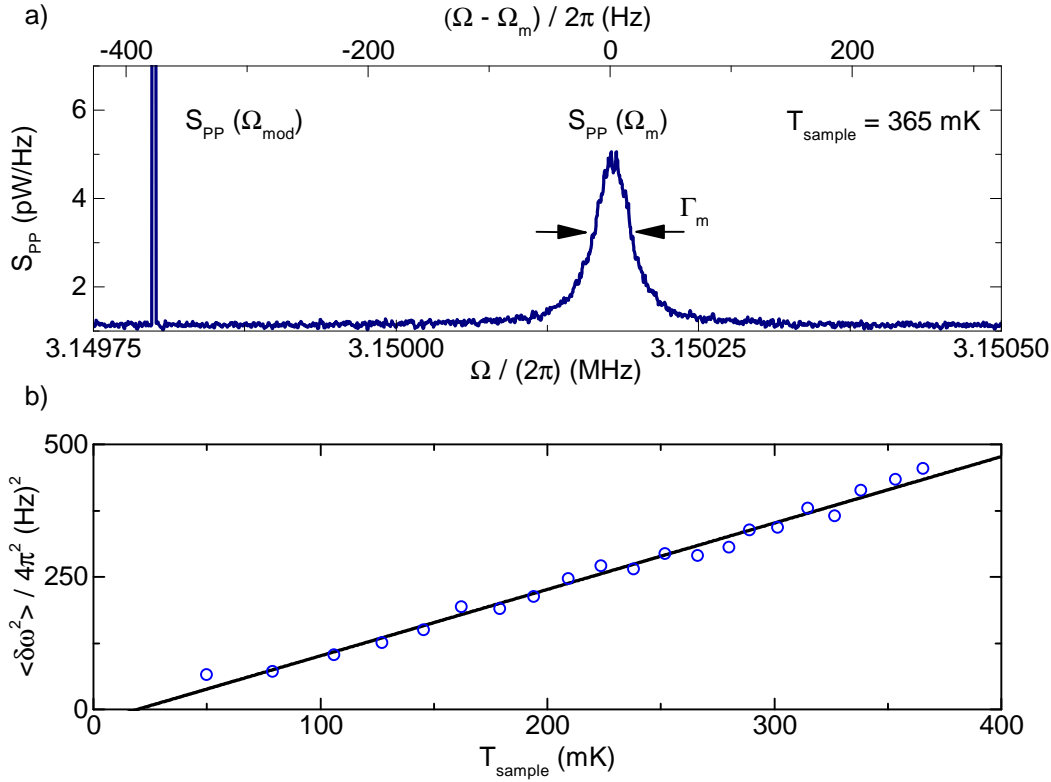
Figure 6.7: *Homodyne detected motion of nanostring.* Panel a) shows the recorded power spectral density of the string's motion for a sample temperature of 365 mK. We find the nanostring in the middle of the plot with a narrow linewidth. We extract peak height and linewidth for the calibration via thermal sidebands. In addition, we determine the peak size of a well-defined frequency modulation, seen on the left. By this we find the fluctuations in frequency, plotted for a systematical temperature sweep in panel b). We fit a linear dependency to the data (black solid line) that allows us to determine the vacuum coupling by Eq.(6.6), assuming thermal equilibrium between sample and nanostring.

$0.57 \pm 0.6 \, \text{Hz}$ in [43]). The nanostring's geometry in our case was more conservative as we additionally were placing a qubit on the microchip, and so a higher yield in the string release was required. Nevertheless, by a proper design of the circuitry higher couplings can in principle by achieved, see also [133].

6.4.3 Microwave resonator decoherence

From Eq. (6.2) we directly see that the average photon number of the resonator depends on its linewidth κ. So for a proper analysis of the resonators occupation the total linewidth dependence has to be taken into account. As it is a combination of internal and external losses, where the later one is only defined by the resonators geometry, we assume the external linewidth to be independent of the working spot or probe power. This allows us to compare x_{qb} and x_{EMIA} by the model of Eq. (6.2). The transmon and electromechanical regime correspond to two different working spots of the qubit, as indicated by A and B in Fig. 6.5a). These lead to different linewidth dependencies which we depicted versus applied power in Fig. 6.8 for the qubit calibration in panel a) and for
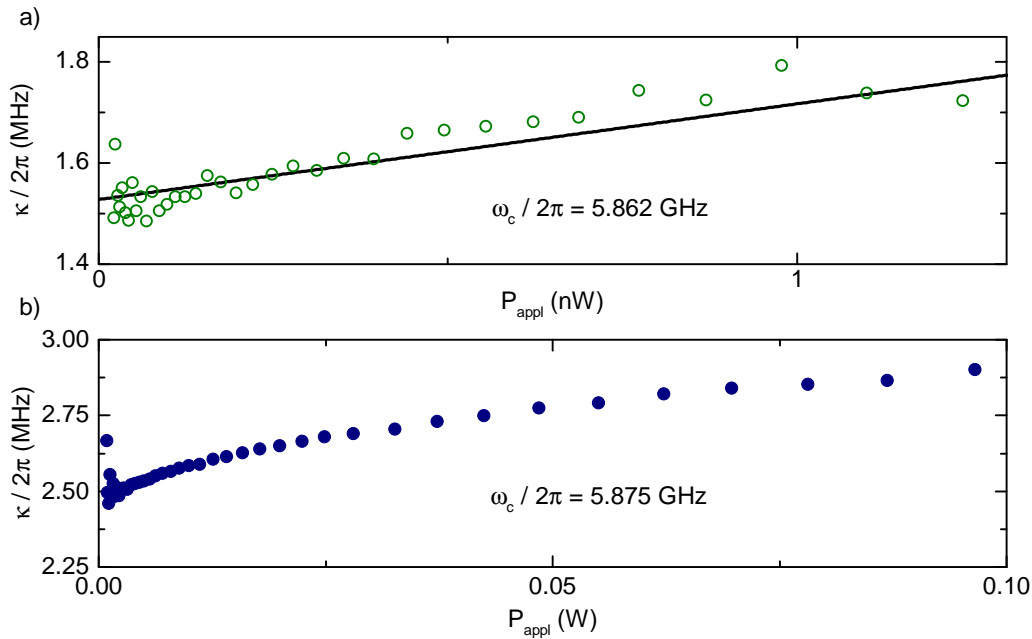
Figure 6.8: *Microwave resonator decoherence in dependence of probe power and working spot.* Panel a) reveals the extracted linewidth in the qubit regime (green dots) for a resonator frequency of $\omega/(2\pi) = 5.862$ MHz [corresponding to point A in Fig. 6.5a)]. The applied power range is $0.02 - 1.2$ nW. We find a linear trend, that is fitted by the black solid line. In panel b) we plot the in-situ observed linewidth of the microwave resonator for the electromechanical calibration (blue dots) in an applied power range of $0.9-97$ mW, for which we find a non-trivial behavior. Here, the operation point of the transmon qubit was set to point B in Fig. 6.5a).

the electromechanical in b), respectively.

We measure the resonator linewidth from 22 pW up to 1.2 nW at the working spot used for the ac-Stark measurements, revealing a linear increase with an offset of (1.53 ± 0.01) MHz and a slope of (181 ± 14) kHz/nW. To calibrate the damping parameter x_{qb} we interpolate this behavior to calculate the $\delta\omega\kappa^2$ product in Fig. 6.10. In contrast to a typically observed decrease of the linewidth for higher occupations, as two-level fluctuators get saturated [134], we find an increase of it. We speculate, that the transmon qubit linewidth of around 7 MHz (see next section), being higher than the resonator's, is causing this broadening as the systems hybridize.

In contrast to this linear trend, a non-trivial behavior is found in the electromechanical regime. First a peak at 0.9 mW with a local maximum of up to 2.7 MHz is observed, before it is quickly dropping down. Afterwards, a continuous increase for probe powers up to $P_{appl} = 97$ mW is determined. Since the statistic fluctuations in this characteristics appear small, we directly take the measured value into account, as we perform this measurement in-situ while determining the EMIA interference. A potential reason for this behavior, in particular the peak at 0.9 mW, could be the Josephson junctions of the transmon qubit switching into the voltage state. As we have no direct measurement of this switching we can only speculate here.
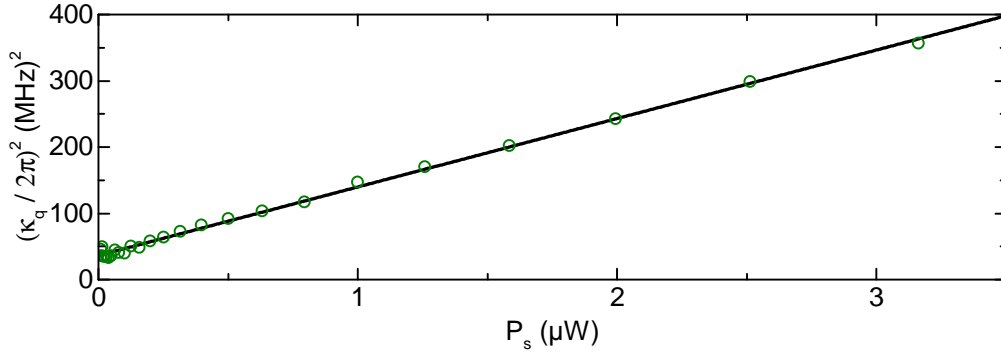
Figure 6.9: *Continuous wave determined transmon qubit decoherence at the sweet spot.* We plot the extracted transmon linewidth squared (green) over the drive power of the spectroscopy tone and find a linearly increasing behavior. By fitting this trend (black solid line) we find the intrinsic transmon decoherence.

6.4.4 Transmon decoherence

In analogy to the discussed resonator linewidth, we will now focus on the transmon linewidth. For this we employ a two-tone spectroscopy as previously introduced, cf. Sec. 5.3.1. By this we determine the qubit response to a drive tone via the antenna, resulting in a Lorentzian peak. By fitting the spectra we obtain the linewidth of the qubit in dependence of the spectroscopy probe tone power P_s, for which we expected a theoretical correlation of [120, 135], cf. Eq. (2.6):

$$\kappa_q/2 = 1/T_2' = \left(\frac{1}{T_2^2} + c_s P_s \frac{T_1}{T_2} \right)^{1/2}.$$ (6.8)

Here a calibration constant c_s was introduced for the proportionality of $c_s P_s = n_s \omega_{vac}$, linking the spectroscopy photons n_s and the vacuum Rabi frequency ω_{vac} to the spectral drive power. For a systematical analysis we therefore plot the squared linewidth over the applied spectroscopy power in Fig. 6.9. Indeed the linear connection is observed, from which we determine an increase of $2\pi \cdot (1.033 \pm 0.018) \cdot 10^{20} \mathrm{Hz}^2/\mathrm{W}$ and an intrinsic qubit linewidth of $\kappa_q/2\pi = (6.0 \pm 1.1) \, \mathrm{MHz}$ in the low power regime ($P_s \to 0$), corresponding to a dephasing time of

$$T_2' = T_2 = (53 \pm 9 \,)\mathrm{ns}.$$ (6.9)

In comparison to literature values reporting up to millisecond lifetime this is rather low [136]. On the other side we like to state that the microchip design has potential for optimizations in the transmon qubit decoherence. In addition, the aim of such electromechanical hybdrid systems is to overcome restrictions in the qubit decoherence by storing the information in the mechanical element. We will discuss potential storage times of the hybrid system in Sec. 6.7. Finally we have to mention that the determination of the transmon decoherence is rather indirect and should be seen as a lower boundary. A detailed, direct analysis requires pulsed schemes which will be the focus of the next section.
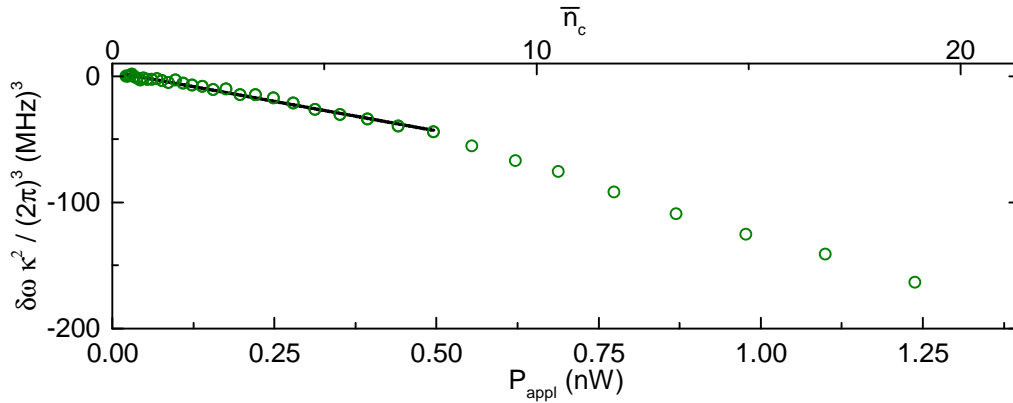
Figure 6.10: *Photon number calibration via ac-Stark shift.* We plot the extracted product $\delta\omega\kappa^2$ (green dots) per probe tone power P_{appl}. We observe a linear decreasing trend for low probe powers. In this regime we apply the linear model from Eq. (6.3) to the data (black solid line) to determine the corresponding photon number (top axis). The deviations from the linear model then are calibrated to start above eight photons.

6.5   Photon number calibration

As we have now fully characterized our electromechanical cQED sample, we can determine the photon numbers in the microwave resonator. We start by measuring the ac-Stark shift of the transmon qubit and then the broadening of the mechanical linewidth via EMIA experiments. As we will see, combining these methods allows for an ultra-wide range calibration of the occupation number $\bar{n}_{\mathrm{c}}$.

6.5.1   Ac-stark shift

First we have to calculate the so called ac-Stark shift of the transmon qubit on its eigen-frequency induced by the microwave photons in the resonator. By the characterization of the transmon-resonator interaction we find the parameters $g_{\mathrm{q}}/2\pi = (134.1 \pm 2.3)\,\mathrm{MHz}$, $\alpha/2\pi = -(188 \pm 1)\,\mathrm{MHz}$, and detuning $\Delta_{\mathrm{qc}}/2\pi = 2.056\,\mathrm{GHz}$. So the expected ac-Stark shift is given by Eq. (3.29) and we derive

$$\frac{\delta\omega_{\mathrm{q}}}{2\pi\bar{n}_{\mathrm{c}}} = -(1.761 \pm 0.055)\,\mathrm{MHz/photon}. \tag{6.10}$$

For the experimental investigation we set the transmon qubit to its maximum transition frequency [working spot A in Fig. 6.5a)] using the mounted superconducting dc-coil. Next we experimentally investigate the transmon qubit frequency in dependence of the applied probe tone power P_{appl}, via the dispersive shift. By this we find $\delta\omega(P_{\mathrm{appl}})$.
Following the approach in Ref. [120], we then plot the product $\delta\omega(P_{\mathrm{appl}})$ times the square of the extracted resonator linewidth from Sec. 6.4.3, and show the result in Fig. 6.10. For low drive powers we find the expected linear behavior as predicted by Eq. (6.3), having a slope of $-(2\pi)^3 \cdot (9.36 \pm 0.02) \cdot 10^{19}\,/\mathrm{s}^3\mathrm{nW}$. Deviations from this linear trend are observed at higher probe tone powers that we speculate to arise from contribution of higher lying transmon levels [137].
   Finally by merging the extracted experimental slope $\delta\omega(P_{\mathrm{appl}})$ with the expected shift from Eq. (6.10) $\delta\omega(\bar{n}_{\mathrm{c}})$ we find the number of photons per applied probe tone power, see

top axis in Fig. 6.10. Plugging these results in Eq. (6.2), we determine a calibration factor of $x_{\mathrm{qb}} = (4.08 \pm 0.25)\,\mathrm{s}^{-1}$. Assuming an external coupling of $\kappa_{\mathrm{ext}}/2\pi = 1\,\mathrm{MHz}$ as observed in prestudies for the given geometry [70], we can quantify the microwave attenuation of $\Lambda = 61.9\,\mathrm{dB}$. Taking the built in attenuation into account this corresponds to a cable loss of $9.9\,\mathrm{dB}$.

Using the ac-Stark shift of the transmon, we demonstrated that we are able to calibrate the average photon populations $\bar{n}_{\mathrm{c}}$ of the microwave resonator stemming from the probe tone to powers equivalent to $\bar{n}_{\mathrm{c}} \lesssim 8$ photons. We note, that this is far below the critical photon number of $n_{\mathrm{crit}} = \Delta_{\mathrm{qc}}^2/(2g_{\mathrm{q}})^2 \approx 60$ for which the assumptions of the dispersive limit are valid [84, 138].

6.5.2 Electromechanical induced absorption

To specify higher resonator photon numbers we set the transmon qubit to its minimum frequency [spot B in Fig. 6.5a)] and turn to the two-tone EMIA spectroscopy scheme [cf. Fig. 6.1b)]. Thus, we apply a drive tone on the red sideband $\omega_{\mathrm{d}} = \omega_{\mathrm{c}} - \Omega_{\mathrm{m}}$ and interfere the resulting anti-Stokes field with a probe tone ω_{p} around ω_{c}. The drive tone strength now sets $\bar{n}_{\mathrm{c}}$ determining the EMIA interference manifesting itself in form of an additional absorption signal close to $\omega_{\mathrm{d}} + \Omega_{\mathrm{m}}$. By fitting a lorentzian lineshape to the EMIA data we extract the effective mechanical linewidth $\Gamma_{\mathrm{eff}}(P_{\mathrm{appl}})$. We display an overview of three drive amplitudes in Fig. 6.11a), where we plot the normalized transmission $|S_{21,\mathrm{n}}|^2$, which sets the cavity transmission off-resonant to the EMIA signal to unity. We find an absorption of up to $25\,\%$ of the initial microwave transmission scattering $|S_{21,\mathrm{n}}|^2$. Next we plot the extracted effective mechanical linewidth Γ_{eff} in Fig. 6.11b) for a systematical sweep of the drive tone amplitude. As predicted by Eq. (6.4) we observe a linear broadening of the damping. By the sample characterization in Sec. 6.4, we are able to fit the model from Eq. (6.4) to the data where we use the intrinsic linewidth Γ_{m} and the calibration factor x_{EMIA} as the only free fit parameters. We note, that here we take the microwave resonator linewidth of the corresponding drive tone power as found in Sec. 6.4.3 directly into account. For low photon numbers we find an intrinsic damping factor of $\Gamma_{\mathrm{m}}/2\pi = (12.4 \pm 0.3)\,\mathrm{Hz}$ corresponding to a quality factor of $2.5 \cdot 10^5$ at $50\,\mathrm{mK}$. This is in good agreement with previous characterized samples fabricated at the WMI, which found $13.3\,\mathrm{Hz}$ at $50\,\mathrm{mK}$ [43], and to reported values from literature for such pure aluminum nanostrings [139, 140] which are found to be in the $Q \approx 10^5$ range.

In addition, we resolve a damping factor of $x_{\mathrm{EMIA}} = (5.41 \pm 0.25)\,\mathrm{s}^{-1}$, corresponding to $\Lambda \kappa_{\mathrm{ext}}$. Again assuming an external coupling of $2\pi \cdot 10^6\,\mathrm{s}^{-1}$ we can calculate the microwave loss of the setup to $\lambda = -60.6\,\mathrm{dB}$ of attenuation, or $-8.6\,\mathrm{dB}$ for the microwave cabling without the installed attenuators, seeming realistically. By this calibration we can translate the applied powers for this measurement corresponding to $\bar{n}_{\mathrm{c}} = 1.4 \cdot 10^6$ up to $1.4 \cdot 10^8$, see top axis in Fig. 6.11b).

6.5.3 Comparison of the calibration results

We have calibrated the resonator photon number via the transmon qubit measuring the ac-Stark shift from 0.5 to 8 photons and obtain a loss coefficient of $x_{\mathrm{qb}} = (4.08 \pm 0.26)\,\mathrm{s}^{-1}$. Higher occupations were determined by EMIA spectroscopy of the effective nanomechanical linewidth measuring the resonator in a population range from $1.4 \cdot 10^6$ to $1.4 \cdot 10^8$
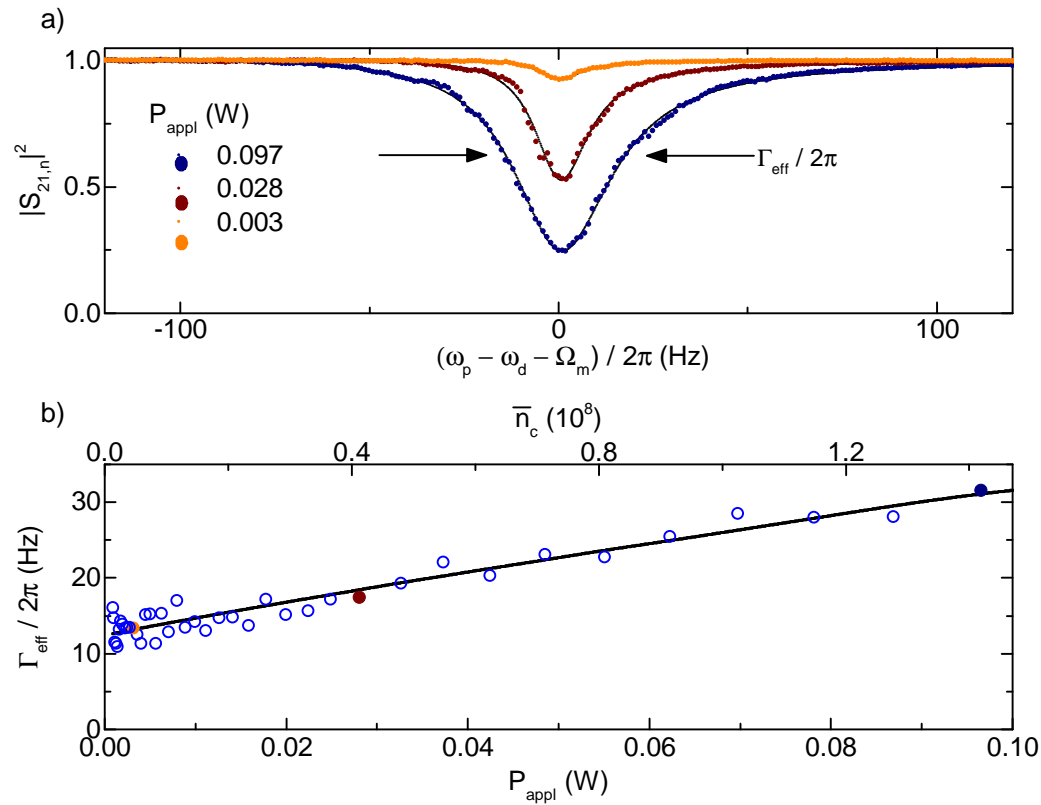
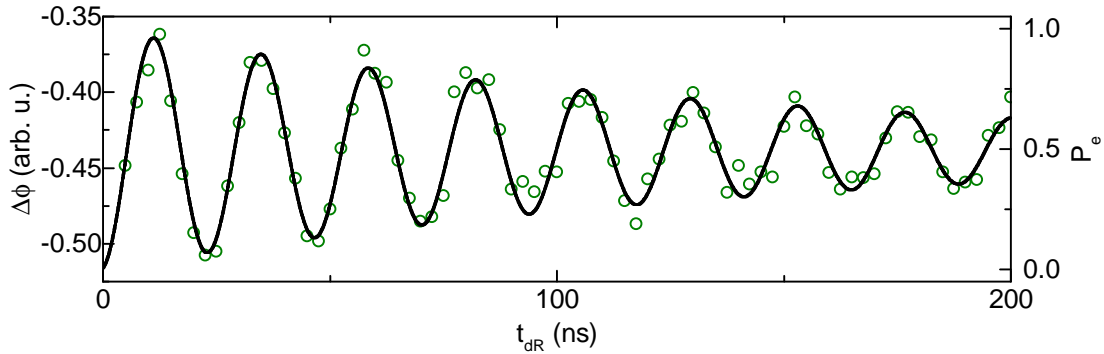**Figure 6.11:** *EMIA spectroscopy on the resonator-nanomechanical hybrid system at about* 50 *mK.* In panel a) the normalized EMIA signature (dotted) is displayed for three drive powers P_{appl} ± 120 Hz around the mechanical response. An EMIA dip is found that increases with drive power. We fit Lorentzian models to the EMIA results (black solid lines) to extract Γ_{eff}. In panel b) the effective linewidth Γ_{eff} (blue dots) is plotted for a sweep of the red-sideband drive amplitude. By applying the EMIA model introduced in the main text, we find x_{EMIA} and hence the photon occupation in the microwave resonator (top axis).

photons. In the electromechanical experiments, we revealed a calibration factor $x_{\text{EMIA}} = (5.41 \pm 0.25)\,\text{s}^{-1}$.

By combining circuit-QED with electromechanical techniques, as described above, we can therefore resolve photon numbers being apart up to nine orders in magnitude. Within this ultra-wide range the calibration agrees within 25 %. In terms of the technical attenuation, given in dB and assuming $\kappa_{\text{ext}} = 2\pi \cdot 10^6\,\text{s}^{-1}$, we find a deviation of 1.2 dB. The obtained uncertainties are lower than this discrepancy but of equal size. Overall we conclude with an averaged calibration of $x = 4.75\,/\text{s}$, corresponding to an attenuation of -61.2 dB when assuming an external linewidth of $\kappa_{\text{ext}}/2\pi = 1\,\text{MHz}$. Besides the built in attenuation this corresponds to a loss of -9.2 dB of the microwave cables in the given setup.

6.6   Time resolved qubit spectroscopy

In the following we start by investigating the qubit performance via Rabi-Oscillations. In particular, we will compare driven Rabi oscillations for two different working points measured via two different methods. Further we apply advanced pulse schemes at the sweet

Figure 6.12: *Rabi oscillations of the transmon qubit on resonance.* The recorded phase change of an incident microwave probe tone on the electric resonator, directly applied after a spectroscopy tone of varying length (green dots) is shown. We find an oscillation decaying over time, corresponding to the qubit excitation. We fit the data applying a Rabi-decay function (black solid line), which allows us to calibrate the transmon excitation P_e (right axis), as well as to extract the time length of $\pi-$ and $\pi/2-$ pulses.

spot to investigate the decoherence of the transmon qubit. The results are summarized and discussed at the end.

6.6.1 Driven Rabi-Oscillations

Sweet spot decoherence   We start our analysis by setting the transmon qubit to the sweet spot. Further we apply a spectroscopy tone via the antenna using a constant amplitude but sweeping its pulse length τ_{Rabi}. Directly after the spectroscopy tone we apply a read-out probe tone on resonance to the microwave resonator, which allows for a direct measurement of the qubit state. This pulse sequence was introduced in Sec. 5.3.5 as *Driven Rabi.* We plot the detected phase change for a spectroscopy on resonance to the transmon qubit in Fig. 6.12, where we find decaying oscillations, indicating the rotation of the qubit on the Bloch sphere. These oscillations have a distinct frequency, the so-called Rabi frequency. On the long run a steady state in the equatorial plane of the Bloch sphere between excited and ground state is reached, corresponding to $P_e = 0.5$. We fit the Rabi-decay behavior by

$$A_0 e^{-\frac{t}{T_{\mathrm{Rabi}}}} \sin\left[\omega_{\mathrm{Rabi}} t/(2\pi)\right] + \Delta\Phi_0 \tag{6.11}$$

revealing the Rabi frequency $\omega_{\mathrm{Rabi}}/2\pi = 42\,\mathrm{MHz}$ and decay time $T_{\mathrm{Rabi}} = 151\,\mathrm{ns}$ for the example set in Fig. 6.12.

Next, we sweep the spectroscopy frequency [cf. Fig. 6.1a)] and show the findings in Fig. 6.13a), revealing the $|g\rangle \rightarrow |e\rangle$ tranistion $\omega_q/2\pi = 7.918\,\mathrm{GHz}$ and the $|g\rangle \rightarrow |e\rangle$ transition at half of its frequency $\omega_{\mathrm{gf}}/4\pi = 7.822\mathrm{GHz}$. The $|g\rangle \rightarrow |e\rangle$ tranistion is observed over a broad frequency range showing a typical driven Rabi response, consisting of oscillations of the qubit state with the Rabi frequency ω_{Rabi}, which has its minimum at the transmon frequency. A finite dent is observed around the qubit frequency, that we attribute to an insufficient magnet field screening and which will be discussed further at another working spot. The signature of the first harmonic, observed at half its frequency, has a higher amplitude as well as a lower Rabi frequency, and a small frequency range
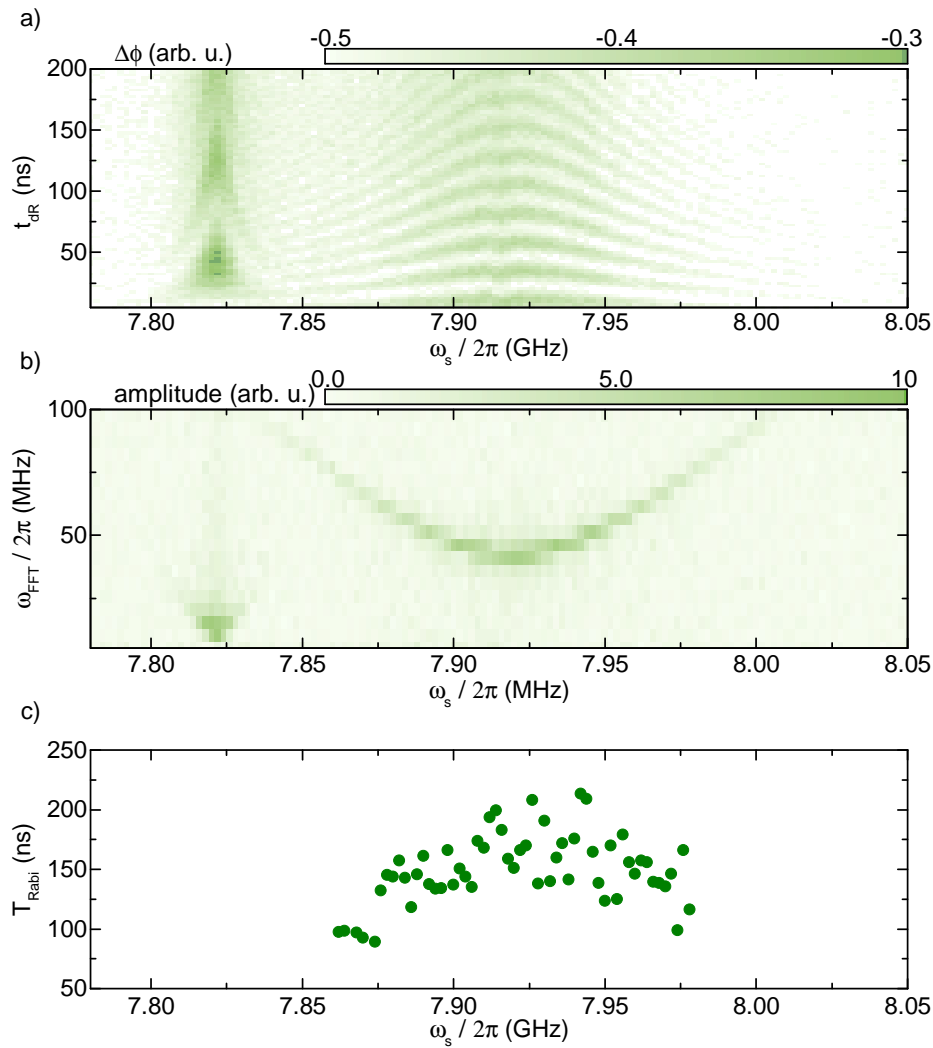
Figure 6.13: *Driven Rabi oscillations of the transmon qubit at the sweet spot.* Panel a) displays the recorded Rabi oscillations for a systematical sweep of the spectroscopic frequency. Typical Rabi oscillations are found for the ground mode and signatures arising from the transmon nonlinearity. A small dent is observed close to the transmon resonance frequency $\omega_q/2\pi = 7.92\,$GHz. In panel b) a discrete fourier analysis of the recorded data is shown. One finds the expected parabolic tuning of the frequencies, the higher harmonic is hard to see due to the limited data. Panel c) shows the extracted decay in relation to the applied spectroscopy tone. Longest coherence is found on resonance to the qubit.

to observe it. As it is excited only via multi-photon processes in this configuration the effective excitation amplitude is highly reduced, leading to a lower Rabi frequency.

Next we apply a Fourier transformation on the recorded data, to determine the spectral frequency contributions. Results are displayed in Fig. 6.13b). We find a minimum Rabi-frequency of the ground mode at about 40 MHz parabolically increasing when the spectroscopy frequency turns of resonant to the qubit. The signature from the $|g\rangle \rightarrow |e\rangle$ transition has a much lower frequency as previously discussed. For a systematical analysis we plot the extracted decay time for the observable range of Rabi oscillations on the $|g\rangle \rightarrow |e\rangle$ transition, as found in Fig. 6.13c). Around the resonance frequency we find a decay time of $T_{\text{Rabi}} = (175 \pm 22)\,$ns. Off the resonance the decay is enhanced. This

indicates a limitation by dephasing processes, since an off-resonant drive pulses the qubit in positions with x-y contributions of the Bloch sphere.

We have now analyzed the Rabi-oscillations at the sweet spot, where the influence of the magnetic field noise is minimized. We found good agreement between expected and measured oscillations. Only a small dent was found not explained by the theory.

Detuned   Now we tune the transmon at a point with finite sensitivity to magnetic fluctuations, $\omega_q/2\pi = 7.776\,\text{GHz}$ to be precise. Here, the field sensitivity extracted from Fig. 6.6a) is $\omega_q'/(2\pi\Phi_0) = 3.4\,\text{GHz}/\Phi_0$.

Again, we record the Rabi oscillations systematically in dependence of ω_s, as plotted in Fig. 6.14a). Like before, we observe the typical Rabi fingerprint, this time with a reduced contrast and the $|g\rangle \to |e\rangle$ transition being barely visible. In addition, the dent around the resonance frequency is increased. Besides the working spot, the experimental environment was kept constant, so we conclude that this feature must arise from field noise. A plausible cause as there was no magnetic shielding used in this experiment.

For a further analysis we perform a Fourier analysis, see Fig. 6.14b). In contrast to the sweet spot we find two equal parabolas, shifted by $\Delta\omega_q/2\pi = (44 \pm 4)\,\text{MHz}$. Since we have determined the field sensitivity above we can connect the frequency shift in a magnetic field value of

$$\Delta\omega_q \omega_q' = \Delta\Phi = 13\,\text{m}\Phi_0, \tag{6.12}$$

or knowing the area of the qubit to be $A_q = 254\,\mu\text{m}^2$ to a field fluctuation of about $0.1\,\mu\text{T}$. To determine the Rabi decay we fit the model in Eq. (6.11) assuming a single Rabi oscillation. The extracted times are found in Fig. 6.14c). Around the minimum of the FFT parabolas we find $T_{\text{Rabi}} = (113 \pm 25)\,\text{ns}$. Approaching the transmon qubit frequency a decrease to $50\,\text{ns}$ is observed. Yet, we note that here the used model of a single oscillation could be optimized by using one with an interference of two oscillations. On the other hand, the data shows that on this resonance the steady state on the equatorial plane of the Bloch sphere is reached fast, leading to a constant phase shift, so only a few datapoints are available. Modeling and a detailed analysis hence becomes challenging.

Nonlinear qubit read-out   Until here we have determined the Rabi frequencies recording the state dependent dispersive shift of the microwave resonator. Yet this read-out is limited to photon numbers within the dispersive regime, here $\bar{n}_c \approx 60$. This also limits the applied radiation pressure in the resonator, and so prevents to boost the effective electromechanical coupling via $g = \sqrt{\bar{n}_c}\, g_{m0}$. In the following we show a driven Rabi read-out using the nonlinear qubit-resonator interaction, based on Refs. [141, 142]. This allows to increase the number of read-out photons by about 280, significantly enhancing the electromechanical coupling. To introduce the principle of this read-out scheme, we start with a spectroscopy of the microwave resonator transmission at the sweet spot of the transmon qubit, as function of the applied probe power. Here, the transmon qubit stays in its ground state. The result is displayed in Fig. 6.15a). At first we find the microwave resonance at $5.862\,\text{GHz}$, as before. Increasing the probe power a bifurcation is observed, at around $-50\,\text{dBm}$ or 40 photons. For higher probe tone powers, a new area of microwave transmission arises. This is found at the bare microwave resonator's

a)

b)

c)
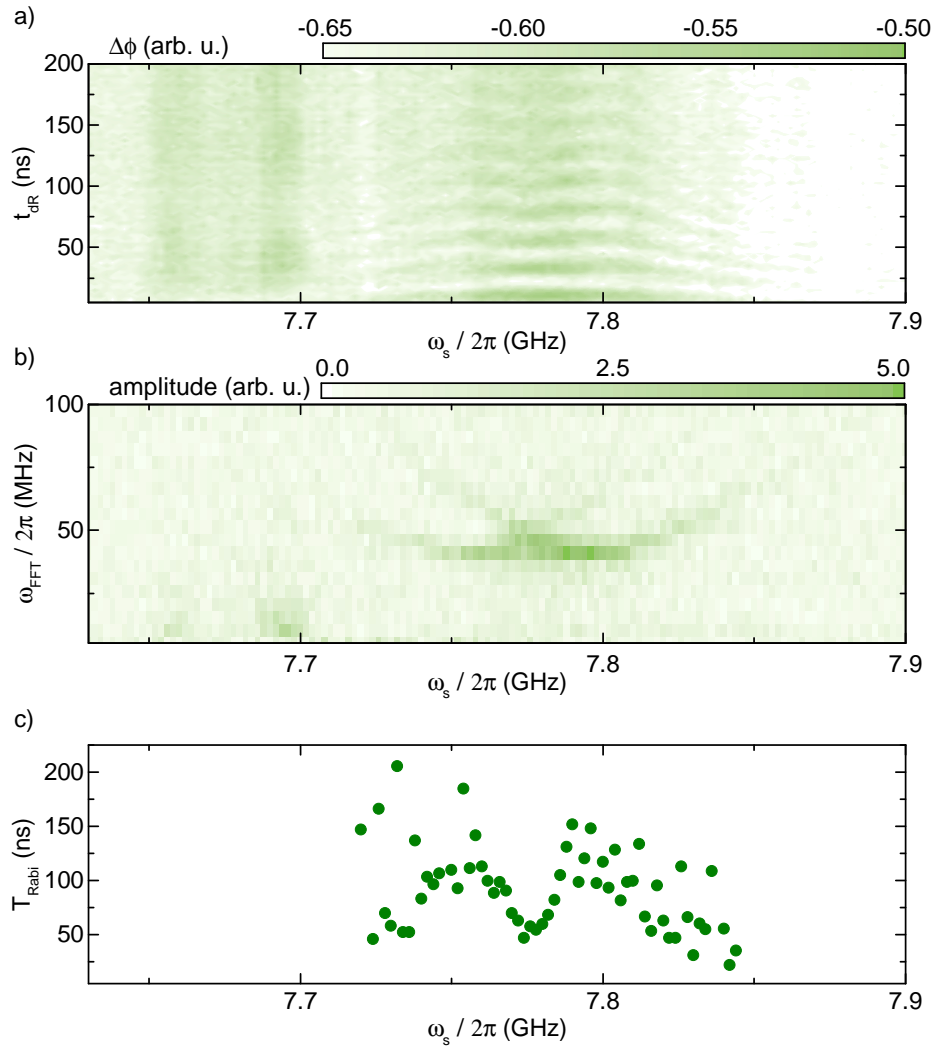
Figure 6.14: *Influence of magnetic field noise on the qubit for a finite field sensitivity.* In panel a) the recorded Rabi oscillations for the detuned transmon are shown. As earlier the oscillation frequency is highest on resonance to the transmon qubit. Yet the dent around it is increased in comparison to the sweet spot. In panel b) the discrete Fourier analysis reveals two oscillations parabolically tuning with the spectral tone. A hint of the higher harmonic is found at lower frequencies. Panel c) shows the extracted Rabi frequency, assuming a single Rabi-oscillation for which we find a minimum of the coherence at the interference point. Besides decay times of about 100 ns are found.

eigenfrequency of 5.875 GHz. We relate this to multi-photon excitation of the transmon qubit by the probe tone, which saturates the transmon qubit and hence the resonator is changing back to its bare transmission, cf. Eq. (3.30). The strongly driven read-out scheme is based on an arising bright state in this high power regime with high contrast in the resonator transmission when the qubit is excited [141]. So, as before, we first pulse the qubit via the antenna and then apply the probe tone, though this time with 5.875 GHz and a power of -32 dBm, corresponding to $8.4 \cdot 10^3$ photons. This allows us to record driven Rabi-oscillations with high radiation pressure as found in Fig. 6.15b). Again a Rabi fingerprint is observed, although due to a lower drive power (-15 dBm here) having a lower oscillation frequency. This can also be seen in the Fourier analysis in Fig. 6.15c),
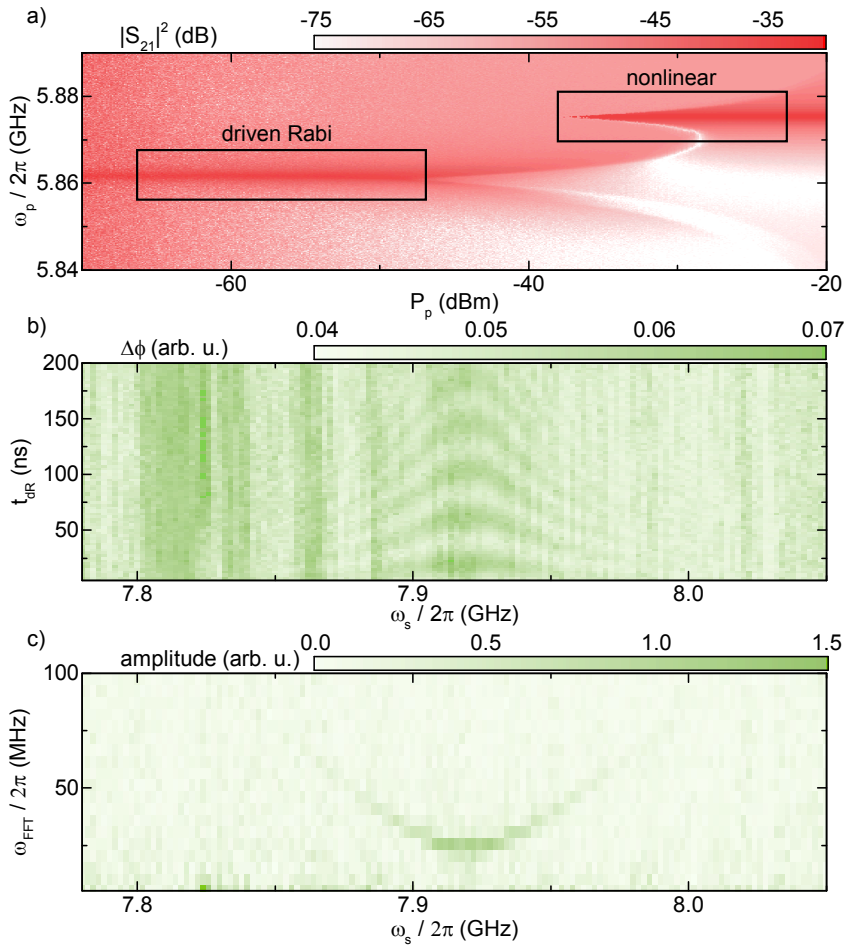
Figure 6.15: *Rabi oscillations applying a strong probe tone.* Panel a) reveals the qubit-resonator transmission behavior at the sweet spot of the transmon qubit for a varying probe tone power. At low probe tone powers the regular transmission of the resonator is found. At intermediate powers a bifurcation is observed and at the bare resonator frequency signal starts to be transmitted. When the probe power is increased beyond this bifurcation, signal is transmitted only on resonance to the bare microwave resonance. In panel b) the extracted Rabi-oscillations of the transmon qubit at the sweet spot are shown. In contrast to the previous results, here the resonator was probed with a power beyond the dispersive regime, on resonance to its bare eigenfrequency. This allowed to push the photon number by a factor of about 400. Frequency and time range is equivalent to Fig. 6.13. The Fourier analysis of the measurement is found in panel c). The parabola tuning of the ground mode's Rabi frequency is visible, while in contrast to the weak read-out, the higher harmonic is hardly observable.

where a parabola displays the expected Rabi frequency tuning. On resonance to the transmon qubit we find a decay time of $T_{\mathrm{Rabi}} = (183 \pm 46)\,\mathrm{ns}$. This is in good agreement to the extracted time of 175 ns we resolved using conventional techniques. We conclude that we are able to measure Rabi oscillations in the nonlinear regime using the described protocol. In principle, this method is not limited to a driven Rabi pulse sequence but can be transferred also to other sequences we will discuss in the next section. However we only recorded Rabi oscillations in this thesis, as a proof of principle. Nevertheless this is a technical realization for future experiments on nanomechanical hybrid devices
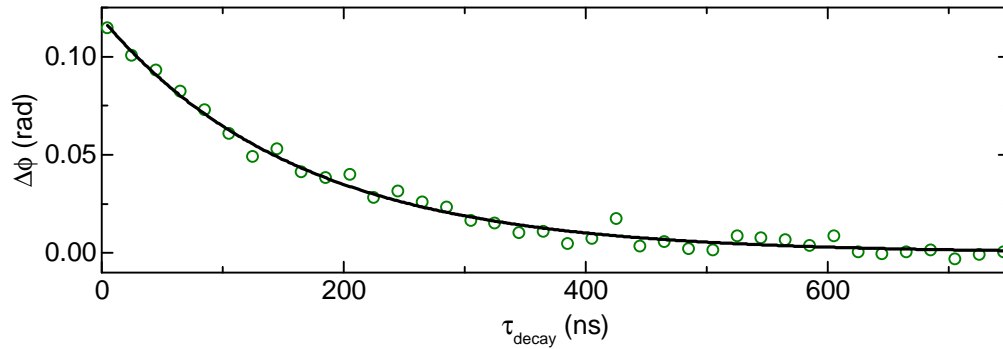
Figure 6.16: *Excitation decay at the sweet spot.* Phase change of the resonator, corresponding to
the transmon excitation (green) read-out after specific delay times. The transmon was excited
using a π−pulse determined from Rabi-experiments. Its excitations decays exponentially with
an energy decay time of 163 ns.

with an enhanced effective coupling by a factor of 17 in comparison to the dispersive regime.

The introduced Rabi frequencies allow us to extract the corresponding pulse length of
a π or $\pi/2$ pulse at a given power of the spectral tone. Combining these pulses in specific
sequences reveals further insight in the transmon qubit's decoherence, which we will show
in the following at the sweet spot of transmon qubit.

6.6.2   Decay measurements

To extract the energy decay of the qubit, along to the z-axis on the Bloch sphere, we apply
a π-pulse as determined by a previous driven Rabi experiment. Further, we measure the
dispersive shift of the resonator after a specific delay time τ_{decay}. This pulse sequence is
displayed in Fig. 5.8 as *Rabi decay*. The extracted phase change, equivalent to the energy
remaining of the transmon qubit at that time, is found in Fig. 6.16. We fit an exponential
decay of the following kind:

$$\Delta\phi(t) = \Delta\Phi_0 \exp\left(-\frac{t}{T_{\text{decay}}}\right). \tag{6.13}$$

Here the delay time τ_{decay} of the read-out pulse corresponds to the measurement time
t, further the phase shift amplitude $\Delta\Phi_0$ corresponds to a fully excited qubit state with
$P_{\text{e}} = 1$. From the fit we extract a shift amplitude of (0.120 ± 3) rad and a decay time of
$T_{\text{decay}} = (163 \pm 6)$ ns. This coincides to the previously determined decay times using Rabi
frequencies.
Including the Rabi experiments have now measured the energy decay rate using three
different methods. This was undertaken by measuring the qubit state along the z-axis of
the Bloch sphere, next we want to analyze the dephasing time, corresponding to a decay
along the equatorial plane.

6.6.3   Ramsey sequence

For an investigation of the dephasing time we now apply a $\pi/2$ pulse, sending the qubit
on the equatorial plane, corresponding to a superposition of excited and ground state. In

this setting the transmon is sensitive to dephasing processes. To analyze this dephasing we apply a second $\pi/2$ pulse after a certain delay time τ_{Ramsey}. This rotates the qubit to the z-axis. Without dephasing the final position of the qubit would be a pure excited state. The more the qubit has dephased during the delay time, the less the spin will align along the z-axis, and thus we can extract the dephasing time T_{Ramsey}. The read-out of its excitation is then performed as before, by recording the phase change of an on-resonance probe tone of the microwave resonator. The pulse sequence is discussed in Sec. 5.3.5 as *Ramsey*

The recorded phase shift is found in Fig. 6.17a), where the spectral frequency was set on-
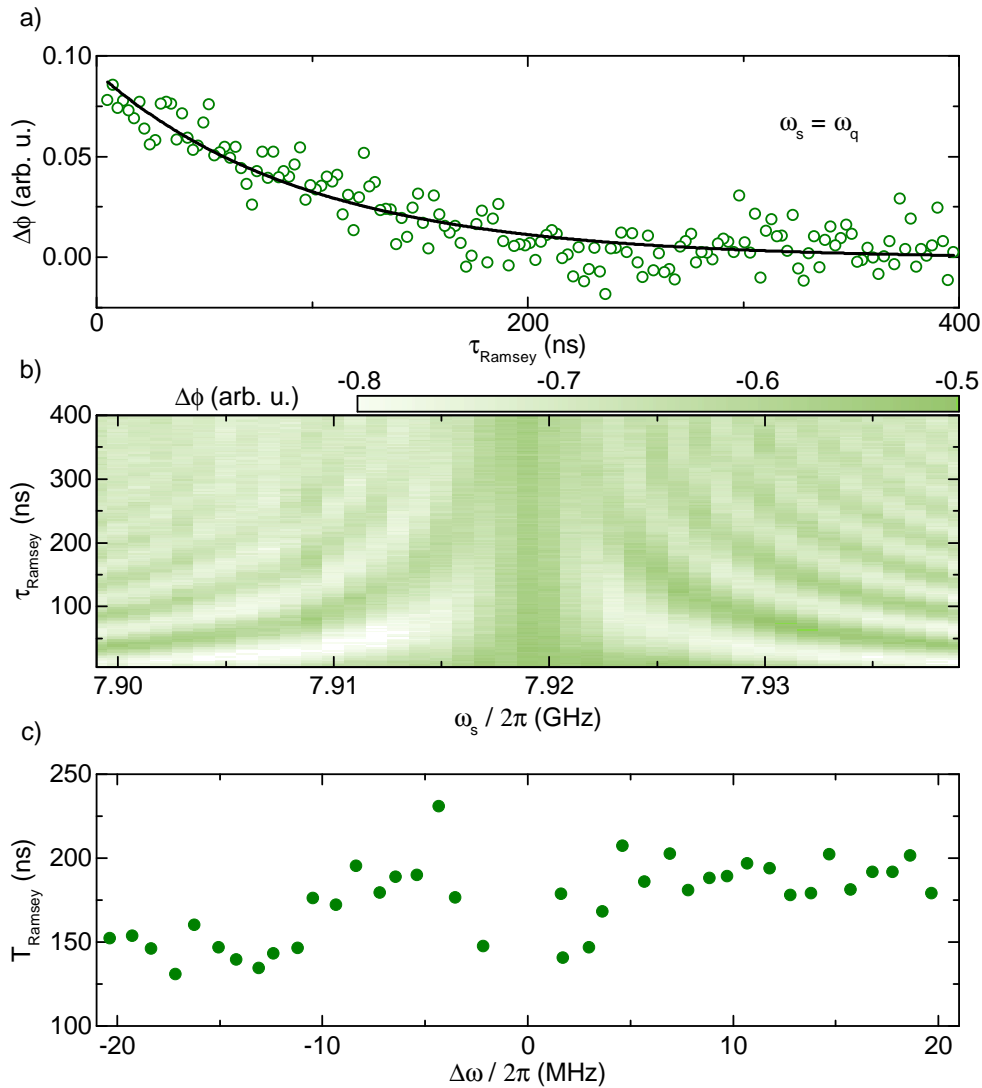
Figure 6.17: *Ramsey fringes at the transmon qubit sweet spot.* Panel a) displays the on-resonance dephasing of the transmon qubit, detected via a Ramsey sequence, in particular the phase change of the microwave resonator. Panel b) shows the phase response for a systematic sweep of the spectroscopy frequency and the read-out delay. Symmetrically to the transmon transition frequency at 7.918 GHz, oscillations of the phase start to appear, increasing in frequency with increasing detuning. In panel c) the extracted decay times arise by modeling the data shown in panel b). The T_2 time fluctuates around 175 ns, except on resonance.

resonance to the qubit ($\omega_{\text{s}} = \omega_{\text{q}}$). As expected the longer the delay time between the pulses,
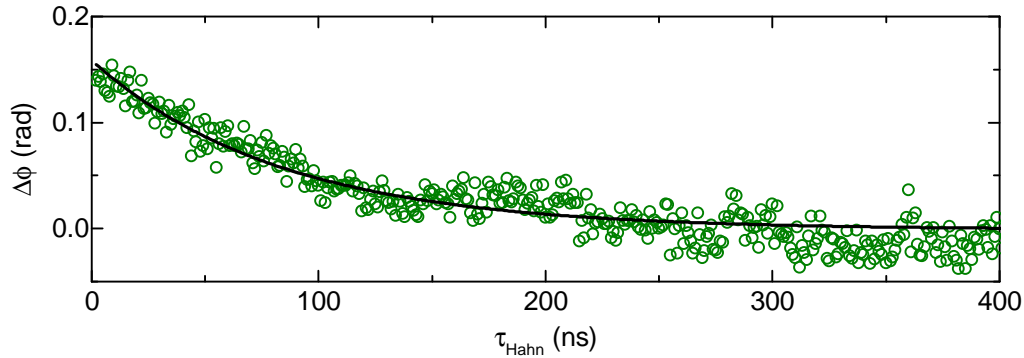
Figure 6.18: *Spin echo response of the transmon qubit.* Detected phase shift (green) plotted over Hahn-pulse time τ_{SE} at the sweet spot. An exponential decay is observed and analyzed (black solid line), revealing a Hahn decay time of 163 ns.

the less excitation is observed, following an exponential law. We extract the decay time by modelling Eq. (6.13) indicated by the black solid line. We note, that in this sequence T_{decay} corresponds to T_2, for which the fit yields $T_2 = (98 \pm 9)$ ns. We proceed by systematically sweeping the spectral frequency and display the measurement results in Fig. 6.17b). We find the so-called Ramsey fringes, decaying oscillations having a frequency $|\omega_{\mathrm{q}} - \omega_{\mathrm{s}}|$ and a decay time T_{Ramsey} which is equivalent to the T_2' time. Similar to Rabi-oscillations we fit Eq. (6.11) to the data. This allows to extract both: the frequency detuning and the Ramsey decay time. These we plot for detuned spectroscopy tones in Fig. 6.17c). When we average the off-resonant values a dephasing time of $T_2' = T_{\mathrm{Ramsey}} = (175 \pm 24)$ ns is found.

We have now measured the on- and off-resonant dephasing of the transmon qubit coupled to an electromechanical resonator. We found a shortened T_2 time on resonance, while off-resonant the T_2' time is round about the extracted value of the T_1 times. Both dephasing times show that the examined qubit seems to be limited by dephasing processes.

For a detailed analysis we next apply a Hahn-Echo sequence, which also allows to extract a T_2 time, but independent of $1/f$ noise as previously stated.

6.6.4   Hahn echo signature

In a spin- or Hahn-echo sequence the qubit is pulsed in the equatorial plane $(\pi/2)$, where the spin dephases for a certain time τ_{Hahn}. Then the spin is rotated by 180° applying a π pulse, which allows to refocus the spin. For a read-out, we apply a final $\pi/2$ pulse after $t = 2\tau_{\mathrm{SE}}$ rotating the spin on the z-axis to determine the remaining amount of excitations. This is achieved by probing the microwave resonator directly after the second $\pi/2$ pulse. We show the measured result in Fig. 6.18. Again, we fit an exponential decay to the data (black solid line) using Eq. (6.13). By this we extract $T_{\mathrm{decay}} = (83.6 \pm 3.1)$ ns. When interpreting this data one has to note, that τ_{Hahn} is only half the read-out time, as the delay time appears twice in the pulse scheme. So the Hahn decay time is double the extracted decay:

$$T_{\mathrm{Hahn}} = 2T_{\mathrm{decay}} = (167 \pm 6)\,\mathrm{ns}. \tag{6.14}$$

Method		t (ns)		Decay time
Continuous wave	T_{CW}	=	(53 ± 9)	T_2
Rabi sweet spot	T_{Rabi}	=	(175 ± 22)	T_1
Rabi finite field	T_{Rabi}	=	(113 ± 25)	T_1
Nonlinear Rabi	T_{Rabi}	=	(183 ± 46)	T_1
Energy decay	T_{decay}	=	(163 ± 6)	T_1
Ramsey decay	T_{decay}	=	(98 ± 9)	T_2
Ramsey off-resonant	T_{Ramsey}	=	(175 ± 24)	T_2'
Hahn-Echo	T_{Hahn}	=	(167 ± 6)	T_2'

Table 6.1: *Summary of collected decay times.*

This is in close proximity to the extract dephasing time via the off-resonant Ramsey sequence, but longer than on-resonance. This can be interpret in such a way that the Ramsey sequence is prone to $1/f$ noise, while the Hahn sequence due to the time reversing π-pulse sufficiently screens the spin from it. These observation indicate the presence of a dominant low frequency field noise.

6.6.5 Decoherence analysis

In the previous sections we have studied the coherence of a transmon qubit coupled to an electromechanical microwave resonator. We used a variety of measurements, continuous and pulsed, to extract the longitudinal and transversal dephasing of the qubit state. An overview of the determined decay times is given in Tab. 6.1. The most important result when comparing the decay times is the observation that we find $T_2 \approx T_1$. This indicates that actually the dephasing of the transmon qubit is the limiting factor. A closer look at the dephasing time via Ramsey and Hahn sequences revealed that the dominant noise stems from $1/f$ fluctuations. These can come from surface two-level systems, one can get rid by a proper chip cleaning [110]. Further reducing the transmon surface by changing from a finger type to a plate capacitor can enhance the coherence [143].

Dephasing happens when the transmon qubit frequency is changed, respectively the energy of the excited state. This is caused either by field noise shifting the working spot, or due to photon number fluctuations inducing ac-Stark shifts.
The influence of the magnetic field noise was found in the Rabi experiments. Even for a slight detuned transmon (140 MHz off the sweet spot), the coherence time was reduced by $1/3$. In addition, a dent in the Rabi fingerprint, leading to two parabolas in the Fourier spectrum disclosed a field noise on the order of 10^{-7} T. To screen these fields a superconducting shield was designed and fabricated out of aluminum, cf. App. C. For a further improvement the transmon frequency parabola can be flattened by lowering its maximum transition via a lower critical current as $\omega_{\mathrm{q}} = \sqrt{8E_{\mathrm{J}}E_{\mathrm{C}}}$ and $E_{\mathrm{J}} \propto I_{\mathrm{c}}$. One could argue,

that in addition also the charging energy can be reduced. This we do not recommend, since it actually could enhance the decay as discussed below:

The remaining source of decoherence is caused by photon fluctuations in the microwave cavity. The benefit of the transmon qubit is that by increasing the anharmonicity, equivalent to the charging energy, the ac-Stark shift is reduced [see Eq. (6.3)] [75]. For our system with a high anharmonicity ($E_J/E_C \approx 200$) a further increase will allow for the undesired excitation of higher modes, and lowering it enhances the ac-Stark induced dephasing. So we suggest to keep the charging energy of future chip generation within that range. Nevertheless we note, that this dephasing process becomes dominant in our experiments, as the measured decay of the continuous read-out, having a finite photon occupation, is the shortest decay time we find. Improvements addressing this limitation can be lower experimental temperature as they affect the thermal photon occupation, minimizing photon fluctuations. In addition, lower coupled transmon qubits, studied in [133], will have less induced dephasing.

6.7 Nanomechanical transmon qubit systems

With the presented work we demonstrate the unification of circuit QED and resonator electromechanics by coupling a transmon qubit and a nanomechanical string oscillator to one and the same microwave resonator.

To this end we introduced how the resonator photon number can be quantitatively compared using the ac-Stark shift as well as electromechanically induced absorption. Further we fabricated the hybrid device and analyzed it at cryogenic temperatures via microwave spectroscopy. In particular, we determine the transmon and string coupling strength of $g_q/2\pi = 134\,\mathrm{MHz}$ and $g_{m0}/2\pi = 0.3\,\mathrm{Hz}$ respectively. Further the microwave resonator decoherence was analyzed. These characterizations enable a calibration of the resonator occupation using the transmon qubit from 0.5 to 8 photons and obtain a loss coefficient of $x_{qb} = (4.08 \pm 0.26)\,\mathrm{s}^{-1}$ or via the nanostring from $1.4 \cdot 10^6$ to $1.4 \cdot 10^8$ photons leading to $x_{EMIA} = (5.41 \pm 0.25)\,\mathrm{s}^{-1}$. Despite the photon numbers being up to 9 orders of magnitude apart, the agreement in the loss coefficient is remarkably below 25%.

Further we investigated the transmon decoherence in the time domain. We found the qubit decoherence to be limited by dephasing processes, dominated by pink noise. To extend the lifetime of a quantum state in the transmon one can reduce the two-level surface fluctuators by a proper chip cleaning, reduce the magnetic field noise using a superconducting shield, and optimize the microchip design, in particular reducing the coupling strength, as well as the critical current in the dc-SQUID loop.

On the other hand, storing the quantum information in the mechanical resonator one can circumvent the limitations of the qubit decoherence. For this doubly clamped nanomechanical string oscillators are promising aspirants as their ultra high mechanical quality corresponds to a thermal coherence times of $38\,\mu\mathrm{s}$ for the examined sample. In this sense the presented work is an important step towards the information storage of quantum mechanical states using vibrational degrees of freedom.

Besides the design improvements for the interplay of a qubit coupled to electromechanical microwave resonator, the direct integration of a mechanical element capacitively coupled to a transmon qubit seems as a promising next step since it allows the generation of non-classical mechanical states [119]. Within this thesis a potential fabrication process was
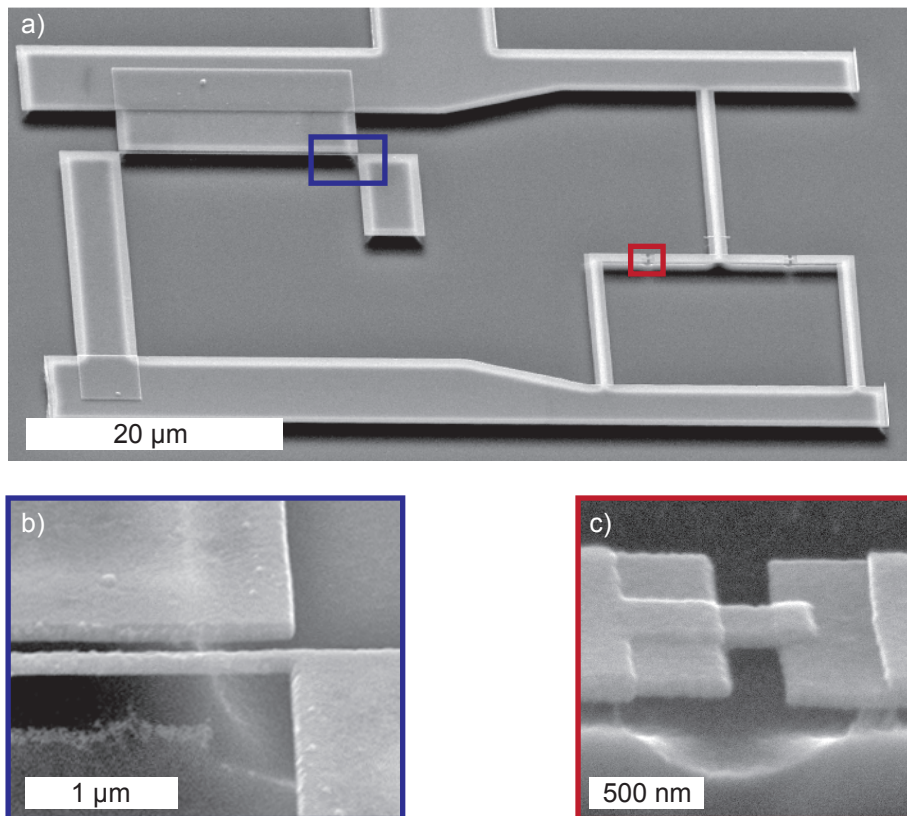
Figure 6.19: *Integration of a nanomechanical aluminum string oscillator in a transmon qubit.* Panel a) shows an overview image of the transmon qubit, consisting of two capactive plates, a superconducting loop containing two Josphson junctions. An additional capacitance is added to the circuit by placing a nanomechanical string in close proximity to an extension of one of the capacitor plates. In panel b) the successful release of the nanostring is shown at the right clamp [blue box in panel a)]. Panel c) shows the suspension of one of the Josephson junctions, due to the fabrication process.

developed in collaboration with Dr. N. Segercrantz. We have attached SEM images of such a system in Fig. 6.19. We find an overview image in panel a), recorded unter a tilded observation angle to show the successful release of the nanostring, which is also highlighted in the zoom image of panel b). Further panel c) shows an image of the transmon's Josephson junctions, that were also underetched in the fabrication process.

The design and fabrication process already included the suggested improvements within this thesis, observable e.g. on the reduced capacitor surface.

7

Inductive coupled cavity electromechanics

It's a real PhD killer!

Garry A. Steele, *private discussion during poster session of the FCQO conference*,
Klosterneuburg 2018

In this chapter we will derive the mechanism of a nanostring coupled inductively via a dc-SQUID to a microwave resonator, which allows for a high vacuum coupling rate exceeding previous realizations. We then introduce the fabrication process we invented for the realization of such samples, before we show spectroscopy data on the hybrid system. We start our experiments by having a detailed look on the individual parts, the microwave resonator and the nanostring. We will investigate their characteristic parameters and discuss the results, before we switch to measurements related to the electromechanical interaction. There, we discuss a measurement of the induced sidebands by the nanostring in thermal equilibrium to the cryogenic environment. By this we can calibrate the vacuum coupling strength exceeding previous publications. In addition, we analyze the displacement spectrum revealing the noise performance of the interaction, confirming the predicted imprecision limitation, cf. Sec. 4.2.2, and find a sub attonewton force sensitivity on the single photon level. Then we will have a closer look at the electromechanical coupling, especially the predicted linearity to the magnetic field and microwave resonator tuning. Further, we show how we can increase the effective coupling by driving the nanostring up to ten times the mechanical eigenfrequency, which allows us to measure the string's mode amplitude. At the end, we will give a short summary and discuss potential future experiments.

7.1   Coupling mechanism

The electromechanical coupling is derived similar to the general case in Sec. 4.1, cf. Fig. 4.1c). For the inductive coupling we use an electric resonator that has an eigenfrequency depending on the penetrating flux, see Fig. 7.1 for details on the modeling of the sample circuit. This flux depends on the applied external field and the SQUID loop area. This area can be split into a constant part, with the nanostring at rest, and the area modulated by the string's motion. The latter one changes the penetrating flux, and so the Josephson inductance of the hybrid circuit, which influences the eigenfrequency of
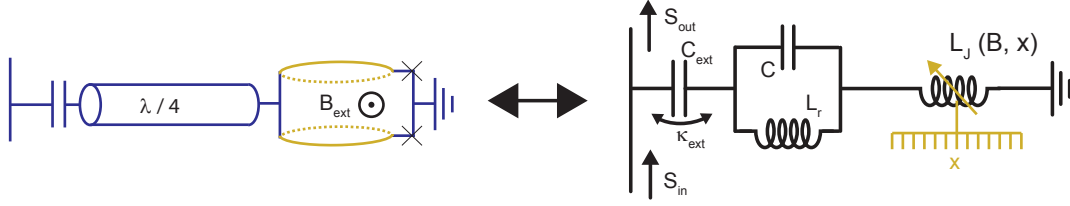
Figure 7.1: *Modelling the inductive coupling.* A $\lambda/4$ microwave resonator is shunted to ground by a dc-SQUID at its current anti-node. The dc-SQUID integrates two released nanomechanical oscillators (bright brown) influencing the SQUID loop area. By this the SQUID's working spot Φ/Φ_0 is modulated by the string, changing the microwave resonator's eigenfrequency. The circuit is modelled by the diagramm on the left: a LC circuit capacitively coupled to a feedline contains a mechanical tuneable inductance (bright brown)

the resonator. We describe the electromechanical resonator frequency $\omega_c(x)$ analogue to Eq. (4.1)

$$\omega_c(x) = \omega_c(\Phi_{ext}) + \partial_x\omega_c(x)|_{x=0} \; x(t). \tag{7.1}$$

We associate $\Phi(x = 0) = \Phi_{ext}$ and have linearized the induced flux by the mechanical element. This linearization is valid since the induced flux in comparison to the external flux is very small. In our samples the total squid length is comparable to the mechanical arm length and as the external field is assumed constant over the SQUID area, the flux contributions are proportional to the displacement of the nanostring, which is on the nanometer length, and the width of the dc-SQUID loop, some micrometer. So the induced flux change is about one permil of the external flux.

The mechanical induced frequency shift is given by

$$\partial_x\omega_c(x) = \frac{\partial\omega_c}{\partial\Phi}\frac{\partial\Phi}{\partial x} = \partial_\Phi\omega_c B_{ext}\gamma_s l, \tag{7.2}$$

consisting of the derivative of the microwave resonator frequency [cf. Eq. (3.22)] with respect to the flux penetrating the loop, the applied external field B_{ext}, as well as a string displacement of a length l and a correctional term α that takes care of the deviations of the mode shape by the doubly clamped strings from a sinusoidal oscillation. When plugging this result back in Eq. (7.1) we identify the electromechanical vacuum coupling strength via Eq. (4.4) to be

$$g_{m0} = \partial_\Phi\omega_c(\Phi_{ext})B_{ext}\gamma_s l x_{zpm}. \tag{7.3}$$

This is in agreement with the coupling determined by several proposals [35–38]. With the displacement of the system quantified by Eq. (4.3), the system is described via the full electromechanical Hamiltonian taking the shape

$$\hat{H} = \hbar\omega_c(\Phi_{ext})\left(\hat{a}^\dagger\hat{a} + \frac{1}{2}\right) + \hbar\Omega_m\left(\hat{b}^\dagger\hat{b} + \frac{1}{2}\right) + \hbar g_{m0}\hat{a}^\dagger\hat{a}\left(\hat{b}^\dagger + \hat{b}\right), \tag{7.4}$$

An important aspect of inductively coupling the electrical to mechanical mode is the potential high vacuum coupling strength, that we will discuss in the following. The coupling consists of five factors contributing equally to it. However, they are imposing limitations among each other and so it is not straightforward to determine the optimal realistic coupling parameters. We discuss aluminum realizations first and later give a short outlook on potential benefits and upcoming challenges for niobium based microchips.

We focused on the flux tuneable resonator to remain stable in the working spot, as this is a requirement for reliable and repeatable measurements. Otherwise random flux jumps occur during the measurements and the recorded data becomes useless.

The conflict for the stability is that the mechanical parts should be long and thin to achieve a high zero-point motion, as well as low decoherence. This requirement is in conflict with high critical currents enable steep frequency slopes and high photon numbers. In addition, the screening parameter β_L becomes large for high critical currents, which leads to a hysteretic behavior of the microwave frequency when tuned with the external flux, as discussed in Sec. 3.2. For the first sample generation, we conservatively went with a string width of 200 nm only.

Next we like to detail the individual factors determining the electromechanical coupling strength and estimate feasible values:

- The flux to frequency transfer function, also referred to as frequency slope, is defined by the microwave resonator design. Given the parameters stated in Sec. 3.3, we find a maximum slope around $10\,\text{GHz}/\Phi_0$ before the resonator becomes no longer observable. In previous studies on FTRs higher values of up to $60\,\text{GHz}/\Phi_0$ were realized [64]. However, one has to note that the steeper the slope becomes, the more sensitive to flux noise the microwave resonator becomes. As this broadens the resonator linewidth, the measured electromechanical signal is reduced. The decoherence of the microwave resonator is studied in Fig. 7.7b).

- The maximum value of the applied external field to the structure is either limited by the critical field of the superconducting material, or by its experimental generation, i.e. the heating effects of the applied current in the coil. We have determined the critical in-plane field of our fabricated circuits in separate experiments discussed in App. E and found microwave transmission through the flux tunable resonators up to 130 mT. In this thesis we employ an out-of-plane field created by a small coil which allows to control precise working points and a calibration of the external field via the dc-SQUID. Hereby, we can experimentally confirm Eq. (7.3) with respect to B_ext. Moreover, this allows for a careful analysis of the field frequency dependence of the microwave resonator and hence $\partial_\Phi \omega_\text{c}$. However in this configuration the accessible field was limited to around 0.5 mT by the dissipation of the coil current.

- A proper string annealing during the sample fabrication takes care of a high pre-stress. This stress results in a high mechanical quality and allows for a mode shape close to a sinus [144]. The shape factor α is then expected to be around $0.9 - 1$ [30].

- Although in principle, the string length can be set to any desired length, two limitations are worth considering. The resonance frequency of the string Ω_m scales with its inverse length l. For ground state cooling using sideband drives , it is required to be in the resolved sideband regime, that is $\Omega_\text{m} > \kappa$ [9]. This limits the string's length to around $70\,\mu\text{m}$ for a linewidth of 2 MHz, cf. Fig. 7.7a) and 7.11a). Improvements on the resonator decoherence can allow for longer strings. But another dominant restriction arises due to the high kinetic inductance imposed by such strings in the SQUID loop, leading to instability. To circumvent this we restricted the string length to $20\,\mu\text{m}$.

- The zero-point motion, derived by Eq. (2.15), depends on the inverse square root of the string's mass and its eigenfrequency. As the latter is set by the limit of the resolved sideband, see previous item, we can optimize the zero-point fluctuation by a low mass of the nanostring. Its mass is connected to the material density. Thus aluminum is a good choice due to its low value of $\rho_{\mathrm{Al}} = 2700\,\mathrm{kg/m^3}$, the ability to fabricate it in the required nanometer dimensions, the relative expansion coefficient with respect to silicon and last but not least its superconducting properties. The string length is compensated by the proportionality of the eigenfrequency in first order. To minimize the mass of the string by its dimension, we like to note, that the length is already set by the resolved sideband regime and so the tuning knob becomes the string's cross-section, which is in this case desired to be as small as possible. We note, that this is also of benefit for the mechanical quality factor [144]. The thickness is however determined by the fabrication process to 110 nm. As we have discussed in Sec. 3.2 a screening parameter of $\beta_{\mathrm{L}} = 0.05$ is desired, the design width is fixed to 200 nm. The corresponding zero-point motion then is 47 fm.

All in all, with the extracted parameters of $\partial_\Phi \omega_{\mathrm{c}} = 10\,\mathrm{GHz/\Phi_0}$, $= 0.5\,\mathrm{mT}$ $\alpha = 1$, $l = 20\,\mu\mathrm{m}$, and $x_{\mathrm{zpm}} = 47\,\mathrm{fm}$ we find an expected coupling of $g_{\mathrm{m0}}/2\pi = 2.35\,\mathrm{kHz}$ in the experimental realization discussed in this chapter. Assuming in contrast to the presented out-of-plane field bias an in plane field of 130 mT, the coupling g_{m0} can be boosted to 611 kHz, corresponding to 20% of the microwave resonator linewidth of $\approx 3\,\mathrm{MHz}$, cf. Fig. 7.7a). Given a string linewidth of $\Gamma_{\mathrm{m}}/2\pi = 25\,\mathrm{Hz}$, see Fig. 7.10a), we conclude a single photon-phonon cooperativity C_0 of:

$$C_0 = \frac{4g_{\mathrm{m0}}^2}{\kappa \Gamma_{\mathrm{m}}} = 19.9 \cdot 10^3 \tag{7.5}$$

being of reach. For further sample generations we see the single photon-phonon coupling therefore within reach, by increasing the string length carefully such that the microwave resonator remains stable, and improvements of the resonator's decoherence, e.g. by a proper surface cleaning.

As the critical field in niobium is ten times higher compared to aluminum [145], it can be beneficial to switch to an all-niobium realization of the sample design. This however requires the use of silicon nitride as a mechanical support material for the nanomechanical string, due to the low pre-stress in niobium [100]. Further, the fabrication of Josephson junctions based on niobium in the low μA range remains challenging [146].

7.2   Fabrication

In the following we will present and discuss the fabrication process we developed within this thesis. Further we will give a short summary on the final device parameters, however not discuss them in detail, as this will be done later, when these parameters are measured. The interaction of a nanomechanical string oscillator coupled via the nonlinear Josephson inductance of a flux tuneable microwave resonator is a challenging task as both the circuit QED elements as well as the nanostring have to be merged. This leads to compromises in both designs and the fabrication procedure. Nevertheless, we were able to develop the following recipe, which is how the sample investigated in this section was fabricated.

First we start with a commercial high resistive silicon waver, sliced in $10 \times 6 \, \text{mm}^2$, and clean its surface by rinsing it in a ultrasonic bath using acetone and isopropanol to remove the cover resist, and dry it in a nitrogen flow. By RIE ashing any remaining organic particles can be removed, which allows higher coherence times, however this was not done with the current sample. We will show later that even without this step an overdamped resonator can be created. Next, a double layer resist consisting of *Allresist AR-P 617.08* (PMMA 33%) and *Allresist AR-P 679.02* (PMMA 950 K) are spin coated with a top speed of 2000 rpm maximum. Typically, the top layer is spin coated with higher rotation speeds, which creates a very thin film with a high writing precision. However, in our case the lower coating speed allows for a thick and stable resist bridge that we require to create Josephson junctions on the order of $1 \, \mu\text{m}$ width, where a precision on a few nanometers is not the most critical step. We further prevent a collapse of the bridge by minimizing the influence of scattered electrons, to be precise by cutting out the ground plane about $25 \, \mu\text{m}$ around the SQUID. This technique developed during this thesis turned out to work very well also for other projects fabricating flux tunable resonator at the WMI facilities [147, 148]. The full sample design including a transmission line, the coplanar waveguides galvanically shunted to ground via mechanical dc-SQUIDS including the nanostrings is then patterned into the resist via a *NanoBeam Limited: nB5 Electron Beam Lithography System* using doses of $7.5 \, \text{C}/\mu\text{m}^2$. Then the resist is developed in *Allresist AR 600-56* and isopropanol cooled to four degrees Celsius. This cooled isopropanol allows for a well defined development of written and unwritten parts of the PMMA 33% especially in the area of the undercut, created by a ghost pattern. Next, the aluminum layers having a height of 40 and 70 nm are deposited using electron beam evaporated shadow-evaporation technique with an angle of ± 17 degrees. After the deposition of the first layer it is oxidized to create a non-conductive interlayer for the Josephson junctions for 120 min under a flow of 5 sccm and a valve position of 45%. After the evaporation of aluminum the remaining resist is removed by a lift-off process using 70°C hot aceton for 60 minutes, applying a turbulent flow with a pipette to assist. Afterwards the sample is annealed at 350°C for 30 minutes to increase the pre-stress in the nanostrings. Then the strings are released via reactive ion etching in two steps: first an anisotropic etch where the reactive ions are strongly accelerated towards the sample, which creates a deep etching pattern in the silicon. This is followed by a second step under high pressure and almost no acceleration voltage, resulting in a isotropically etch, releasing the strings.

We show images of the finalized sample in Fig. 7.2. The coplanar waveguide, found in panel a), has a conductor width of $10 \, \mu\text{m}$ and a gap width of of $8 \, \mu\text{m}$ to the ground plane resulting in a $56 \, \Omega$ impedance, matched to the 50Ω feed line. The bare eigenfrequency without the SQUIDs inductance corresponds to $\omega_0/2\pi = 7.7 \, \text{GHz}$, assuming an effective dielectric constant of $\epsilon_{\text{eff}} = 6.45$ [64]. Another important resonator parameter is its linewidth. It depends on its working spot, applied probe power and environmental temperature. We found the highest coherence at the sweet spot and about $B_{\text{ext}} = 0.5 \, \text{mT}$ applied perpendicular to the SQUID loop having intrinsic losses of $\kappa_{\text{int}}/2\pi = 1 \, \text{MHz}$ and an external coupling rate of $\kappa_{\text{ext}}/2\pi = 1.8 \, \text{MHz}$.

We show a scanning electron microscopic image of such a mechanical dc-SQUID in panel b). We find two released nanostrings. The length of the measured nanostrings later is $l = 20 \, \mu\text{m}$, the ones in the figure differ as the shown SQUID was not further investigated. The string's mechanical in- and out-of-plane modes show eigenfrequencies from
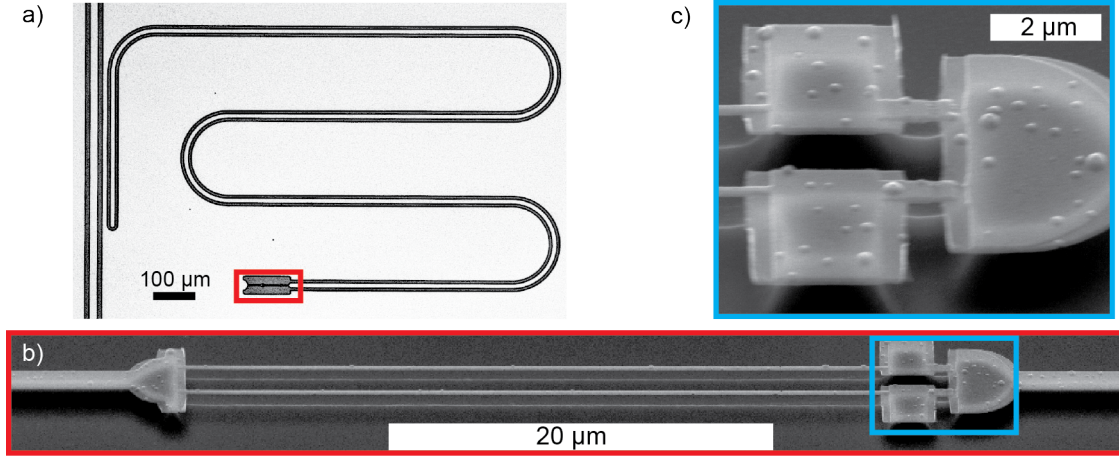
Figure 7.2: *Microscope images of the investigated sample generation.* Panel a) presents a microscopic image of a flux tunable microwave resonator, consisting of a coplanar waveguide and a dc-SQUID shunting the center conductor to ground. In addition the microwave feedline is shown on the left. In panel b) a tilted SEM image of the electromechanical SQUID is depicted, showing the successful suspension of the two nanomechanical strings. The corresponding Josephson junctions are shown in a zoom via panel c).

$\Omega_{\mathrm{m}}/2\pi = 5.7$ to $6.4\,\mathrm{MHz}$. The string's cross-section of $110\mathrm{x}200\,\mathrm{nm}^2$ corresponds to a mass of $1.2\,\mathrm{pg}$. Under the assumption of a highly stressed string, we find $m_{\mathrm{eff}} = m/2$ and a zero point motion of $47\,\mathrm{fm}$ for mode number 4 with an eigenfrequency of $6.343\,\mathrm{MHz}$, which we will mostly focus on. For a cryostat temperature of about $120\,\mathrm{mK}$ we find a mechanical linewidth of $\Gamma_{\mathrm{m}}/2\pi = 25\,\mathrm{Hz}$ for this mode, corresponding to a quality of $2.5\cdot 10^5$. Further the dc-SQUID loop contains two symmetric Josephson junctions with a design width of $0.5\,\mu\mathrm{m}$ and total area of $1.3\cdot 10^5\,\mathrm{nm}^2$ (per junction), see panel c). As further explained in the text, we extract a total critical current of $1.8\,\mu\mathrm{A}$ from the frequency shift of the microwave resonator from its bare eigenfrequency. This corresponds to a critical current density of $6.9\,\mu\mathrm{A}/\mu\mathrm{m}^2$, in accordance to previous findings [65]. The whole SQUID loop area is determined by its design to $44.6\mu\mathrm{m}^2$, so a field of $46.4\,\mu\mathrm{T}$ corresponds to a flux quantum ($\Phi_0 = 2.056\cdot 10^{-15}\,\mathrm{Tm}^2$ [53, 54]). We like to comment that in panel c) we finds blow-ups of the aluminum layer. We speculate these to stem from resist residues due to insufficient development and/or surface cleaning. When annealing the sample these residues expand underneath the film and cause these visible bubbles. We speculate that the dielectric resist remains might act as loss channels for the microwaves and thus cause an undesired linewidth broadening. For future generation we therefore recommend a RIE ashing of the sample before spin coating and a longer development time to avoid such blow-ups. However, the measured sample is in the resolved sideband regime, and the microwave resonator had an overcoupled regime accessible [cf. Fig. 7.7b)].

7.3 Setup including active mechanical excitation

For the investigation of the electromechanical device we employ the principle of a cryogenic microwave interferometer, as introduced in Sec. 5.2. Details on the configuration are sketched in Fig. 7.3a): a microwave source (MW) and a vector network analyzer (VNA) send a probe tone to the microchip, or (VNA only in this configuration) drive a piezo
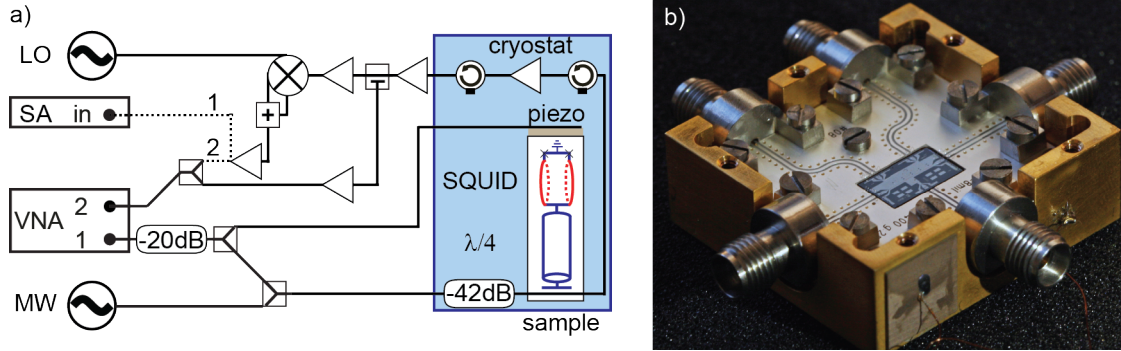
Figure 7.3: *Experimental arrangement of microwave wiring and cryogenics.* Panel a) reveals the full setup including several microwave drives and detectors at room temperature on the left, as well as the cryogenic structure of the experiment on the right. Panel b) shows the sample box including the piezo crystal and the mounted sample
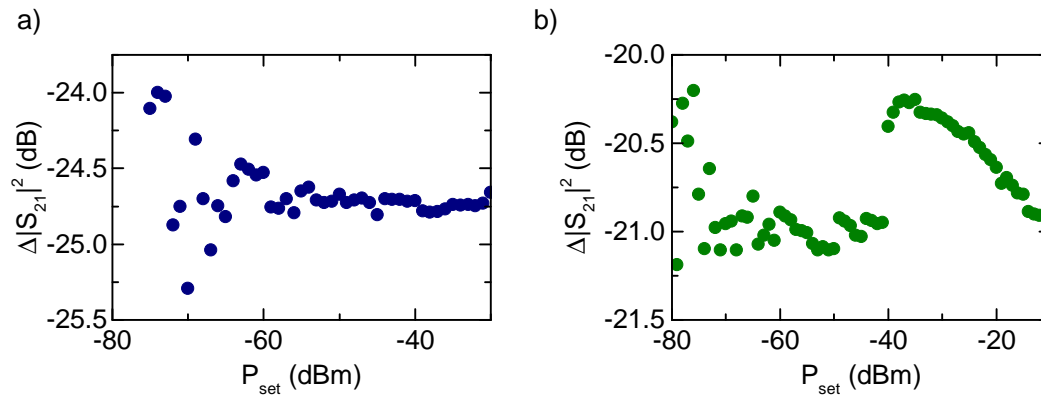
Figure 7.4: *Power calibration of the microwave pathes.* Both times we plot the difference in the detected power. In panel a) we show the probe tone calibration, measured at the position of the power combiner, see Fig. 7.3. We find an average deviation of about $-24\,$dB. Panel b) displays the drive power calibration, for the microwave signal send to drive the piezo actuator. Here we have rewired the setup such that the ZVA signal is directly send to the piezo, reducing the microwave deviation to about $-21\,$dB.

actuator mounted on the sample box, see Fig. 7.3b). The probe input line is attenuated by $-42\,$dB before it is capacitively coupled to the electromechanical resonator. On the outcoming path two circulators prevent thermal noise to enter the microwave circuit and a high electron mobility transistor (HEMT) amplifies the outcoming sample signal with a cryogenic background noise level. Outside the cryostat the signal is further amplified before it is divided in a directional coupler acting as a beam splitter. The majority (99%) is further amplified and homodyne downconverted in *Marki IQ 0307 LXP* IQ mixer using an additional microwave source (LO). Then the I and Q quadrature is added as described and discussed in Sec. 5.2.2 allowing a frequency independent detection of the phase modulations the mechanical oscillator adds on the probe tone. A final amplification is performed before the downconverted signal is detected either by the network analyzer or a spectral analyzer. The remaining 1% of the signal are further amplified and send directly to the VNA, which allows for a direct investigation of the microwave resonator transmission. The sample box was placed in a full aluminum capsule (cf. App. C) screening magnetic field noise. In our setup we use two different microwave sources: a network analyzer (*R&S*

ZVA-8A) with a $-20\,\mathrm{dB}$ attenuator directly after its output, and a microwave generator (*R&S SMF-100A*), see Fig. 7.3. For a comparison of the probe tone photons and the applied voltage of the piezo drive we therefor apply a power calibration similar to the one in Sec. 6.3.

In detail, we connect either the network analyzer path, including attenuator and a *Marki PD-02220*, to the input port of the ZVA and measure the detected power for a systematic sweep of the set power of the microwave device. We repeat the measurement with the SMF path, and subtract the detected powers in units of dBm $\Delta|S_{21}|^2 = P_{\mathrm{ZVA}}[\mathrm{dBm}] - P_{\mathrm{SMF}}[\mathrm{dBm}]$. The result is plotted in Fig. 7.4a). We find fluctuations for low set powers that decrease by higher powers. Altogether we find a calibration value of $\Delta|S_{21}|^2 = -(24.7 \pm 0.2)\,\mathrm{dB}$ indicating the additional losses by the attenuator ($-20\,\mathrm{dB}$), the power divider ($-3.5\,\mathrm{dB}$) and the remaining due to the microwave cables.

We note, that by this we have determined the transmission losses from the devices to the power divider where ZVA and SMF are combined. In this section, we will refer to the power $P_{\mathrm{p}} \equiv$ as the power at the microwave resonator. The power is determined taking a further attenuation of $-6\,\mathrm{dB}$ of power by the divider, the build in attenuators of $-42\,\mathrm{dB}$, and the microwave wiring which was calibrated to $-9.2\,\mathrm{dB}$ in Sec. 6.5.3, into account. For a determination of the photon numbers we further have to consider the resonator's linewidth, see Eq. (6.2). As it depends on the working spot and cryostat temperature, we will use $\kappa_{\mathrm{ext}}/2\pi = 2\,\mathrm{MHz}$ and $\kappa/2\pi = 3\,\mathrm{MHz}$ as determined for weak detunings from the sweet spot for rough estimations, while precise values are calculated from measuring the microwave resonator linewidth in-situ with the measurements.

A second calibration becomes necessary for experiments with a constantly driven string (Sec. 7.8). Here we rewire the setup such that the SMF source is switched to the power splitter (*Marki PD-02220*) and the ZVA to the divider (*Miteq PD2000/8000-S*), see Fig. A.1d) in the appendix. The remaining connectors are shunted by a $50\,\Omega$ resistor. We perform an analogue calibration and plot the transmission change in Fig. 7.4b). This time fluctuations for low power are also observed, however we find an additional peak of about $0.5\,\mathrm{dB}$ (or 1.12), stemming from the SMF RF output power. In total we find a calibration factor of $-(20.8 \pm 0.3)\,\mathrm{dB}$ in this configuration.

7.4 Flux tunable microwave resonators

In the following we will have a detailed look at the fabricated microwave resonator. We discuss the obtained frequency tuneability and compare it with the predictions given the design values. Further, we will investigate its decoherence in dependence of the environmental temperature, as well as the tuning slope. These insights help to fabricate a higher coherence in future samples. Furthermore, we will have a look at the nonlinearity induced by the Josephson junctions and quantify critical photon numbers for the investigation of the electromechanical interaction.

7.4.1 Frequency tuning

We start at a cryostat temperature of $81.2\,\mathrm{mK}$, probing a microwave signal of $P_{\mathrm{p}} = 0.26\,\mathrm{fW}$ at the microwave resonator corresponding to about 1.8 photons through the microwave setup, while sweeping a dc-bias current at an external coil. We find a periodic tuning
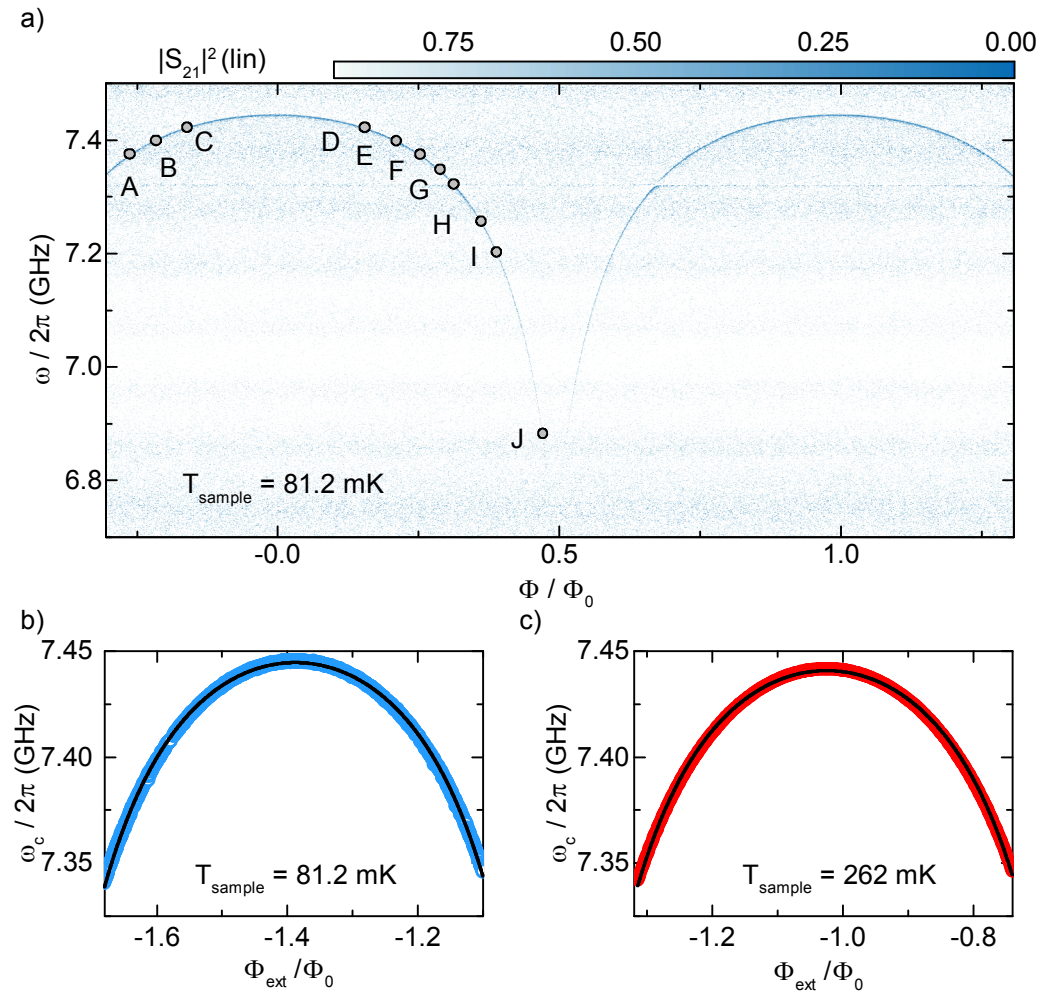
Figure 7.5: *Frequency tuning of the flux tunable resonator.* Panel a) displays the frequency tuning for low applied fields at 82 mK. In panel b) the extracted resonator eigenfrequency ω_c from panel a) is plotted around the maximum transition frequency. Panel c) shows the extracted resonance at higher temperature, to determine changes of the resonator parameters. For better comperability the last two plots are shown in flux values Φ_{ext}/Φ_0

with a spacing of (1.165 ± 0.005) mA. Knowing the SQUID loop area of $44.6\,\mu m^2$ we can determine the applied external magnetic field bias from the superconducting coil to (39.8 ± 0.2) mT/A.

Next, we determine the transmission of the microwave setup $S_{21,MW}$ by averaging over 200 traces with the microwave resonator tuned to a frequency outside the region of interest resonator not present. All transmission data presented is then calibrated in the sense that we compute $S_{21}(\Phi_{ext})/S_{21,MW}$ in the complex space. We plot the absolute value of this complex transmission parameter ($|S_{21}|^2$) in Fig. 7.5a) as function of the applied magnetic flux.

We find the microwave resonator periodically tuning from 6.7 GHz up to its sweet spot at 7.45 GHz. An external mode coupling to the microwave transmission is found at ≈ 7.3 GHz. Further we have noted eleven working spots, labeled with letters from A to J, which we will refer to in later experiments. From the frequency tuning behavior, we can determine that the fabricated junctions are symmetric and expect a screening parameter

T_{cryo}	81.2 mK	262 mK
$I_\Sigma\,(\mu\mathrm{A})$	1.792	1.774
$L_{\mathrm{Loop}}\,(\mathrm{pH})$	52.0	59.8
$\beta_{\mathrm{L}}(\%)$	4.5	5.1

Table 7.1: *Temperature dependence of the flux tunable resonator.*

$\beta_{\mathrm{L}} \ll 1$, (see Sec. 3.2).

For a quantitative analysis of the dc-SQUID shunting the microwave resonator we extract the eigenfrequency of it from panel a) and plot it for moderate flux detunings in panel b) (blue dots). We fit the data in accordance to Ref. [58], cf. Eq. (3.22), for low detunings only ($\Phi_{\mathrm{ext}}/\Phi \approx n \in \mathbb{N}$), assuming a bare resonator frequency of $\omega_0/2\pi = 7.654\,\mathrm{GHz}$, and a resonator inductance of $L_{\mathrm{c}} = 7\,\mathrm{nH}$, determined by the resonator design. With the critical current I_Σ and the SQUID loop inductance as remaining free fit parameter, we find the extracted values shown in Table 7.1 for the resonator tuning at 81.2 and 262 mK.

We find a total critical current of $1.79\,\mu\mathrm{A}$, with a vanishing influence of the environmental temperature. This result is in good agreement to the designed value of $1.6\,\mu\mathrm{A}$, and corresponds to a Josephson energy of $E_{\mathrm{J}}/h = I_\Sigma\Phi_0/(h\pi) = 1.78\,\mathrm{THz}$, within the typical range of such flux tunable resonators [58]. From the design, we would further expect a geometric inductance of 28 pH and 47 pH for the kinetic inductance for the SQUID loop. We see that the inductance is dominated by the kinetic one, which arises from the thin and long strings forming the loop. The total sum of 75 pH is 30 % higher than the extracted 52 pH. We suspect one main reason for a measured lower inductance is that the string's width ended up broader than designed. This leads to a decrease in the assertive kinetic inductance and so a lower inductance L_{Loop} is found. In addition, the temperature dependence of L_{Loop} as found in Tab. 7.1 is associated with an increased kinetic inductance, as the geometric inductance remains constant over T.

We like to commend on the loop design, that in order to avoid a hysteretic flux tuning, which would also reduce the accesible slopes $\partial_\Phi\omega_{\mathrm{c}}$, the screening parameter has to stay not only below, but well below one [58]. Calculating β_{L} via Eq. (3.13) from the fitted parameters we find the parameter indeed in the single digit percent range, indicating a sufficiently balanced SQUID design.

We proceed by a further analysis of the resonator tuning. For this we extract the frequencies of the resonator from Fig. 7.5a) up to $\Phi/\Phi_0 = 0.5$. We plot the result in Fig. 7.6a). Besides a gap attributed to the coupling mode of the sample at 7.3 GHz the tuning is fully extracted. From this we numerically compute the frequency slope $\partial_\Phi\omega = \partial\omega/(\partial\Phi)$. The benefit of this is to experimentally determine the slope, in contrast to a model fit to the data and derive the resulting frequency function. There, the question arises whether the applied model [cf. Eq. (3.22)] describes the resonator sufficiently well at working spots close to the singularity of the Josephson inductance (at $\Phi/\Phi_0 = 0.5$). This could lead to deviations from the experimental obtained values especially for high slopes, were we expect to reach the highest coupling strength. So, we remain closest to the experiment by the described method of directly measuring the slope.

a)

b)
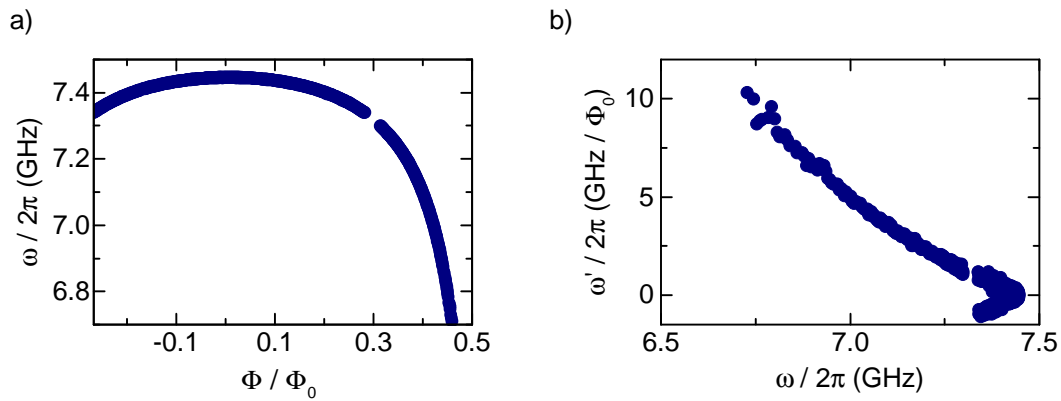
Figure 7.6: *Insights in the frequency tuneability.* Panel a) displays the extracted frequencies of the microwave resonator around a Φ_0 at $82\,\mathrm{mK}$. In panel b) the frequency slope $\partial_\Phi \omega_c \equiv \omega'$ is shown over the frequency setpoint, which is extracted from the frequencies in panel a). Up to $10\,\mathrm{GHz}\,/\,\Phi_0$ are found, decreasing with an increasing frequency until the sweet spot. After the slope is again increasing, however in negative direction then.

We show the extracted slope over the resonator working spot in Fig. 7.6b). We find tunings up to $10\,\mathrm{GHz}/\Phi_0$. As we have analyzed the resonator tuning on both sides of the sweet spot, we find a symmetric tuning. When we investigate characteristics related to the slope, we will extract it from this measurement in accordance to the working spot frequency.

7.4.2 Resonator linewidth

Next we will analyze the flux tunable resonator's decoherence. For this we bias the resonator to working spot J at $\omega_c/2\pi = 6.89\,\mathrm{GHz}$, corresponding to $\partial_\Phi \omega_c/2\pi = 6.6\,\mathrm{GHz}/\Phi_0$ and sweep a weak probe tone across it. We then fit the extracted transmission $|S_{21}|^2$ in accordance to Ref. [109], revealing the resonators internal (κ_{int}) and external linewidth (κ_{ext}). We start by examining the temperature dependency. For this we apply a probe tone of $P_{\mathrm{p}} = 0.26\,\mathrm{fW}$, equivalent to about two photons, and ramp the sample temperature from 120 to $300\,\mathrm{mK}$. We bias the dc-coil with a current higher than $10\,\mathrm{mA}$, corresponding to a field value of $B_{\mathrm{ext}} = 431\,\mathrm{mT}$. This high current heats up the sample environment such that the lowest examined temperature is around $120\,\mathrm{mK}$. In Fig. 7.7a) we show the determined internal (blue dots) and external (orange squares) linewidth behavior.

As the latter is only influenced by the coupling capacitance, and therefor determined by design, we expect it to be constant. Here, we find it to be nearly constant by $\kappa_{\mathrm{ext}}/2\pi = (865 \pm 111)\,\mathrm{kHz}$. However a slight increase for higher temperature is found. We attribute this to a fitting challenge: a Lorentzian with total linewidth is fitted, consisting of both external and internal contributions. When one of those becomes dominant, contributions from the other one have only minor effect. By this the external linewidth follows the internal one and appears larger.

A carefull analysis of superconducting microwave losses is found in Ref. [134]. Here, the total loss channel is systematically analyzed as a sum of individual channels with specific contributions. Temperature dependent loss channels are found to be two-level-scattering
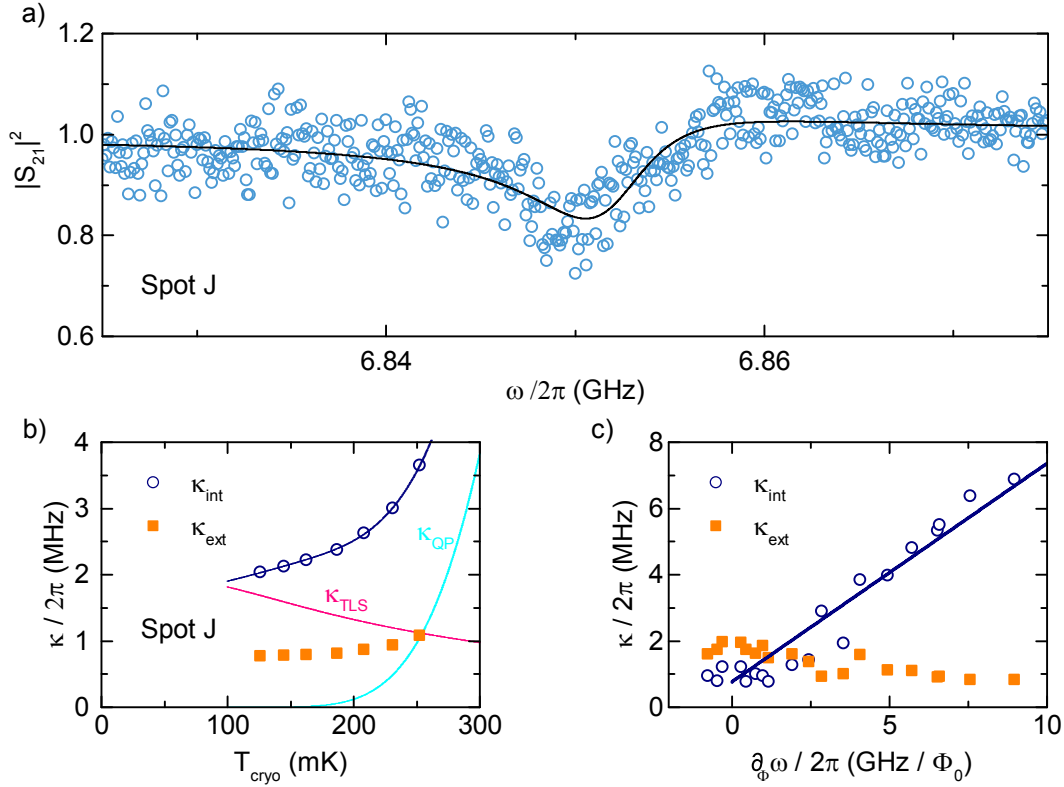
Figure 7.7: *Resonator decoherence at external magnetic fields of* $|B_{\text{ext}}| = 0.45\,mT$*.* Panel a) shows an example transmission (blue dots) on working spot J, including the fitted model of Ref. [109] (black solid line), being in good agreement with the measurement. Further panel b) displays the extracted internal (blue), and external (orange) linewidth over the cryostat temperature at a working spot of $\omega_{\text{c}}/2\pi = 6.89\,$GHz. We find a constant external linewidth, while the internal one, larger than the external, increases exponentially with the sample temperature. We model the internal losses (blue line) with contributions from quasiparticle (turquoise line) and two-level-fluctuators (pink line) and find a good agreement with the data. Panel c) plots the same parameters, this time for a fixed temperature of 125 mK, sweeping the working spot of the resonator. As expected, we find an increase in the internal linewidth when decreasing the frequency, since field fluctuations cause larger frequency shifts. The external linewidth has a much smaller variation, becoming smaller for lower resonator frequencies.

($\propto \tanh(1/x)$) and quasiparticle losses ($\propto e^T$). To model these decoherence channels we use the following temperature parameters for aluminum:

$$\xi = \frac{\hbar\omega_{\text{c}}}{2k_{\text{B}}T} = 0.165/T,$$
$$\zeta = \frac{\Delta_0}{k_{\text{B}}T} = 2.09/T. \tag{7.6}$$

Where we use a energy gap in aluminum of $\Delta_0 = 180\,$eV [145]. In this simple approach we assume that the linewidth is only influenced by losses due to quasi-particles and two-level fluctuator scattering as:

$$\kappa_{\text{int}} = A_{\text{qp}} \frac{e^{-\zeta}\sinh(\xi)\text{K}_0(\xi)}{1 - e^{-\zeta}\left(\sqrt{2\pi/\zeta} - 2e^{-\xi}I_0(\xi)\right)} + A_{\text{TLS}} \frac{\tanh(\xi)}{\sqrt{1 + B_{\text{TLS}}}}. \tag{7.7}$$

We have introduced the modified Bessel functions of first, and second kind K_0, I_0. When modeling this to the data we have the amplitude factors A_{qp} and A_{TLS} as well as the pa-

rameter B_{TLS} describing the saturation of the two-level-fluctuators by the applied power, as remaining free fit parameters. For the measured data, we obtain $A_{\text{qp}}/\omega_{\text{c}} = 1.2$, $A_{\text{TLS}}/\omega_{\text{c}} = 1.0 \cdot 10^{-3}$, and $B_{\text{TLS}} = 12$. We have added the contributions from two-level fluctuators (pink line) and quasiparticles (turquois line) as well as the total internal linewidth (blue line) in Fig. 7.7a). The amplitude parameters are divided by the resonators frequency as Ref. [134] fits the scattering parameter $\delta = 1/Q = \kappa/\omega_{\text{c}}$. Then we can interpret $A_{\text{qp}}/\omega_{\text{c}} = 2\gamma_{\text{qp}}/\pi$, where $\gamma_{\text{qp}} = 1.9$ for the extracted parameter, describes the ratio of kinetic to the total inductance of the cpw resonator. We speculate that the losses due to quasiparticles at the surface to become dominant, and as the Josephson inductance, a kinetic one, is not included in Ref. [134], γ_{qp} can exceed one.

The intrinsic quality factors, dominated by the two-level fluctuators, can be calculated from Eq. (7.7) by $Q_0 = \sqrt{1 + B_{\text{TLS}}}\omega_{\text{c}}/A_{\text{TLS}} = 3.6 \cdot 10^3$ or $\kappa_0/2\pi = 1.9\,\text{MHz}$. These arise from the fabrication process. Similar to Sec. 6.6.5 we suggest this can be improved by a proper surface treatment. For a detailed analysis of the factor $B_{\text{TLS}} = (P_{\text{r}}/P_{\text{c}})^{\beta/2}$ describing the power ratio of the circulating power in the resonator P_{r} and a characteristic power of the two-level fluctuators P_{c} and a geometrically defined parameter β, further experiments on the power dependence are required.

Another important aspect of the resonator's linewidth is its sensitivity to the working spot. We have seen that the electromechanical coupling is predicted to increase linearly with the frequency slope. However, a steeper slope will make the resonator more susceptible to field noise resulting in a broadening of the resonator linewidth. So we are interested how the linewidth of the resonator behaves as a function of the resonator frequency tuning ($\partial_\Phi \omega_{\text{c}}$). To determine this we record its transmission for several working spots at $125\,\text{mK}$. We obtain the slope of the working spot by Fig. 7.6b). Then we fit the resonance as introduced above, and plot the resulting external (orange) and internal (blue) linewidth in panel b) of Fig. 7.7.

Close to the sweet spot we find the resonator to be overcoupled ($\kappa_{\text{ext}} > \kappa_{\text{int}}$). Both relaxation rates appear constant. However when the frequency slope is increased by tuning the resonator further down in frequency, the external linewidth is slightly decreased from around $1.80\,\text{MHz}$, in agreement with Fig.7.7a), down to about $1\,\text{MHz}$. A similar behavior was found in [69]. The decrease can be partly explained as the external linewidth depends on the eigenfrequency of the resonator: $\propto \omega_{\text{c}}^2$. Since we shift the resonator from $7.45\,\text{GHz}$ down to $6.70\,\text{GHz}$, this explains a decrease from $1.80\,\text{MHz}$ down to $1.46\,\text{MHz}$.

For higher slope values the internal linewidth seems to increase linearly, and indeed a linear model (solid line) fits the data quite well. We obtain an intrinsic linewidth of $\kappa_{\text{int}0}/2\pi = (762 \pm 146)\,\text{kHz}$ and an increase of $(660 \pm 56)\,\text{kHz}\Phi_0/\text{GHz}$. From this we see that the quantum parameter '$g_{\text{m}0}/\kappa$' [9] is not increased when tuning the resonator down, as the linear effects cancel out. However the cooperativity $C = g_{\text{m}0}^2/(\kappa\Gamma_{\text{m}})$ can be enhanced by this. To overcome this restriction we suggest to enhance the coupling by an external in-plane field and biasing the working spot with a small coil, including a persistent current switch. This experimental setup has been developed in [149], cf. App. E.

In conclusion we like to note, that the resonator decoherence given our circuit is dependent on the cryostat temperature, the applied probe power, the working spot, and also the experimental history, in the sense that during a cooldown at some point flux vortexes can get trapped on the circuit which cause additional decoherence. This makes a comparison between individual measurement runs difficult. E.g. when comparing the two
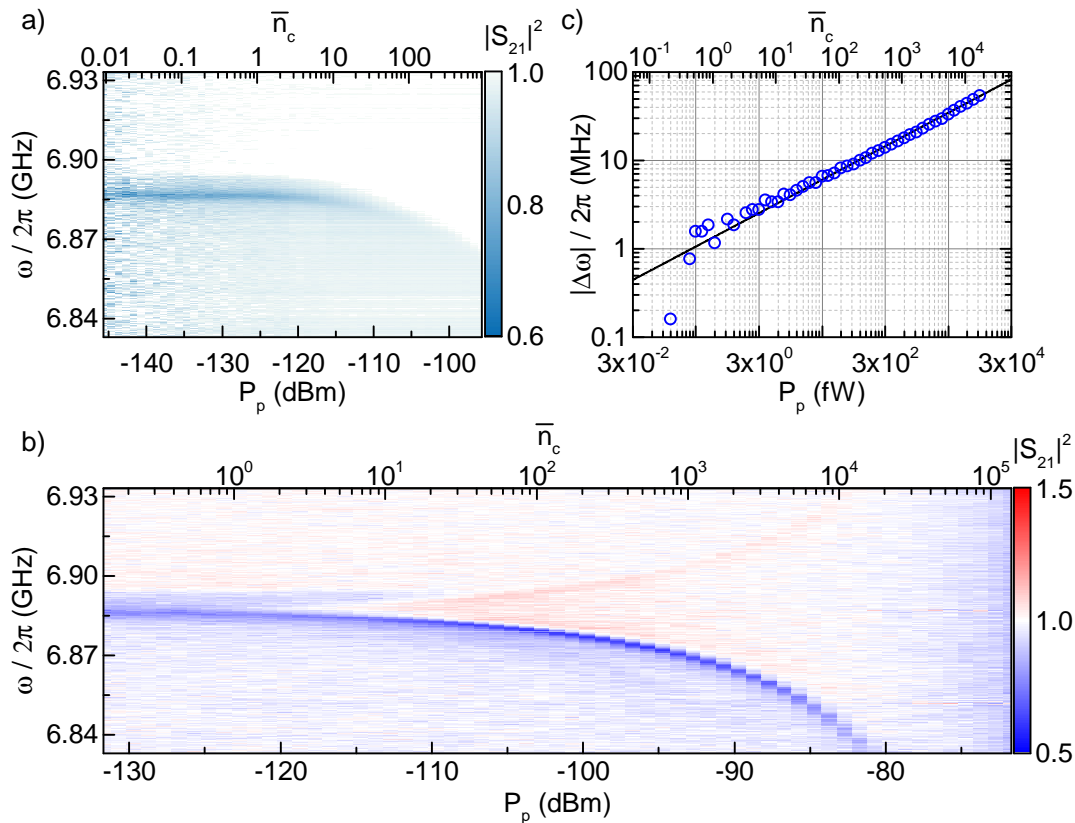
Figure 7.8: *Influence of the Josephson nonlinearity on the microwave resonator at working spot J.* Panel a) displays the transmission of a probe tone with a varying power from 0.01 photons up to 500. Below one photon a symmetric Lorentzian response is found. Above the frequency starts to shift downwards. In addition the Lorentzian peaks turns into a Duffing shape with a sharp cut-off at lower frequencies. In panel b) a second experiment we apply a constant excitation tone on resonance to the initial eigenfrequency and measure the resonator transmission via a weak probe tone. Again we find a downshift starting around 1 photon. In contrast, in this setup we find a splitting with a weak branch of enhanced transmission (red) symmetric to the downshift of the resonator (blue). In panel c) we plot the deviation from the original frequency as a function of the constant tone's power (blue dots). By fitting a linear model (black solid line), we reveal a functionality of $|\Delta\omega| \propto P_{\mathrm{appl}}^{1/3}$.

panels b) and c) in Fig. 7.7, we have to note that b) was measured at a slope of around $7\,\mathrm{GHz}/\Phi_0$, and panel c) at a temperature of 125 mK. We find some deviations in both external (0.8/1 MHz) and 2/5 MHz internal linewidth. We attribute this to flux being trapped within the measurements, which in particular increased the internal linewidth.

7.4.3   Nonlinear effects related to the Josephson inductance

By integrating a dc-SQUID in a coplanar waveguide resonator, we add a nonlinear element, in particular the Josephson inductance L_{J}. We showed that this can be modeled in a Duffing behavior, where the effect of the nonlinearity becomes higher the more excitations are in the resonator, cf. Sec. 2.3 and Sec. 3.3. However, in cavity electromechanics the weak radiation pressure coupling is typically enhanced by increasing the photon pressure

and so the coupling is effectively increased as $g_{\mathrm{eff}} = \sqrt{\bar{n}_{\mathrm{c}}}\, g_{\mathrm{m0}}$. By this technique strong electromechanical coupling, as well as ground state cooling, was reached by applying 10^4 photons [14, 15]. So the questions arise at what photon number the nonlinearity becomes relevant and whether we can influence this by design?

For an experimental check on this we set the tunable resonator to a frequency of 6.89 GHz (Spot J), at an external field of $B_{\mathrm{ext}} = 0.43\,\mathrm{mT}$ and a temperature of 125 mK. We then probe the transmission of the resonator, as a function of the probe power. We plot the result in Fig. 7.8a) over the calibrated applied power send to the cryostat. We further express the probe tone power in terms of a photon number (top axis) assuming a resonant excitation. We find a nonlinear response of the microwave resonator above 1 photon, as here the resonator's eigenfrequency starts to tune downwards. The shift to lower frequencies indicates a Duffing parameter $\alpha < 0$, for an harmonic oscillator based on a test mass connected to a spring, this would correspond to a spring constant that becomes softer with drive power [48]. As the nonlinearity originates from the Josephson junctions it can be adjusted by the applied flux ratio, hence the working spot. By this the critical photon number is increased the further we reach the resonator's sweet spot. This has already been studied in Refs. [64, 88], which revealed that the sign of the duffing parameter can even be switched when asymmetric Josephson junctions are placed in the SQUID (corresponding to a stiffer spring for high drive powers).

Here, we will focus on the particular working spot J and send a constant tone on resonance to the microwave resonator while probing the transmission with a weak ($\bar{n}_{\mathrm{c}} < 1$) tone. Then the constant tone's power sets the number of photons in the resonator and by systematically increasing it, we can examine the resonators response for a fixed photon number (in the previous measurement the probe tone setting the photon number had a detuning depending on the probe tone frequency, and so the excitation of the resonator was not constant). The measured spectrum is shown in panel b) of Fig. 7.8. In agreement to the previous measurement we find the resonator to detune starting around 1 photon. In contrast, the resonator appears not in a Duffing shape. Further we find a weak resonance mirroring the downshift having an increased transmission (above 1, red).

For a functional analysis we extract the transmission minimum of panel b) and plot its deviation from the original frequency $|\Delta\omega|$ over the applied power in Fig. 7.8c) (blue dots). By displaying it in a log-log scale we find a linear context. The proportionality of (0.378 ± 0.012) obtained from the fit to the data (black line) is in close proximity to a $P_{\mathrm{appl}}^{1/3}$ dependence of the splitting. We briefly like to comment on a second feature arising, a weak enhanced transmission tuning symmetrically to the downshift up in frequency, cf. Fig. 7.8b). Such features have been reported in strongly driven systems [150].

7.5 Mechanical characteristics of aluminum nanostrings at millikelvin temperatures

Similar to the previous section, we will now investigate the mechanical attributes of the fabricated microchip. We will briefly discuss the full spectrum of mechanical peaks and then focus on the highest mechanical mode. Its mechanical coherence and eigenfrequency tuning over temperature will be examined. As within this thesis a 20 μm long aluminum string is investigated, we compare our results to previous findings in literature, Refs.

a)

b)

c)
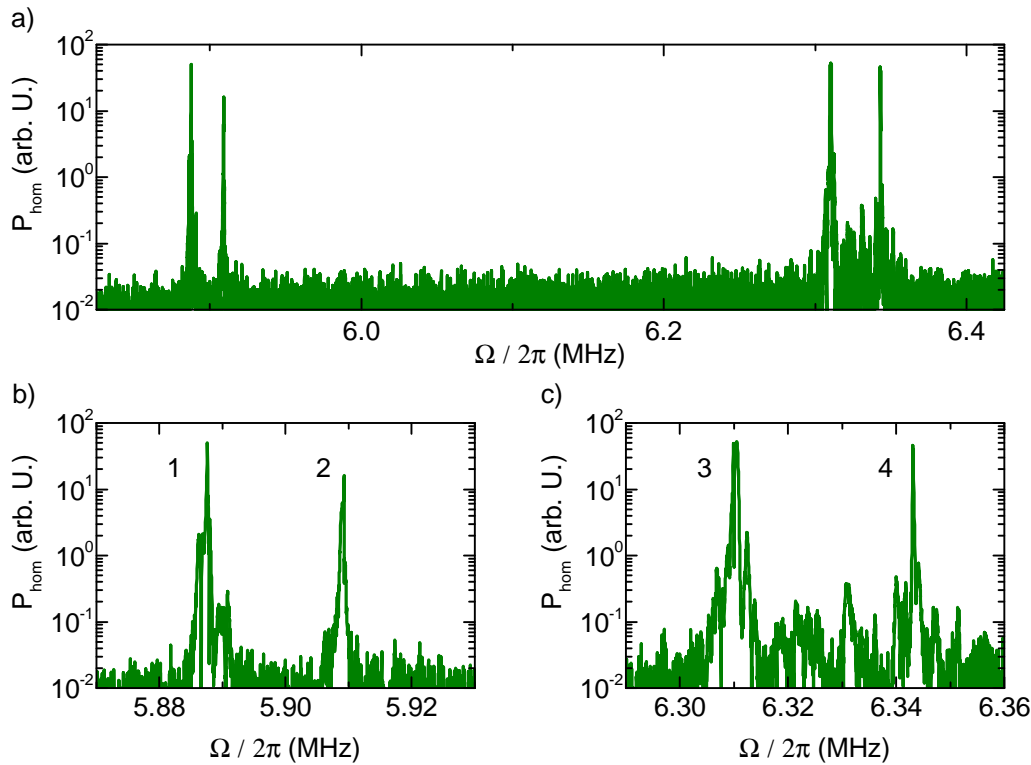
Figure 7.9: *Resonance response of the driven mechanical strings.* Panel a) reveals the overview
spectra of the two nanomechanical strings. Panel b) and c) show a zoom in the lower (higher)
frequency modes respectively. We find two pair of modes for the two nanostrings, we assign
to the in- and out-of-plane modes. Minor indications of other modes are found in between
them, as discussed in the text.

[43, 127, 139, 140]. Previously only strings up to $5\,\mu$m length were fully analyzed. So by
this we gain a detailed insight for design estimation on future samples. We conclude by
discussing some future applications and the optimal string designs for it.

7.5.1 Driven string response

The investigated sample consists of two nanostrings in the SQUID loop. For a single string
we expect an in- and one out-of-plane mode to have a dominant displacement from the
string's rest position. So by placing two of them in one resonator we expect to find four
modes: for an external field applied perpendicular to the sample plane we expect to ob-
serve two in-plane modes. The observation of out-of-plane modes should be suppressed,
nevertheless imperfections of the field alignment (i.e. an out-of-plane field component) will
allow their observation.

  We begin our experiments on the nanostring via the configuration of the cryogenic inter-
ferometer (cf. panel c. in Fig. A.1). and setting the microwave resonator at working spot
J, at a magnetic field bias of $B_{\mathrm{ext}} = -462\,\mu$T, and a sample temperature of $111\,$mK. We
apply a probe tone on the electromechanical resonator's eigenfrequency of $6.89\,$GHz, hav-
ing a power of $P_{\mathrm{p}} = 0.26\,$fW, or two probe photons. Then we sweep a drive tone around the
expected mechanical eigenfrequency via the piezo actuator and obtain the spectra shown
in Fig. 7.9.

As expected we find four dominant peaks at the spectrum at frequencies of $\Omega_{\mathrm{m}i}/2\pi = 5.888$, 5.909, 6.310, and 6.343 MHz. We like to note, that due to the detection configuration of a measurement bandwidth of 20 Hz, exceeding the mechanical linewidth, the detected power is neither proportional to the displacement, nor related to the coupling strength. To identify the out-of-plane and in-plane modes we like to comment, that in further experiments we have not found signals of the lower two modes when they were only thermally excited, so they must be weaker coupled than the higher frequency ones. By that, we identify the higher modes as in-plane modes coupling to the perpendicular applied external magnetic field. The lower modes, swinging in out-of-plane direction, couple to imperfections of the magnetic field, e.g. an awry mounted coil.

Next, we like to comment on the two strings and their possible mechanical coupling due to their shared clamping port as introduced in Ref. [151]. There, two silicon nitride strings of identical design length were coupled with each other by a shared support. The two non-metalized strings were having a frequency deviation of 8 kHz and a coupling of 830 Hz. In our case we use aluminum strings instead of silicon nitride so a direct comparison is challenging. Also our geometry deviates. However, we find a mode spacing of 21 and 33 kHz, which is slightly larger than for the non-metalized strings. From this we can set an upper boundary for the potential coupling, as the coupled strings will create an avoided crossing of twice the coupling frequency in case of strong coupling. So by the current spacing we can determine an upper boundary of 11 and 17 kHz if the strings are coupled but not higher. This upper boundary is much higher than the coupling determined by Ref. [151], and so can only be seen as a rough limit. As for the strong coupling regime the linewidth of the mechanical element, being on the order of 20 Hz, we suspect a clever design of the shared support can easily achieve the strong coupling regime, allowing a state transfer between the mechanical elements. However within this thesis we did not observe any indications of the strings being coupled.

In the approximation of a tensile stressed string, its eigenfrequency is determine by [43]

$$\frac{\Omega_{\mathrm{m}}}{2\pi} = \frac{1}{2l}\sqrt{\frac{\sigma}{\rho}} \cdot \frac{l\sqrt{S\sigma}}{l\sqrt{S\sigma} + 2\sqrt{E_{\mathrm{Y}}I_{\mathrm{m}}}}, \tag{7.8}$$

given a material density $\rho = \rho_{\mathrm{Al}} = 2700\,\mathrm{kg/m^3}$, the string cross section $S = t \times w = 110 \times 200\,\mathrm{nm^2}$, a mode inertia of $I_{\mathrm{m}}^{\mathrm{ip}} = w^3 t/12$ for the in-plane and $I_{\mathrm{m}}^{\mathrm{oop}} = wt^3/12$ for the out-of-plane motion. Further a pre-stress of σ and a Young modulus of E_{Y} depending on the aluminum film growth. To determine these two material parameters, we solve Eq. (7.8) with the parameters above for mode 2 as out-of-plane and mode 4 as in-plane mode. By this we can quantify the values of $\sigma = 0.13\,\mathrm{GPa}$ and $E_{\mathrm{Y}} = 75\,\mathrm{GPa}$, which is in good agreement with previous studies on aluminum nanostrings that have determined $\sigma = 0.15$ and $E_{\mathrm{Y}} = 70\,\mathrm{GPa}$ [140].

For a full insight in the complex structure of the nanostrings we suggest simulations using finite element techniques, as described in Ref. [43]. This could allow to study other modes like torsional ones as well, since we see indications of other excitations in Fig. 7.9b) at 5.891 and c) at 6.331 MHz. Though those modes were coupled so low a further investigation of them was not achievable within this thesis. So we focused in the following on mode 4 only.
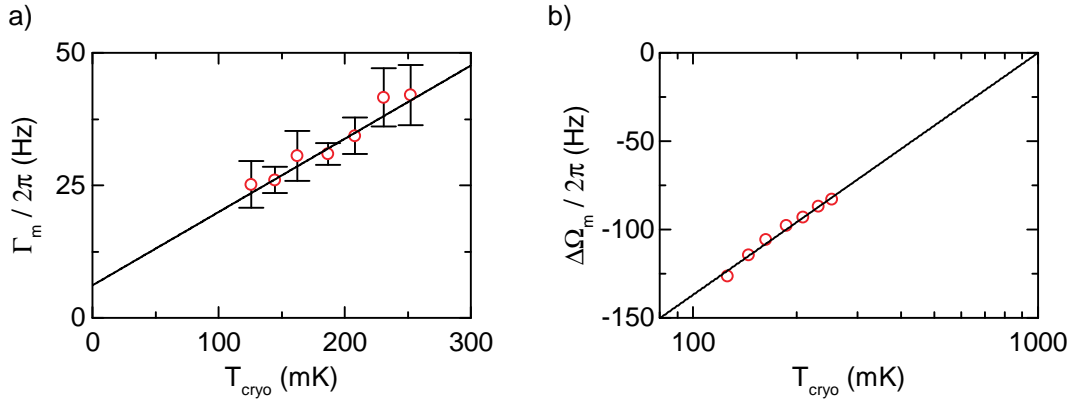
Figure 7.10: *Characterization of the nanomechanical string oscillator versus cryogenic temperature.* In panel a) the linewidth of the nanostring over the cryostat temperature, determined by thermal sideband spectroscopy is shown. A linear decrease is found, revealing an intrinsic linewidth of $\Gamma_0/2\pi = 6\,$Hz. Datapoints were averaged over the probe tone sweep, error bars indicate the standard deviation from the averaging. In panel b) the string's change in eigenfrequency is plotted, extrapolated to its frequency at $1\,$K (red dots). Deviations are less than the marker size. We find an increase when increasing the environmental temperature, as predicted by Eq. (7.9), which we model to the data (black solid line).

7.5.2 Temperature dependencies of a $20\,\mu$m long aluminum nanostring

Next, we examine the temperature dependencies of the pure aluminum string, in particular its linewidth and eigenfrequency. We do this by measuring the thermal motion, when the string is only coupled to the thermal bath of the environment and potential other driving forces that could distort the measurements are suppressed. This allows to study the mechanical attributes in the absence of thermal contractions as the corresponding coefficients have vanished in the millikelvin regime [152].

Figure 7.10a) shows the linewidth of the nanostring over the sample temperature, averaged over the applied probe tone power. The error bars indicate the standard deviation from the averaging. We find a linear behavior of the form $\Gamma_m(T) = \Gamma_0 + \gamma_m T$, where we refere to the intrinsic linewidth $\Gamma_0 = \Gamma_m(T_{\text{cryo}} = 0\,K)$, and a temperature damping coefficient γ_m. A linear model fit reveals $\Gamma_0/2\pi = (6 \pm 3)\,$Hz and $\gamma_m/2\pi = (138 \pm 17)\,$Hz/K. The intrinsic linewidth is in good agreement with the reported values from previous work at the WMI on pure aluminum nanostrings ($7\,$Hz [127], and $10\,$Hz [43]). For a comparison with the literature we determine a quality factor of $3.2 \cdot 10^5$ at $100\,$mK.

The linear increase in the linewidth over temperature was already confirmed in [43, 127, 139, 140]. It has been shown, that this linear behavior can be attributed to the dominant loss channel being the scattering of phonons to two-level-systems (TLS) [139]. In panel b) we have applied the same averaging over the probe tone power on the string's eigenfrequency. However there the error bars are less than the circle diameters.

In previous studies on short aluminum strings the frequency increase was modeled in analogy to sound waves in amorphous insulators (e.g. glasses) at the millikelvin regime [153]. Then the frequency is described by [139]

$$\Delta\Omega/\Omega_m = C \cdot \ln(T/T_0) \quad \text{where} \quad C = \nu_{\text{TLS}}\gamma_C^2/E, \tag{7.9}$$

in the low temperature range below $< 1\,\mathrm{K}$ [139]. Here, the constant C links the density of states of the TLS ν_{TLS} with the interaction constant γ_{C} and the Young's modulus E. This model was introduced to describe sound waves in amorphous insulators (e.g. glasses) in the millikelvin regime [153]. The interaction constant γ_{C} found to be, independent of the material, in the range of 10^{-3} to 10^{-4} [154, 155], which we will refer to as the universal amorphous regime.

For a solid analysis of Eq. (7.9) a measurement up to T_0 would be desirable. However with the microwave losses becoming dominated by exponentially increasing quasiparticle losses, our experimental data is limited to $250\,\mathrm{mK}$, cf. Fig. 7.7a). As the literature reports a clear limit of $1\,\mathrm{K}$ for such nanostrings [139], we take this as transition temperature T_0. Then by plotting the frequency shift over $\mathrm{Log}(T)$ extrapolated to T_0, we fit Eq. (7.9) (black solid line) and obtain $C = (9.38 \pm 0.06) \cdot 10^{-6}$, which is more than an order of magnitude below the universal amorphous regime. We note, that the slope extracted in Fig. 7.10b) describes $\Delta\Omega_{\mathrm{m}}$, while the constant C in Eq.(7.9) refers to $\Delta\Omega_{\mathrm{m}}/\Omega$.

We also like to note, that in previous work on capacitively coupled aluminum strings, frequency shifts as predicted by Eq. (7.9) were not observed [43]. It was speculated that electrostatic charge between the two capacities of string and ground plane could have prevented this. In our configuration, an inductively coupled system, where such electrostatic charge is not present, however the predicted tuning [cf. Eq. (7.9)] being observed, seems to confirm this speculation.

7.5.3 Collection of data on aluminum nanostrings

In the following we will discuss the collected data for the eigenfrequency, the quality factor Q_{m}, and their related temperature parameters, e.g. the temperature shift C, and the quality change γ_{m}. We will systematically compare our results with the published work on pure aluminum strings from Refs. [127]$\rightarrow$ 1, [43]$\rightarrow$ 2, [140]$\rightarrow$ 3, and [139]$\rightarrow$ 4. The present work is referred to as 5. As the samples were developed using similar but not identical processes and the nanostrings deviate within a factor of 2 in width, a precise analysis seems challenging. However we will see, that some context can be revealed already on the existing database.

Eigenfrequency We start our analysis with the mechanical eigenfrequency of the nanostrings Ω_{m}. The eigenfrequency is predicted in first approximation by $\Omega_{\mathrm{m}}/2\pi = v_{\mathrm{phase}}/2l$ [156] including the phase velocity $v_{\mathrm{phase}} = \sqrt{\sigma/\rho}$, described by the tensile stress σ, and the string's density, here $\rho = \rho_{\mathrm{Al}} = 2700\,\mathrm{kg/m^3}$. This statement however is only valid for highly tensile stressed strings. Lower stresses strings scale with l^{-2}. We show the reciprocal behavior in a log-log plot, see Fig. 7.11a). The datapoints from all publications are aligned on a allometric model with $\Omega_{\mathrm{m}}/2\pi = kl^{-b}$ (black solid line), for which we obtain $k = 9.6 \pm 5$, and $b = 1.26 \pm 0.03$. k^{-b} is slightly deviating from the expected linear behavior for highly tensile stressed strings (cf. Sec. 2.2). We attribute this to a lower pre-stress in the metalized aluminum string, in contrast to, e.g. highly pre-stressed silicon-nitride strings. For tensile stressed strings with simple support ends, one expects $b = 2$ [43]. So the observed $b = -1.26$ can be seen as a correction of the highly stressed model. To determine the tensile stress of the nanostring fabricated here, we however em-
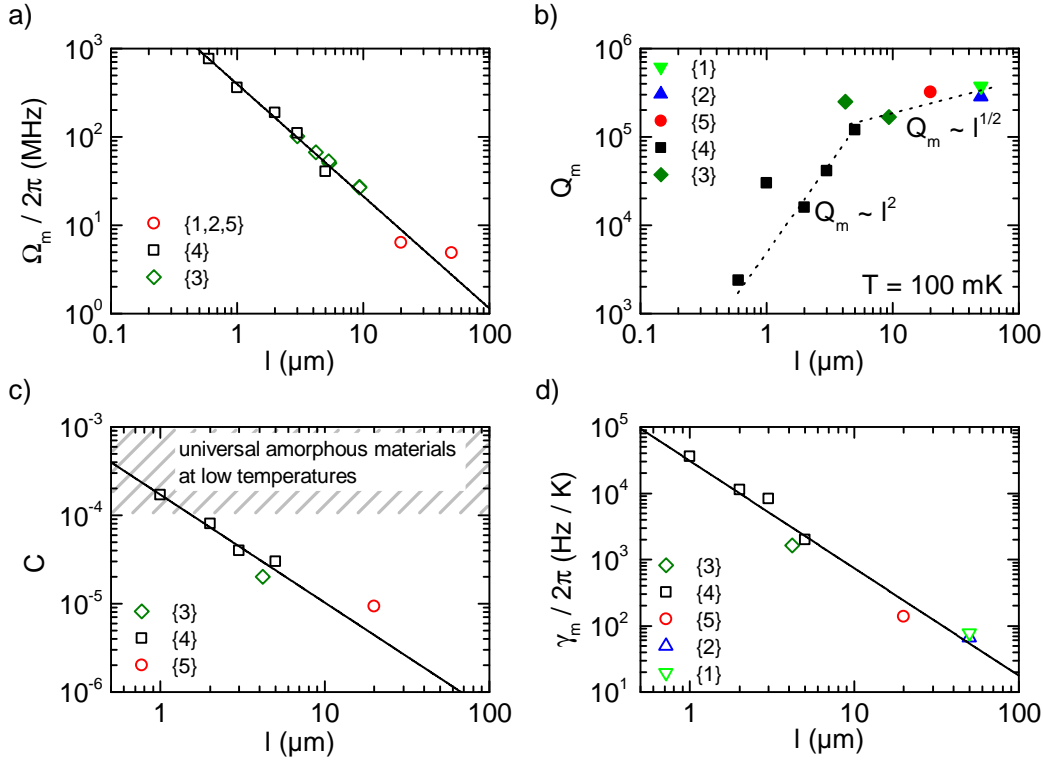
Figure 7.11: *Comparison of the extracted parameters with the literature.* In panel a) we explore the dependence of the mechanical eigenfrequency by the length of the nanostring. We find a reciprocal behavior (black solid line). Panel b) shows the mechanical quality factors at an environmental temperature of $100\,\mathrm{mK}$, for nanostrings from $1-50\,\mu\mathrm{m}$. Starting at small length, the quality factor is increased when its length is enlarged. However around $10\,\mu\mathrm{m}$ the quality grows slower. Panel c) displays the frequency shift of the strings. We find a decrease of the proportionality of 1.6 by a linear model to the log-log plot (black solid line), and by the comparable long length of our nanostring we determine a factor well below the universal regime for amorphous insulators. In panel d) we plot the temperature dependence γ_{m} of the nanostrings over length. In contrast to the quality factor saturating at a certain length, the dependence continuously shrinks for longer strings, indicating a lower increase of the linewidth when the environment is heated.

ploy the linear model from above, revealing a phase velocity of $250\,\mathrm{m/s}$. This corresponds to $\sigma_{\mathrm{Al}} = 175\,\mathrm{MPa} < \sigma_{\mathrm{SiN}} = 830\,\mathrm{MPa}$, calculated from the phase velocity. Nevertheless, this is sufficiently high for the assumption of pre-stressed strings, defined by [144]

$$\sigma = 175\,\mathrm{MPa} \gg \frac{\pi^2 E t^2}{12 l^2} = 0.5\,\mathrm{MPa}, \tag{7.10}$$

given the current string design, and using a Young modulus of $70\,\mathrm{GPa}$ [140].

Mechanical Quality   As the quality factors of the mechanical string are influenced by a multitude of parameters and processes [144], we will stick to a qualitative description for estimations on future sample designs. We determine the power laws of the quality dependency via a log-log plot and revealing two regimes, as indicated in Fig.7.11b):
(i) for short strings (0.6 to $5\,\mu\mathrm{m}$) a parabolic behavior is found. The quality factor is significantly rising when increasing the length. We attribute this to losses by the bending,

which lead to $Q_{\mathrm{m}} \propto (l/t)^2$ [157]. The longer the string becomes, the less the string is bended and so losses induced by lattice defects become less significant. When the string becomes longer we seem to enter a regime where this is no longer the dominating loss channel:

(ii) for longer strings ($l > 5\mu$m) the parabolic trend saturates and, given the current data, we find a square root behavior. However, the data is not clear, as this seems to be a transition regime. We note, that clamping losses, known to be a dominant factor in strings' decoherence, are described by a linear behavior, so when interpreting the current data, it seems that a transition from bending losses (l^2), to clamping losses (l), to intrinsic material losses due to the elastic strain (constant) is found. This would mean that simple, doubly clamped strings reach a limit of about $Q_{\mathrm{m}} \approx 10^6$, which can be overcome by soft clamping and/or strain engineering if required, as shown in Ref. [157] for silicon nitride beams.

Temperature shift   In the millikelvin regime we found the mechanical frequency shifting as predicted for amorphous insulators, indicating phonon scattering a dominant contribution. In previous studies the strength of the shift C was found to be in agreement with the statement, that 'remarkably, the value of C is known to be almost universal for all amorphous materials, $C \approx 10^{-3} - 10^{-4}$' [139, 154, 155]. This was determined for short strings up to $5\,\mu$m. Being motivated by storage applications in circuit-QED, nanomechanics at the WMI have focused on longer strings $50 - 60\,\mu$m, capacitively coupled to an electric resonator [43, 100]. There, however, this behavior was not observed, potentially due to thermally induced charge between the ground plane and center conductor [43]. Via the inductive coupling we are now able to observe a value exceeding the universal regime by more than an order of magnitude, as we have measured a string four times longer than previously reported. In figure 7.11c) we plot the literature findings as well as the determined shift (red dot) and obtain a power decline of

$$C = (17.1 \pm 0.7)l^{(-1.2\pm0.1)}. \tag{7.11}$$

By Eq. (7.9), we can directly relate this behavior to the scattering rate $\gamma_{\mathrm{C}} \propto l^{-0.6}$, as neither the density of the TLS nor the Young modulus is depending on the string's length. We see that we can design the strings either short, having a high temperature sensitivity, or as desired for storage application, long strings with a temperature stability exceeding the 'universal regime' for $l > 1.5\mu$m. This corresponds to an aspect ratio of $wt/L = 0.015$ for a typical cross-section of $wt = 150^2\,\mathrm{nm}^2$.

Temperature dependent quality factor   We have seen that the mechanical quality factor tends to saturate for long string lengths. While we were sweeping the sample temperature, we found a linear increase in the linewidth of the nanostring. When comparing the slope of this trend γ_{m}, we found a systematic decrease for shorter strings, as shown in Fig. 7.11d). A power law modeling revealed

$$\gamma_{\mathrm{m}} = (36.1 \pm 0.7) \cdot 10^3 l^{(-1.6\pm0.1)}. \tag{7.12}$$

We see that the temperature dependent loss scales with $l^{-3/2}$. For the dominant loss channels we discuss two contributions:

$\Omega_{\mathrm{m}}/2\pi$ (Hz)	$9.6 \cdot l^{-5/4}$
$Q_{\mathrm{m}}(T = 100\,\mathrm{mK})$	$4.8 \cdot 10^{15} \cdot l^2 \; l < 5\,\mu\mathrm{m}$
	$6.4 \cdot 10^7 \cdot l^{1/2} \; l > 10\,\mu\mathrm{m}$
C	$1.61 \cdot 10^{-10}/l$
γ_{m} (kHz/K)	$3.4 \cdot 10^{-5} l^{-3/2}$

Table 7.2: *Predicted aluminum string parameters for sample designs over string length.*

i) the scattering by electrons to TLS systems which can be identified via $\gamma_{\mathrm{m}}^e/2\pi = (\nu_e\gamma_e)^2 k_{\mathrm{B}}/\hbar = 10^{-2}$, for the typical found density times scattering product of $10^{-1}\mathrm{Hz/K}$. So the electron contributions are much smaller, as we have found $\gamma_{\mathrm{m}} = 10^5\mathrm{Hz/K}$.

ii) for short strings phonon scattering to TLS seems the dominant factor. As the nanostructures are smaller than the phonon wavelength $\lambda > 0.25\,\mu\mathrm{m}$, they can be treated one-dimensional [139]. The linear phonon spectrum leads to a constant density of states [145] and we relate [139, 158]

$$\hbar\Gamma_{\mathrm{m}}(T) = a_{\mathrm{Al}}^2/(wt)k_{\mathrm{B}}T, \tag{7.13}$$

where the lattice constant of aluminum at low temperatures is $a_{\mathrm{Al}} = 4.03\,\text{Å}$[159]. We determine $\gamma_{\mathrm{m}} = a_{\mathrm{Al}}^2 k_{\mathrm{B}}/(\hbar wt)$ and find a predicted value of $\gamma_{\mathrm{m}}/2\pi = 1.5 \cdot 10^5\mathrm{Hz/K}$ for cross-section of $wt = 150^2\,\mathrm{nm}^2$. As we see this is slightly higher than the reported values and as the length of the string is increased this discrepancy is increased as well.

We conclude from these observations, that the scattering is dominated by phonons to TLS systems. The origin of such systems are kinks or dislocations at the clamps, which are getting smaller the longer the string becomes, explaining the drop in the scattering value. The influence of electron scattering is negligible, as such kinks are smooth in soft materials like aluminum, and so the Peierls barrier is low [160] and their interaction with electrons reduced [161].

7.5.4 Predictions of design parameters

In the following we collect the extracted parameter dependencies from Sec. 7.5.3 and like to give a guideline for future sample designs. The collected parameters are found in Table 7.2. We like to discuss four potential applications and the respective optimized nanostring parameters:

Capacitively coupled nanostrings for electromechanical resonators   Due to the low electromechanical interaction in capacitively coupled electromechanical resonators (cf. Sec. 6) a long string length is desired, as it directly enhances the vacuum coupling strength g_{m0}. Further it allows for a high mechanical quality [cf. Fig. 7.11b)], and so long thermal coherence times [$\tau_{\mathrm{th}} = Q_{\mathrm{m}}\hbar/(k_{\mathrm{B}}T)$]. An upper boundary of the string length is set by the limitation of the resolved sideband regime ($\Omega_{\mathrm{m}}/\kappa$), which can be influenced by the external coupling κ_{ext}, and a proper fabrication process (κ_{int} small). A further point worth mentioning is the enhancement of the electromechanical coupling by the use of relatively thick strings, which form the coupling capacitor plates, but this has to be done carefully as it also influences the mechanical quality [144].

Cavity electromechanics using inductive coupling   Integrating the nanostring in the dc-SQUID loop of a microwave resonators sets high demands on the optimization of the string's parameter. To achieve high coupling, the flux tunable resonator requires a high critical current, without the screening parameter β_L becoming too large. However the screening parameter is dominated by the kinetic inductance of the SQUID, see Sec. 7.4.1, and so by the string's thin and long geometry. For our device geometry the layer thickness was fixed to 110 nm. To achieve a suitable β_L, we broadened the string to a width of 200 nm and designed the length to 20 μm. This geometrical setting allows for a decent mechanical quality, while keeping Ω_m in the resolved sideband limit, even for working points with large $\partial_\Phi \omega_c$ [cf. Fig. 7.7b)]. A moderate single junction critical current of $I_c = 0.9\,\mu$A guarantees that the flux tuning remains non-hysterical and that large frequency slopes of $10\,\text{GHz}/\Phi_0$ are accessible.

Integrated nanostrings in superconducting qubits   The capacitive coupling of a nanostring to a qubit allows for the generation of non-classical states [119]. In this proposal, one design criteria is that the mechanical resonance frequency is of the size of the anticrossing $\Omega_m \approx 2g_q$. A long string (causing small Ω_m) therefor reduces the accessible transmon coupling, and the transmon signal can become overlapped from noise contributions, or even no longer strongly coupled. So here, a string length of around 10 μm seems preferable in accordance to the data in Tab. 7.2. It allows for moderate quality factor and a maximum transmon coupling being around 11 MHz. Time resolved transmon spectroscopy has already been shown for such coupling rates and an internal resonator linewidth of up to 1 MHz [22].

High precision temperature sensing   Another application of such nanostrings arises from their temperature sensitivity of their resonance frequency $\Omega_m(T)$ in the millikelvin regime, expressed by the parameter C. This parameter is largest for short strings, cf. Tab. 7.2. In the following we will compare a string published in Ref. [139] having dimensions of $l = 1\mu$m, $w = 0.06\,\mu$m, and $t = 0.1\,\mu$m, to derive its temperature sensitivity δT_Ω, and compare it to the sensitivity using a resistive state-of-the-art read-out δT_R. From the temperature dependence of the string [cf. Eq. (7.9)] follows a sensitivity of

$$\delta T_\Omega = \frac{T}{C}\frac{\delta\Omega_m(T)}{\Omega_m(T)}. \tag{7.14}$$

As the strings frequency shifts with $\Delta\Omega \propto C$ the relative change is rather low. So the strings total frequency is assumed to be constant in the following $\Omega_m(T)/2\pi = (\Omega_m + \Delta\Omega(T))/2\pi = 360\,$MHz, the error of this approximation is highest at 1 mK and there around 0.1%. However the high mechanical quality factor of the nanostring allows for a very precise measurement of the resonance frequency shift. The frequency resolution is determined by half a linewidth, so $\delta\Omega_m(T) = \Gamma_m(T)/2$. The linewidth increases linear with the temperature, so from the parameters of Ref. [139] we extract:

$$\Gamma_m(T)/2\pi = (\gamma T + \Gamma_0)/2\pi = 36\,\text{kHz/K} \cdot T + 8.4\,\text{kHz}. \tag{7.15}$$

By this we have collected all parameters necessary to quantify Eq. (7.14).
Next, we determine the temperature resolution of a resistive read-out of the sample's
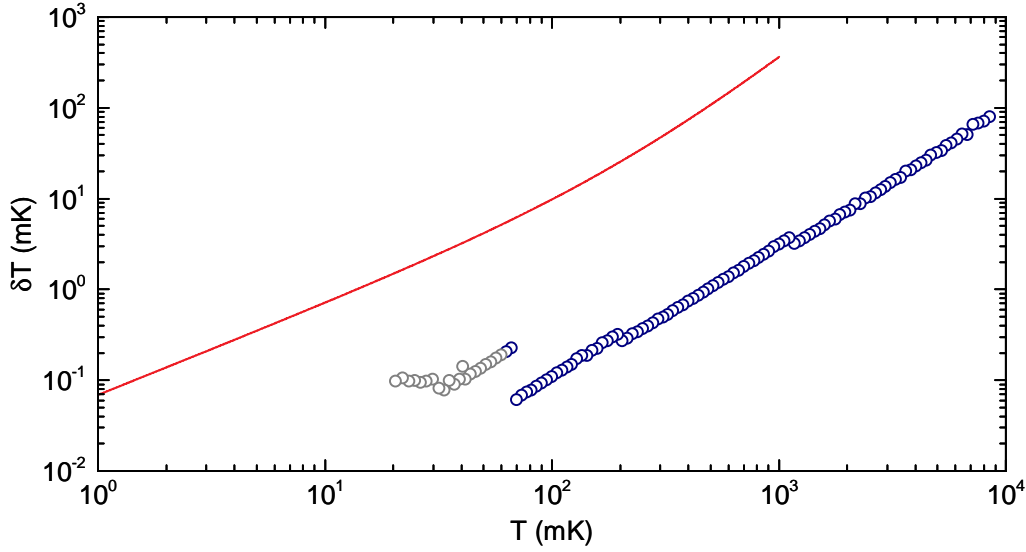
Figure 7.12: *Temperature sensitivity of an on-chip nanostring vs. a resistive read-out.* Start-
ing from measurements at 10 K the resistance sensitivity (blue) decreases until it reaches a
minimum around 20 mK given the current read-out parameters. As the resistance grows expo-
nentially, the read-out steps of the resistance bridge appear closer the cooler the temperature.
The grey dots are deviations of the calibration from the theoretical resistance. These and the
switching of the bridge seem to limit the sensitivity to around 10^{-1} mK. The strings resolution
(red line) can only be read-out below $1K$. Over the full frequency range it remains about an
order of magnitude higher than the resistive read-out, however it does not saturate at lower
temperatures.

temperature sensor (*ldd0*) using a commercial *Lakeshore 372* resistance bridge. Similar to
the string we obtain the temperature precision via

$$\delta T_{\mathrm{R}} = \delta R \left(\frac{\partial R}{\partial T} \right)^{-1}. \tag{7.16}$$

The first term is a step wise function determined by the resistance bridge precision. It
depends on the sensing range of the measurement and the applied excitation voltage,
which is in our case $6.32\,\mu$V. The steps are found in Ref. [162] and have to be adjusted with
the sensor resistivity. The second term is determined from the calibration measurement,
as it directly allows to determine the slope of the resistance curve ($\partial R / \partial T$). We derive
both parameters in App. D in detail. Then Eq. (7.16) is quantified and we can compare
the measurement precision of both methods, as shown in Fig. 7.19.

We find the resistive read-out reaching from 10 K to 20 mK (shown in blue). Three
challenges in the resistive read-out are observable here: i) the switching of the resistance
bridge, striking especially around 70 mK as the resistance resolution has to be adapted
to the total resistance of the sensor. ii) deviations in the calibration from the ideal
resistance tuning (indicated in grey) lead to a saturation of the read-out precision. iii)
the calibration and so the read-out range is only accessible within the calibration range,
here down to 20 mK.

The introduced read-out principle of the nanostring can only be applied below a critical
temperature of 1 K, when the eigenfrequency obeys Eq. (7.9). The total precision remains
an order of magnitude higher than the resistive read-out over the full temperature range.

As the string's eigenfrequency tuning can be derived from Eq. (7.9) a sensing over the full temperature range becomes feasible. A further benefit of a mechanical read-out is that the sensor - the nanostring - is placed directly at the microchip, hence the sample. An additional sensor, thermally well anchored to the sample is not necessary.

However by now, given the current data, a resistive read-out remains more precise. For a read-out via the eigenfrequency of a nano-oscillator, the string's parameter have to be further optimized.

To conclude, in this section we have given a prediction on the design parameters for all aluminum nanostrings in devices operated in the millikelvin range. Further, we have had a detailed look in four potential application, capacitively and inductively coupled electromechanical resonators, as well as capacitively coupled mechanical transmon qubits and an on-chip temperature read-out. However we like to note, that the database of this analysis stems from the reported literature [43, 127, 139, 140] as well as this thesis and has not been determined in a systematical parameter study using a constant fabrication procedure, nor identical string geometries. So the collected parameters in Tab. 7.2 should be seen as a rough estimation only, when designing future samples.

7.6 Thermal motion analysis on the blue sideband

In this section we measure the displacement noise of the thermal motion of the nanostring. This measurement allows to determine the single photon-phonon coupling rate g_{m0}. We will focus on mode 4.

7.6.1 Experimental configuration

For the determination of g_{m0} and the measurement of the thermal displacement noise $S_{xx}(\Omega)$ we configure the device to operate at the bias point J (cf. Fig. 7.5) and an out-of-plane magnetic field of $B_{ext} = -471\,\mu T$. As we discuss in more detail during this section, we will operate the device on the blue sideband regime to obtain the thermal spectra with highest signal to noise ratio. We will furthermore use a temperature dependent measurement of the mechanical sideband, calibrated by a modulation tone, to determine the electromechanical coupling [13, 106], for which we find a record value of $g_{m0}/2\pi = 1.6\,\mathrm{kHz}$.

In particular we employ the method derived in Ref. [106] using a homodyne detection of the phase modulation induced by the mechanical element. These are then compared to an additionally inserted phase modulation with a frequency close to the mechanical element. This allows to transform the detected voltage fluctuations S_{UU} to frequency fluctuations $S_{\omega\omega}$, which are linked to the thermal displacement motion S_{xx} via the electromechanical coupling ($S_{\omega\omega} = g_{m0}^2/x_{zpm}^2 S_{xx}$). As the mechanical occupation in thermal equilibrium is known, the electromechanical coupling is determined. By this the measured mechanical displacement spectrum is quantified, as well as the corresponding electromechanical noise contributions (cf. Sec. 4.2). So, the full performance of the electromechanical system is characterized.

We like to note, that the mentioned method was developed in the optical domain, using a phase modulation on both arms of the interferometer, a beam splitter, and an intensity
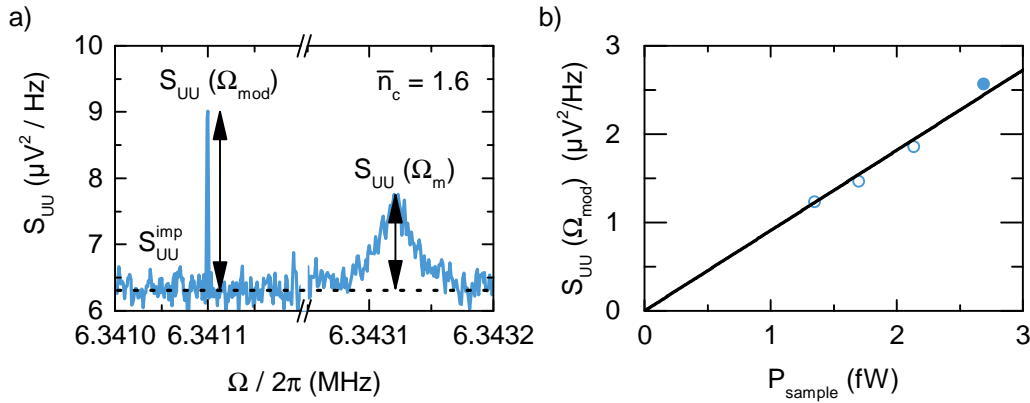
Figure 7.13: *Recorded data of the thermal sideband spectroscopy.* Panel a) displays the recorded voltage spectral density of the mechanical string (right) and an additional induced calibration tone (left) for a sample temperature of 186 mK and an average photon occupation of $\bar{n}_c = 1.6$. The voltage spectral density is later transformed in a frequency density as explained in the text. For this a calibration is required, which we perform by inserting a modulation tone of known frequency depth. In panel b) we plot the extracted modulation tone amplitude of each probe tone power. As expected, we find a linear behavior, that we model (black solid line) to obtain an averaged calibration function. The higher modulation stems from the imprecision noise floor being reduced linearly via the photon number.

detector. Here, in the microwave domain, we apply the modulation tone only through the sample arm, use an I-Q mixture for the homodyne measurement, and detect the voltage of the quadrature. In this configuration, the phase modulation tone and the mechanical induced phase shift do not obey the same transfer function. However this is overcome simply by the factor the transfer functions deviate $\mathcal{Y}$.

7.6.2 Sideband spectroscopy of the thermal motion of the string

Fig. 7.14a) shows the sideband noise measured with a spectrum analyzer using the measurement configuration in Fig. A.1c). We observe a mechanical signature at 6.343122 MHz with a linewidth of $\Gamma_m/2\pi = 34$ Hz. As we use the calibration tone technique introduced by Gorodetsky [106], we further obtain a signature stemming from the modulation tone at 6.341100 MHz. Note, that the y-axis of the spectrum given in $\mu V^2/$Hz, is the actual recorded voltage spectral density of the spectral analysis, thus all amplifiers and attenuators contribute to this value. The peak amplitudes are modulated on top of the background $S_{UU}^{imp} = 6.32 \mu V^2/$Hz. For the data displayed in Fig. 7.14a), recorded at $T_{cryo} = 186$ mK, an average photon number of $\bar{n}_c = 1.6$, the flux bias point J with $\partial_\Phi \omega_c/2\pi = 6.6$ GHz$/\Phi_0$, we find $S_{UU}(\Omega_m) = 1.39 \mu V^2/$Hz, $S_{UU}(\Omega_{mod}) = 2.69 \mu V^2/$Hz. In this experiment we have used a phase modulation of $\phi_0 = 3.94 \cdot 10^{-4}$ and a measurement bandwidth of ENBW= 1 Hz.

In addition to the spectra obtained in panel a), we have measured the sideband noise as function of the probe tone power. This discloses any power or photon number dependent effects. As the imprecision noise decreases with increased power, we find a linear increase in the modulation tone amplitude, as shown in 7.14b), where we have highlighted the
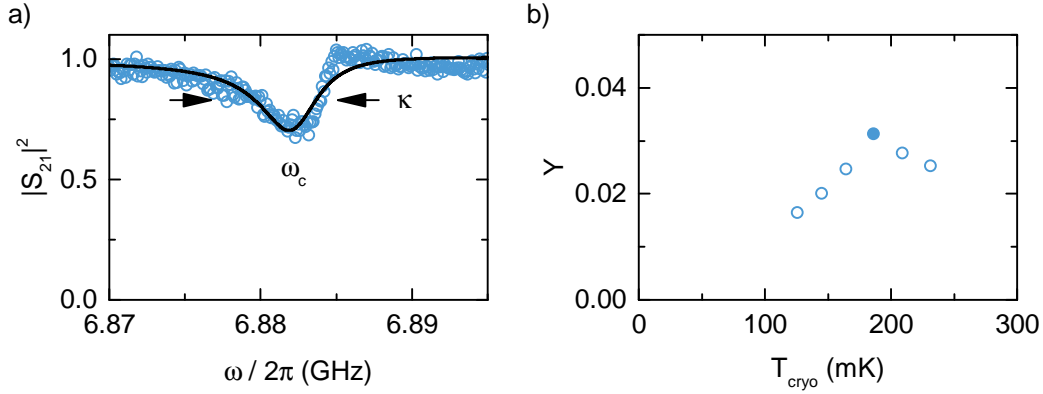
Figure 7.14: *Towards the calibration function $\mathcal{Y}$.* In panel a) the in-situ measured microwave transmission (blue dots) revealing the resonator decoherence by the electromechanical resonator model (black solid line) is found. Panel b) displays the summary of extracted transfer functions, ranging around $0.01 - 0.03$. At $186\,\mathrm{mK}$ the highest value is found, indicating a minimal linewidth in this measurement run.

value extracted from panel a) by a color filling. Modeling the linear trend allows to average over statistical fluctuations within the individual spectras, for which we find a calibration function of $\bar{S}_{\mathrm{PP}}^{\Omega_{\mathrm{mod}}}(P_{\mathrm{appl}}) = (908 \pm 24)\,\mathrm{V^2/W^{-1}Hz}$ (black solid line).

In addition to the mechanical spectrum, we require the ratio between probe tone modulation and mechanical amplitude. For the given experimental setup, that is the detection of voltage fluctuations of a homodyne downconverted signal using an I-Q mixer. Following the approach presented in Ref. [106], we find

$$\mathcal{Y} \approx \frac{16\eta^2\kappa^2\Omega^2}{(4\Delta^2 + \kappa^2)\left(4(\Delta - \Omega)^2 + (1 - 2\eta)^2\kappa^2\right)}, \tag{7.17}$$

using the external to total linewidth ratio $\eta = \kappa_{\mathrm{ext}}/\kappa$.

The required decoherence rate of the microwave resonator are not trivial deterministic as they depend on the applied photon number, the temperature, the flux bias point, and additional 'aging' effects, when flux get trapped on the microchip, an in-situ measurement becomes necessary. For this we apply the probe tone which we use for the mechanical element set to the parameters for the experiment (Δ, P_{appl}), while sweeping a weak probe tone around the resonator. By this we guarantee to record the correct microwave transmission function for the analysis of the transfer function $\mathcal{Y}$. In Fig. 7.17a) we show an example transmission corresponding to the mechanical spectrum of Fig. 7.14a), where we have subtracted a linear background due to a non-uniformal microwave transmission of the cabling. Here, we require to fit the model of our calculations deriving Eq. (7.17) and so we fit

$$|S_{21}|^2 = \left|\frac{s_{\mathrm{out}}}{s_{\mathrm{in}}}\right|^2 = (\mathrm{o1} - i\,(\mathcal{K}))\,(\mathrm{o1} + i\bar{\mathcal{K}}), \tag{7.18}$$

with

$$\mathcal{K} = \mathrm{o2} + \frac{2\eta\kappa}{2\Delta + i\kappa}. \tag{7.19}$$

Here, we have taken an additional complex background into account, due to undesired interferences between resonator and feedline, which is normalized by $\mathrm{o2} = \sqrt{1 - \mathrm{o1}^2}$. For

a)

b)
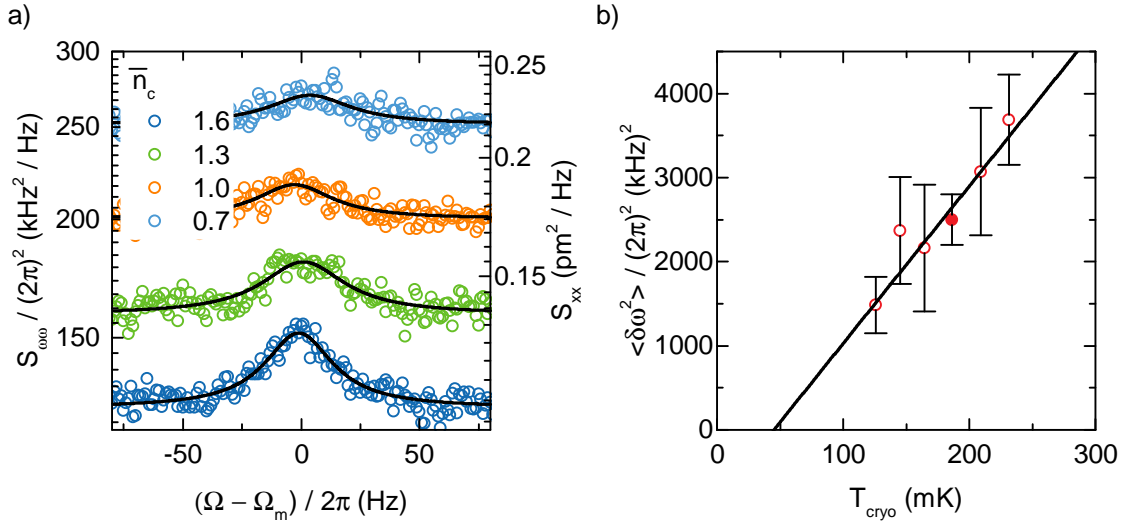
Figure 7.15: *Mechanical induced frequency fluctuations.* In panel a) the calibrated frequency density is shown for a variety of probe photons, as indicated by the inset. The area of the signal corresponds to the thermal photon number (here ≈ 600) times the coupling squared. The background is reduced at higher photon numbers, as the phase imprecision is reduced. We extract the peak height and the linewidth of the mechanical signal. We average the results over the photon numbers and plot the product of them, the total frequency fluctuations, in panel b) over the sample temperature. The observed linear trend (black solid line) is directly related to the coupling strength and so allows for a calibration of the vacuum coupling strength. The obtained coupling then allows to determine the mechanical displacement density, right axis in panel a).

the fitparameters we find $\omega_c/2\pi = 6.882\,\text{GHz}$, $\kappa/2\pi = 4.64\,\text{MHz}$, $\eta = 0.082$, and o1 = 0.966, which lead to the model shown as black solid line. With the probe tone set to the mechanical blue sideband ($\Delta = +\Omega_m$), we find a transfer function of $\mathcal{Y} = 0.034$ at a temperature of $T_{\text{cryo}} = 186\,\text{mK}$.

For the calibration by thermal sidebands we require a temperature sweep of the cryostat. The temperature dependence of the transfer function is found in Fig. 7.14b). Here we have repeated the measurements of the microwave transmission for cryostat temperatures of $T_{\text{cryo}} = \{126, 145, 165, 186, 209, 232\}\,\text{mK}$. We find the highest transfer function at the presented 186 mK (bold dot), which is derived from a local minimum in the microwave decoherence. We speculate that for this set, the saturation of two-level fluctuators balance the created quasi-particles in the material for this temperature.

7.6.3 From frequency fluctuations to the electromechanical coupling

In the following we outline the transformation from the detected signal in voltage fluctuations S_{UU} in a frequency spectral density $S_{\omega\omega}$, which allows us to calibrate the electromechanical coupling. The applied method has the benefit that a precise knowledge of the amplification and attenuation chain is not necessary, as g_{m0} is directly determined by the thermal motion. Here, we focus on the principle procedure. The transformation is based on the dependency

$$S_{\text{UU}} = \frac{2K_\Psi}{\Omega^2} S_{\omega\omega}, \tag{7.20}$$

which is derived by the resonator shift of a mechanical oscillation $x_0 \cos(\Omega_\mathrm{m} t)$ [106]. Here the function K_Ψ describes the ratio between the mechanical motion and the measured voltage fluctuation, which relies on a precise knowledge of the full electric attenuation and amplification chain. Using the calibration tone at Ω_mod and modulation ϕ_0 we overcome this, as it only requires the extraction of the modulation tone amplitude $S_\mathrm{UU}(\Omega_\mathrm{mod})$ to find

$$K_\Phi = \frac{2\mathrm{ENBW}}{\phi_0^2} S_\mathrm{UU}(\Omega_\mathrm{mod}). \tag{7.21}$$

We note, that the frequency modulation of the probe tone and the mechanical element do not necessary obey the same functionality. In general one can express

$$K_\Psi = \mathcal{Y} K_\Phi, \tag{7.22}$$

and derive the transfer function $\mathcal{Y}$ depending on the applied measurement configuration. We have stated the result of $\mathcal{Y}$ for the applied configuration previously in Eq. (7.17). Summarizing Eq. (7.20)-(7.22), we transform the detected voltage fluctuations into a frequency spectral density by

$$S_{\omega\omega} = \frac{\phi_0^2 \Omega_\mathrm{m}^2}{4\mathrm{ENBW}} \frac{S_\mathrm{PP}}{\mathcal{Y} \bar{S}_\mathrm{PP}^{\Omega_\mathrm{mod}}(P_\mathrm{appl})}. \tag{7.23}$$

The next step toward the determination of the vacuum coupling strength g_m0 is to transform all voltage spectras using Eq. (7.23). We plot the example set at $T_\mathrm{cryo} = 186\,\mathrm{mK}$ for all applied probe tone powers spanning $240\,\mathrm{Hz}$ around the mechanical eigenfrequency in Fig. 7.15a). The corresponding probe photons are indicated in the inset, where the value of 1.6 (dark blue) corresponds to the power spectral density shown in Fig. 7.14a). The increase in the background level when decreasing the probe tone power is discussed later in detail.

The frequency fluctuations are directly related to the displacement spectra by the electromechanical coupling ($S_{\omega\omega} = g_\mathrm{m0}^2/x_\mathrm{zpm}^2 S_\mathrm{xx}$), which we display already as right axis in Fig. 7.15b) using the later determined coupling strength $g_\mathrm{m0}/2\pi = 1.6\,\mathrm{kHz}$ and the zero-point fluctuations of the nanostring $x_\mathrm{zpm} = 47\,\mathrm{fm}$. We initially assume that the area of the mechanical signal is independent of the probe tone power and thus corresponds to twice the thermal phonon population. This is difficult to observe when displayed like here in the log-scale, however we will have a detailed look at this after the determination of the coupling strength, when we can determine any influence of the probe tone. For a quantitative analysis we fit the data in accordance to Ref. [106] to a Lorentzian lineshape

$$S_{\omega\omega} = \frac{2A\Gamma}{\Gamma^2 \Omega^2 + (\Omega^2 - \Omega_\mathrm{m}^2)^2} + \mathrm{BCK}. \tag{7.24}$$

Hereby, we obtain the mechanical frequency Ω_m, the linewidth Γ_m, signal amplitude on resonance $S_{\omega\omega}(\Omega_\mathrm{m}) = 2A/(\Gamma\Omega_\mathrm{m}^2)$, the background value BCK, and the peak area A linked to the phonon number. We show the resulting fits as black solid lines in Fig. 7.15a). The temperature dependencies of frequency and linewidth have already been discussed in Sec. 7.5. The frequency fluctuations, that is the peak area above the background next is obtained by [106]

$$\langle \delta\omega^2 \rangle = \int_{-\infty}^{\infty} S_{\omega\omega}(\Omega) \frac{d}{2\pi} = A = S_{\omega\omega}(\Omega_\mathrm{m}) \frac{\Gamma_\mathrm{m}}{2} = 2 n_\mathrm{m} g_\mathrm{m0}^2. \tag{7.25}$$

Next, we average the obtained frequency fluctuations for all measured probe tone powers. The deviations are statistical uncertainties and so define the error bars of the measurement. Plotting the result in Fig. 7.15b) as function over temperature, we find a linear increase. Then we model the result with a weighted linear fit ($\langle \delta\omega^2 \rangle = s(T) + s_0$), leading to a functionality of $s(T) = (18.7 \pm 2.6)\,\mathrm{GHz/K}$ and a finite offset $s_0 = (0.84 \pm 0.45)\mathrm{GHz}$. This can be explained when expressing the phonon numbers via [13]

$$n_{\mathrm{m}} = \frac{k_{\mathrm{B}}}{\hbar\Omega_{\mathrm{m}}} \left(T_{\mathrm{sample}} + T_{\mathrm{ba}} \right), \tag{7.26}$$

containing a finite back-action temperature from the electromechanical interaction. So by Eq, (7.26) we only link the slope of the frequency fluctuations $s(T)$ to the electromechanical coupling in Eq. (7.27), and find

$$g_{\mathrm{m0}} = \sqrt{\frac{s(T)\hbar\Omega_{\mathrm{m}}}{2k_{\mathrm{B}}}} = 2\pi \cdot (1.69 \pm 12)s^{-1}, \tag{7.27}$$

for the given working spot.

However the shown calibration experiment relies on the thermalization of the mechanical element. As we apply a probe tone on the blue mechanical sideband ($\Delta = \Omega_{\mathrm{m}}$), Stokes scattering is highly enhanced. This is the insertion of a phonon by the probe tone, effectively heating the mechanical element. By this the mechanical damping rate is modified by the electromechanical or optomechanical damping rate [c.f Eq. (4.22), $\Delta_{\mathrm{p}} = +\Omega_{\mathrm{m}}$, $\Omega_{\mathrm{m}}^2 \gg \kappa^2$]

$$\Gamma_{\mathrm{opt}} = -\frac{4\bar{n}_{\mathrm{c}}g_{\mathrm{m0}}^2}{\kappa}, \tag{7.28}$$

as already derived in Sec. 4.3, however here for the blue sideband $\Gamma_{\mathrm{opt}} < 0$ and so the effectively measured linewidth is expected to shrink when increasing the blue probe tone power ($\Gamma_{\mathrm{eff}} < \Gamma_{\mathrm{m}}$). The determination of the coupling strength $g_{\mathrm{m0}}/2\pi = 1.6\,\mathrm{kHz}$, was performed with an average photon number of $\bar{n}_{\mathrm{c}} = 1.18$, average resonator decoherence $\kappa/2\pi = 5.86\,\mathrm{MHz}$ and mechanical linewidth of $\Gamma_{\mathrm{m}}/2\pi = 33\,\mathrm{Hz}$. So by Eq. (7.28) we expect an optical linewidth of $\Gamma_{\mathrm{opt}}/2\pi = 2\,\mathrm{Hz}$, which allows to quantify the phonon number of the nanostring in analogy to Eq. (7.29) by

$$n_{\mathrm{m}}^{\mathrm{heated}} = \frac{n_{\mathrm{m}}^{\mathrm{th}}\Gamma_{\mathrm{m}}}{\Gamma_{\mathrm{eff}}}, \tag{7.29}$$

indicating an increase of 6.5% in the experiment. However, the coupling scales with $\sqrt{n_{\mathrm{m}}}$ and so the vacuum coupling is systematically overestimated by 2.5%. This is below our statistical uncertainty of $120/1600 = 7.5\%$, which is why expect not to be able to resolve this effect in measurements, which we indeed show in App. H. Nevertheless, we take this systematic deviation into account by reducing the measured coupling strength by the determined overestimation and conclude with $g_{\mathrm{m0}}/2\pi = (1.65 \pm 0.12)\,\mathrm{kHz}$. This corresponds to $G = g_{\mathrm{m0}}/x_{\mathrm{zpm}} = 35\,\mathrm{MHz/nm}$.

In comparison to the theoretical prediction with the experimental parameters of $\omega'/2\pi = 6.6\,\mathrm{GHz}/\Phi_0$, $B_{\mathrm{ext}} = 0.47\,\mathrm{mT}$, $\alpha = 1$, $l = 20\,\mu\mathrm{m}$, and $x_{\mathrm{zpm}} = 47\,\mathrm{fm}$, we expect a coupling strength of 1.5 kHz, in good agreement with the measurement. This value is already higher than previous realizations in nano-electromechanics [24], yet the full magnetic field range of up to 130 mT has not yet been exhausted.
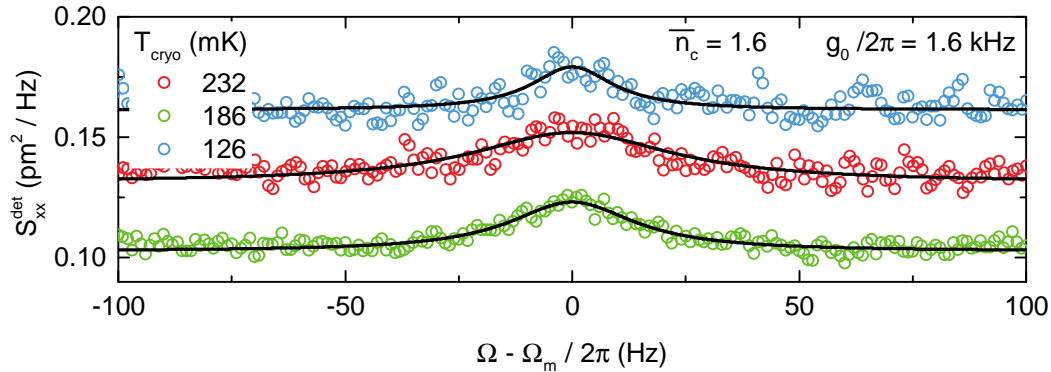
Figure 7.16: *Detected mechanical displacement density over sample temperature.* We show the
mechanical displacement for selected temperatures, with an decrease in the mechanical signal
area and linewidth when cooling down the sample temperature. The area is reduced as
it displays the phonon occupation, which is dominated by the thermal excitation given the
experimental configuration. The photon number for these measurements was around 1.6. The
decrease in linewidth is discussed in detail in Sec. 7.5

7.6.4   Detected thermal displacement density

Via this coupling we are now able to determine the measured displacement spectral density,
as we have already indicated in Fig. 7.15a) by the transformation $S_{xx} = S_{\omega\omega} x_{zpm}^2 / g_{m0}^2$.
We now discuss the obtained spectrum at a probe strength of around 1.6 photons, for
temperatures of 232 (red, cf. Fig. 7.15a)), 186 (green), and 125 mK (blue) in Fig. 7.16.
Here, we find the signal area and the linewidth decreasing when the temperature is reduced.
The decrease in linewidth over temperature was discussed in Sec. 7.5. The shrinking of the
peak area is explained by the reduced thermal phonon occupation, decreasing linear in T,
cf. Eq. (7.27). As the linewidth is already linearly decreasing we find this the dominant
contribution to the area reduction, the signal amplitude above the background remains of
identical size. The background shows no systematic trend over temperature, as it depends
on a multitude of parameters, like the resonator linewidth, the applied probe photons, as
well as technical noise sources, e.g. the cold amplifier performance.

We like to comment on the ratio between measured displacement density S_{xx}^{det} to the
theoretical thermal displacement density S_{xx}^{th}, cf. Eq. (4.10), as this becomes important
for the force detection sensitivity. For the bare (theoretical) displacement density of the
nanostring we obtain a value of $S_{xx}^{th}(\Omega_m) = 2.58 \cdot 10^{-2}\,\mathrm{pm^2/Hz}$ at $186\,\mathrm{mK}$ (not shown in the
figure), while the detection states $S_{xx}^{det}(\Omega_m) = 1.26 \cdot 10^{-1}\,\mathrm{pm^2/Hz}$, and so we find a ratio
of $S_{xx}^{det}/S_{xx}^{th} = 4.8$ between detected and ideal displacement on resonance. Off-resonant
this value increases, as the imprecision noise then dominates the detection, while the bare
displacement density decreases by the mechanical linewidth.

7.6.5   Electromechanical noise contributions

For a closer look at the noise contributions, we extract the displacement background level
from each measurement, which we will refer to S_{xx}^{det} in the following. In Fig. 7.16 this
corresponds to a value of $1.03 \cdot 10^{-1}\,\mathrm{pm^2/Hz}$ at $186\,\mathrm{mK}$ and 1.6 photons, or in terms of
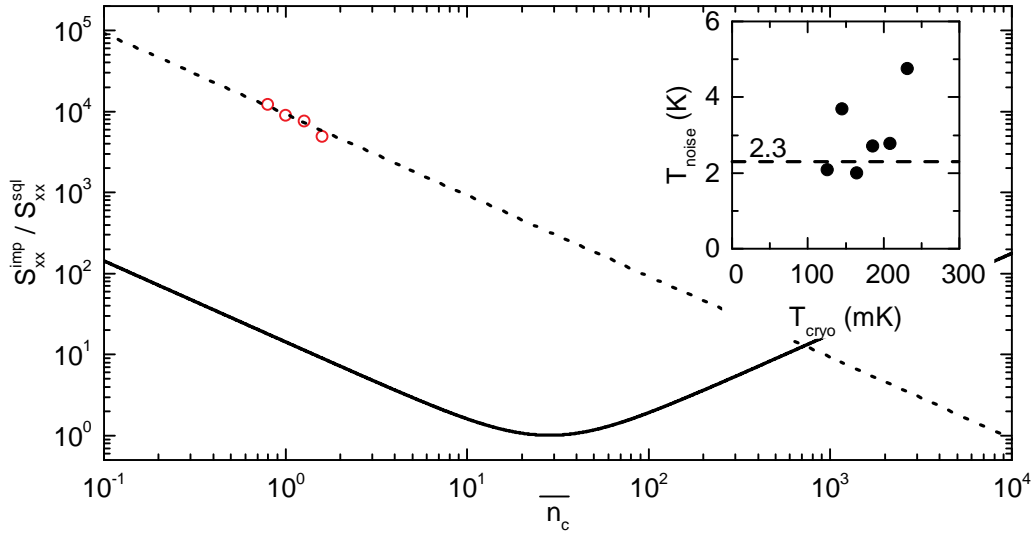
Figure 7.17: *Electromechanical noise contributions in inductively coupled systems.* We show
the detected background noise level over photon numbers in units of the standard quantum
level. We find a linear decrease indicating an imprecision limitation, that we model (black
dotted line) to obtain the average detection level. The ideal - or quantum limited level is
indicated by a black solid line. For the given coupling strength we find an optimal photon
power around 10^3. As we measure on the single photon level, we operate deep within the
imprecision limited regime. Form the deviation between ideal and detected noise we can
extract the noise temperature, as shown in the inset. The contributions shown in the full
frame correspond to the breakaway at 5.6 K, besides that the noise level is close to the HEMT
noise level of 2.3 K, indicated by the black line.

the standard quantum limit $S_{xx}^{sql} = \hbar/(m_{eff}\Omega_m\Gamma_m) = 1.8 \cdot 10^{-29} \mathrm{m}^2/\mathrm{Hz}$ (cf. Sec. 4.2.2) to a
ratio of about 10^4. In Fig. 7.17, we show the obtained ratio (in red) for a temperature of
186 mK and all applied probe powers ranging from 0.7 to 1.6 photons. The black solid line
indicates the quantum limited detection, cf. Eq. (4.16) and the average system parameters
of $\kappa/2\pi = 4.9\,\mathrm{MHz}$, $\Gamma_m/2\pi = 39\,\mathrm{Hz}$, $\Omega = \Omega_m = 2\pi \cdot 6.3431 \cdot 10^6/\mathrm{s}$, $g_{m0}/2\pi = 1.6\,\mathrm{kHz}$, and
$x_{zpm} = 47\,\mathrm{fm}$ at this temperature. For these parameters we find a decreasing imprecision
noise of $S_{xx}^{imp}/S_{xx}^{sql} = 14/\bar{n}_c$ [cf. Eq.(4.12)]. In addition, we determine an optimal photon
power of $\bar{n}_c^{opt} = 28$. By this we conclude that we are within the imprecision limited
regime. The observation that the off-resonant noise linearly decreases with the microwave
power supports this. So we model a linear trend to the data (black dotted line) and find
$S_{xx}^{det}/S_{xx}^{sql} = (9.2 \pm 1.1) \cdot 10^3/\bar{n}_c$. We see, that the electromechanical imprecision S_{xx}^{imp} is
negligible in comparison to the technical one S_{xx}^{det}. So, the ratio $S_{xx}^{det}/S_{xx}^{sql}$ can be interpret
as technical noise phonons

$$n_{m,xx}^{tech} = 9.2 \cdot 10^3. \tag{7.30}$$

This figure can be recast as noise photons. As $\omega_c \approx 10^3 \cdot \Omega_m$, the noise level corresponds
to 9.2 photons. To compare this value with the performance of the microwave cryogenic
HEMT amplifier, we use $T_{noise} = n_{m,xx}^{tech}\hbar\Omega_m/k_B = 2.7\,\mathrm{K}$. The noise temperature of the
cold HEMT amplifier is specified to '2.3 K typically' [163]. Thus, the technical noise
observed is in reasonable agreement with the equipment used.
In the inset of Fig. 7.17 we plot the result of the extracted noise temperature T_{noise} over

the full temperature sweep T_{cryo}. Overall we find a temperature around the specified noise figure of $2.3\,\text{K}$ (black dotted line). However two of the six datapoints break out of this, nevertheless staying below $5\,\text{K}$.

A further decrease of the noise temperature can be realized by an additional quantum limited amplifier, e.g. a JPA. Here, the typical noise temperature is around $500\,\text{mK}$ [164], improving the detection by one magnitude. The benefits of quantum limited detection in electromechanical systems are discussed in detail in Refs. [15, 164]. Further the non-linearity of the Josephson junctions should allow for a squeezing of the deployed resonator's vacuum phase, further reducing the measured imprecision [17].

7.6.6 Total measurement precision

An important parameter for the characterization is the achieved measurement precision in terms of the standard quantum limit. As we drive off-resonant on the blue mechanical sideband we expect a minimum value of $S^{\text{sql}} = \sqrt{2}\hbar$ [98, 105]. Next, we have to determine the product of the displacement and force density $S_{\text{xx}}^{\text{tech}}S_{\text{FF}}^{\text{ba}}$. It is lowest at the lowest temperature and highest drive power. Here, we find a measurement imprecision of $S_{\text{xx}}^{\text{tech}} = 1.66\cdot10^{-25}\,\text{m}^2/\text{Hz}$. The backaction force is approximated in first order to stem from thermal contribution $S_{\text{FF}}^{\text{ba}} = S_{\text{FF}}^{\text{th}} = 4\hbar\Omega_{\text{m}}\Gamma_{\text{m}}(n_{\text{m}} + 1/2) = 5.0\cdot10^{-37}\,\text{N}^2/\text{Hz}$ [100]. This results in a measurement precision of $S_{\text{xx}}^{\text{tech}}S_{\text{FF}}^{\text{ba}} = 1.9\cdot10^3\sqrt{2}\hbar$. This is a higher value than previously found in capacitively coupled systems using the same setup, as there a value of $165\sqrt{2}\hbar$ was found [100]. The high value has two reasons: First, by the limitation of the photon numbers a high imprecision noise floor is present, enhanced also by the use of non-quantum limited amplification, as discussed in Sec. 7.6.5. The second factor is the high thermal excitation of the nanostring, as we do not employ any sideband cooling techniques.

The later increases the detected displacement as $S_{\text{xx}}^{\text{th}} \propto n_{\text{m}}$, cf. Eq. (4.17). However, we can give an estimation on the measurement precision for sufficiently cooled nanostrings by excluding the thermal contributions, as derived in [165]. The respective force sensitivity then is given by $S_{\text{FF}}^{\text{cryo}} = 4m_{\text{eff}}k_{\text{B}}T_{\text{sample}}\Gamma_{\text{m}}$ [165]. For this we obtain a precision of $66\sqrt{2}\hbar$. Since previously in capacitively coupled systems a value of $100\sqrt{2}\hbar$ was found [100] for this particular setup, we have indeed an improvement by almost a factor of 2.

So, besides all limitations discussed above for the first sample generation, we already obtain an improvement in comparison to capacitively coupled electromechanics. However, given the current electronic setup configuration, the obtained value exceeds the standard quantum limit by about 50 for sideband-cooled nanostrings. This shows that the imprecision limitations will become a challenge when reducing the thermal string occupation (reducing $S_{\text{xx}}^{\text{th}}$), as the remaining background is significantly higher. By this we conclude that the reason for the detected signal to noise ratio in e.g. Fig. 7.16 seems to be caused by the high electromechanical vacuum coupling in combination with the high phonon occupation of the string.
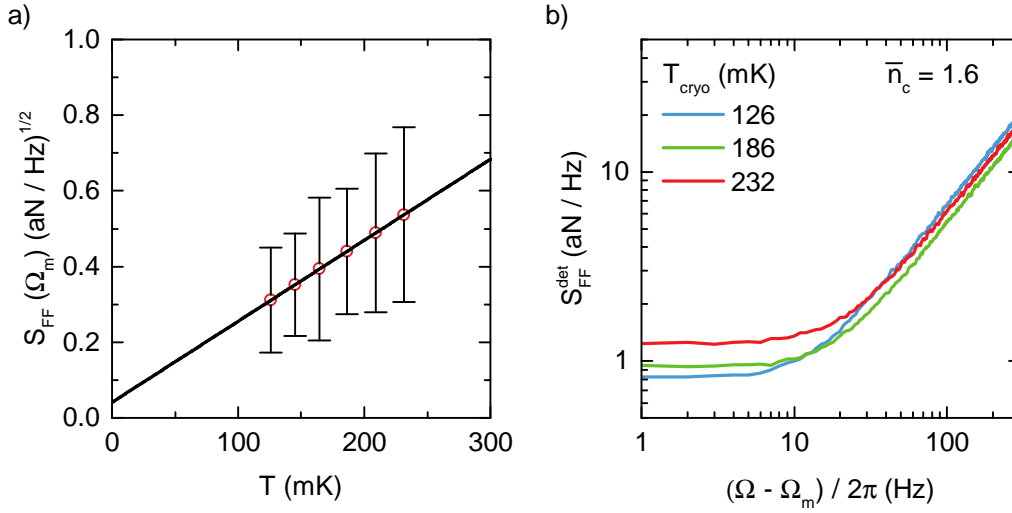
Figure 7.18: *Details on the force sensitivity in inductively coupled electromechanics.* Panel a) plots the on-resonance achievable force sensitivity. We find a linear decrease with an intrinsic sensitivity of $50\,\text{zN/Hz}^{1/2}$. Panel b) shows the detected force sensitivity over frequency. We find the highest sensitivity on resonance, increasing via the mechanical linewidth. We are able to detect a force sensitivity already close to the theoretical limit ($\times 2.8$).

7.6.7 Sub-attonewton force detection

We like to conclude our discussions about the measurement performance of inductively coupled nanomechanics by discussing the force sensitivity. The quantum limited force sensitivity on resonance to the mechanical string is given by [164, 166]

$$S_{\text{FF}}(\Omega_{\text{m}}) = 4m_{\text{eff}}k_{\text{B}}T_{\text{sample}}\Gamma_{\text{m}}. \tag{7.31}$$

identical to the contribution from the thermal bath, in Sec. 7.6.6. Here, the low mass of the thin aluminum nanostring, as well as its high mechanical quality factor are beneficial to obtain the high force sensitivity stated here.

As we have determined the oscillator's linewidth as a function of the cryostat temperature, cf. Fig. 7.10a), we plot the result of Eq. (7.31) in Fig. 7.18a) (red dots). We quantify $S_{\text{FF}}(\Omega_{\text{m}}) = (2.14\pm0.10)\cdot T_{\text{sample}}[K]\,\text{aN/Hz}^{1/2} + (41\pm19)\,\text{zN/Hz}^{1/2}$ (black solid line). The intrinsic force sensitivity at $T_{\text{sample}} \to 0$ stems from the intrinsic mechanical linewidth of $\Gamma_0/2\pi = 6\,\text{Hz}$. The uncertainties arise from the fluctuations of the mechanical linewidth. Further we find that, by reducing the cryostat temperature to $20\,\text{mK}$, we can achieve a sensitivity of $84\,\text{zN/Hz}^{1/2}$. However in our experiment we were limited by the heat dissipations of the field bias coil to $120\,\text{mK}$.

Having discussed the theoretical force sensitivity we next quantify the detected one. We derive the spectral force density from the detected mechanical displacement density (cf. Fig. 7.16) via [164]

$$S_{\text{FF}}^{\text{det}}(\Omega) = \frac{2S_{\text{xx}}^{\text{det}}(\Omega)}{|H(\Omega)|^2}, \quad \text{with} \quad H(\Omega)^{-1} = m_{\text{eff}}(\Omega^2 - \Omega_{\text{m}}^2 - i\Gamma_{\text{m}}\Omega) \tag{7.32}$$

We plot the results for selective temperatures in Fig. 7.18b). We find the lowest force density - corresponding to the highest sensitivity - for Ω close to Ω_{m}. This plateau scales

with the mechanical linewidth Γ_{m} which is itself temperature dependent. In addition, the sensitivity is enhanced when cooling the sample, as linewidth and phonon occupation decrease. The lowest experimentally detected force sensitivity is close to the theoretical limit from panel a) of the respective temperature, where we achieve a sub-attonewton force sensitivity of $S_{\mathrm{FF}}^{\mathrm{det}}(\Omega_{\mathrm{m}}, T_{\mathrm{cryo}} = 126\,\mathrm{mK}) = 0.82\,\mathrm{aN/Hz}^{1/2}$, versus an optimal theoretic value of $0.31\,\mathrm{aN/Hz}^{1/2}$. We benefit here from the high coupling, that allows to resolve a high displacement to thermal motion ratio besides the high imprecision noise - even for a low photon number of 1.6.

We like to mention previous work, using an all aluminium electromechanical resonator, consisting of a capacitively coupled doubly clamped nanostring, and employing a JPA, which achieved a force sensitivity of $0.51\,\mathrm{aN/Hz}^{1/2}$ at $77\,\mathrm{mK}$ [164]. Three dimensional drum resonator that achieve a higher electromechanical coupling strengths than nanostring oscillators suffer in the force sensitivity S_{FF} due to their high mechanical mass ($48\,\mathrm{pg}$ in [15] vs. $m_{\mathrm{eff}} = 0.6\,\mathrm{pg}$ used here). Moreover, our results have also to be compared to the sensitivity achieved by the use of ultra-light carbon nanotubes where a record force sensitivity of $(12 \pm 8)\,\mathrm{zN/Hz}^{1/2}$ was experimentally achieved at a moderate cryogenic temperature of $1.2\,\mathrm{K}$ [166], and a sensitivity of $1\,\mathrm{zN/Hz}^{1/2}$ derived from resonator's characteristics at $44\,\mathrm{mK}$ [167].

7.7 Tuneable inductive coupling in nano-electromechanics

We next confirm the tuneability to the electromechanical interaction as proposed by Eq. (7.3), in particular the linearity in the frequency slope $\partial_{\Phi}\omega_{\mathrm{c}}$ and the external field B_{ext}. To reduce the measurement time for theses experiments, we switch to the cryogenic interferometer which enhances the phonon number by active driving and so the mechanical signal. We will show the nanostring's response measured systematically over the resonator's tuning. Further, we extract the measured response $\delta\omega_{\mathrm{d}}(\Omega_{\mathrm{m}})$, proportional to the coupling strength. We will compare this quantitatively with the resonator's slope and find a linear dependency. In addition, we repeat the measurements at a frequency tuning corresponding to working spot J and sweep the magnetic field. Here, we also show the measured response and combine the result with four measurements in which we have determined the electromechanical coupling via a spectroscopy of the thermal sideband, cf. Sec. 7.6.1. By this we also confirm the linearity of the coupling to the applied external field.

7.7.1 Mechanical response along the resonator tuning

We record the string's response to a drive voltage of $V_{\mathrm{piezo}} = 0.42\,\mathrm{mV}$, for a probe tone on resonance to the microwave resonator, corresponding to a photon number of $2 - 3$ photons. In particular, we record the homodyne detected microwave power P_{hom}, as well as the microwave resonator characteristics. From the later we obtain the on-resonance transfer function K, cf. Eq. (5.2). With that, we can calculate the induced frequency shifts $\delta\omega_{\mathrm{d}}$ from the recorded power, cf. Eq. (5.1). When the mechanical excitation is on resonance with the mechanical string's eigenfrequency this is proportional to the coupling strength, cf. Eq. (5.3). As a side note, the resonator is coupling to a loss channel around $7.325\,\mathrm{GHz}$
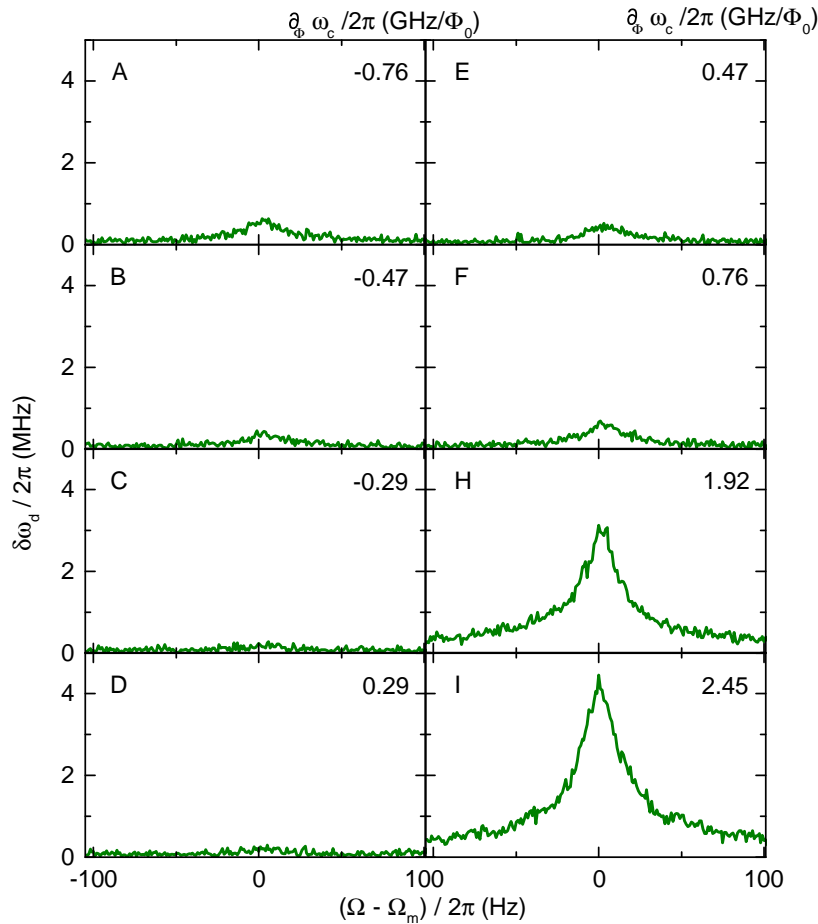
Figure 7.19: *Detected string motion for different resonator working spots.* From top left to bottom right the detected signal of the driven nanomechanical string is shown via sweep along the working spots of the microwave resonator, indicated in Fig. 7.5a). We start at moderate flux tunings, from which we approach the sweet spot. As we do so, the tuning is decreased and so does the on-resonance peak height, which is proportional to the coupling. Around the sweet spot the mechanical peak vanishes in the background noise. When increasing the tuning again, it reappears and follows the linear dependency.

(at spot G, as found in the Fig. 7.5a)). There, the resonator's response did not allow to obtain the transfer function, which is why we exclude this working point in our analysis. We show the recorded shifts in Fig. 7.19 for the remaining working spots. As we start at a moderate working spot A, corresponding to a flux tuneability of $-0.76\,\mathrm{GHz}/\Phi_0$, we find a peak amplitude of $0.6\,\mathrm{MHz}$. As the slope is reduced from spot A - C, the peak amplitude decreases, until it vanishes for point C. Afterwards it increases again, as the slope is rising.

7.7.2 Frequency slope dependence

The next step is to systematically investigate the peak height over the resonator tuning to confirm Eq. (7.3). For this, we refer to the resonator tuning on points $A - C$ as negative tuning, and account for this by multiplying the obtained peak amplitude by -1. Therefor, we expect a straight line through the origin for the case of a linear relation between
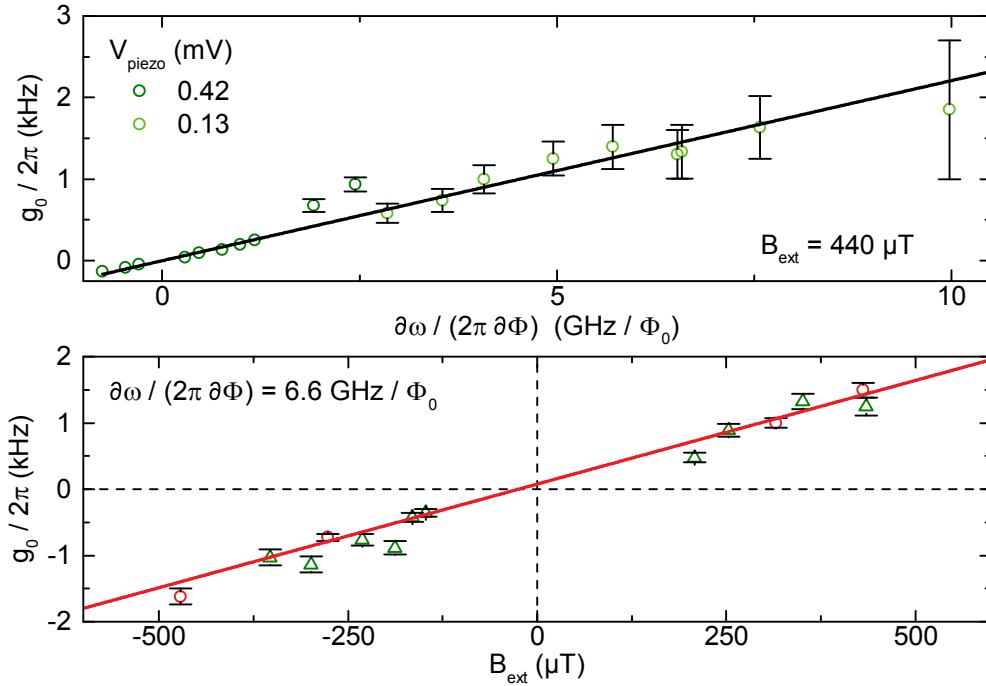
Figure 7.20: *Tuneability of the electromechanical coupling in inductively coupled systems.* Panel a) shows the in terms of vacuum coupling transformed frequency shifts at high (dark green) and low drive power (bright green). We find a linear increase for both drive strengths when the resonator's tuning is increased. This agrees with the predicted tunebality of the coupling, cf. Eq. (7.3). In panel b) we plot the extracted vacuum coupling strength for both the driven (dark green) and thermal motion analysis (red). Both confirm the expected linearity of the coupling.

g_{m0} and $\partial_\Phi\omega_c$. This is indeed what we find with a proportionality of $\delta\omega_d(\Omega_m)/2\pi = 0.97\,\mathrm{MHz}\Phi_0/\mathrm{GHz} = 0.97\,\mathrm{m}\Phi_0$. By the thermal motion measurements we determine a coupling of $g_{m0}/2\pi = 0.22\,\mu\Phi_0 \cdot \partial\omega/(2\pi\partial\Phi)$ for the sample parameters, an external field of $B_{\mathrm{ext}} = 440\,\mu\mathrm{T}$, and so we find a transformation constant of

$$x_{V_{\mathrm{piezo}}=0.42\,\mathrm{mV}} = \frac{0.97\,\mathrm{m}\Phi_0}{0.22\,\mu\Phi_0} = 4.41 \cdot 10^3. \tag{7.33}$$

This transformation constant then allows us to display the extracted on resonance frequency shift $\delta\omega_d(\Omega_m)$ in calibrated vacuum coupling $g_{m0} = x_{V_{\mathrm{piezo}}}\delta\omega_d(\Omega_m)$, cf. App. F for details. We show this in Fig. 7.20a) in dark green for the results of Fig. 7.19, following the linear increase of $0.22\,\mu\Phi_0 \cdot \partial\omega/(2\pi\partial\Phi)$(black solid line). The two highest values are slightly higher than the linearity proposes. We suspect, that at some point the induced electromechanical shift becomes sufficiently large, such that higher order effects have to be taken into account and the reduction of the induced shift on only the phase of the resonator fails, cf. Eq. (4.38) and Sec. 4.4. We avoid this by reducing the drive tone power, as well as the probe tone power by an order of magnitude. The obtained peak amplitudes ($\delta\omega_d(\Omega_m)$) for the lower drive amplitude of $V_{\mathrm{piezo}} = 0.13\,\mathrm{mV}$ is plotted in the same figure in bright green. For the lower drive, we find a decreased slope of $\delta\omega_d(\Omega_m) = 0.27\,\mathrm{mHz}\Phi_0$ and so

$$x_{V_{\mathrm{piezo}}=0.13\,\mathrm{mV}} = 1.22 \cdot 10^3. \tag{7.34}$$

The decrease is expected, as we drive now with less power and so induce less displacement. In this drive voltage regime we therefore can confirm the expectation of the ideal piezo susceptibility ($V_{\text{piezo}} \propto x_0$) as

$$\frac{0.42\,\text{mV}}{0.13\,\text{mV}} = 3.2 \approx 3.6 \frac{x_{V_{\text{piezo}}=0.42\,\text{mV}}}{x_{V_{\text{piezo}}=0.13\,\text{mV}}}. \tag{7.35}$$

The ratio we obtain is slightly lower, which we attribute to the aspect that the excitation force provided by the piezo is not perfectly linearwith the driving voltage in this regime. Overall we conclude that the inductive coupling can indeed be tuned via the resonator detuning and that they are directly proportional to each other, cf. Eq. (7.3).

7.7.3   Field dependence

In addition to the tuneability via the frequency slope, we now analyze the coupling as function of the applied external magnetic field. For this, we bias the resonator to working point J and repeat the measurements via the cryogenic interferometer for several applied field values B_{ext}. We multiply the findings by -1 for negative field values to show the proportionality [as we did previously for the slope dependence in Fig. 7.20a)]. The extracted on-resonance frequency shifts $\delta\omega_{\text{d}}(\Omega_{\text{m}})$ are transformed to the calibrated coupling strength g_{m0} as before in Sec. 7.7.2 and plotted in Fig. 7.20b) (dark green). They obey a linear dependency. For a quantification of the electromechanical coupling strength, we further include the results of the vacuum coupling strength obtained by the spectroscopy of thermal sidebands at this flux bias point of $\partial\omega_{\text{c}}/(2\pi\partial\Phi) = 6.6\,\text{GHz}/\Phi_0$ (red), cf. Sec. 7.6.1. We find the highest vacuum coupling at an external field of $-471\,\mu\text{T}$ corresponding to $g_{\text{m0}}/2\pi = (1.62 \pm 0.12)\,\text{kHz}$, or $G = 34.5\,\text{MHz/nm}$.

This exceeds previous realizations, as to our knowledge the highest single photon-phonon coupling in resonator nano-electromechanics was reported in Ref. [24] to be $g_{\text{m0}}/2\pi = 280\,\text{Hz}$. This value was realized using a three dimensional drum oscillator capacitively coupled to superconducting lumped element resonator, where the drum acted as capacitive element. Further, the drum was biased by a dc-voltage to decrease the distance between the two capacitor plates.

By using the complete dataset of the thermal spectra we can fit a linear relation $g_{\text{m0}}/2\pi = \{(3.13 \pm 0.20)\,B_{\text{ext}}[\mu\text{T}] + (80 \pm 70)\}\,\text{Hz}$ at this flux bias point. This allows to restrict the value of the mode shape factor in the range $\gamma_{\text{s}} = [1 - 0.94]$ for the string parameters stated in Sec. 7.1.

We now have confirmed the tuneability of inductively coupled electromechanics by the frequency slope of the flux tuneable resonator as well as the applied external magnetic field, which are predicted by Eq. (7.3).

7.8   Strong mechanical coupling

In Sec. 4.4 we have found that by a strong drive of the mechanical oscillator, we can increase the induced frequency shift $Gx_0 = g_{\text{m0}}\sqrt{2n_{\text{m}}}$, even beyond the mechanical eigenfrequency. Then the microwave transmission minimum of the resonator starts to split with a separation defined by the mechanical frequency, following a Bessel-type behavior, as derived via Eq. (4.34). In the following, we will explore these signatures under
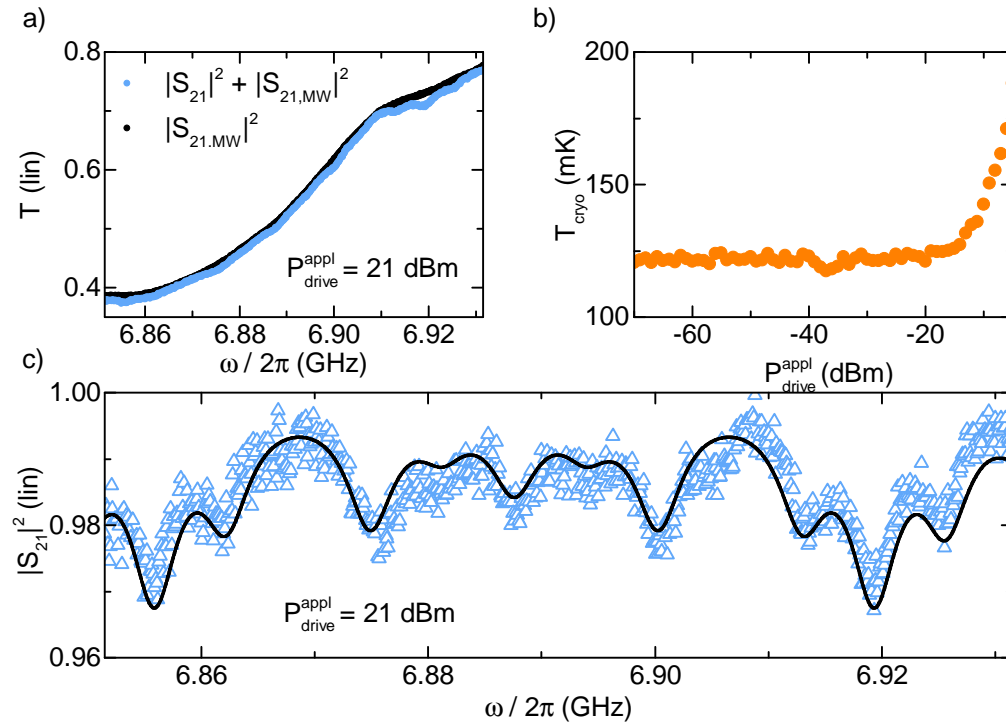
Figure 7.21: *Technical details for mechanical driven resonator spectroscopy.* In panel a) the microwave transmission is plotted with (blue) and without (black) the tuneable resonator at a working spot of 6.9 GHz. Panel b) displays the sample temperature under a strong mechanical drive tone applied to the piezo. For intermediate drive powers no signature of the drive tone can be found. However at very high drive powers, the sample temperature is increased almost twice its initial value. Panel c) shows a typical theory fit to the extracted microwave transmission. Details on the fit in the text. Overall an agreement is found. Deviations are further discussed in the text.

strong mechanical drives at a highly coupled working spot of the microwave resonator. We will find induced frequency shifts (corresponding to an effective driven coupling $g_{m0}\sqrt{2n_m}$) on the order of one percent of the microwave resonator's eigenfrequency.

7.8.1 Experimental procedure

For this we rewire the microwave setup as detailed in Fig. A.1d), such that the microwave source is directly send to the piezo actuator and the vector network analyzer only probes the microwave transmission. By the rewiring a second calibration of the room temperature attenuation was necessary, which we take into account in the following, cf. Fig. 7.4b). The benefit of this configuration is that both the mechanical and the electric element only receives their explicit probe tones. However, we like to note, that an in-situ observation of the mechanical string by the piezo drive is no longer possible in this setup.

We start by biasing the resonator to working point J, and apply an external field of $+0.45\,\mu$T. Here, the electromechanical coupling strength is $g_{m0}/2\pi = 1.41$ kHz. We measure the microwave transmission via the network analyzer within a frequency range of 80 MHz around the microwave resonator frequency, and send a drive tone on resonance with the mechanical oscillator Ω_m via the microwave source. By this the displacement is
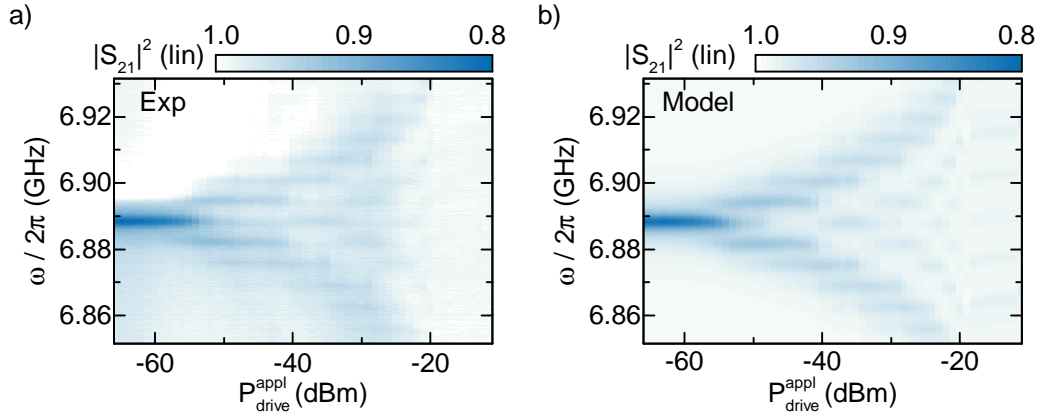
Figure 7.22: *Extracted resonator transmission and model for mode* 4 *of the nanostring.* We plot the calibrated transmission of the microwave resonator over applied drive power. Panel a) displays the measured data, panel b) shows the modeled transmission using Eq. (4.34) with the eigenfrequency and phonon number as only free fit parameters. The experimental data is in good agreement with the model. For weak drives the resonator transmission remain Lorentzian. When the effective shift $g_{m0}\sqrt{n_m}$ exceeds the mechanical eigenfrequency, a splitting up to 7nth order with a spacing of the mechanical frequency is found.

driven coherently with an amplitude $\propto \sqrt{n_m}$. In Figure 7.21a) we show an exemplary data trace of the uncalibrated microwave transmission T (blue). To reveal the pure resonator response, we calibrate the transmission using a trace of the microwave resonator detuned (black). This calibration is done by a normalization of the complex scattering parameter. For the realization of large displacements, strong drive powers are required. Nevertheless, in the given configuration, the piezo drive power is dissipated by the piezo actuator and limits the experimental range by heating the mixing chamber stage, see Fig. 7.21b).

At low drive powers P_{drive}, the microwave transmission shows the characteristic microwave resonator transmission feature, which allows us to extract the loss rates at this particular working point $\kappa_{ext}/2\pi = 0.5$ MHz and $\kappa_{int}/2\pi = 4.6$ MHz in agreement with previous results [cf. Fig. 7.7b)]. Using the vacuum coupling strength of $g_{m0}/2\pi = 1.41$ kHz, we can fit the data to Eq. (4.34), where the microwave resonator frequency ω_c and the displacement x_0 remaines as only free fit parameters. Figure 7.21c) shows the calibrated dataset from panel a) (blue triangles) and the described fit to the data (black). We find a good agreement between the fit and the data, which is also confirmed when comparing the full datasets, as found in Fig. 7.22:

7.8.2 Effective strong mechanical coupling

Figure 7.22a) shows the detected transmission of the microwave resonator as a function of the piezo drive power P_{drive}, with the piezo drive frequency set to Ω_m. For low drive powers we find the unperturbed Lorentzian transmission of the microwave resonator. When the drive is increased the single peak splits up, in spacings $\propto n\Omega_m$, where $n \in \mathbb{Z}$ and $\Omega_m/2\pi = 6.3431$ MHz. We are able to detect 7 orders of the splitting. Though, for very high drive powers the splitting becomes large and the remaining peak height low, so the transmission approaches unity. Further, the induced heating via the drive tone [cf. Fig. 7.21b)] might have influenced the magnetization of the setup shifting the electrical
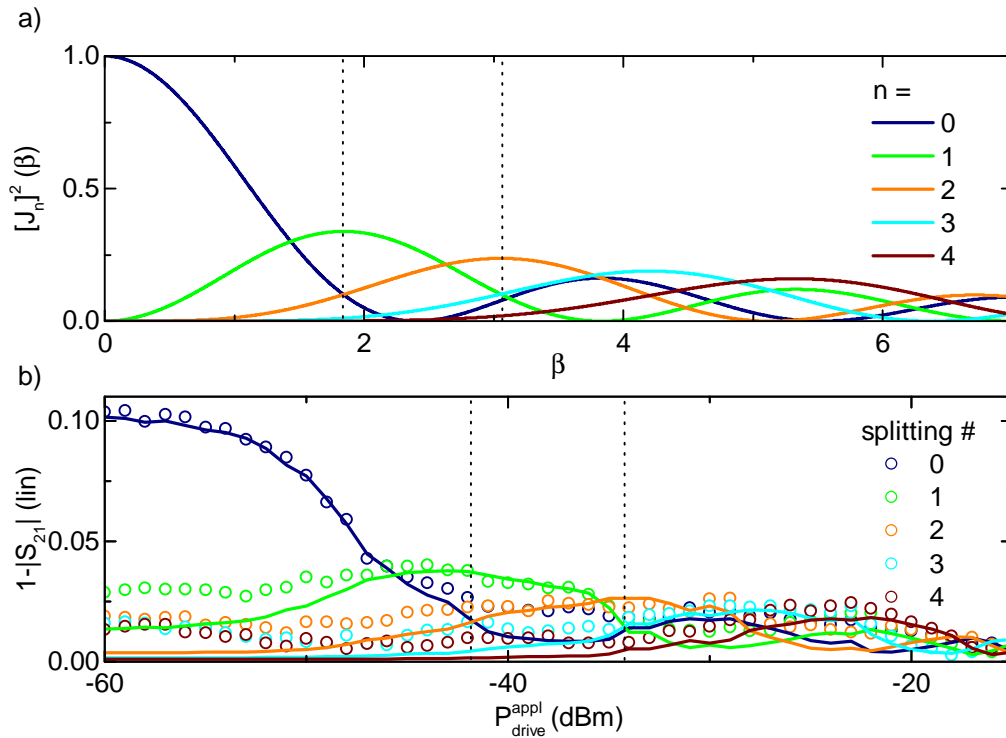
Figure 7.23: *Bessel function behavior of the driven electromechanical resonator.* In panel a)
we plot the squared Bessel function of first kind, for zero to fourth order. We find the first
maximum of the n-th order to be located at the intersection of $n - 1$ and $n + 1$, as indicated
for the first two maxima. In panel b) we show the absolute value of the scattering parameter
for n-th mechanical order of mechanical mode 4 as dots. By plotting its difference to unity,
we find a directly proportionality Bessel functions of the upper panel. The lines are the
corresponding values of the fit to the data. In agreement with the mathematical prediction,
we find the n-th maximum at the intersection as stated before.

resonator off-resonance (given the resonator slope of $6.7\,\mathrm{GHz}/\Phi_0$ and a SQUID loop are of
$44.6\,\mu\mathrm{m}^2$, $33\,\mathrm{nT}$ are sufficient to tune the resonator by one linewidth κ). In addition such
temperature changes also influence the mechanical eigenfrequency, cf. Fig. 7.10b), such
that both systems became tuned out of resonance.

7.8.3 Mathematical description by Bessel functions

Next, we compare the result of the detected splitting to the model of Sec. 4.4 based on
Bessel functions to describe the modulated mechanical oscillation onto the electric reso-
nance $\{\exp[I\cos(\Omega_\mathrm{m}t)]\}$. For an easy quantitative comparison we plot the square of the
Bessel functions of first kind up to fourth order of the argument β from 0 to 7, as found in
Fig. 7.23a). Here, the nth-maximum is located at the intersection between the $n - 1$ and
$n + 1$ order. We have indicated this in Fig. 7.23a) by dotted lines for the $n = 1$ maximum,
located at the function arguments $\beta = 1.83$ and $n = 2$ at $\beta = 3.06$.

Further, we extract the resonant transmission of the microwave resonator $S_{21}(\omega_\mathrm{c})$ and the
nearby orders $S_{21}^n(\omega_\mathrm{c} + n\Omega_\mathrm{m})$ of up to fourth order. We plot this data as a function of
P_drive in Fig. 7.23b) (dots). In addition, we show the obtained transmission of the modeled
data from Sec. 7.8.2 (line). As we calculate the transmission change from unity, the plotted
data is expected to show the behavior from the top panel, cf. Eq. (4.34). We find good
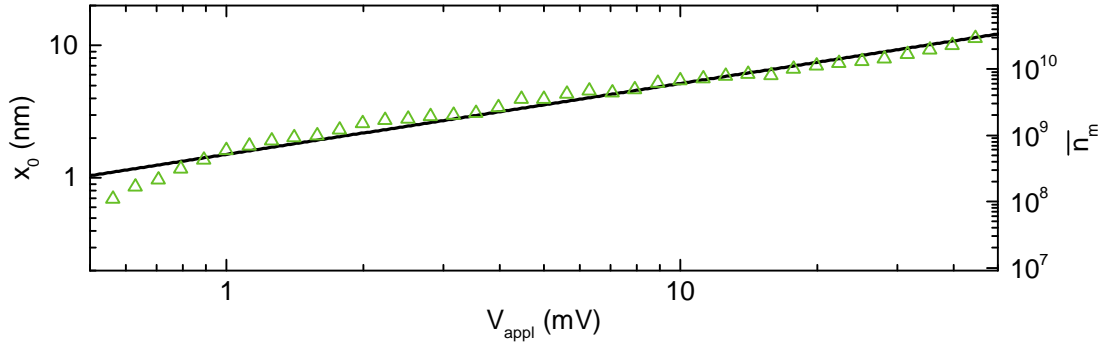
Figure 7.24: *Piezoelectric translation at millikelvin temperatures.* We show the extracted displacement obtained by modelling Eq. (4.34) to the data systematically over the applied piezo drive voltage. We were able to detect displacements between 0.7 and 10 nm. Analogue we can describe the displacement by the zero-point motion and the phonon numbers (right axis), for which we find excitations between 10^8 and $3 \cdot 10^{10}$. The scaling exponent of an allometric fit applied to the data (black solid line), reveals a square root behavior between displacement and piezo drive voltage, as expected. Minor deviations from this model are found for low drive voltages.

agreement with the Bessel theory, in particular as the intersection of $n+1$ with the $n-1$ order is identical with the maximum of the nth order. E.g. the maximum of $n=1$ (green) corresponds here to -42 dBm, or $n=2$ (orange) to -34 dBm.

7.8.4   Piezoelectric transduction

Previously, we have identified the experimental measurement to the mathematical description by a Bessel-model and identified two drive powers to the argument of the mathematical function β. In the following, we will now systematically compare the extracted β factors from the modeling to the drive power. This is realized by the identification of $\beta = Gx_0/\Omega_{\mathrm{m}}(\mathrm{or} = g_{\mathrm{m}0}\sqrt{2n_{\mathrm{m}}}/\Omega_{\mathrm{m}}$, cf. Eq. (4.30). Since the electromechanical coupling and mechanical frequency are already determined, we can use this to calibrate the string's displacement to the piezo driving force - and obtain the phonon numbers for highly driven strings.

In Fig. 7.24 we plot the obtained displacement from the fit model described by Eq. (4.34) to the data in Fig. 7.22a) as function of the piezo drive voltage $V_{\mathrm{drive}} = P_{\mathrm{drive}} \cdot 50\Omega$. We find displacements ranging from 0.7 to 10 nm, increasing with the piezo drive voltage. As we can express the displacement by $x_0 = \sqrt{2n_{\mathrm{m}}}x_{\mathrm{zpm}}$, we can calculate the phonon occupation number which we display on the right axis. Here, the obtained excitations range from 10^8 to above 10^{10}. For the functionality between displacement and piezo voltage we fit a power function (black solid line) and obtain

$$x_0 = (46 \pm 2) \cdot 10^{-6} V_{\mathrm{appl}}^{0.47 \pm 0.01} \tag{7.36}$$

revealing a proportionality of $x_0 \propto V_{\mathrm{appl}}^{1/2}$. The model deviates from the data for low drive powers, that we suspect to stem from only small deviations in the mechanical sideband transmission for low drive powers. Via the mechanical susceptibility of $\chi^{-1} = 2.2 \cdot 10^{-6}$ kg/s^2 on resonance, linking the displacement to a driving force,
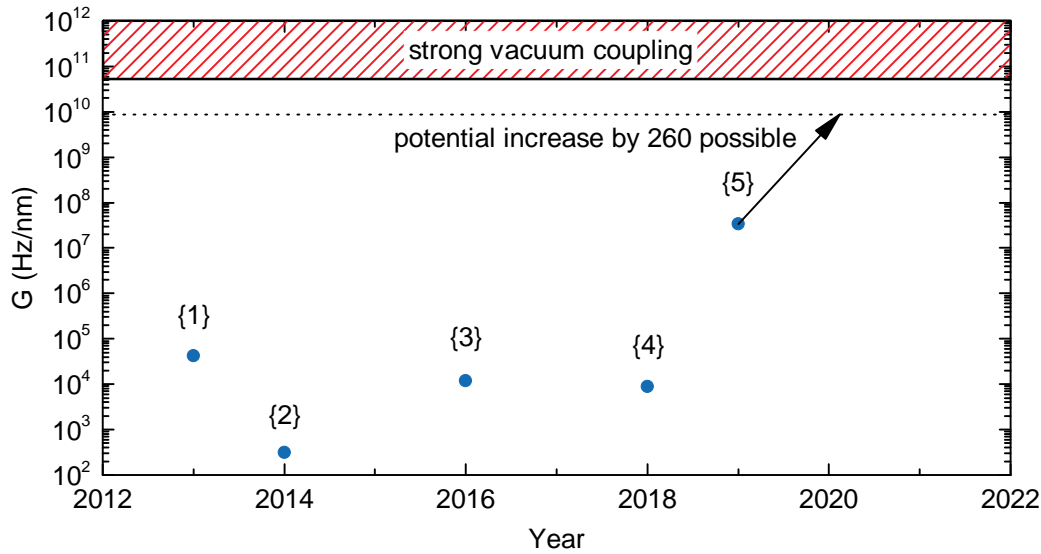
Figure 7.25: *Coupling development over time at the WMI.* In 2013 the development of electrome-
chanics was triggered by initial work of F. Hocke achieving a coupling strength in the kHz/nm
range. A dielectric coupling then was invented with ultra-high mechanical Q values, however
with a reduced coupling strength. All aluminum microchips with capacitively coupled strings
allowed a slight increase in the coupling strength. The integration of Josephson elements
showed only a minor loss in coupling strength in comparison to bare coupled resonators. By
the use of inductively coupled strings the coupling strength was enhanced by three orders of
magnitude, for moderate field strength already. We expect an additional increase by a fac-
tor of 260 when switching to an in-plane field configuration (dotted line). Given the current
resonator decoherence the strong single photon-phonon coupling is not yet in reach. Though
we expect the remaining gap can be reach by a design optimization of both the mechanical
coupling and the microwave resonator decoherence.

we can determine the induced force of the piezo to $0.1\,\mathrm{nN/V^2}$. The relatively small
force translation has to be seen in the context that the piezo is mounted on the sam-
ple box and the direction of its excitation is perpendicular to the nanostring, cf. Fig. 7.2b).

All in all we were able to push the electromechanical interaction having a high coupled
system and driving the mechanical motion to a region of $g_{\mathrm{m0}}x_0/\Omega_{\mathrm{m}} = 9.2$, revealing a
splitting of the electromechanical resonator up to 7th order. Further, we were able to
calibrate the phonon drive of the piezo for mechanical excitations in the billions.

7.9   Summary & Outlook

Within this chapter we have presented first experiments on inductively coupled systems.
The main motivation for this was to study a strong coupled electromechanical system. In-
deed, we reached coupling strengths above previous realizations in nano-electromechanics.
Also the predicted tuneability was confirmed.
By applying the magnetic field via an external (small) superconducting coil in out-of-plane
direction, we where able to precisely measure the fields, however only on a moderate scale
up to $0.5\,\mathrm{mT}$. The induced coil currents already heated the cryostat, such that the lowest
cryogenic temperature was limited to $120\,\mathrm{mK}$. Sideband cooling of the mechanical motion

was prevented by the negative nonlinearity stemming from the Josephson junctions. Further the junctions limited the applicable photon numbers to below 10 photons, setting the experiment on the imprecision limited range. Also, the external antenna of the sample was not working, such that the benefits of the tuneable coupling could not be investigated.

We therefor suggest for next experiments the application of in-plane magnetic fields, which are available in the cryostat. There, the field is not limited by the coils but the critical field of the superconducting aluminum film, which we found to be above 130 mT [cf. Sec. E]. Then the potential higher mechanical coupling of up to 0.4 MHz might allow for ground state cooling of the mechanical motion. For the detection of such low excited strings we however suggest the installation of quantum limited amplifiers. It will also be of interest how the noise performance turns out in the highly coupled configuration.

An additional external antenna can be used to squeeze the microwave field in the resonator, which allows to control the noise contributions potentially reaching higher force sensitivities. Also, the electromechanical coupling can be tuned parametrically such that the mechanical motion can be amplified or cooled.

We like to conclude by a short summary of the realized coupling values G to demonstrate the future road map towards strong vacuum coupling. For this we have plotted previous results from the Walther-Meißner-Institut ([100]$\rightarrow$ {1}, [90]$\rightarrow$ {2}, [43]$\rightarrow$ {3}, and [34]$\rightarrow$ {4}) in combination with the current work ({5}) in Fig. 7.25. It shows the realized increase of the coupling strength by a factor of 400 within this framework. Further, we have indicated the limitations when switching to in-plane fields (black dotted line) for this sample of first generation. For a strong vacuum coupling both mechanical and electric elements have to be further optimized, as with the given sample a gap by a factor 20 remains.

Chapter 8

Future prospects in hybrid c-QED devices

It is difficult to make predictions, especially about the future.

Niels Bohr, [168].

Within this thesis we studied mechanical oscillators integrated in superconducting quantum circuits, by using evaporated aluminum on silicon microchips as a basis. The hybrid circuits form coupled systems of a mechanical oscillators and electromagnetic resonators allowing for the realization of photon-phonon interaction. The electromagnetic resonator is made intrinsically nonlinear by building in a dc-SQUID acting as nonlinear loss-less inductance. In this way, a novel inductive coupling scheme with enhanced coupling strength has been implemented. As we use quasi-onedimensional doubly clamped nanostring oscillators as the mechanical element, the resulting total coupling strength of 1.6 kHz is significantly higher than any previous realization in superconducting resonators. In addition, we showed how such nanomechanical quantum systems can be used as an ultra-wide range photon, and precise temperature sensor.

This thesis builds up on previous work by F. Hocke and M. Pernpeintner, who built up electromechanical hybrid systems, realized by coupling nanostring oscillators capacitively to a superconducting linear LC-circuit. M. Pernpeintner *et al.* then theoretically described a a coupled qubit-mechanical resonator system and showed how such a system can be used to generate non-classical mechanical states. D. Schwienbacher then developed a fabrication process that allowed the combined fabrication of transmon qubits and mechanical string oscillators on the same microchip. In this thesis one of these samples was spectroscopically analyzed in detail. We then unfolded a fabrication process that allows the direct integration of a mechanical element in a Josephson junction circuit and investigated a transmission line resonator containing a mechanical dc-SQUID. This system is based on an inductive coupling scheme and for the first time led to a photon-phonon coupling in the kHz-regime. Together with N. Segercrantz we were also able to fabricate the circuit design proposed by Pernpeintner consisting of a capacitively coupled string in a transmon qubit.

In the first parts of this thesis we theoretically describe the concepts and methods deployed here.

Beginning with the example of a classical harmonic oscillator we showed how both mechanical oscillators and electric resonators can be reduced to this configuration and highlighted the differences between time and frequency domain measurements. Next we compared the classical oscillator to an harmonic quantum oscillator. This made clear that the observation of quantum mechanical states in the literal sense requires a sufficient cooling of the mechanical motion. As the lowest phonon number shown here was around 130 phonons, overcoming the limitations of sideband cooling imposed by the use of quantum circuits for electromechanical systems remains an important point to exploit in future studies.

We then discussed the concepts of circuit electrodynamics and described the dynamics of a nonlinear circuit consisting of a dc-SQUID integrated in a transmission line resonator, which allows to read-out the dc-SQUID flux in the microwave domain (FTR). We additionally showed that a transmon qubit can be derived from such a system, highlighting the similarities between a FTR and a transmon qubit. We further showed an important limitation of such systems, a reduced applicable photon number. Due to this limitation, the typical electromechanical approach of enhancing the coupling by the amount of photons is no longer possible on the typical orders.

Next we discussed the optomechanical concepts employed here. We focused on the displacement spectra and discussed the electromechanical noise contributions. Due to the limited amount of photons, we found out to be imprecision limited even for the relatively high coupling strength observed here. In such a scenario the signal peak area is drastically reduced. As the area scales with the amount of phonons in the mechanical oscillator this was overcome by sensing thermally excited states far above the single phonon level, and externally driven ones.

Future potential studies in the single phonon range could benefit from quantum limited detection, realized by the use of Josephson parametric amplifiers, which we tested within this framework. Another achievement which can be leveraged further, was the realization of a cryogenic microwave interferometer by placing a piezo-actuator at the sample box. The active drive of the mechanical oscillator allowed to overcome the restrictions of the low photon numbers in the nonlinear quantum circuits and detect the mechanical motion on the single photon level. Additionally we implemented a time domain setup to study the qubit state decoherence. In combination with the cryogenic microwave interferometer this allows to study the dephasing of the qubit in the presence of a high mechanical displacement density, which could act as a fast qubit reset.

The capacitive coupling of a transmon qubit and a nanostring oscillator to the exact same microwave resonator was analyzed spectroscopically. We were able to characterize the subsystems individually. In combination, we were able to determine the photon number in the shared microwave resonator spanning nine orders of magnitude between lowest and highest detected occupation.

Further we used the electromechanical resonator to perform transmon measurement in the time domain to detail its coherence. We found a limitation caused by two-level fluctuators and magnetic field fluctuations. The magnetic field fluctuations can be reduced in future experiments by superconducting screening boxes that we developed. A final conclusion whether the fluctuators on the surface of the microchip, arise from the fabrication of the

qubit (e.g. insufficient surface cleaning), or from etching processes when releasing the nanostring (RIE etching), remains open for future studies on these electromechanical hybrid microchips. However, the qubit decoherence only needs to be sufficient long for a state transfer protocol, as we aim for a state storage within the mechanical element. So the coupled qubit-mechanical system's state storage time will be limited by the thermal storage time of the mechanical element. We were able to show a potential thermal storage time of $38\,\mu$s for the given sample of first generation.

The lower coupling to the electric resonator and its linewidth broadening for high photon numbers prevented an effective cooling of the mechanical motion, such that we were only able to cool to 130 phonons using a red detuned sideband drive.

The low electromechanical coupling strength can be enhanced by directly integrating the nanostring in the qubit. The fabrication techniques introduced here allowed the development of such a sample.

Also a mechanical dc-SQUID was integrated in a transmission line resonator. The resulting frequency tuning was described by the theory introduced previously.

The decoherence of the microwave resonator was limited by two-level fluctuators, similar to the qubit. Additionally we found that the loss due to scattering on quasi-particles becomes dominant above $250\,$mK. We speculate this scattering to arise at the surface oxide. Further, we found a linear dependence on the resonator linewidth to the frequency slope, which sets a limit for the quantum parameter g_{m0}/κ

The nanostring' frequency tuning over temperature suggests that in previous studies on capacitive coupled systems thermally induced charge prevented the observation of the intrinsic string behavior. Without the coupling capacitance in the explored inductively coupled system we found agreement to previous studies on aluminum nano-oscillators at millikelvin temperatures. Moreover, we were able to extend the observed lengthscale, which showed a significant deviation from the universal regime of amorphous materials, due to the longer string length. We also compared the temperature precision one can achieve using the string parameters of a published aluminum string as an on-chip temperature sensor to the regular resistive read-out, and found the string's sensitivity one order of magnitude higher than the resistive one.

As this thesis shows the first observation of an inductively coupled electromechanical system, we characterized the electromechanical interaction in detail for moderate magnetic field values to precisely determine its characteristics. The highest determined electromechanical coupling was $g_{\mathrm{m0}} = (1.62 \pm 0.12)\,$Hz. In addition, the limitations of the critical photon number induced by the Josephson junctions lead to a dominant imprecision noise floor. However, due to the low mass of the nanostring and the high coupling strength, we found a sub-attonewton force sensibility accessible at the single photon level. We further confirmed the predicted linearity of the coupling strength to the frequency slope and the applied external field.

The negative nonlinearity of the flux tunable resonator made a sideband cooling challenging as an increasing red sideband drive power shifted the resonance towards it, further increasing the photon numbers and so the shift. With this, instabilities and flux jumps occurred, preventing an effective cooling given the current coupling strength. Therefore we suggest to investigate the cooling in future studies at higher fields enhancing the interaction, as the required photon numbers are reduced quadratically by the coupling

strength.

We further showed that the external driving of the mechanical oscillator allowed to push the electromechanically induced frequency shift above the oscillators frequency, leading to the observation of discrete splittings on the microwave transmission. The analyzed shift was on the order of $Gx/\Omega_{\mathrm{m}} = 9.2$ and $Gx/\omega_{\mathrm{c}} = 8.5 \cdot 10^{-3}$, becoming comparable to the eigenenergies of the system. Further increasing the single photon-phonon coupling using higher magnetic fields could lead to a potential coupling strength of $400\,\mathrm{kHz}$. Reaching the strong single photon-phonon coupling regime however requires future effort on the microwave decoherence. A lower decoherence is of particular interest, as the string's length then can be increased, remaining still within the resolved sideband regime. The longer string length then enhances the electromechanical vacuum coupling strength.

Further studies on inductively coupled systems could arise from an external microwave drive, e.g. by adding an antenna in close proximity to the dc-SQUID. This could allow to squeeze the electric (vacuum) field of the microwave resonator. A hybridization of the electrical and mechanical system (red sideband drive), could allow for the generation of highly squeezed mechanical states, and thus enhance the resolution of the mechanical displacement. An additional feature of such an antenna in combination with the tunable coupling is that it would allow for a fast tuning of the coupling on the time scale of the mechanical oscillator, driving it parametrically.

The similarities between a flux tunable resonator and a transmon qubit derived in Sec. 3.4.1 show that the inductive coupling realized within this thesis can be directly transformed to transmon or charge qubit designs. Those have a much higher nonlinearity as they can be approximated as two-level system, and so quantum superposition states can be generated [57]. With the mechanical element directly integrated in the qubit circuit the realization of, e.g. mechanical cat states, then seems straightforward.

The main achievement within this work was the detection of mechanical motion via a dc-SQUID integrated in a microwave resonator. In this realization, the study of the mechanical motion benefits from established electromechanical techniques, such as sideband cooling. Further, the nonlinearity of the electric resonator can be parametrically driven and so apply squeezed light for the investigation of the mechanical motion. By this a higher precision in the read-out sensitivity can be reached in comparison to coherent light. The observed behavior of such flux tunable resonators as a mechanical displacement detector are an important technical development for the detection of quantum gravitational motion emphasized within the framework of the MaQSens project.

In summary we realized electromechanical hybrid systems consisting of nanostring oscillators and electrical quantum circuits. This combination allows precise sensing applications, like photon numbers, temperatures, displacements, and forces. Further the high mechanical quality can be used as a compact on-chip storage of quantum information processed within c-QED circuits.

Appendix A

Detailed microwave setups

A.1 Ultra-wide range photon number calibration

The setup consists of two *Rhode & Schwarz SMF100A* and a *Agilant E8257D* microwave sources as well as a *Rhode & Schwarz ZVB8* vector network analyzer and *FSV signal analyzer*. One SMF and the network analyzer are combined by a *Marki PD 0220* power combiner. The signal is lead into an *Oxford Instruments Triton* cryofree dilution fridge. The input line is attenuated by 10 dB at 40 K, 6 dB at 4 K and another 6 dB at 700 mK. At the mixing stage the input signal is additionally attenuated by 10 dB and a *Miteq 2000-18000-20C* 20 dB directional coupler before it reaches the sample. After it a *QuinStar CTH0408KCS* circulator and for symmetry an additional 20 dB directional coupler, this time in through connection, is placed. Before leaving the mixing chamber stage, a second circulator is placed. After, the signal is lead to another circulator at the 4 K stage, followed by a *MiniCircuits VBFZ-5500+* bandpass filter before it reaches a *Low noise factory LNC4-8A* low noise cold amplifier and is send outside the fridge. At room temperature the signal is filtered by a *MiniCircuits MC-VBFZ-5500+* bandpass filter and amplified by an *Agile-amt-A0033* broadband amplifier before it reaches a *MITEQ CD 401-802-20s* coupler. 1 % of the signal is amplified by a broadband microwave amplifier and send to the network analyzer. The rest of the signal is lead to the rf input of a *Marki IQ 0307 LXP* IQ mixer. The second SMF is send to the lo input after the mw phase was adjusted by a *Aeroflex/Weinschel Coaxial Phase Shifter*. One quadrature was shunted while the other one, containing the full signal, is filtered by a *MiniCircuits LowPass 0-48MHz*, amplified via a *FEMTO DHPVA-200 voltage amplifier*, and send to the signal analyzer. The Agilent microwave source is directly lead to the cryostat where it is attenuated by 10 dB at 40 K, 20 dB at 4 K, 20 dB at 700 mK and 20 dB at the mixing chamber stage before the signal reaches the antenna of the qubit. To control the current through the magnetic coil we use a *Yokogawa GS-200* current source.

A.2 Inductively coupled electromechanics

The microwave setup for the detection of inductively coupled nanostrings is depicted in Fig. A.1. The microwave tones are generated using a *Rhode & Schwarz SMF100A* or *Rhode & Schwarz ZVA8* vector network analyzer (VNA). The VNA output is attenuated by

$-20\,\mathrm{dB}$ and equally split up by a Marki PD 0220. One part is send to the piezo actuator, while the other is combined with the SMF source by a Miteq PD 2-2000/8000-30S. The input line is attenuated by $-42\,\mathrm{dB}$ in total, where $-20\,\mathrm{dB}$ are achieved by the use of a microwave coupler *Miteq 2000-18000-20C*, In particular the signal is attenuated by $-10, -6$ and -6 at the $40, 4.2$ and $1.5\,\mathrm{K}$ stage. Next, the signal is guided to the sample, where it capacitively couples to the electromechanical resonator, c.f. panel b). The output line is further screened from thermal noise using three circulators *QuinStar CTH0408KCS* before it is amplified using a high electron mobility amplifier (HEMT) *Low noise factory LNC4-8A*, thermalized at $4\,\mathrm{K}$. At room temperature the signal is send to a *DITOM D3I4080* ciculator and further amplified using a *Miteq AFS*. Afterwards, the signal is splitted up by a *Miteq CD-402-802-20S* $-20\,\mathrm{dB}$ coupler. One percent of the signal then is amplified by a AMT A0033 and detected via the vector network analyzer. The other part is also amplified in a *AMT A0284* before it is homodyne downconverted using a *Marki MLIQ 0416-L* mixer. An additional Rhode & Schwarz SMF100A acts as local oscillator. We add I and Q and amplify the signal via a *Femto DHPVA*. The signal is then either directly send to a *Rhode & Schwarz FSV* spectral analyzer or to a *MiniCircuits ZFRSC-183-S+* where it is combined with the high frequency signal.

The dc-field bias was set by a self-made superconducting coil with a current controlled by a *Yokogawa GS 200*. Antenna lines were not used.

In a second configuration, shown in Fig. A.1d) we rewire the input signal, such that the network analyzer only probes the microwave transmission and the SMF source directly drives the piezo crystal. By this we make sure that the high drives required in the specific experiments in Sec. 7.8 are only send to the particular elements.
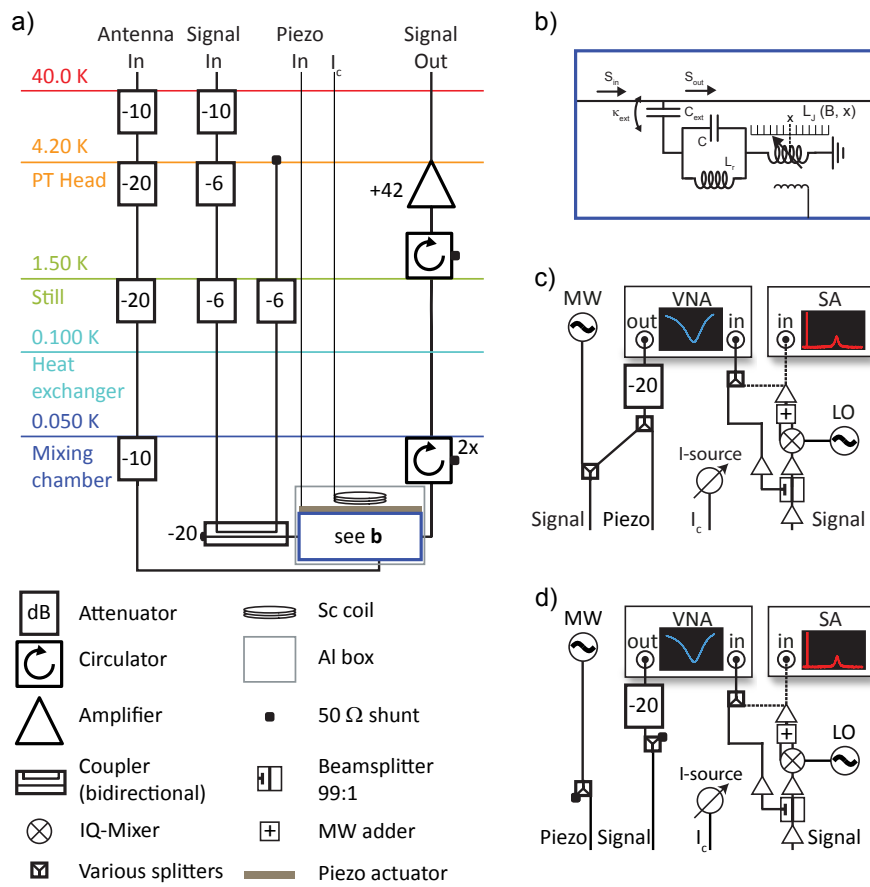
Figure A.1: *Details on the employed microwave setup.* Panel a) shows the cryogenic microwave cabling. Panel b) displays the circuit diagram of the nanomechanical sample. Panel c) and d) detail the room temperature wiring.

Appendix B

Frequency downshift of a flux tunable microwave resonator

The integrated dc-SQUID causes a power-dependent shift of the resonator's eigenfrequency, since a probe tone causes a current through the Josphson junctions. This can be modeled an additional inductance. We can account this power or current dependent inductance by [36]

$$L_{\mathrm{S}}(I, \Phi) = L_{\mathrm{J}} + L_2 (I/I_{\mathrm{c}})^2, \tag{B.1}$$

including a parabolic correction term. Then the resonator's eigenfrequency [c.d Eq. (3.22)] becomes

$$\omega_{\mathrm{c}}(I, \Phi_{\mathrm{ext}}) = \omega_0 \left(1 + \frac{L_{\mathrm{Loop}}}{4L_{\mathrm{c}}} + \frac{L_{\mathrm{J}}}{L_{\mathrm{c}}} + \frac{L_2 (I/I_{\mathrm{c}})^2}{L_{\mathrm{c}}} \right)^{-1}. \tag{B.2}$$

The definition of the unperturbed resonator frequency $\omega_{\mathrm{c}}^0(\Phi_{\mathrm{ext}}) = \omega_{\mathrm{c}}(0, \Phi_{\mathrm{ext}})$ allows to describe Eq. (B.2) via the nonlinear terms:

$$\omega_{\mathrm{c}}(I, \Phi_{\mathrm{ext}}) = \omega_{\mathrm{c}}^0(\Phi_{\mathrm{ext}}) \left[1 - \frac{L_2}{L_{\mathrm{c}} + L_{\mathrm{Loop}}/4 + L_{\mathrm{J}}} \left(\frac{I}{I_{\mathrm{c}}} \right)^2 \right] \tag{B.3}$$

In the experiment, c.f. Sec. 7.4.3, we set the resonator at a certain flux bias at ω_{c}^0. Next, we apply a weak probe tone at the resonator's initial frequency $\omega_{\mathrm{p}} = \omega_{\mathrm{c}}^0$. Then an additional weak tone probes the resonators transmission for a systematic sweep of the (constant frequency) probe tone power. At a certain power, the resonator starts to shift downwards. We find a shift increasing with $P_{\mathrm{appl}}^{1/3}$.

To derive this behavior we describe the currents in the SQUID loop being proportional to the probe tone power, that is $(I/I_{\mathrm{c}})^2 = c\bar{n}_{\mathrm{c}}$. For the experimental setup the photon number in the $\lambda/4$ microwave resonator is described by [98]

$$\bar{n}_{\mathrm{c}} = \frac{4P_{\mathrm{p}}}{\hbar\omega_{\mathrm{p}} \left(\kappa^2 + 4\Delta_{\mathrm{p}}^2 \right)}. \tag{B.4}$$

Further, as in the experiment, we set $\omega_{\mathrm{p}} = \omega_{\mathrm{c}}^0$. Solving Eq. (B.3) and (B.4) then leads to

$$\omega_{\mathrm{c}} \approx \omega_{\mathrm{c}}^0 - (\frac{L_2 L_{\mathrm{c}}}{L_{\mathrm{J}} + L_{\mathrm{Loop}}/4} \frac{c\kappa_{\mathrm{ext}}}{\hbar})^{1/3} \ P_{\mathrm{p}}^{1/3} \tag{B.5}$$

when the resonator is sufficiently shifted from the initial frequency ($\Delta_\mathrm{p} > \kappa$). As in the experiment confirmed, the microwave resonator is expected to shift by $P_\mathrm{p}^{1/3}$.

C
Appendix

Aluminum magnetic field screening boxes

For the sufficient magnetic field screening we constructed aluminium boxes that become superconducting at the typical experimental temperatures. The challenge in the construction was to fit them for both sample boxes and JPA devices. This allows for full flexibility in planning the experimental setup. However the samples require up to 5 microwave lines, while the JPA requires 2. A solution was found by constructing an asymmetric lid. Then a rotation by π blocks the asymmetrically designed wiring, while symmetric ones remain open.

We show an image of the constructed boxes in Fig. C.1a). Here, the mounted sample is shown in panel a). We see up to 5 lines that are potentially addressable.

The lid asymmetry is shown in panels b) for the open configuration, and panel c) for a closed one. One finds the center lines on the left, open always independent of the lid rotation. On the right side of each figure the additional microwave lines for the sample are shown, that can be closed depending on the lid rotation.

In addition, we allowed a thermalization of the sample, which is important as the superconducting aluminum has a very low thermal conductivity. Further some feedthroughs for dc-cables were also added to the box design.

The construction design is attached in the next pages.

4x45° M2 8mm tief

Ø 48,00

Reihenfolge:
DC
MW
Therm

HM 14,00

8,25 8,25

MW

MW

A   A

Reihenfolge:
DC
MW
Therm

C
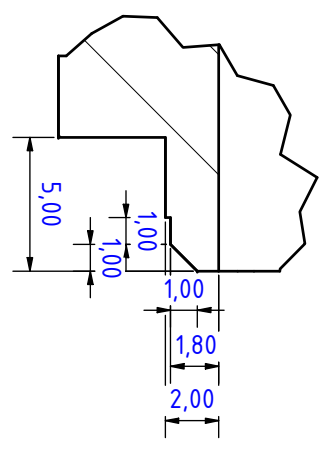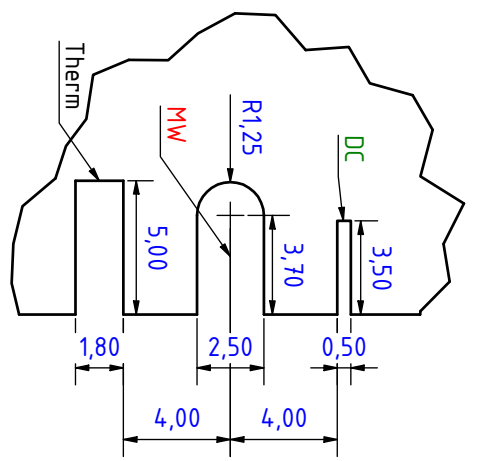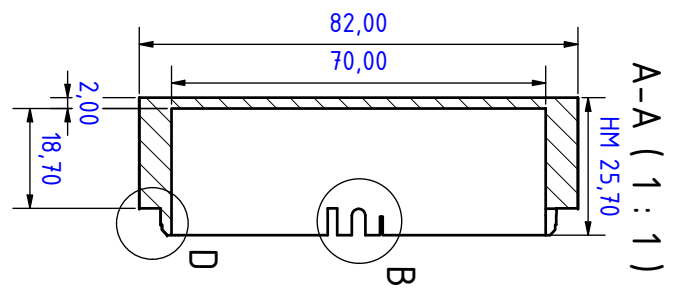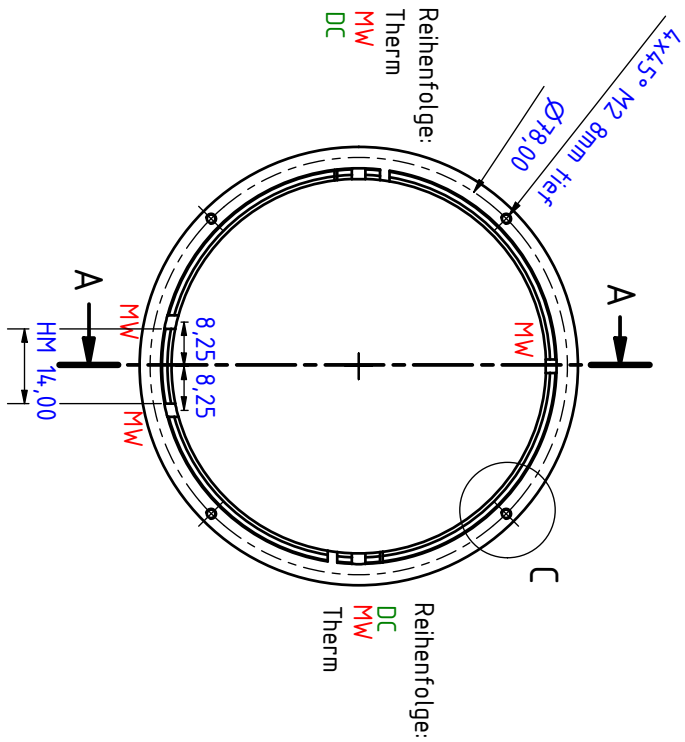
C (5 : 1)

Alle Größen
in C = HM

R41,00
R37,00
R36,80
R35,80
R35,00

A–A (1 : 1)

82,00
70,00
2,00
18,70
HM 25,70

D

B

B (5 : 1)

Therm

MW

R1,25

DC

5,00
3,70
3,50
1,80
2,50
0,50
4,00
4,00

D (5 : 1)

5,00
1,00
1,00
1,00
1,80
2,00

Teil:
Schmidt_Triton_Alushielding_top
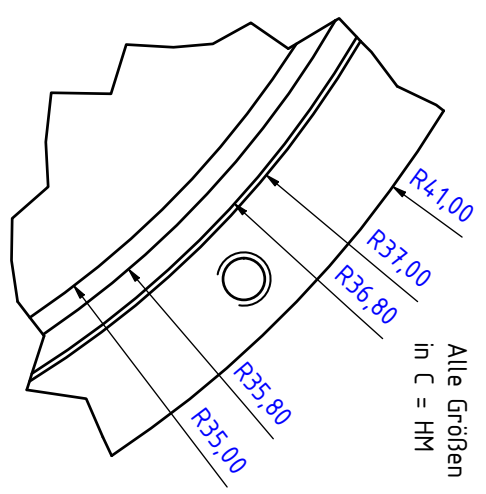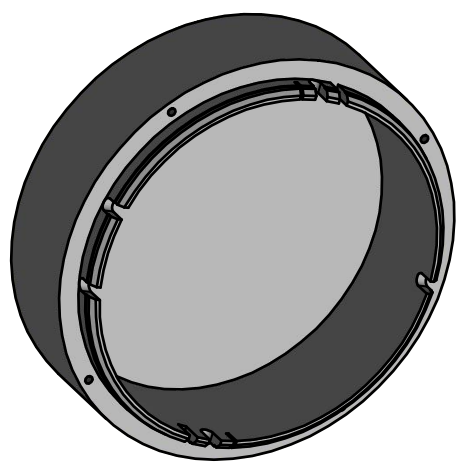
Name: Philip Schmidt
Datum: 12.12.2016
Stückzahl: 1 Stk.
Maßstab 1:1
Material: Aluminium
HM: Hilfsmaß zur Orientierung

Teil:
Schmidt_Triton_Alushielding_bottom
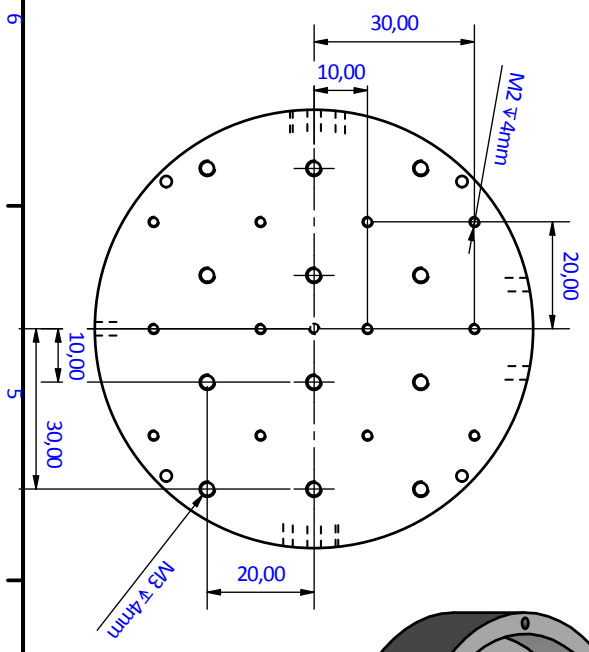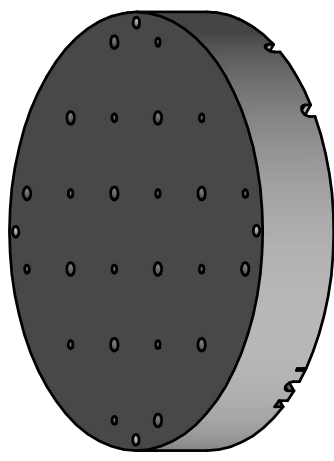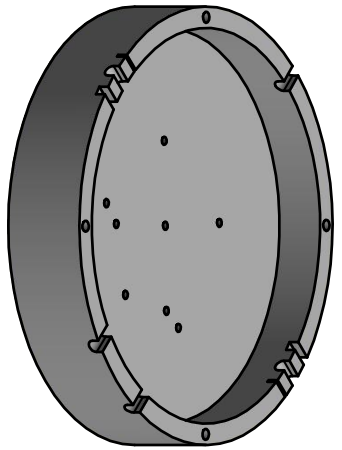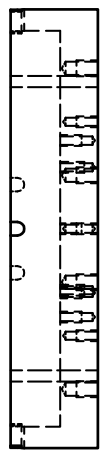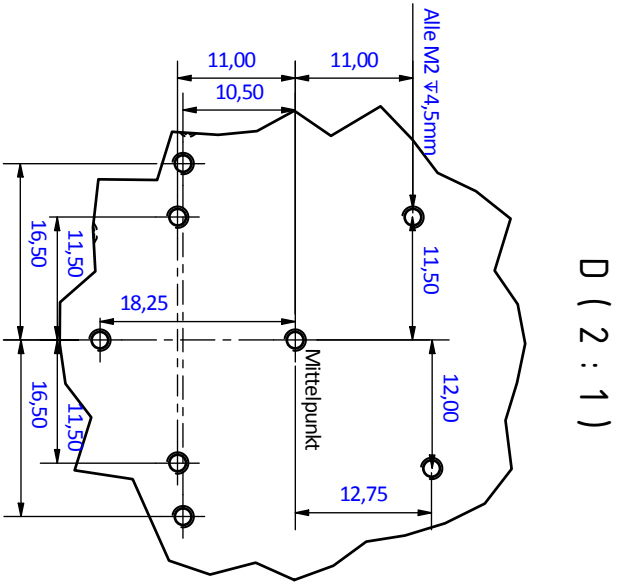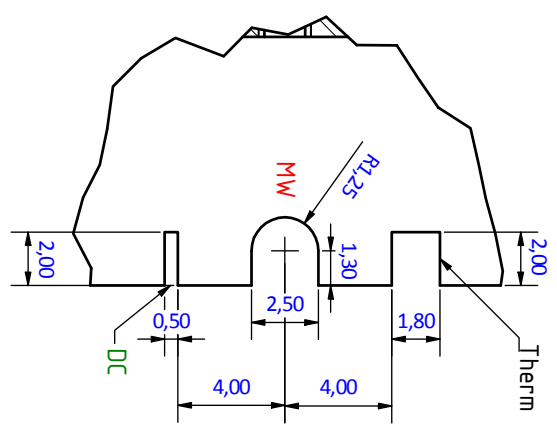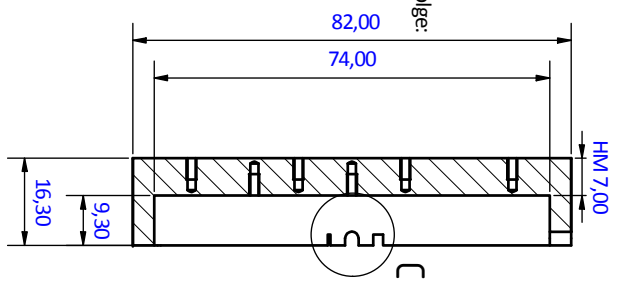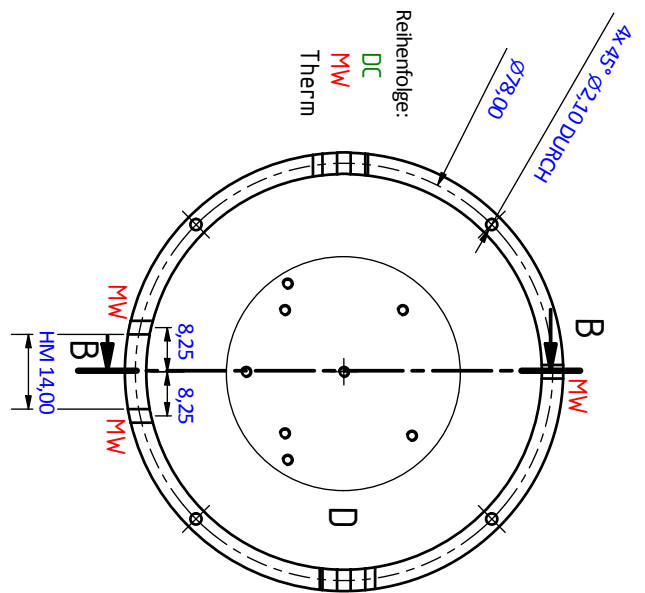
Name: Philip Schmidt
Datum: 15.12.2016
Stückzahl: 1 Stk.
Maßstab 1:1
Material: Aluminium
HM: Hilfsmaß zur Orientierung

30,00
10,00
M2 ▽4mm
20,00
10,00
30,00
M3 ▽4mm
20,00

Reihenfolge:
DC
MW
Therm

Ø78,00
4x 45° Ø2,10 DURCH

MW
HM 14,00
8,25
8,25
B
MW
B
MW
D
Reihenfolge:
Therm
MW
DC

82,00
74,00
B-B (1 : 1)
HM 7,00
16,30
9,30
C

MW
R1,25
1,30
2,00
2,00
0,50
2,50
1,80
DC
4,00
4,00
Therm
C (5 : 1)

11,00
11,00
Alle M2 ▽4,5mm
10,50
16,50
11,50
18,25
11,50
12,00
16,50
Mittelpunkt
12,75
D (2 : 1)

Figure C.1: *Magnetic screening boxes.* Panel a) mounted sample in the constructed aluminum box. Panelb) and c) show the flexibility to use the boxes either for JPA microchips (two MW input lines) or for multiplex sample gemeometries (up to five MW lines).

Details on the temperature calibration

The discussion of the resistive temperature sensitivity is based on the calibration measurements by Dr. K. Neumaier, who determined the resistivity of the sensor at a calibrated temperature. The results are shown in Fig. D.1. An exponential increase is found, in accordance to the literature prediction [169]:

$$R = R_0 \exp\left[\left(\frac{T}{T_0}\right)^x\right], \text{(D.1)}$$

for which we find an intrinsic resistance of $R_0 = 630\,\Omega$, an critical temperature of $T_0 = 1.69\,\text{K}$ and an temperature scaling of $x = 0.39$. For the model we have excluded deviations from the model (grey) that might have been caused by the calibration measurement and only take the data at higher temperatures (blue) into account [170]. With the stated parameters we find good agreement between data and theory.
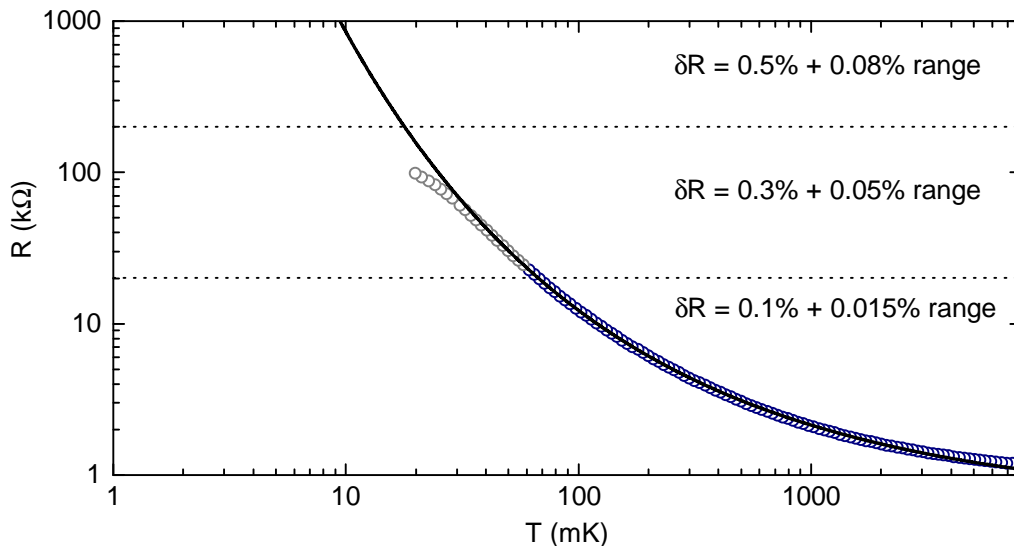
Figure D.1: *Calibration of the applied temperature sensor 'ldd0'.* The resistivity measured by K. Neumaier over a calibrated temperature is for the temperature sensor used in Sec. sec:ChapInductive is shown. An exponential increase is modeled to the data (black solid line). Deviations at low temperatures (grey) were excluded from the data of the modeling (blue). Further, the resistance bridge accuracy ranges are indicated.

By this we can determine the slope of the resistivity by either deriving Eq. (D.1) over temperature:

$$\frac{\partial R}{\partial T} = R_0 \exp\left[\left(\frac{T}{T_0}\right)^x\right] \frac{x}{T}\left(\frac{T}{T_0}\right)^x, \tag{D.2}$$

or we derive the measured data, as shown directly from the measurement data.

Important for the read-out accuracy is the precision of the resistance measurement set by the resistance bridge. This is specified by the manufacturer in Ref. [162]. The corresponding ranges for the employed excitation voltage of $6.32\,\mu$V are displayed in Fig. D.1.

Flux tunable resonators in high in-plane magnetic fields

Within this thesis we discussed an inductively coupled circuit for electromechanical devices. An advantage of this coupling scheme is that it allows us to reach a record coupling strength of 1.6 kHz. Another benefit is the tunability of the coupling by the applied magnetic field. The measurements present here were done for moderate out-of-plane fields of 0.5 mT maximum, which has the positive effect, that we can precisely set and determine the external field to study its influence on the coupling strength. However the question arises how far the coupling can be boosted when switching to an in-plane field configuration, where the critical field of the superconductor is supposed to be higher than in the out-of-plane one.

To determine the critical field, we have mounted a similar circuit as presented within this work (however without any mechanical element) within the center of a 1-1-7 T x-y-z vector magnet, as shown in Fig. E.1a). The z-direction has the ability to use a persistent current
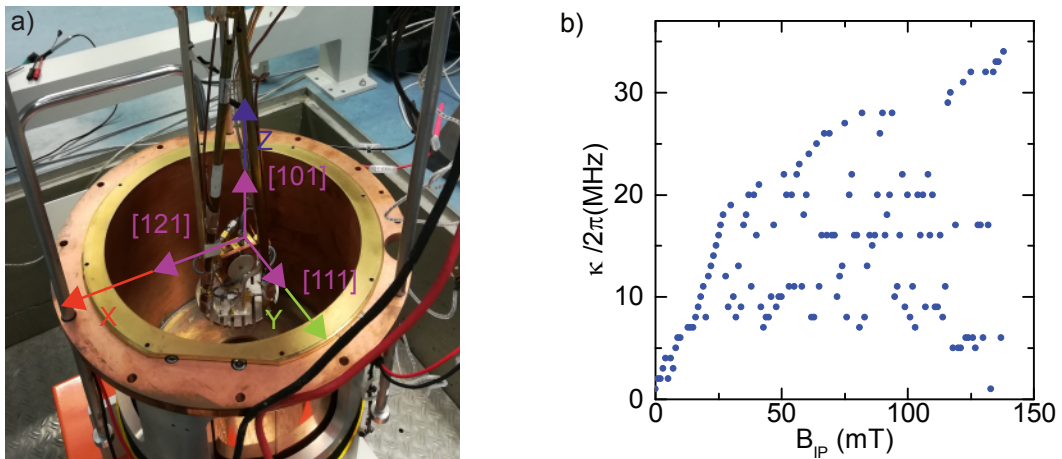
Figure E.1: *Aluminum flux tunable microwave resonators exposed to high in-plane fields.* Panel a) shows the measurement configuration, consisting of large vector magnets (unmounted) that allow us to apply up to 7 T via a persistent current switch in z (in-plane). Additionally an external coil found at the center allows to set precise out-of-plane fields. Panel b) displays the extracted resonator linewidth at the sweet spot over the applied in-plane field. We were able to follow its signature up to 130 mT.

switch, which reduces field fluctuations from the applied coil current. Further, we mounted a small coil on top of the sample box, which allows us to set the resonator flux bias.

We then set an in-plane field in z-direction using the persistent current switch. We probed the microwave transmission to determine the eigenfrequency ω_c and linewidth κ of the resonator. Further, we swept the out-of-plane field to determine these parameters in dependence of the resonators working spot. Then we increased the in-plane field and repeated the flux bias sweep.

By this we were able to observe the resonator transmission for in-plane fields of up to $130\,\text{mT}$, a potential enhancement of the coupling by 260, with a maximum coupling strength of $460\,\text{kHz}$.

We like to note, that when trying to reach the strong-coupling regime, $g_{m0} > \kappa$, one also has to study the effects of such high fields on the resonator linewidth. This we study in Fig. E.1b), where we plot the extracted linewidth of the resonator at its sweet spot ($\kappa(\Phi = 0)$). We find an increase of up to $30\,\text{MHz}$, so a factor of 10.

We conclude that the in-plane field configuration shows the potential to come closer to the strong coupling regime as the broadened linewidth is weaker than the increase in the coupling strength. Moreover the cooperativity is drastically enhanced, as here the coupling enters quadratically ($C = 4g_{m0}^2/(\kappa\Gamma_m)$).

Calibration of the electromechanical coupling strength via driven strings

A big benefit of the inductive coupling is that it is flux tunable ($\partial\omega_{\mathrm{c}}/\partial\Phi$) and controllable by the applied magnetic field [cf. Eq. (7.3)]. By that we expect a linear scaling of the vacuum coupling rate g_{m0} with both parameters. A possible solution to explore this scaling behavior are experiments using the thermal displacement noise of the nanostring. A more time efficient way however, is to measure the frequency shift $\delta\omega_{\mathrm{d}}$ of the microwave resonator at a fixed mechanical drive power. Here, the string displacement is significantly increased which allows a faster data acquisition. In particular, we use a piezo actuator mounted on the sample box to drive the mechanical motion. For a fixed drive power we then measure the driven frequency shift $\delta\omega_{\mathrm{d}}$ of the microwave resonator as functions of $\partial\omega_{\mathrm{c}}/\partial\Phi$ and .

The setup used for this experiment is shown in Fig. A.1a) and c). The cryostat is set to $T_{\mathrm{sample}} \approx 120\,\mathrm{mK}$. We will begin with the investigation via $\partial\omega_{\mathrm{c}}/\partial\Phi$ at a constant value of $\approx -440\,\mu\mathrm{T}$. We measure $\delta\omega_{\mathrm{d}}$, by subjecting a constant microwave tone on-resonance to the microwave resonator ($\Delta = 0$). The signal is then homodyne down-converted using a local oscillator. Moreover, we use the VNA to drive the piezo and so apply an oscillating force to the nanostring. When the mechanical resonance is matched, we induce a mechanical displacement which causes the microwave resonator frequency to shift, according to the electromechanical Hamiltonian. Then this shift is recorded via the VNA. In a more detailed way, the detected power of the vector network analyser P_{hom} is proportional to the frequency shift $\delta\omega_{\mathrm{d}}$. In analogy to Ref. Pernpeintner2014 we define

$$\frac{P_{\mathrm{hom}}}{Z_0} \equiv \frac{2}{\Omega^2} \left(\delta\omega_{\mathrm{d}}\right)^2 . \tag{F.1}$$

Here, contains the characteristics of the microwave resonator and so relates to the induced resonance frequency shift of the nanostring to the recorded power. These characteristics, in particular κ_{ext} and κ_{int} setting are determined from measurements on the microwave resonator transmission after each experiment. With this we are able to relate the measured P_{hom} to a quantity proportional to the frequency shift $\delta\omega_{\mathrm{c}}$. We show such spectra in Fig. 7.19 as frequency shift $\delta\omega_{\mathrm{d}}$ derived from Eq. (F.1) and the recorded P_{hom}. Next, we extract the amplitude of the peak at Ω_{m} by fitting a lorentzian lineshape to the data Ω_{m}. The extracted amplitudes ($\delta\omega_{\mathrm{d}}(\Omega_{\mathrm{m}})$) are found in Fig. F.1 for two different piezo drive
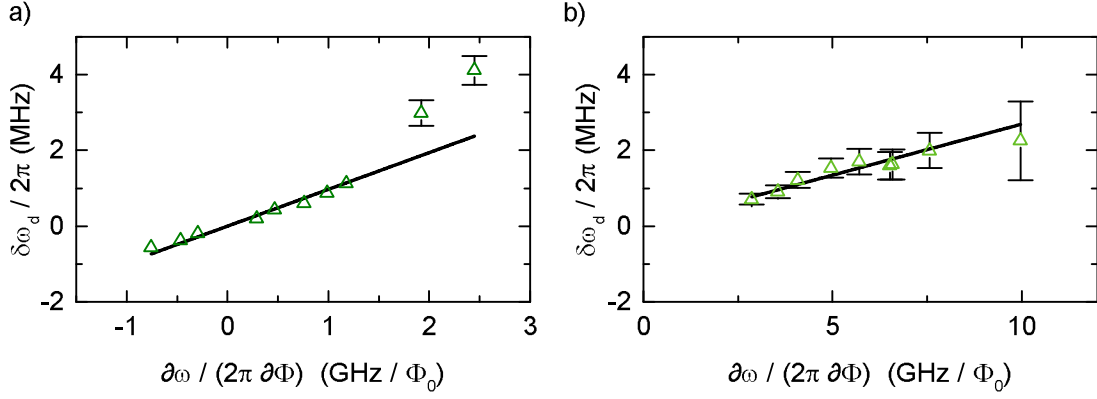
Figure F.1: *Driven frequency shift.* Panel a) displays the extracted frequency shift from Fig. **??** over the resonator responsivity $\partial\omega_\mathrm{c}/\partial\Phi$. We multiplied the coupling strength by -1 in the case of negative responvities to highlight the linear dependence beyond the sweet spot. We confirm the linear tuning. Panel b) shows the frequency shift for higher responsitivities, with a reduced piezo drive power. Here, we confirm the linearity for responsitivites up to $10\,\mathrm{GHz}/\Phi_0$. If not shown, the error bars are smaller than the marker size.

amplitudes.

For our analysis we further assume, that independent of the particular coupling strength, the fixed mechanical drive power is exciting a fixed mechanical amplitude. So the recorded $\delta\omega_\mathrm{d}(\Omega_\mathrm{m})$ is proportional to g_m0 and allows us to rescale these datapoints to the scaling presented in Fig. 7.20.

Figure F.1a) and b) show the extracted $\delta\omega_\mathrm{d}(\Omega_\mathrm{m})$ as function of the flux responsivity $\partial\omega_\mathrm{c}/\partial\Phi$. In both panels, a linear dependence is observed. To remain in the linear transduction regime of the mechanical motion, we have reduced the excitation power in panel b) at higher responsitivities (hence larger coupling rates), which leads to a reduced linearity.

As mentioned above, next we relate the results of Fig. F.1 to the electromechanical coupling rate measured via the thermal displacement spectra of the nanostring and so determine $g_\mathrm{m0}(\partial\omega_\mathrm{c}/\partial\Phi)$ as presented in Fig. 7.20a).

In analogy to the procedure detailed above, we repeat this method with respect to the magnetic field bias at a resonator frequency of $6.6\,\mathrm{GHz}$ resulting in Fig. 7.20b).

Appendix G

Mathematical details on strongly driven strings

In the following we consider a driven mechanical motion of a nanostring, described by

$$x(t) = x_0 \sin\left(\Omega_\mathrm{m} t\right). \tag{G.1}$$

Here the motional amplitude is x_0. This string is embedded in a electromechanical resonator, for which the field amplitude $a(t)$ can be derived from a coupled mode theory [106]:

$$\partial_\mathrm{t} a(t) + \left[\frac{\kappa}{2} - i\left(\omega_\mathrm{c} - Gx(t)\right)\right] a(t) = \sqrt{\kappa_\mathrm{ext}} s_\mathrm{in}(t). \tag{G.2}$$

This is a inhomogeneous differential equation of the shape $a' + ba = r$, with the general solution $a(t) = a_\mathrm{h}(t) + a_\mathrm{p}(t)$ derived from the full solution of the homogeneous equation $a_\mathrm{h}(t)' + ba_\mathrm{h}(t) = 0$ and a partial solution $a_\mathrm{p}(t)$ of the inhomogeneous one ($r \neq 0$). The homogenous solution is derived from $a_\mathrm{h}(t) = c_\mathrm{h} \cdot \exp(-A(t))$, where

$$A(t) = \int b \cdot dt = \left(\frac{\kappa}{2} - i\omega_\mathrm{c}\right) t - i\frac{Gx_0}{\Omega_\mathrm{m}} \cos\left(\Omega_\mathrm{m} t\right). \tag{G.3}$$

We introduce the dimensionless parameter $\beta = Gx_0/\Omega_\mathrm{m} = g_{\mathrm{m}0}\sqrt{n_\mathrm{m}}/\Omega_\mathrm{m}$, which relates the effective driven electromechanical coupling to the energy scale of the mechanical element. So the homogenous solution reads

$$a_\mathrm{h}(t) = c_\mathrm{h} \exp\left[\left(-\frac{\kappa}{2} + i\omega_\mathrm{c}\right) t + i\beta\cos\left(\Omega_\mathrm{m} t\right)\right]. \tag{G.4}$$

The particular solution is found from $a_\mathrm{p} = c_\mathrm{p} a_\mathrm{h}$ with $c_\mathrm{p}' = r \cdot \exp(A(t))$, which requires the anti-derivative of

$$c_\mathrm{p}' = \sqrt{\kappa_\mathrm{ext}} s_0 \cdot \exp\left[\left(\frac{\kappa}{2} - i\omega_\mathrm{c} + i\omega\right) t - i\beta\cos\left(\Omega_\mathrm{m} t\right)\right]. \tag{G.5}$$

Here, we have introduced the probe field $s_\mathrm{in}(t) = s_0 \cdot \exp(i\omega t)$. Further we introduce the probe tone detuning $\Delta = \omega - \omega_\mathrm{c}$. In addition, we make use of the Bessel functions of first kind J_n using [105]

$$\exp\left[-i\beta\cos(\Omega_\mathrm{m} t)\right] = \sum_{n=-\infty}^{\infty} (-i)^n J_n(\beta)\exp(in\Omega_\mathrm{m} t). \tag{G.6}$$

Combining the introduced abbreviations and Eq. (4.31), we find the anti-derivative of
Eq. (G.5) to be

$$c_{\rm p} = \sqrt{\kappa_{\rm ext}} s_0 \sum_{n=-\infty}^{\infty} \frac{(-i)^n J_n(\beta)}{\frac{\kappa}{2} + i(\Delta + n\Omega_{\rm m})} \exp\left\{\left[\frac{\kappa}{2} + i(\Delta + n\Omega_{\rm m})\right] t\right\}. \qquad (G.7)$$

We can now describe the particular solution via

$$\begin{aligned}
a_{\rm p} &= \sqrt{\kappa_{\rm ext}} c_{\rm h} s_0 \sum_{n=-\infty}^{\infty} \frac{(-i)^n J_n(\beta)}{\frac{\kappa}{2} + i(\Delta + n\Omega_{\rm m})} \exp\left[i(\omega + n\Omega_{\rm m})t + i\beta\cos\left(\Omega_{\rm m}t\right)\right]. \\
&= \sqrt{\kappa_{\rm ext}} c_{\rm h} s_0 \sum_{n,m=-\infty}^{\infty} \frac{(i)^{m-n} J_n(\beta) J_m(\beta) \exp\left\{i[\omega + (n-m)\Omega_{\rm m}]t\right\}}{\frac{\kappa}{2} + i(\Delta + n\Omega_{\rm m})}
\end{aligned} \qquad (G.8)$$

Now the mathematical solution is found by the sum of $a_{\rm h}(t) + a_{\rm p}(t)$, as introduced before.
Yet we find an exponential decay of $a_{\rm h}(t)$ by $\kappa/2$, that has canceled out for $a_{\rm p}(t)$. As we
measure with a bandwidth in the order of $1\,{\rm kHz}$ or less, corresponding to $t_{\rm meas} \gg \kappa/2$,
the experimental measured probe field is sufficiently described by $a_{\rm p}(t)$. Therefore the
measured field transmitted through this mechanically driven electromechanical resonator
is given by $s_{\rm out} = s_0\exp(i\omega t) - \sqrt{\kappa_{\rm ext}} a_{\rm p}(t)$ and so the scattering parameter becomes

$$\begin{aligned}
S_{21} &= \frac{s_{\rm out}}{s_{\rm in}} = 1 - \sqrt{\kappa_{\rm ext}} a_{{\rm p}(t)/s_{\rm in}} \exp(-i\omega t) \\
&= 1 - \kappa_{\rm ext} c_{\rm h} \sum_{n,m=-\infty}^{\infty} \frac{(i)^{m-n} J_n(\beta) J_m(\beta) \exp\left[i(n-m)\Omega_{\rm m}t\right]}{\frac{\kappa}{2} + i(\Delta + n\Omega_{\rm m})} \\
&= 1 - \kappa_{\rm ext} c_{\rm h} \sum_{n,m=-\infty}^{\infty} \frac{J_n(\beta) J_m(\beta)}{\frac{\kappa^2}{4} + (\Delta + n\Omega_{\rm m})^2} \\
&\qquad\qquad i^{m-n} e^{i(n-m)\Omega_{\rm m}t} \left[\frac{\kappa}{2} + i(\Delta + n\Omega_{\rm m})\right]
\end{aligned} \qquad (G.9)$$

As we perform our measurements with network analyzers, we only have to consider rotations of the signal with $m = n$. Further, we later like to fit the absolute transmission of
the signal, and so we derive [105]

$$|S_{21}|^2 = 1 - \kappa_{\rm ext}\left(\kappa - \kappa_{\rm ext}\right) \sum_{n,m=-\infty}^{\infty} \frac{[J_n(\beta)]^2}{(\kappa/2)^2 + (\Delta + n\Omega_{\rm m})^2}, \qquad (G.10)$$

in agreement with Ref. [100] for capacitively coupled electromechanics. Discuss real and
imaginary part. From this follows t^2 and ϕ, which should be reducible for $1 \gg \beta$ to the
known shape.

weakly driven string   In the following we will discuss the solution of Eq. 4.28 in the
sense $\beta \ll 1$, for which we will neglect all higher orders in β. The homogenous solution
remains unchanged by this. However, in this case we can expand the exponential function
for β in $c'_{\rm p}$ and find a homogenous solution for

$$c'_{\rm p,w} = \sqrt{\kappa_{\rm ext}} s_0 \cdot \exp\left[\left(\frac{\kappa}{2} + i\Delta\right) t\right] \left[1 - i\beta\cos\left(\Omega_{\rm m}t\right)\right]. \qquad (G.11)$$

An integration yields:

$$c_{\rm p,w} = \sqrt{\kappa_{\rm ext}} s_0 \cdot \exp\left[(\kappa/2 - i\Delta)t\right] \left\{\frac{1}{\kappa/2 - i\Delta} + i\beta\frac{(\kappa + 2i\Delta)\cos(\Omega_{\rm m}t) + 2\Omega_{\rm m}\sin(\Omega_{\rm m}t)}{[\kappa/2 + i(\Delta - \Omega_{\rm m})][i\kappa - 2(\Delta + \Omega_{\rm m})]}\right\}, \qquad (G.12)$$

from which we derive the partial solution

$$a_{\mathrm{p,w}} = \sqrt{\kappa_{\mathrm{ext}}} \frac{c_{\mathrm{h}} s_{\mathrm{in}}(t)}{\frac{\kappa}{2} + i\Delta} \left\{ 1 + 2\beta\Omega_{\mathrm{m}} \frac{-2\Omega_{\mathrm{m}}\cos(\Omega_{\mathrm{m}}t) + (\kappa + 2i\Delta)\sin(\Omega_{\mathrm{m}}t)}{(\kappa + 2i\Delta)\left[\kappa + 2i(\Delta + \Omega_{\mathrm{m}})\right](i\kappa + 2(-\Delta + \Omega_{\mathrm{m}}))} \right\}.$$
(G.13)

Again, the homogenous solution decays during the continuous measurement, and so the output field is given by $s_{\mathrm{out,w}} = -\sqrt{\kappa_{\mathrm{ext}}} a_{\mathrm{p,w}}$, which allows to similarly calculate the scattering parameter $S_{21,\mathrm{w}}$, which is for an on-resonance drive ($\Delta \to 0$) given by

$$S_{21,\mathrm{w}} = 1 - 2\frac{\kappa_{\mathrm{ext}}}{\kappa} + i4\frac{\kappa_{\mathrm{ext}}}{\kappa}\beta\Omega_{\mathrm{m}}\frac{2\Omega_{\mathrm{m}}\cos(\Omega_{\mathrm{m}}t) - \kappa\sin(\Omega_{\mathrm{m}}t)}{\kappa^3 + 4\kappa\Omega_{\mathrm{m}}^2}.$$
(G.14)

This allows directly to determine the real and imaginary part of the scattering parameter. For a physical interpretation of this result we calculate the transmission $|S_{21,\mathrm{w}}|^2$ and phase ϕ.

$$|S_{21,\mathrm{w}}|^2 = S_{21,\mathrm{w}}\bar{S}_{21,\mathrm{w}} = 1 - 4\frac{\kappa_{\mathrm{ext}}}{\kappa} + 4\left(\frac{\kappa_{\mathrm{ext}}}{\kappa}\right)^2 + 16(\frac{\kappa_{\mathrm{ext}}^2}{\kappa^2}\beta^2\Omega^2(\dots)^2 \approx \left(1 - 2\frac{\kappa_{\mathrm{ext}}}{\kappa}\right)^2,$$
(G.15)

in first order independent of the string's motion. However for the phase one find a direct linearity:

$$\varphi = \arctan\left[\frac{\mathrm{Im}\,(S_{21,\mathrm{w}})}{\mathrm{Re}\,(S_{21,\mathrm{w}})}\right] = \arctan\left[\frac{4\frac{\kappa_{\mathrm{ext}}}{\kappa}\beta\Omega_{\mathrm{m}}(\cdots)}{1 - 2\frac{\kappa_{\mathrm{ext}}}{\kappa}}\right] \propto \Omega_{\mathrm{m}}\beta = Gx_0.$$
(G.16)

So, weak driven strings modulate the phase transmission of the electromechanical resonator. Only for higher elongations or couplings the absolute value of the transmission begins to be influenced by the string. When the induced modulation becomes comparable to the frequency of the string, mechanical sidebands occur in the transmission, as discussed above.

Influence of sideband drives on the nanostring's phonon occupation

In Sec. 7.6.3 we have determined the electromechanical coupling strength between the nanostring and the microwave resonator. For this we have applied a probe tone on the blue mechanical sideband, that is $\Delta = +\Omega_\mathrm{m}$. In this configuration, the probe tone effectively heats the mechanical element by amplifying the mechanical motion, as discussed in Sec. 4.3. As for the determination of g_m0 we require the nanostring to be thermalized with the cryostat this can potentially falsify the calibration. An estimation of this systematic induced photons showed that overall the coupling is overestimated by 2.5%, three times smaller than the statistic fluctuations of 7.5%. By this estimation we suspect that in the experiment we are not able to resolve these heating effects.

In the following we will quantify this, by investigating the effective mechanical linewidth. Its the sum of the intrinsic mechanical linewidth and the electro/opto- mechanical induced
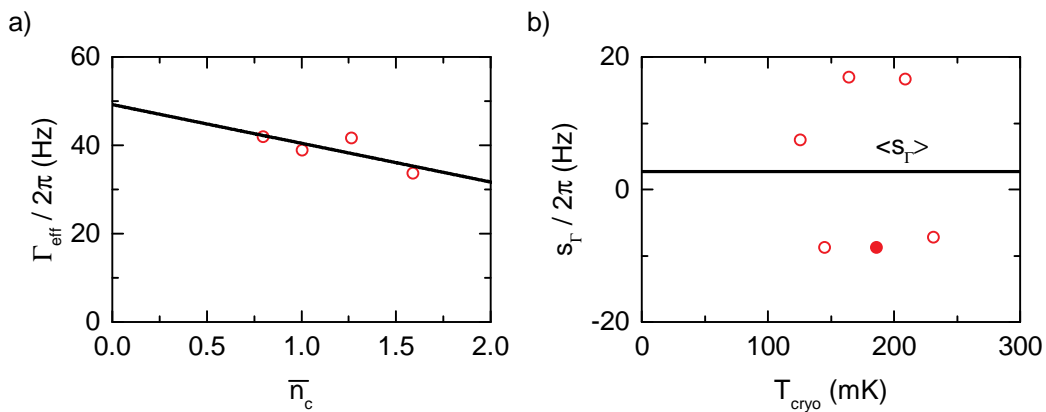
Figure H.1: *Influence of the radiation pressure on the mechanical linewidth.* In panel a) the linewidth depending on the blue detuned drive tone power in resonator photons is displayed. We find a decrease by the power, a potential indication of induced heating. In panel b) we compare this result (red) to the other sample temperatures (blue). We find fluctuations between $\pm 15\,\mathrm{Hz}$. The average value of $+2\,\mathrm{Hz}$ indicates that the measurement precision is not suffering from induced mechanical phonons given the applied power, as this leads to negative values.

linewidth $= \Gamma_\mathrm{m} + \Gamma_\mathrm{opt}$. In Sec. 7.6.3 we have highlighted that a heating of the mechanical element corresponds to $\Gamma_\mathrm{opt} < 0$, respectively a shrinking of when the photon number is increased.

Figure H.1a) plots the extracted mechanical linewidth over the probe tone power for the example set at $T_\mathrm{cryo} = 186\,\mathrm{mK}$. Indeed we find a decrease in when the probe tone is enhanced. To quantify the effect, we model a linear trend revealing $s_\Gamma/2\pi = -(8 \pm 4)\,\mathrm{Hz/photon}$ and a power independent offset of $\Gamma_\mathrm{m}^0 = (49 \pm 6)\,\mathrm{Hz}$. The increase is slightly higher than the first estimation in Sec. 7.6.3 predicted, which was a value of 2Hz/photon.

However, when we plot the extracted change s_Γ for all temperatures in Fig. H.1b), where we have highlighted the extracted value at $186\,\mathrm{mK}$ in bold, we find fluctuations around -10 to $+20\,\mathrm{Hz}$. The average shown by the black solid line is found at the positive value of $\langle s_\Gamma \rangle/2\pi = (2.6 \pm 5.1)\,\mathrm{Hz/photon}$, which indicates a cooling of the nanostring. Nevertheless, it fits to the predicted slope of 2Hz/photon within the statistical fluctuations, c.f. Sec. 7.6.3.

So we conclude, that the influence of the blue sideband drive does not significantly influence our calibration measurement.

Appendix I

Further Statistics
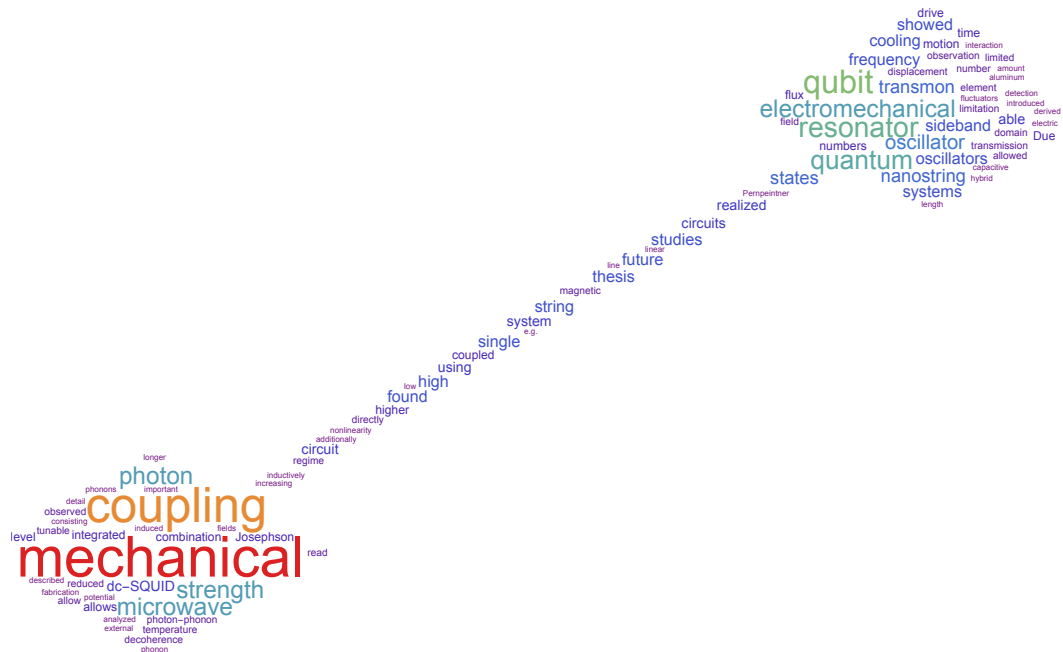
In this section we will have a look at recent developments in cavity opto / resonator electromechanics. For this, we have collected the data from current publications, as found in Tab. I.1. We have tried to cover a broad range and include most important works. Further, we sorted the mechanical systems in two dimensional string (three dimensional drums) and display them in the following as squares (circles). Similar we use red (blue) for optical (microwave) realizations. In addition, we focus on opto/electromechanical resonators, so qubit or two level systems are excluded in the data visualization. For the table we have used the following abbreviations for simplicity: SAW: surface accoustic wave, BAW: bulk acoustic wave, OM: optomechanical, SC: superconducting, CPW: coplanar waveguide, WGM: whispering gallery mode, FPC: Fabry-Perot cavity, LE: lumped element, SP: superpolished, SC 3D: superconducting 3D cavity, O: optical, FTR: flux tunabel superconducting microwave resonator.

Table I.1: *Summary of the collected parameters.*

Ref.	date ddmmyyyy	T_sample mK	Mechanics	$\Omega_m/2\pi$ Hz	m_{eff} kg	x_{zpm} m	$\Gamma_m/2\pi$ Hz	Q_m	τ_{th} s	Optics	$\omega_c/2\pi$ Hz	$\kappa/2\pi$ Hz	Q_c	$\bar{n}_c^{min}$	g_{m0} Hz	G Hz/nm	g_{m0}/κ	C_0	g_{m0}/Ω_m	g_{m0}/ω_c
[13]	18.05.2008	17	String	2.30E+06	4.27E-14	2.03E-12	103	1.20E+05	1.00E-05	SC CPW	4.91E+09	4.90E+05	1.02E+04		4.95E-02	1.16E-07	1.01E-07	1.94E-10	2.15E-08	1.01E-11
[171]	03.11.2008	50	String	1.53E+08	2.98E-14	7		2.18E+05	3.33E-05	SC CPW	5.22E+09	2.30E+05	2.27E+04		1.91E-01	6.40E+07	8.29E-07	9.03E-08	1.25E-09	3.65E-11
[104]	31.12.2008		Drum	1.07E+07	4.10E-14	3.20E-15	30	3.60E+05	6.80E-05	SC LE	7.47E+09	1.70E+05	4.39E+04		2.30E+03	5.60E-07	1.35E-02	4.13E-02	2.15E-05	3.07E-08
[172]	11.10.2009	3.00E+05	String	1.04E+06	5.50E-15	3.83E-15	2.03E+02	5.30E+04	1.35E-09	WGM	1.93E+14	4.90E+06	3.94E+07		2.95E+02	2.00E+09	6.01E-05	3.50E-04	2.74E-05	1.53E-12
[164]	01.11.2009	77	String	4.82E+06	5.35E-15	1.68E-01		6.15E+05	SC CPW	7.49E+09	2.88E+06	2.60E+03		1.23E+00	3.20E+04	4.25E-07	1.24E-06	1.18E-06	1.64E-10
[173]	13.11.2009	3.00E+05	Drum	1.10E+06	8.44E-12	3.21E+00	1.50E+06		FPC	3.21E+14	2.50E+07	1.28E+07							
[174]	23.09.2010	3.00E+05	Microtoroid	7.14E+07	5.50E-07	8.09E+00	1.36E+05		WGM	2.83E+14	2.40E+04	1.18E+10		1.30E+00	3.50E+08	5.43E-05	3.50E-05	1.18E-06	4.60E-15
[125]	19.10.2010		Microtoroid	5.18E+07	9.00E-17	4.10E+04	1.26E+03		WGM	5.70E+14	1.20E+03			5.70E+02	1.20E+10	7.58E-02	7.20E-05	7.58E-12	
[106]	10.12.2010		Microtoroid	2.00E-11	4.27E-14	9.03E-16	4.25E-14	6.62E-15		WGM	1.08E+13	2.30E+04	1.29E+07		1.20E+03	2.30E-03	8.06E-03	2.15E-05	5.59E-12	
[14]	10.03.2011	40	Drum	1.07E+07	4.67E-14	3.20E-15	30	3.60E+05	6.80E-05	SC LE	7.47E+09	1.70E+05	4.39E+04		2.30E+03	5.60E-07	1.35E-02	4.13E-02	2.15E-05	3.07E-08
[15]	21.07.2011	15	Drum	1.06E+07	4.10E-14	3.20E-15		2.00E+05	SC LE	7.54E+09	2.00E+05	3.77E+04	18	2.01E+02	4.90E+07	1.00E-03	2.52E-02	1.90E-05	2.66E-08
[176]	02.02.2012	650	Microtoroid	7.80E+07	4.80E-14	3.32E-16	3.55E+01	4.17E+01	WGM	3.84E+14	3.40E+08	7.10E+06		3.40E+03	2.58E+10	1.00E-05	1.90E-05	8.85E-12	
[175]	24.06.2012	3.00E+05	String	2.88E+06	9.00E-15	1.80E-14	6.00E+00	4.80E+05	1.22E-08	Microdisc	1.94E+14	2.98E+09	6.50E+04		5.22E+01	2.90E+06	1.75E-08	1.81E-05	4.36E-13	
[177]	26.11.2012	5.00E+03	Drum	1.60E+06	6.75E-12	8.81E-16	1.16E-01	1.36E+07	2.11E+05	SP Cavity	2.93E+14	1.20E+06	2.44E+08	6.00E+06	1.67E+01	3.63E-04	1.40E-05	1.05E-05	5.71E-14	
[103]	31.12.2012	200	Drum	1.45E+06	7.00E-15	3.00E-14	11	1.32E+05	1.53E-04	SC CPW	6.07E+09	7.42E+05	8.18E+03		4.50E+06	1.13E-12	7.50E-01	8.06E-03	3.10E+00	2.08E-10
[97]	14.02.2013	30	String	7.20E+07	3.00E-15	2.42E+00	6.00E+05		SC CPW	2.81E+09	7.59E+05			4.20E+04	1.70E-06	1.66E+06	1.70E-05	8.69E-07	2.08E-10
[123]	20.01.2013	30	String	1.45E+06	7.00E-15	3.00E-14	1.32E+00	1.53E-04	SC CPW	6.00E+05	6.00E+05			3.63E+04	7.61E-07	8.69E-07	2.08E-10		
[178]	15.02.2013	4.90E+03	String	1.55E+06	8.79E-16	4.70E-01	1.31E-04	SC CPW	2.82E+14	1.00E+08	2.82E+08		1.60E+01	1.82E-07	7.50E-01	6.25E-02	1.03E-05	1.60E-03
[179]	14.03.2013	25	Drum	2.40E-14	4.10E-14	3.30E+00	9.17E+05		SC LE	7.50E+09	3.60E+05	2.08E+04		2.18E+01	4.16E+02	1.27E-02	1.90E-05	2.08E-08	
[180]	05.06.2013	26	Drum	7.14E+05	1.08E-11	8.10E-01	3.00E+05		SC LE	4.67E+09	2.80E+05	9.17E+05	3.00E+02	5.56E+04	2.12E-06	1.90E-05	3.22E-06	4.92E-10	
[181]	09.06.2013	4.50E+03	String	1.52E+06	4.25E-14	7.26E+03		1.15E-05	FPC	2.82E+14	1.70E+06	1.66E+08		1.60E+06	2.67E+11	2.17E-05	1.17E-13		
[182]	03.09.2013	4.60E+03	Drum	6.75E+07	6.62E-15	2.20E-01	6.93E+06	1.15E-05	FPC	2.82E+14	6.60E+05			2.00E+02	4.16E+07	3.03E-04	1.93E-05	2.60E-08	
[95]	15.06.2013	20	Drum	1.03E+07	1.00E+05	620	SC LE	7.10E+09	1.59E+06	6.47E+03		2.70E+00	4.16E+02	1.70E-06	4.58E-06	2.60E-07	2.94E-08	
[183]	23.03.2014	4.00E+03	Drum	5.60E+05	2.95E+05	1.40E+05	SC 3D	2.90E+13	2.42E+05	1.00E+04	7.00E+05	4.00E+00	7.00E+08	4.55E-01	4.82E-06	5.17E-11		
[126]	24.08.2014	14	Drum	3.62E+06	2.76E-16	4	1.59E+05	8.67E+05	SC 3D	3.30E+11	1.59E+06	8.80E+05	1.26	4.16E+05	2.65E-04	3.43E-06	4.99E-08	1.41E-14	
[90]	23.09.2014	550	String	1.40E+07	2.90E-14	28	2.90E+05	5.22E-06	SC 3D	2.42E+13	2.44E+08		1.50E+07	2.00E+01	3.12E-06	1.66E-07	2.44E-11	2.03E-12	
[184]	29.09.2014	400	String	1.45E+07	3.70E-16	29	4.80E+05	6.68E+05	SC CPW	6.07E+09	7.49E+05			1.15E-02	5.56E-04	8.24E-11	2.03E-10		
[185]	17.11.2014		SAW	1.06E+10	2.88E-14	15	9.67E+04	1.85E-06	SC CPW	7.00E+09	7.57E+05	8.00E+03	1.26	4.38E+04	1.54E-08	5.58E-07	2.08E-10		
[186]	27.04.2015	20	Drum	6.50E+07	3.58E-15	1.50E-01	4.33E+03	1.65E-06	O CPW	4.00E+14				8.00E+08	8.53E+04				
[22]	15.06.2015	25	Drum	1.59E+06	6.00E-15	150	3.95E+05	7.53E-06	SC Qubit	4.93E+09	8.00E+06	6.16E+02		1.60E+06	2.00E-01	8.53E+01	2.46E-02	3.25E-04	
[187]	20.08.2015	4.40E+03	String	4.30E+06	2.60E-14	35	1.00E+05	3.24E-05	SC Qubit	1.02E+10	2.20E+09		7.00E+05	3.00E+02	9.50E+02	2.40E-04	1.89E-05	2.94E-08	
[188]	09.09.2015	4.80E+03	String	1.51E+06	2.90E-14	4	5.70E+00	1.31E-06	Microdisc	3.87E+14	4.40E+08	8.80E+05		2.00E+04	7.00E+08	4.55E-05	4.65E-03	5.17E-11	
[124]	09.10.2015	13	Drum	1.23E+06	4.60E-01	3.28E+05	2.06E-02	FPC	2.81E+14	1.80E+05	1.56E+08		3.30E+04	3.64E-07	1.83E-05	2.19E-05	1.17E-13		
[189]	30.11.2015	17	Drum	9.56E+06	1.00E-10	3.50E-03	25	1.72E-04	SC 3D	7.40E+09	4.55E+04	1.10E-01	1.00E+02	2.20E-02	3.67E+05	4.84E-06	1.22E-06	1.79E-06	2.97E-11
[190]	07.12.2015	30	Drum	1.50E+07	2.14E-14	9.2	1.63E+06	3.82E-04	SC 3D	7.34E+09	2.10E+06	2.94E+03		1.70E+02	4.20E-07	1.08E-04	4.67E-03	1.13E-05	2.82E-05
[191]	28.12.2015	14	Drum	1.21E+06	3.75E-11	1.90E-03	9.2	4.15E+06	SC CPW	9.93E+09	4.50E+04		2.20E-01	4.89E-06	5.98E-03	2.26E-03	1.82E-06	4.34E-11
[192]	06.01.2016	40	Drum	9.36E+06	1.36E-15	24.4	3.83E+05	7.32E+05	SC CPW	6.71E+09	1.06E+07	6.35E+05		6.97E+07	2.18E-05	8.21E-04	2.46E-03	3.43E-06	
[193]	26.01.2016	30	Drum	6.71E+06	4.25E-14	3.30E-15	1.63E+06	4.15E-04	SC CPW	9.93E+09	2.10E+06	4.73E+03		1.70E+02	8.10E-05	1.66E-06	1.13E-05	1.71E-08	
[194]	08.02.2016	70	Drum	1.50E+07	8.22E+06	8.97E-04	O CPW	2.60E+06				8.00E+08							
[17]	28.03.2016	40	Drum	1.48E+06	1.80E-14	22	SC Qubit	6.88E+09	2.20E+07	3.13E+02		1.70E+02	7.73E-06	1.96E-05	2.47E-08			
[195]	26.05.2016	3.00E+05	String	4.40E+06	1.00E-14	1.38E-14	1.50E-01	2.93E+05	7.47E+05	Microdisc	3.87E+14	3.87E+14	3.52E+02		6.00E+09	4.35E+09	2.39E-04	1.36E-02	2.47E-06	1.55E-10
[196]	06.01.2017	6.00E+03	String	4.30E+06	6.14E+05	7.00E+00	6.14E-04	O Cavity	1.10E+09						0.3				
[18]	12.01.2017	37	Drum	1.01E+07	7.00E+05	7.82E-07	SC CPW	3.88E+14	2.70E+07	2.37E+02		2.60E+02	9.63E-06	6.68E-04	4.06E-08			
[197]	18.04.2017	120	Drum	1.60E+06	4.99E-02	15	1.39E-04	SC CPW	6.40E+09	2.50E+06			3.90E+01	1.56E-05	2.44E-05	4.06E-08			
[198]	15.05.2017	10	Drum	6.35E+06	3.20E+07	1.00E+02	2.50E-04	SC LE	4.13E+09	1.97E+05	2.10E+04		1.06E+02	5.38E-04	2.28E-03	2.57E-08		
[199]	06.07.2017	19	Drum	6.70E+06	9.07E-16	1.00E+02	1.80E-04	SC LE	6.53E+09	1.30E+05	5.02E+03		6.00E+00	4.62E-05	7.38E-04	8.96E-06	9.19E-09	
[24]	18.09.2017	25	Drum	9.30E+06	6.40E-15	15	4.47E+05	1.80E-04	SC LE	7.28E+09	3.00E+06	2.43E+03		2.80E+02	9.33E-05	7.21E-03	3.01E-05	3.68E-08	
[200]	19.09.2017	200	Drum	6.50E+06	2.17E+05	8.27E-06	SC LE	4.10E+09	2.00E+06	2.05E+03		9.10E+01	4.55E-05	1.40E-05	2.22E-08			
[23]	13.10.2017		Drum	6.65E+09	3.00E-07	2.17E+05	6.41E+05	1.37E-04	SC Qubit	6.65E+09	8.30E+04			2.60E+05	3.13E+01	4.55E-05	1.40E-05	3.91E-13	
[201]	02.04.2018	4.00E+03	BAW	1.23E+10	6.10E-19	23000	5.30E+05	SC Qubit	1.94E+14			8.20E+01	8.69E-09		6.69E-09	4.23E-13		
[25]	30.05.2018	30	SAW	4.25E+06	2.00E+05	2.12E+04	5.40E+05	O Cavity	5.08E+09	1.10E+06	4.62E+03		6.48E+06	1.53E-03	1.28E-03			
[202]	16.07.2018	35	SAW	1.47E+06	2.52E-11	2.00E+05	1.34E+01	SC Qubit	6.60E+09	2.50E+05	2.64E+03		3.80E+00	1.52E-06	2.58E-05	5.76E-10		
[203]	16.07.2018	200	Drum	6.50E+06	9.50E-01	1.10E+01	SC LE	4.08E+09	1.76E+06			6.00E+00	3.41E-04	9.23E-06	1.47E-08			
[204]	25.08.2018	2.95E+05	String	3.40E+06	9.50E-14	5.10E-14	1.50E-01	5.87E-09	Microdisc	3.84E+14	4.50E+09	8.53E+04		9.17E+04	2.04E-05	2.70E-02	2.70E-06	2.39E-10
[34]	25.08.2018	50	String	3.15E+06	1.00E-15	5.16E-14	2.54E+05	4.00E+03	SC CPW	5.88E+09	1.47E+06	4.00E+03	1.40E+06	3.10E-01	2.11E-07	9.84E-08	5.28E-11		
[26]	11.10.2018	18	String	2.50E-07	2.59E-14	12.4	2.66E+05	1.13E-04	SC CPW	3.82E+09	3.70E+06	1.03E+03		1.95E+14	6.11E+12	5.95E+00	5.76E-03		
[205]	29.10.2018	25	Drum	9.20E+06	3.60E-15	94	7.67E+04	2.63E+02	SC LE	7.31E+09	2.78E+07			9.10E+01	4.55E-05	1.40E-05	2.22E-08		
[206]	14.12.2018	25	Drum	9.24E-06	7.67E+04	9.34E+05	SC LE	5.63E+09	6.03E+03			2.60E+05	4.55E-05	1.40E-05	3.91E-05			
[207]	12.03.2019	200	Drum	5.30E-09	8.40E+04	6.31E+04	1.14E-06	O Crystal	1.95E+14	1.70E+09	1.15E+05		4.59E-04	1.70E-02	1.47E-04	4.00E-09		
[208]	07.05.2019	2.00E+03	SAW	7.13E+06	5.00E-16	8	9.00E+05	2.13E+04	FTR	5.22E+09	2.00E+06	7.73E+03		9.27E+00	1.96E-03	1.20E-03	3.23E-05	4.41E-08	
[27]	20.06.2019	15	String	4.25E-09	3.30E-14	2.50E+01	SAW	2.30E+09	5.50E+05	1.15E+05		2.30E+02	6.40E-07	1.15E-02	1.20E-03	1.20E-03	4.00E-09
Ch.7	tba	125	String	6.34E+06	6.00E-16	4.70E-14	2.50E+01	1.55E-05	FTR	7.45E+09	2.50E+06	3.00E+01	8.00E-01	1.60E+02	6.40E-07	2.52E-04	1.64E-01	2.52E-04	2.15E-07

Figure I.1: *Development of the single photon-phonon coupling strength.* The time evolution of the single photon-phonon coupling strength g_{m0} is shown. In general, optical systems seem to allow higher coupling rates. For microwave realizations drum oscillators showed a much higher coupling than nanostrings, however recently by the use of inductively coupled systems the drum values were overcome.

We start by an analysis of the bare vacuum coupling strength g_{m0}. It describes the required time for a state transfer between optic/electric and mechanical system. Hence, a high rate allows for fast transfer. We plot the reported coupling strengths in Fig. I.1. We find a trend to higher coupling strengths for optical systems, but this has to be seen in the context of a much higher optical cavity frequency (THz vs. GHz). The microwave realizations were first developed using string oscillators [13], until three dimensional drum oscillators were invented [14]. These show in general a higher coupling strength. However recently using inductively coupled systems, [208], and Sec. 7, comparable coupling rates were achieved. The coupling presented in this thesis exceeds all microwave realizations. As we have discussed in Secs. 7, and App. E, we expect the presented sample to allow for an enhanced coupling by 260 when in-plane magnetic fields are used, which we indicate by a black arrow. This would even exceed coupling strengths realized in optical systems.

Next, we discuss the 'quantum parameter' g_{m0}/κ, that relates the coupling strength g_{m0} to the cavity/resonator decoherence κ. Its name describes the fact, that a high ratio can be seen as an increase in $\hbar$ [9]. In the strong coupling regime ($\Omega_m > \kappa$), the discreteness of the photons in the cavity can be observed, and so it is also been referred as 'granularity parameter' [209]. The evolution of this parameter is found in Fig. I.2. Here, a clear trend between the systems is not observed. So, the optical systems cannot benefit from their bare higher coupling (c.f. Fig. I.1) due to their higher decoherence. The highest value reported was achieved using a high coherent superconducting lumped element circuit and a three dimensional nanodrum [14]. The in-plane magnetic field configuration for our sample in Sec. 7 allows to overcome previous realization by almost two orders of
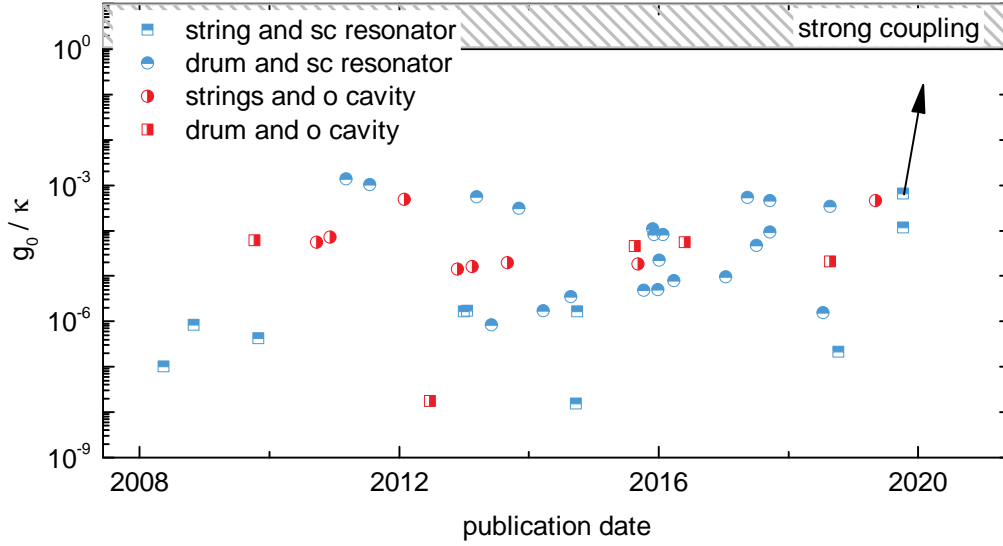
Figure I.2: *Towards strong coupling in cavity optomechanics.* In terms of the 'quantum' or 'granularity' parameter g_{m0}/κ both optical and electric systems perform similar. Highest ratios were reported for superconducting resonators. Further, the inductively coupled systems from Sec. 7 seem promising candidates to reach the strong coupling regime $g_{m0}/\kappa > 1$, as the in-plane field configuration allows for highest coupling ratios. However, for the first sample generation the strong coupling regime seems out of reach (black arrow).

magnitude. Yet, reaching the strong coupling regime requires further optimization on both the mechanical coupling and resonator decoherence as previously discussed in Sec. 7. These considerations towards strong coupling have to be seen in the context, that we assume only a negligible influence of the magnetic field on the resonator decoherence.

Besides the comparison of coupling strength to the decoherence rate, the comparison to the systems energy level is also of interest. We take this into account by analyzing the ratio of g_{m0}/ω_c, that is the coupling strength g_{m0} over the optical/electric eigenfrequency. Above $g_{m0}/\omega_c = 0.1$ the system enters the ultra-strong coupling regime. This has been demonstrated in cQED by coupling a qubit to a microwave resonator [20]. So far, the weaker photon-phonon coupling has prevented the investigation of this regime in optomechanics. We collected the data in Fig. I.3. Here, we find the optical systems to suffer from their high intrinsic frequency. The highest ratio reported is on the order of 10^{-7} and found in Sec. 7 of this thesis. The in-plane field configuration (black arrow) allows to push even further towards the ultra-strong coupling regime, yet with some space in between remaining. Superconducting resonators demonstrate once again their potential for high coupling rates due to their small field confinement.

We conclude these comparisons by having a look at the thermal coherence τ_{th} in nanomechanical hybrid systems. It refers to the storage time within the mechanical system. As optomechanical systems are considered to overcome the higher loss rates within the cavity or resonator by storing the state in the mechanical oscillator, τ_{th} is the theoretically maximum of the state storage within the system. The extracted data is plotted
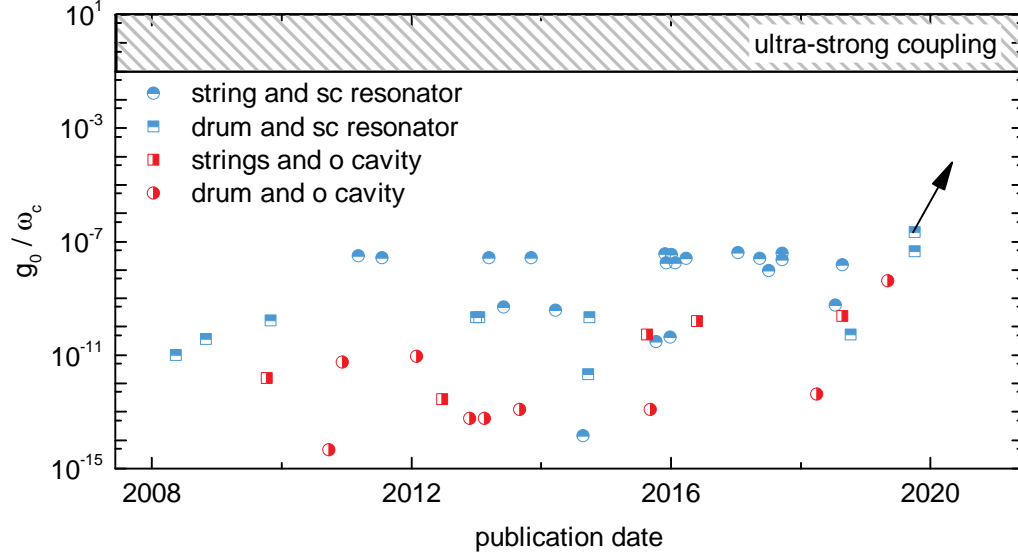
Figure I.3: *The path to ultra-strong coupled electromechanics.* The relation of coupling strength to the system's eigenenergy shows a clear advantage of superconducting resonators (blue) versus optical cavities (red). The highest ratio is found by the realization in Sec. 7 of this thesis, which can be further boosted towards 10^{-4} using in-plane fields. Yet the ultra-strong coupling requires further efforts on the circuit design, as three orders of magnitude remain. Nevertheless, the inductive coupling demonstrates the advantage of superconducting microchips as they allow for (ultra) high coupling strengths.

in Fig. I.4. Here, cryogenic systems, and especially superconducting resonators, benefit from the low environmental temperature that allows for a long storage ($\tau_{\text{th}} \propto T_{\text{sample}}$). Highest coherence times have been published for a 3D superconducting cavity that is capacitively coupled to a mechanical membrane oscillator [124, 191] reaching up to 35 ms. The presented work in Sec. 7 suffered from the induced heating currents of the magnetic field bias in two ways: i) the high temperature of 125 mK directly reduces the available time and ii) due to the high temperature the mechanical linewidth becomes unnecessary broadened, c.f. Fig. 7.10a). Considering a cryogenic temperature of 15 mK, the potential storage time is drastically enhanced as indicated by the black arrow and reaches a value around previous realizations using an aluminum string of same length [208].
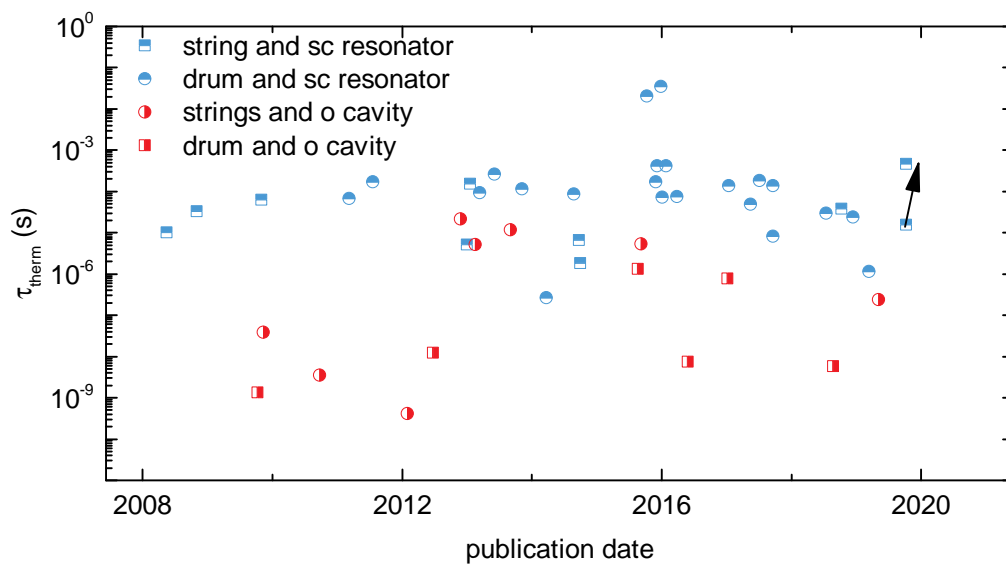
Figure I.4: *Potential state storage times using optomechanical hybrid samples.* The highest values exceeding milliseconds were found for superconducting 3D-resonators coupled to mechanical drum oscillators. In addition, a clear trend is found indicating higher coherence times using superconducting resonators. The work discusses in Sec. 7 suffered from the induced heating currents. Excluding them allows to approach the millisecond range as previously reported for an aluminum string of identical length.

Bibliography

[1] R. Feynman, *private letter to Koichi Manom* (1966).

[2] E. Schrödinger, Sci. Nat. **23**, 807 (1935).

[3] A. Einstein, B. Podolsky, and N. Rosen, Phys. Rev. **47**, 777 (1935).

[4] Bell, Physics **1**, 195 (1964).

[5] F. Hund, Z. Phys. **43**, 805 (1927).

[6] T. H. Maiman, Phys. Rev. Lett. **4**, 564 (1960).

[7] T. Schulz, Der Spiegel (2019).

[8] A. J. Leggett, J. Phys. Condens. Matter **14**, 415 (2002).

[9] M. Aspelmeyer, T. Kippenberg, and F. Marquardt, Rev. Mod. Phys. **86**, 1391 (2014).

[10] I. Pikovski, M. R. Vanner, M. Aspelmeyer, M. S. Kim, and Č. Brukner, Nat. Phys. **8**, 393 (2012).

[11] B. P. Abbott *et al.*, Phys. Rev. Lett. **116**, 061102 (2016).

[12] P. Lebedew, Ann. Phys. **11**, 433 (1901).

[13] C. A. Regal, J. D. Teufel, and K. W. Lehnert, Nat. Phys. **4**, 555 (2008).

[14] J. Teufel, T. Donner, D. Li, J. Harlow, M. Allman, K. Cicak, A. Siruis, J. Whittaker, K. Lehnert, and R. Simmonds, Nature **475**, 359 (2011).

[15] J. Teufel, D. Li, M. Allman, K. Cicak, A. Siruis, J. Whittaker, K. Lehnert, and R. Simmonds, Nature **471**, 204 (2011).

[16] E. E. Wollman, C. U. Lei, A. J. Weinstein, J. Suh, A. Kronwald, F. Marquardt, A. A. Clerk, and K. C. Schwab, Science **349**, 952 (2015).

[17] J. B. Clark, F. Lecocq, R. W. Simmonds, J. Aumentado, and J. D. Teufel, Nat. Phys. **12**, 683 (2016).

[18] J. B. Clark, F. Lecocq, R. W. Simmonds, J. Aumentado, and J. D. Teufel, Nature **541**, 191 (2017).

[19] A. Wallraff, D. I. Schuster, A. Blais, L. Frunzio, R.-S. Huang, J. Majer, S. Kumar, S. M. Girvin, and R. J. Schoelkopf, Nature **431**, 162 (2004).

[20] T. Niemczyk, F. Deppe, H. Huebl, E. P. Menzel, F. Hocke, M. J. Schwarz, J. J. Garcia-Ripoll, D. Zueco, T. Hümmer, E. Solano, A. Marx, and R. Gross, Nat. Phys. **6**, 772 (2010).

[21] A. D. O'Connell, M. Hofheinz, M. Ansmann, R. C. Bialczak, M. Lenander, E. Lucero, M. Neeley, D. Sank, H. Wang, M. Weides, J. Wenner, J. M. Martinis, and A. N. Cleland, Nature **464**, 697 (2010).

[22] F. Lecocq, J. D. Teufel, J. Aumentado, and R. W. Simmonds, Nat. Phys. **11**, 635 (2015).

[23] Y. Chu, P. Kharel, W. H. Renninger, L. D. Burkhart, L. Frunzio, P. T. Rakich, and R. J. Schoelkopf, Science **358**, 199 (2017).

[24] A. P. Reed, K. H. Mayer, J. D. Teufel, L. D. Burkhart, W. Pfaff, M. Reagor, L. Sletten, X. Ma, R. J. Schoelkopf, E. Knill, and K. W. Lehnert, Nat. Phys. **13**, 1163 (2017).

[25] B. A. Moores, L. R. Sletten, J. J. Viennot, and K. W. Lehnert, Phys. Rev. Lett. **120**, 227701 (2018).

[26] J. J. Viennot, X. Ma, and K. W. Lehnert, Phys. Rev. Lett. **121**, 183601 (2018).

[27] L. R. Sletten, B. A. Moores, J. J. Viennot, and K. W. Lehnert, Phys. Rev. X **9**, 021056 (2019).

[28] O. Romero-Isart, L. Clemente, C. Navau, A. Sanchez, and J. I. Cirac, Phys. Rev. Lett. **109**, 147205 (2012).

[29] O. Romero-Isart, Phys. Rev. A **84**, 73 (2011).

[30] S. Etaki, M. Poot, I. Mahboob, K. Onomitsu, H. Yamaguchi, and H. S. J. van der Zant, Nat. Phys. **4**, 785 (2008).

[31] M. Poot, S. Etaki, I. Mahboob, K. Onomitsu, H. Yamaguchi, Y. M. Blanter, and H. S. J. van der Zant, Phys. Rev. Lett. **105**, 207203 (2010).

[32] M. Poot, S. Etaki, H. Yamaguchi, and H. S. J. van der Zant, Appl. Phys. Lett. **99**, 013113 (2011).

[33] S. Etaki, F. Konschelle, Y. M. Blanter, H. Yamaguchi, and H. S. J. van der Zant, Nat. Commun. **4**, 1803 (2013).

[34] P. Schmidt, D. Schwienbacher, M. Pernpeintner, F. Wulschner, F. Deppe, A. Marx, R. Gross, and H. Huebl, Appl. Phys. Lett. **113**, 152601 (2018).

[35] M. P. Blencowe and E. Buks, Phys. Rev. B **76**, 165 (2007).

[36] P. D. Nation, M. P. Blencowe, and E. Buks, Phys. Rev. B **78**, 480 (2008).

[37] P. D. Nation, J. Suh, and M. P. Blencowe, Phys. Rev. A **93**, 022510 (2016).

[38] O. Shevchuk, G. A. Steele, and Y. M. Blanter, Phys. Rev. B **96**, 014508 (2017).

[39] T. Fließbach, *Mechanik* (Spektrum Akademischer Verlag, Heidelberg, 2009).

[40] D. Meschede and C. Gerthsen, eds., *Gerthsen Physik*, 24th ed., Springer-Lehrbuch (Springer, Berlin, 2010).

[41] A. B. Kaul, *Microelectronics to nanoelectronics: Materials, devices & manufacturability* (CRC Press, Taylor & Francis Group, Boca Raton, 2017).

[42] Q. P. Unterreithmeier, T. Faust, and J. P. Kotthaus, Phys. Rev. Lett. **105**, 027205 (2010).

[43] M. Pernpeintner, *Nanomechanical hybrid systems*, Ph.D. thesis, Walther-Meißner-Institut and Technische Universität München (2016).

[44] F. Schwabl, *Quantenmechanik* (Springer Verlag, Berlin, 2005).

[45] I. N. Bronstein and K. A. Semendjajew, *Taschenbuch der Mathematik*, 7th ed. (Harri Deutsch Verlag GmbH, Frankfurt am Main, 2008).

[46] M. I. Dykman, *Fluctuating nonlinear oscillators: from nanomechanics to quantum superconducting circuits* (Oxford Univ. Press, Oxford, 2012).

[47] K. F. Wulschner, *Controlled interactions in superconducting quantum circuits*, Ph.D. thesis, Walther-Meißner-Institut and Technische Universität München (2016).

[48] A. Nayfeh and D. Mook, *Nonlinear oscillations* (Wiley-VCH, Weinheim, 1995).

[49] E. Madelung, Z. Phys. **40**, 322 (1927).

[50] P. E. Schmidt, Junge Wissenschaft **84**, 38 (2009).

[51] B. D. Josephson, Phys. Lett. **1**, 251 (1962).

[52] R. Gross and A. Marx, *Applied superconductivity: Josphson effect and superconducting electronics* (Walther-Meißner-Institut, Garching, 2005).

[53] B. S. Deaver Jr. and W. M. Fairbank, Phys. Rev. Lett. **7**, 43 (1961).

[54] R. Doll and M. M. Näbauer, Phys. Rev. Lett. **7**, 51 (1961).

[55] M. H. Devoret, A. Wallraff, and J. M. Martinis, "Superconducting qubits: A short review," (2008).

[56] J. Clarke and A. I. Braginski, *The SQUID Handbook.*, Vol. 1, Fundamentals and Technology of SQUIDS and SQUID Systems (Wiley-VCH Verlag GmbH & Co. KGaA, Weinheim, 2004).

[57] J. Bourassa, F. Beaudoin, J. M. Gambetta, and A. Blais, Phys. Rev. A **86**, 013814 (2012).

[58] S. Pogorzalek, K. G. Fedorov, L. Zhong, J. Goetz, F. Wulschner, M. Fischer, P. Eder, E. Xie, K. Inomata, T. Yamamoto, Y. Nakamura, A. Marx, F. Deppe, and R. Gross, Phys. Rev. Appl. **8**, 024012 (2017).

[59] T. P. Orlando and K. A. Delin, *Foundations of applied superconductivity* (Addison-Wesley, Reading, Mass., 1991).

[60] A. J. Annunziata, D. F. Santavicca, L. Frunzio, G. Catelani, M. J. Rooks, A. Frydman, and D. E. Prober, Nanotechnology **21**, 445202 (2010).

[61] M. J. Schwarz, *Gradiometric tunable-gap flux qubits in a circuit QED architecture*, Ph.D. thesis, Walther-Meißner-Institut and Technische Universität München (2014).

[62] F. E. Terman, *Radio Engineers' Handbook*, 1st ed. (McGraw-Hill Book Compancy Inc., New York, 1943).

[63] C. Girardi, "In3otd's web site," (2015).

[64] P. E. Schmidt, *Inductive switchable cavity electromechanics*, Master's thesis, Walther-Meißner-Institut and Technische Universität München (2015).

[65] L. Wang, *Fabrication stability of Josephson junctions for superconducting qubits*, Master's thesis, Walther-Meißner-Institut and Technische Universität München (2015).

[66] M. Göppl, A. Fragner, M. Baur, R. Bianchetti, S. Filipp, J. M. Fink, P. J. Leek, G. Puebla, L. Steffen, and A. Wallraff, J. Appl. Phys. **104**, 113904 (2008).

[67] K. Watanabe, K. Yoshida, T. Aoki, and S. Kohjiro, Jpn. J. Appl. Phys **33**, 5708 (1994).

[68] D. M. Pozar, *Microwave engineering*, 4th ed. (John Wiley & Sons, Inc., Hoboken, NJ, 2012).

[69] S. Pogorzalek, *Displacement of Squeezed Propagating Microwave States*, Master's thesis, Walther-Meißner-Institut and Technische Universität München (2015).

[70] U. Schaumburger, *Ketten von Resonatoren mit einstellbarer Nichtlinearität*, Master's thesis, Walther-Meißner-Institut and Technische Universität München (2014).

[71] F. Deppe, S. Saito, H. Tanaka, and H. Takayanagi, J. Appl. Phys. **95**, 2607 (2004).

[72] M. Wallquist, V. S. Shumeiko, and G. Wendin, Phys. Rev. B **74**, 791 (2006).

[73] W. Wustmann and V. Shumeiko, Phys. Rev. B **87**, 184501 (2013).

[74] P. Bhupathi, P. Groszkowski, M. P. DeFeo, M. Ware, F. K. Wilhelm, and B. L. T. Plourde, Phys. Rev. Appl. **5**, 024002 (2016).

[75] J. Koch, T. Yu, J. Gambetta, A. Houck, D. Schuster, J. Majer, A. Blais, M. Devoret, S. Girvin, and R. Schoelkopf, Phys. Rev. A **76**, 042319 (2007).

[76] R. Barends, J. Kelly, A. Megrant, D. Sank, E. Jeffrey, Y. Chen, Y. Yin, B. Chiaro, J. Mutus, C. Neill, P. O'Malley, P. Roushan, J. Wenner, T. C. White, A. N. Cleland, and J. M. Martinis, Phys. Rev. Lett. **111**, 080502 (2013).

[77] Y. Chen, C. Neill, P. Roushan, N. Leung, M. Fang, R. Barends, J. Kelly, B. Campbell, Z. Chen, B. Chiaro, A. Dunsworth, E. Jeffrey, A. Megrant, J. Y. Mutus, P. J. J. O'Malley, C. M. Quintana, D. Sank, A. Vainsencher, J. Wenner, T. C. White, M. R. Geller, A. N. Cleland, and J. M. Martinis, Phys. Rev. Lett. **113**, 220502 (2014).

[78] D. F. Walls and G. Milburn, *Quantum optics*, 2nd ed. (Springer-Verlag Berlin Heidelberg, 2008).

[79] D. Ballester, G. Romero, J. J. García-Ripoll, F. Deppe, and E. Solano, Phys. Rev. X **2**, 021007 (2012).

[80] E. T. Jaynes and F. W. Cummings, Proc. IEEE **51**, 89 (1963).

[81] A. Blais, R. Huang, A. Wallraff, S. Girvin, and R. Schoelkopf, Phys. Rev. A **69**, 062320 (2004).

[82] E. Xie, *A scalable 3D quantum memory*, Ph.D. thesis, Walther-Meißner-Institut and Technische Universität München (2019).

[83] G. Kirchmair, B. Vlastakis, Z. Leghtas, S. E. Nigg, H. Paik, E. Ginossar, M. Mirrahimi, L. Frunzio, S. M. Girvin, and R. J. Schoelkopf, Nature **495**, 205 (2013).

[84] M. Boissonneault, J. M. Gambetta, and A. Blais, Phys. Rev. A **79**, 013819 (2009).

[85] Deadmau5, ⟩ *album title goes here* ⟨ (mau5trap, Hollywood, CA, 2012).

[86] C. K. Law, Phys. Rev. A **51**, 2537 (1995).

[87] D. J. Griffiths, *Introduction to Quantum Mechanics* (Pearson Prentice Hall, 2004).

[88] C. Utschick, *Inductively Coupled Nano-Electromechanics in Flux Tunable Superconducting Resonators*, Master's thesis, Walther-Meißner-Institut and Technische Universität München (2018).

[89] R. Kumme, J. Illemann, V. Nesterov, and U. Brand, PTB-Mitteilungen **118**, 145 (2008).

[90] M. Pernpeintner, T. Faust, F. Hocke, J. P. Kotthaus, E. M. Weig, H. Huebl, and R. Gross, Appl. Phys. Lett. **105**, 123106 (2014).

[91] J. Chan, T. P. M. Alegre, A. H. Safavi-Naeini, J. T. Hill, A. Krause, S. Gröblacher, M. Aspelmeyer, and O. Painter, Nature **478**, 89 (2011).

[92] J. M. Fink, M. Kalaee, A. Pitanti, R. Norte, L. Heinzle, M. Davanço, K. Srinivasan, and O. Painter, Nat. Commun. **7**, 12396 (2016).

[93] A. Noguchi, R. Yamazaki, M. Ataka, H. Fujita, Y. Tabuchi, T. Ishikawa, K. Usami, and Y. Nakamura, New J. Phys. **18**, 103036 (2016).

[94] J.-M. Pirkkalainen, E. Damskägg, M. Brandt, F. Massel, and M. A. Sillanpää, Phys. Rev. Lett. **115**, 243601 (2015).

[95] T. Palomaki, J. Teufel, R. Simmonds, and K. Lehnert, Science **342**, 710 (2013).

[96] A. O'Connel, M. Hofheinz, M. Ansmann, R. C. Bialczak, M. Lenander, E. Lucero, M. Neeley, D. Sank, H. Wang, M. Weides, J. Wenner, J. Martinis, and A. N. Cleland, Nature **464**, 697 (2010).

[97] J.-M. Pirkkalainen, S. U. Cho, J. Li, G. S. Paraoanu, P. J. Hakonen, and M. A. Sillanpaa, Nature **494**, 211 (2013).

[98] A. Clerk, M. Devoret, S. Girvin, F. Marquardt, and R. Schoelkopf, Rev. Mod. Phys. **82**, 1155 (2010).

[99] L. Boltzmann, Wiener Berichte **63**, 679 (1871).

[100] F. Hocke, *Microwave circuit-electromechanics in a nanomechanical hybrid system*, Ph.D. thesis, Walther-Meißner-Institut and Technische Universität München (2013).

[101] A. H. Safavi-Naeini, J. Chan, J. T. Hill, T. P. M. Alegre, A. Krause, and O. Painter, Phys. Rev. Lett. **108**, 033602 (2012).

[102] T. J. Kippenberg, H. Rokhsari, T. Carmon, A. Scherer, and K. J. Vahala, Phys. Rev. Lett. **95**, 033901 (2005).

[103] F. Hocke, X. Zhou, A. Schliesser, T. Kippenberg, H. Huebl, and R. Gross, New J. Phys. **14**, 179 (2012).

[104] J. M. Dobrindt, I. Wilson-Rae, and T. J. Kippenberg, Phys. Rev. Lett. **101**, 263602 (2008).

[105] A. Schliesser, R. Rivière, G. Anetsberger, O. Arcizet, and T. J. Kippenberg, Nat. Phys. **4**, 415 (2008).

[106] M. L. Gorodetsky, A. Schliesser, G. Anetsberger, S. Deleglise, and T. Kippenberger, Opt. Express **18**, 23236 (2010).

[107] *Triton - The new generation Cryofree dilution refrigerator*, Oxford Instruments Ltd. (2019).

[108] R. Gross, *Low temperature physics* (Walther-Meißner-Institut, Garching, 2005).

[109] C. Deng, M. Otto, and A. Lupascu, J. Appl. Phys. **114**, 054504 (2013).

[110] J. Goetz, *The Interplay of Superconducting Quantum Circuits and Propagating Microwave States*, Ph.D. thesis, Walther-Meißner-Institut and Technische Universität München (2016).

[111] A. Schweiger and G. Jeschke, *Principles of pulse electron paramagnetic resonance*, reprinted. ed. (Oxford Univ. Press, Oxford, 2005).

[112] F. Yan, S. Gustavsson, A. Kamal, J. Birenbaum, A. P. Sears, D. Hover, T. J. Gudmundsen, D. Rosenberg, G. Samach, S. Weber, J. L. Yoder, T. P. Orlando, J. Clarke, A. J. Kerman, and W. D. Oliver, Nat. Commun. **7**, 12964 (2016).

[113] J. D. Teufel, "Scientists bring 'nonsensical' quantum physics into the real world for the first time," (2017).

[114] C. U. Lei, A. J. Weinstein, J. Suh, E. E. Wollman, A. Kronwald, F. Marquardt, A. A. Clerk, and K. C. Schwab, Phys. Rev. Lett. **117**, 100801 (2016).

[115] V. C. Vivoli, T. Barnea, C. Galland, and N. Sangouard, Phys. Rev. Lett. **116**, 070405 (2016).

[116] S. G. Hofer, K. W. Lehnert, and K. Hammerer, Phys. Rev. Lett. **116**, 070406 (2016).

[117] M. Abdi, P. Degenfeld-Schonburg, M. Sameti, C. Navarrete-Benlloch, and M. J. Hartmann, Phys. Rev. Lett. **116**, 233604 (2016).

[118] K. Børkje, Phys. Rev. A **94**, 043816 (2016).

[119] M. Abdi, M. Pernpeintner, R. Gross, H. Huebl, and M. Hartmann, Phys. Rev. Lett. **114**, 17360 (2015).

[120] D. Schuster, A. Wallraff, A. Blais, L. Frunzio, R.-S. Huang, J. Majer, S. Girvin, and R. Schoelkopf, Phys. Rev. Lett. **94**, 123602 (2005).

[121] F. R. Ong, M. Boissonneault, F. Mallet, A. Palacios-Laloy, A. Dewes, A. C. Doherty, A. Blais, P. Bertet, D. Vion, and D. Esteve, Phys. Rev. Lett. **106**, 167002 (2011).

[122] T. Yamamoto, K. Inomata, K. Koshino, P.-M. Billangeon, Y. Nakamura, and J. S. Tsai, New J. Phys. **16**, 015017 (2014).

[123] X. Zhou., F. Hocke, A. Marx, H. Huebl, R. Gross, and T. Kippenberg, Nat. Phys. **9**, 179 (2013).

[124] M. Yuan, V. Singh, Y. Blanter, and G. A. Steele, Nat. Commun. **86**, 1391 (2015).

[125] S. Weis, R. Rivière, S. Deléglise, E. Gavartin, O. Arcizet, A. Schliesser, and T. J. Kippenberg, Science **330**, 1520 (2010).

[126] V. Singh, S. J. Bosman, B. H. Schneider, Y. M. Blanter, A. Castellanos-Gomez, and G. A. Steele, Nat. Nanotechnol. **9**, 820 (2014).

[127] D. Schwienbacher, *Circuit nano-electromechanics transmon qubits, nano-strings and resonators*, Master's thesis, Walther-Meißner-Institut and Technische Universität München (2016).

[128] J. Goetz, F. Deppe, P. Eder, M. Fischer, M. Muetting, J. Martinez, S. Pogorzalek, F. Wulschner, E. Xie, K. Federov, A. Marx, and R. Gross, Quantum Sci. Technol. **2**, 025002 (2017).

[129] J. Goetz, S. Pogorzalek, F. Deppe, K. Federov, P. Eder, M. Fischer, F. Wulschner, E. Xie, A. Marx, and R. Gross, Phys. Rev. Lett. **118**, 103602 (2017).

[130] L. S. Bishop, J. M. Chow, J. Koch, A. A. Houck, M. H. Devoret, E. Thuneberg, S. M. Girvin, and R. J. Schoelkopf, Nat. Phys. **5**, 105 (2008).

[131] J. Braumüller, J. Cramer, S. Schlör, H. Rotzinger, L. Radtke, A. Lukashenko, P. Yang, S. T. Skacel, S. Probst, M. Marthaler, L. Guo, A. V. Ustinov, and M. Weides, Phys. Rev. B **91**, 054523 (2015).

[132] P. Weber, J. Güttinger, A. Noury, J. Vergara-Cruz, and A. Bachtold, Nat. Commun. **7**, 12496 (2016).

[133] L. Rosenzweig, *Design and Realisation of Superconducting Quantum Circuits for Nano-Electromechanical Experiments*, Master's thesis, Walther-Meißner-Institut and Technische Universität München (2018).

[134] J. Goetz, F. Deppe, M. Haeberlein, F. Wulschner, C. W. Zollitsch, S. Meier, M. Fischer, P. Eder, E. Xie, K. G. Fedorov, E. P. Menzel, A. Marx, and R. Gross, J. Appl. Phys. **119**, 015304 (2016).

[135] A. Abragam, *The principles of nuclear magnetism* (Oxford University Press, Oxford, 1961).

[136] M. Kjaergaard, M. E. Schwartz, J. Braumüller, P. Krantz, J. I.-J. Wang, S. Gustavsson, and W. D. Oliver, "Superconducting qubits: Current state of play," (2019).

[137] A. Schneider, J. Braumüller, L. Guo, P. Stehle, H. Rotzinger, M. Marthaler, A. V. Ustinov, and M. Weides, Phys. Rev. A **97**, 062334 (2018).

[138] J. Raftery, D. Sadri, S. Schmidt, H. E. Türeci, and A. A. Houck, Phys. Rev. X **4**, 031043 (2014).

[139] F. Hoehne, Y. A. Pashkin, O. Astafiev, L. Faoro, L. B. Ioffe, Y. Nakamura, and J. S. Tsai, Phys. Rev. B **81**, 231 (2010).

[140] J. Sulkko, M. A. Sillanpää, P. Häkkinen, L. Lechner, M. Helle, A. Fefferman, J. Parpia, and P. J. Hakonen, Nano Lett. **10**, 4884 (2010).

[141] M. D. Reed, L. DiCarlo, B. R. Johnson, L. Sun, D. I. Schuster, L. Frunzio, and R. J. Schoelkopf, Phys. Rev. Lett. **105**, 173601 (2010).

[142] M. D. Reed, *Entanglement and quantum error correction with superconducting qubits*, Ph.D. thesis, Yale University (2013).

[143] J. M. Gambetta, C. E. Murray, Y.-K.-K. Fung, D. T. McClure, O. Dial, W. Shanks, J. W. Sleight, and M. Steffen, IEEE Trans. Appl. Supercon. **27**, 1 (2017).

[144] S. Schmid, K. D. Jensen, K. H. Nielsen, and A. Boisen, Phys. Rev. B **84** (2011).

[145] R. Gross and A. Marx, *Festkörperphysik* (Oldenburg Wissenschaftsverlag, München, 2012).

[146] K. F. Wulschner, *Nb/AlOx/Nb Josephson-Kontakte für supraleitende Quantenschaltkreise*, Master's thesis, Walther-Meißner-Institut and Technische Universität München (2011).

[147] M. Fischer, *t.b.a.*, Ph.D. thesis, Walther-Meißner-Institut and Technische Universität München (2019).

[148] D. Arweiler, *Multi-SQUID Josephson Parametric Amplifiers*, Master's thesis, Walther-Meißner-Institut and Technische Universität München (2018).

[149] M. T.-Amawi, *Coherent coupling between superconducting quantum circuits and ferrimagnetic magnons*, Master's thesis, Walther-Meißner-Institut and Technische Universität München (2019).

[150] J. S. Huber, G. Rastelli, M. J. Seitner, J. Kölbl, W. Belzig, M. I. Dykman, and E. M. Weig, "Detecting squeezing from the fluctuation spectrum of a driven nanomechanical mode," (2019).

[151] M. Pernpeintner, P. Schmidt, D. Schwienbacher, R. Gross, and H. Huebl, Phys. Rev. Appl. **10**, 4448 (2018).

[152] R. J. Corruccini and J. J. Gniewek, *Thermal expansion of technical solids at low temperatures; a compilation from the literature* (U.S. Government Printing Office, Washington D.C., 1961).

[153] W. A. Phillips, Rep. Prog. Phys **50**, 1657 (1987).

[154] C. C. Yu and A. J. Leggett, Comments Condens. Matter Phys. **14**, 231 (1988).

[155] A. J. Leggett, Physica B. **169**, 322 (1991).

[156] S. S. Verbridge, J. M. Parpia, R. B. Reichenbach, L. M. Bellan, and H. G. Craighead, J. Appl. Phys. **99**, 124304 (2006).

[157] A. H. Ghadimi, S. A. Fedorov, N. J. Engelsen, M. J. Bereyhi, R. Schilling, D. J. Wilson, and T. J. Kippenberg, Science **360**, 764 (2018).

[158] S. Hunklinger and A. Raychaudhuri, Progress in Low Temperature Physics **9**, 265 (1986).

[159] M. E. Straumanis and C. L. Woodward, Acta. Cryst. A **27**, 549 (1971).

[160] J. P. Hirth and J. Lothe, *Theory of Dislocations* (Wiley, New York, NY, 1981).

[161] J. A. Mydosh, *Spin Glasses: An Experimental Introduction* (Taylor and Francis, London, 1993).

[162] *Model 372 performance*, Lakeshore (2019).

[163] *LNF-LNC4-8*, Low noise factory (2019).

[164] J. D. Teufel, T. Donner, M. A. Castellanos-Beltran, J. W. Harlow, and K. W. Lehnert, Nat. Nanotechnol. **4**, 820 (2009).

[165] R. Rivière, S. Deléglise, S. Weis, E. Gavartin, O. Arcizet, A. Schliesser, and T. J. Kippenberg, Phys. Rev. A **83**, 986 (2011).

[166] J. Moser, J. Güttinger, A. Eichler, M. Espandiu, D. Liu, M. Dykman, and A. Bachtold, Nat. Nanotechnol. **8**, 493 (2013).

[167] J. Moser, A. Eichler, J. Güttinger, M. I. Dykman, and A. Bachtold, Nat. Nanotechnol. **9**, 1007 (2014).

[168] K. K. Steinke, *Farvel Og Tak*, originally 'Det er vanskeligt at spaa, især naar det gælder Fremtiden' by (Fremad, 1948).

[169] N. F. Mott and E. A. Davis, *Electronic properties in non-crystalline materials*, 2nd ed. (Oxford university press, Oxford, New York, 1979).

[170] K. Uhlig, *private communication* (2019).

[171] J. D. Teufel, J. W. Harlow, C. A. Regal, and K. W. Lehnert, Phys. Rev. Lett. **101**, 197203 (2008).

[172] G. Anetsberger, O. Arcizet, Q. P. Unterreithmeier, R. Rivière, A. Schliesser, E. M. Weig, J. P. Kotthaus, and T. J. Kippenberg, Nat. Phys. **5**, 909 (2009).

[173] D. J. Wilson, C. A. Regal, S. B. Papp, and H. J. Kimble, Phys. Rev. Lett. **103**, 207204 (2009).

[174] J. Hofer, A. Schliesser, and T. J. Kippenberg, Phys. Rev. A **82**, 143 (2010).

[175] E. Verhagen, S. Deléglise, S. Weis, A. Schliesser, and T. J. Kippenberg, Nature **482**, 63 (2012).

[176] E. Gavartin, P. Verlot, and T. J. Kippenberg, Nat. Nanotechnol. **7**, 509 (2012).

[177] T. P. Purdy, R. W. Peterson, P.-L. Yu, and C. A. Regal, New J. Phys. **14**, 115021 (2012).

[178] T. P. Purdy, R. W. Peterson, and C. A. Regal, Science **339**, 801 (2013).

[179] T. A. Palomaki, J. W. Harlow, J. D. Teufel, R. W. Simmonds, and K. W. Lehnert, Nature **495**, 210 (2013).

[180] J. Kerckhoff, R. W. Andrews, H. S. Ku, W. F. Kindel, K. Cicak, R. W. Simmonds, and K. W. Lehnert, Phys. Rev. X **3**, 829 (2013).

[181] R. Thijssen, E. Verhagen, T. J. Kippenberg, and A. Polman, Nano Lett. **13**, 3293 (2013).

[182] T. P. Purdy, P.-L. Yu, R. W. Peterson, N. S. Kampel, and C. A. Regal, Phys. Rev. X **3**, 653 (2013).

[183] R. W. Andrews, R. W. Peterson, T. P. Purdy, K. Cicak, R. W. Simmonds, C. A. Regal, and K. W. Lehnert, Nat. Phys. **10**, 321 (2014).

[184] F. Hocke, M. Pernpeintner, X. Zhou, A. Schliesser, T. J. Kippenberg, H. Huebl, and R. Gross, Appl. Phys. Lett. **105**, 133102 (2014).

[185] S. A. Tadesse and M. Li, Nat. Commun. **5**, 5402 (2014).

[186] J.-M. Pirkkalainen, S. U. Cho, F. Massel, J. Tuorila, T. T. Heikkilä, P. J. Hakonen, and M. A. Sillanpää, Nat. Commun. **6**, 6981 (2015).

[187] D. J. Wilson, V. Sudhir, N. Piro, R. Schilling, A. Ghadimi, and T. J. Kippenberg, Nature **524**, 325 (2015).

[188] T. P. Purdy, P.-L. Yu, N. S. Kampel, R. W. Peterson, K. Cicak, R. W. Simmonds, and C. A. Regal, Phys. Rev. A **92**, 031802 (2015).

[189] R. W. Andrews, A. P. Reed, K. Cicak, J. D. Teufel, and K. W. Lehnert, Nat. Commun. **6**, 10021 (2015).

[190] F. Lecocq, J. B. Clark, R. W. Simmonds, J. Aumentado, and J. D. Teufel, Phys. Rev. X **5**, 041037 (2015).

[191] M. Yuan, M. A. Cohen, and G. A. Steele, Appl. Phys. Lett. **107**, 263501 (2015).

[192] J. D. Teufel, F. Lecocq, and R. W. Simmonds, Phys. Rev. Lett. **116**, 013602 (2016).

[193] F. Lecocq, J. B. Clark, R. W. Simmonds, J. Aumentado, and J. D. Teufel, Phys. Rev. Lett. **116**, 043601 (2016).

[194] R. W. Peterson, T. P. Purdy, N. S. Kampel, R. W. Andrews, P.-L. Yu, K. W. Lehnert, and C. A. Regal, Phys. Rev. Lett. **116**, 063601 (2016).

[195] R. Schilling, H. Schütz, A. H. Ghadimi, V. Sudhir, D. J. Wilson, and T. J. Kippenberg, Phys. Rev. Appl. **5**, 054019 (2016).

[196] V. Sudhir, D. J. Wilson, R. Schilling, H. Schütz, S. A. Fedorov, A. H. Ghadimi, A. Nunnenkamp, and T. J. Kippenberg, Phys. Rev. X **7**, 011001 (2017).

[197] N. S. Kampel, R. W. Peterson, R. Fischer, P.-L. Yu, K. Cicak, R. W. Simmonds, K. W. Lehnert, and C. A. Regal, Phys. Rev. X **7**, 021008 (2017).

[198] L. D. Tóth, N. R. Bernier, A. Nunnenkamp, A. K. Feofanov, and T. J. Kippenberg, Nat. Phys. **13**, 787 (2017).

[199] G. A. Peterson, F. Lecocq, K. Cicak, R. W. Simmonds, J. Aumentado, and J. D. Teufel, Phys. Rev. X **7**, 031001 (2017).

[200] N. R. Bernier, L. D. Tóth, A. Koottandavida, M. A. Ioannou, D. Malz, A. Nunnenkamp, A. K. Feofanov, and T. J. Kippenberg, Nat. Commun. **8**, 604 (2017).

[201] W. H. Renninger, P. Kharel, R. O. Behunin, and P. T. Rakich, Nat. Phys. **14**, 601 (2018).

[202] A. P. Higginbotham, P. S. Burns, M. D. Urmey, R. W. Peterson, N. S. Kampel, B. M. Brubaker, G. Smith, K. W. Lehnert, and C. A. Regal, Nat. Phys. **14**, 1038 (2018).

[203] L. D. Tóth, N. R. Bernier, A. K. Feofanov, and T. J. Kippenberg, Phys. Lett. A **382**, 2233 (2018).

[204] S. A. Fedorov, V. Sudhir, R. Schilling, H. Schütz, D. J. Wilson, and T. J. Kippenberg, Phys. Lett. A **382**, 2251 (2018).

[205] C. F. Ockeloen-Korppi, E. Damskägg, G. S. Paraoanu, F. Massel, and M. A. Sillanpää, Phys. Rev. Lett. **121**, 243601 (2018).

[206] L. Mercier de Lépinay, E. Damskägg, C. F. Ockeloen-Korppi, and M. A. Sillanpää, Phys. Rev. Appl. **11**, 034027 (2019).

[207] I. Shomroni, L. Qiu, D. Malz, A. Nunnenkamp, and T. J. Kippenberg, Nat. Commun. **10**, 2086 (2019).

[208] I. C. Rodrigues, D. Bothner, and G. A. Steele, "Coupling microwave photons to a mechanical resonator using quantum interference," (2019).

[209] K. W. Murch, K. L. Moore, S. Gupta, and D. M. Stamper-Kurn, Nat. Phys. **4**, 561 (2008).

List of Figures

List of Tables

List of Publications

- M. Pernpeintner, P. Schmidt, D. Schwienbacher, R. Gross, and Hans Huebl. Frequency Control and Coherent Excitation Transfer in a Nanostring-resonator Network. *Phys. Rev. Appl.* **10**, 034007 (2018); doi: 10.1103/PhysRevApplied.10.034007

- P. Schmidt, D. Schwienbacher, M. Pernpeintner, F. Wulschner, F. Deppe, A. Marx, R. Gross, and Hans Huebl. Ultrawide-range photon number calibration using a hybrid system combining nano-electromechanics and superconducting circuit quantum electrodynamics *Appl. Phys. Lett.* **113**, 152601 (2018); doi: 10.1063/1.5052414

- P. Schmidt, M. T. Amawi, S. Pogorzalek, F. Deppe, A. Marx, R. Gross, and H. Huebl. Sideband-resolved resonator electromechanics on the single-photon level based on nonlinear Josephson inductance *in preparation*

Acknowledgments